NAS 1.60:1591

FULL-SCALE WIND-TUNNEL INVESTIGATION OF THE ADVANCED
TECHNOLOGY LIGHT TWIN-ENGINE AIRPLANE (ATLIT) ...
NASA TECHNICAL PAPER 1591... NATIONAL AERONAUTICS
AND SPACE ADMINISTRATION... MAY 1980

1 OF 4
24X
SUPTDOCS
GPO

Item 830-H-15
NAS1.60:1591
COMPLETED
MAY 20 1980

NASA Technical Paper 1591

Full-Scale Wind-Tunnel Investigation of the Advanced Technology Light Twin-Engine Airplane (ATLIT)

James L. Hassell, Jr., William A. Newsom, Jr.,
and Long P. Yip

MAY 1980

NASA

212

NASA Technical Paper 1591

Full-Scale Wind-Tunnel Investigation of the Advanced Technology Light Twin-Engine Airplane (ATLIT)

James L. Hassell, Jr., William A. Newsom, Jr.,
and Long P. Yip
Langley Research Center
Hampton, Virginia

National Aeronautics
and Space Administration

**Scientific and Technical
Information Office**

1980

a

SUMMARY

An investigation has been conducted in the Langley Full-Scale Tunnel to evaluate the aerodynamic performance, stability, and control characteristics of the Advanced Technology Light Twin-Engine airplane (ATLIT). Data were measured over an angle-of-attack range from -4° to 20° for various angles of sideslip between -5° and 15° at Reynolds numbers of 2.30×10^6 and 3.50×10^6 for various settings of power and flap deflection. Measurements were also made by means of special thrust-torque balances to determine the installed propeller characteristics. Additional aspects of study were drag cleanup of the basic airplane and the evaluation of the effect of winglets on drag and stability.

The investigation showed that aerodynamic performance was seriously degraded by excess drag at lift coefficients representative of climbing flight. Premature flow separation near the wing-fuselage juncture and leakage through the wing (as a result of the particular flap and spoiler installation) were the two most significant sources of this excess drag. Installation of a revised wing-fuselage fillet and elimination of flap and spoiler leak paths provided significant reductions in drag at climb conditions but had little effect on drag at cruise conditions. Engine cooling drag (for both engines) amounted to approximately 15 percent of total airplane drag for both the climb and cruise conditions. Stalling of the tail produced static longitudinal instability at lift coefficients below 2.4 for the configuration with a flap-deflection angle of 37° under conditions representative of a full-power wave-off. The airplane was directionally stable and had positive effective dihedral throughout the entire angle-of-attack range for all flap deflections and for all power conditions. Lateral-directional asymmetries caused by a simulated engine failure (one engine inoperative) were quite large but could be easily trimmed with reasonable deflections of spoilers and rudder. During an engine-out climb, performance penalties associated with lateral trim requirements were minimized by using spoiler control to trim out rolling-moment asymmetry rather than by sideslipping the airplane into the dead engine.

INTRODUCTION

The Advanced Technology Light Twin-Engine airplane (ATLIT) was developed by the University of Kansas Flight Research Laboratory as part of a general-aviation research project sponsored by grant (NGR 17-002-072) from the NASA Langley Research Center. Background information on this program together with the history of the ATLIT development and performance predictions are given in reference 1. The broad objective of the project was to apply existing jet-transport wing technology and advanced airfoil technology to general-aviation airplanes for the purpose of improving safety, efficiency, and utility. The ATLIT project was managed by the University of Kansas with additional involvement of (1) the Robertson Aircraft Corporation for detailed design; (2) the Piper Aircraft Corporation for modification, fabrication, and initial flight tests; and (3) Wichita State University for wind-tunnel tests in support of flap and spoiler lateral-control-system development.

The concept for the ATLIT design involved (1) wing planform modifications to improve cruise efficiency by means of taper, increased aspect ratio, and reduced area; (2) use of an advanced general-aviation airfoil (17-percent-thick GA(W)-1)[1] to improve high-lift and induced-drag characteristics; (3) full-span Fowler flaps to maintain low-landing speed at the higher wing loading; (4) a spoiler lateral control system in lieu of ailerons to provide roll control with the full-span Fowler flaps; and (5) advanced technology propellers incorporating a supercritical airfoil. The Piper PA-34-200 Seneca I, which was regarded as a typical current twin-engine design, was selected for the modifications.

The investigation of the ATLIT airplane has included flight tests at the Langley Research Center as well as wind-tunnel static-force tests in the Langley Full-Scale Tunnel. Preliminary flight-test results are reported in reference 1. The results of the Langley Full-Scale Tunnel tests are published here. The test objectives of the wind-tunnel program were to provide fundamental research information in the following areas:

1. Propeller performance
2. Drag evaluation and cleanup
3. Wing pressure distribution characteristics
4. Boundary-layer characteristics
5. Wake-survey characteristics
6. Effects of winglets
7. Flap effectiveness
8. Stability characteristics
9. Spoiler effectiveness
10. Engine-out trim drag

Preliminary results of measurements to obtain wing pressure distributions, wake momentum, and boundary-layer characteristics (items 3 to 5 in the foregoing list) are presented in reference 2. The results of the remaining tests are presented here.

Use of trade names or names of manufacturers in this report does not constitute an official endorsement of such products or manufacturers, either expressed or implied, by the National Aeronautics and Space Administration.

---

[1] Now designated LS(1)-0417 airfoil.

SYMBOLS

The three systems of axes used in the present investigation are presented in figure 1. Stability axes (fig. 1(a)) were used for longitudinal data for test conditions at 0° sideslip; wind axes (fig. 1(b)) were used for longitudinal data when the airplane was tested under sideslipped conditions; and body axes (fig. 1(c)) were used for all lateral-directional data. Unless otherwise specified, all data are referenced to the ATLIT aft center-of-gravity position, which corresponds to 25 percent of the mean geometric chord.

All measurements and calculations were made in U.S. Customary Units; however, all values contained in this investigation are presented in the International System of Units (SI) with the equivalent values given parenthetically in the U.S. Customary Units. (See ref. 3.)

A	aspect ratio, b^2/S
b	wing span, m (ft)
C_D	drag coefficient, Drag/$q_\infty S$
$C_{D,S}$	drag coefficient due to propeller slipstream, $C_T'' - C_T'$, or $C_{D,S} = (C_T - C_{T,e})\dfrac{2D^2}{(V/nD)^2 S}$
C_L	lift coefficient, Lift/$q_\infty S$
$C_{L,max}$	maximum lift coefficient
C_{L_α}	lift-curve slope, per deg
C_l	rolling-moment coefficient, Rolling moment/$q_\infty Sb$
C_{l_β}	effective dihedral parameter (or rolling moment due to sideslip), $\partial C_l/\partial \beta$, per deg
$C_{l_{\delta_r}}$	rolling-moment coefficient due to rudder deflection, $\partial C_l/\partial \delta_r$, per deg
C_m	pitching-moment coefficient, Pitching moment/$q_\infty S\bar{c}$
C_{m_α}	slope of pitching-moment curve, per deg
$C_{m_\alpha,tail}$	C_{m_α} of horizontal tail, per deg
$C_{m_{\delta_{stab}}}$	pitching-moment coefficient due to stabilator deflection, per deg
C_n	yawing-moment coefficient, Yawing moment/$q_\infty Sb$

C_{n_β}	directional stability parameter (or yawing moment due to sideslip), $\partial C_n/\partial \beta$, per deg
$C_{n_{\delta_r}}$	rudder effectiveness parameter (or yawing moment due to rudder deflection), $\partial C_n/\partial \delta_r$, per deg
C_P	power coefficient, $\dfrac{2\pi Q}{\rho n^2 D^5} = 2\pi C_Q$
C_Q	torque coefficient, $Q/\rho n^2 D^5$
C_T	propeller thrust coefficient, $T_{shaft}/\rho n^2 D^4$
C_T'	effective thrust coefficient, $T_e/q_\infty S$
C_T''	shaft thrust coefficient, $T_{shaft}/q_\infty S$
$C_{T,e}$	effective propeller thrust coefficient, $T_e/\rho n^2 D^4$
C_Y	side-force coefficient, Side force/$q_\infty S$
C_{Y_β}	side-force parameter (or side force due to sideslip), $\partial C_Y/\partial \beta$, per deg
$C_{Y_{\delta_r}}$	side-force coefficient due to rudder deflection, $\partial C_Y/\partial \delta_r$, per deg
c	local chord, m (ft)
$\bar{c}$	wing mean geometric chord, m (ft)
c_n	section normal-force coefficient obtained from integration of pressure measurements
D	propeller diameter, m (ft)
e	Oswald's airplane efficiency factor, $(1/\pi A)\ d(C_L^2)/d(C_D)$
i_p	incidence of propeller thrust axis, positive nose up, deg
n	propeller rotational speed, rps
Q	propeller shaft torque, N-m (ft-lbf)
q_S	propeller slipstream dynamic pressure, Pa (lbf/ft^2)
q_∞	free-stream dynamic pressure, $\rho V^2/2$, Pa (lbf/ft^2)
R	Reynolds number, $\rho V\bar{c}/\mu$
S	wing area, m^2 (ft^2)

T_e	effective thrust, $\text{Drag}_{\text{propeller removed}} - \text{Drag}_{\text{propellers operating}}$ (measured on tunnel scales), N (lbf)
T_{shaft}	shaft thrust (measured on propeller balance), N (lbf)
V	free-stream velocity, m/sec (ft/sec)
V/nD	propeller advance ratio
X,Y,Z	body axes
X_s,Y_s,Z_s	stability axes
X_w,Y_w,Z_w	wind axes
x,y,z	longitudinal, lateral, and vertical distances, m (ft)
y'	spanwise distance along winglet span, m (ft)
α	angle of attack (referenced to airplane longitudinal axis, see fig. 2), deg
β	angle of sideslip, deg
$\beta_{.75}$	propeller blade angle at 0.75 of the radius, deg
δ_f	flap-deflection angle, deg
δ_r	rudder-deflection angle, positive with trailing edge left, deg
δ_{spl}	spoiler-deflection angle, positive with spoiler up, deg
δ_{stab}	stabilator-deflection angle, positive trailing edge down, deg
ε	downwash angle, deg
η	propeller efficiency, $(C_T/C_P)(V/nD)$
μ	viscosity of air, N-sec/m^2 (slugs/ft-sec)
ρ	mass density of air, kg/m^3 (slugs/ft^3)

Subscripts:

f	flap
lt	left
prop	propeller
rt	right

W	wing
W.M.	windmilling
w	wind

Abbreviations:

c.g.	center of gravity
F.S.	fuselage station
L.E.	leading edge
T.E.	trailing edge
W.L.	water line

AIRPLANE

Description of Airplane

The airplane tested was the Advanced Technology Light Twin-Engine airplane (ATLIT), which is an extensively modified Piper PA-34-200 Seneca I general-aviation low-wing monoplane. Principal dimensions of the ATLIT are given in the three-view sketch of figure 2 and are compared with the corresponding Seneca I dimensions in table I. Figure 3 shows the ATLIT in flight, on the ground, and mounted for testing in the Langley Full-Scale Tunnel.

The advanced technology modifications implemented on the ATLIT were (1) replacement of the basic untapered, aspect-ratio-7.25 Seneca I wing having an NACA 65_2-415 airfoil and an area of 19.40 m^2 (208.7 ft^2) with a newly designed taper-ratio-0.50, aspect-ratio-10.32 wing having a 17-percent-thick GA(W)-1 airfoil and an area of 14.40 m^2 (155.0 ft^2); (2) installation of full-span, 30-percent-chord Fowler flaps to replace the partial-span, 20-percent-chord plain flaps used on Seneca I; and (3) use of a spoiler lateral control system instead of the conventional Seneca I ailerons. The ATLIT wing had 0.2° incidence at the root and -2.5° incidence at the tip, resulting in 2.7° of washout. The fuselage and empennage of the Seneca I were unmodified except for provision to attach the newly designed wing to the fuselage structure. Likewise, the engine nacelles of the Seneca I were unmodified forward of the fire wall; the aft portions of the nacelles were modified to fit the new wing structure. The main landing gear was fully retracted into the lower surface of the wing for both the Seneca I and ATLIT airplanes.

Geometric comparisons of these overall plan view modifications are shown in figure 4(a), and details relating to differences in wing geometries are given in figure 4(b). Coordinates and geometry of the Fowler flaps are given in figure 5. Details of the spoiler lateral control system are presented in figure 6. Although advanced technology propellers were evaluated during flight tests of the ATLIT, only the standard Hartzell two-bladed 1.93-m (76-in.) diameter HC-C2YK-ICEF/FO 7666A propellers were tested in the present wind-tunnel investigation. The propeller thrust axes were inclined 2.66° nose down with respect to the fuselage reference axis. The airplane was powered with two Lycoming IO360-CIE6 four-cylinder fuel-injected engines rated at 149 kW (200 bhp) at 2700 rpm. Propeller rotation was down at the center of the airplane. Special thrust-torque balances of the type illustrated in figure 7(a) were installed on the propeller shafts as shown in figure 7(b) to measure the propeller characteristics in the presence of the standard nacelles.

Drag Cleanup Modifications

During the initial flight investigation of ATLIT (ref. 1), tuft studies indicated that during climb, regions of flow separation exist on the wing upper surface inboard of the nacelles and on the sides of the fuselage. Several modifications, illustrated in figure 8, designed to alleviate the flow separation problem were evaluated during the flight tests. The drooped strakes (or wing-root leading-edge gloves) and the fuselage- and wing-vortex generators from the flight tests were evaluated in the present wind-tunnel investigation. The wing-body fillet shown in figure 8 was redesigned for the wind-tunnel investigation in order to provide better contouring with the refaired underside of the fuselage. Figure 9 shows top and bottom views of the wing-fuselage juncture without the fillet; figure 10 shows corresponding views with the fillet installed.

Several modifications were made to the ATLIT to reduce drag caused by protuberances. The bottom of the fuselage was refaired (fig. 11); the spoilers were rigged to fit flush with the wing upper surface; the flap tracks were faired; round-head rivets on the wing upper surface outboard of the nacelles were faired over; and 16 fuel tank inspection hatches along the lower surface of the wing were redesigned to fit flush with flush fasteners rather than lapped to the skin with round-head fasteners.

In order to evaluate the consequences of deviations in airfoil thickness from the GA(W)-1 section near the wing trailing edge (ref. 1), a special modification was made for the present wind-tunnel test. The entire Fowler flap system was removed, and a new wing trailing edge was fabricated to true GA(W)-1 airfoil geometry based on the coordinates given in table II. This wing trailing-edge modification essentially represents the wing without the irregularities associated with the original Fowler flap installation.

Figure 12 illustrates configuration modifications related to power-off testing with the propellers removed, engine inlets sealed, and engine cowl flaps closed. In this configuration the propeller spinners were sealed and faired to provide streamlining of the engine nacelles equivalent to that for the propellers-operating case. Because the nacelle inlets were sealed, there was essentially no internal flow in this configuration, which therefore represented a condition of zero cooling drag. Figure 13 illustrates a related configuration with the engine cowl flaps fully open.

Winglets

The ATLIT wing was modified with the winglet installation illustrated in figure 14. Each untwisted winglet had a span of 0.7925 m (31.2 in.) and an area of 0.279 in^2 (3.00 ft^2). A more complete description of the winglet geometry together with its airfoil coordinates is given in figure 15 and table III. The winglet cant angle could be varied from 5° to 20° in 5° increments, and the winglet skew angle could be varied from 5.0° to -7.5° in 2.5° increments. The juncture between the wing tip and the winglet root chord was refaired with each change in cant angle or skew angle. In conjunction with the investigation of the effect of winglets, chordwise pressure profiles were obtained at several wing spanwise stations by means of pressure belts cemented to the wing surfaces as illustrated in figure 14. The sketch of figure 16(a) provides a layout of the spanwise location of these wing surface-pressure measurements. Surface-pressure orifices were also installed in one of the winglets to obtain the winglet pressure distribution. Details of the winglet pressure-orifice locations at three spanwise locations are given in figure 16(b).

TESTS AND APPARATUS

Drag Cleanup

Tests were made to evaluate the effects of various drag cleanup modifications on the aerodynamic efficiency of the airplane. These tests were conducted with the propellers removed, winglets off, flaps retracted, and with all control surfaces neutral. The airplane was tested over an angle-of-attack range from -4° to 20° at a Reynolds number of 2.30×10^6 (based on $\bar{c}$) and from -4° to 12° at Reynolds numbers of 3.50×10^6 and 4.10×10^6. Wool tufts were taped over various areas of the airplane surface to evaluate regions of separated flow. Cameras were used to document the flow patterns depicted by the tufts. All drag cleanup tests were conducted at 0° sideslip.

Winglet Investigation

Similar tests were made to evaluate the effectiveness of winglets in reducing induced drag and thereby improving the aerodynamic efficiency of the airplane (particularly for conditions appropriate for climb). For this part of the investigation the airplane was tested over an angle-of-attack range from -4° to 20° at a Reynolds number of 2.30×10^6 and from -4° to 12° at a Reynolds number of 3.50×10^6, all at 0° sideslip. The effects of winglets on static lateral-directional characteristics were measured at sideslip angles from -4.3° to 15.7° throughout the angle-of-attack range at a Reynolds number of 2.30×10^6. In addition to conventional force data, surface-pressure measurements were made on the upper and lower surfaces of the left wing and winglet airfoil.

Stability and Control Investigation

Tests were made to evaluate the stability and control characteristics of the "as received" airplane for various conditions of symmetrical and engine-out (one engine inoperative) power. These tests were conducted over an angle-of-attack range from -4° to 20° and over a sideslip angle range from -4.3° to 15.7° at a Reynolds number of 2.30×10^6. A range of stabilator deflections from 4° to -12° was investigated for each of five flap deflections: 0°, 10°, 20°, 30°, and 37°. A range of spoiler deflections from 0° to 45° and a range of rudder deflections from 30° to -30° were investigated independently and in combination for several cases of symmetrical and engine-out power and for several of the five flap deflections.

In this part of the investigation, power settings were used for conditions corresponding to power for level flight and excess power for climb or wave-off. The advance ratio for each power condition was appropriate for the flight condition represented and for that which could be achieved in actual flight, although for these tests the propeller blade angles were fixed at $\beta_{.75} = 18^\circ$. Propeller thrust coefficients were then established for these test conditions from the propeller calibrations described in the next section.

Propeller Performance Tests

The propeller characteristics were evaluated in the presence of the nacelles by tests conducted at 0° angle of attack with the propeller thrust-torque strain gage balances illustrated in figure 7. The installation of these balances resulted in an extension of the propeller shafts of about 20.3 cm (8.0 in.); therefore, equivalent nacelle extensions were provided so that the engine inlets were properly spaced in relation to the propeller disc planes. Tests were conducted at tunnel speeds of 16.4, 27.4, and 41.2 m/sec (54, 90, and 135 ft/sec) for each of six fixed propeller blade angles ($\beta_{.75}$ = 16°, 18°, 20°, 22°, 24°, and 26°) and in each test for the full range of engine speed from idle to maximum manifold pressure. (The actual airplane engines were used to drive the propellers in these and all other power-on tests of this investigation.) This matrix of test conditions provided overlapping ranges of advance ratio V/nD, so that the range of speed and propeller variables associated with the normal constant-speed propeller operation was covered. Simultaneous measurements of effective thrust were obtained from the wind-tunnel scale system. The left and the right propellers were evaluated independently during these tests.

PRESENTATION OF RESULTS

Corrections

The longitudinal data from these tests have been corrected for blockage, airstream misalignment, buoyancy effects, mounting strut tares (including propeller slipstream effects), and wind-tunnel jet boundary effects on both wing and tail. Propeller slipstream effects at the tail are also accounted for in the tail-on jet boundary corrections. Application of jet boundary corrections in accordance with the method described in reference 4 was made using the data reduction programs of reference 5. Lift and drag have been corrected for the integrated average airstream misalignment, although no correction has been applied for an effective washout of about 1° due to the variation of flow angularity across the tunnel test section. Lateral data were not corrected for the lateral variation of stream angle, which produced asymmetries in rolling moment at 0° sideslip similar to the asymmetric moments noted in references 6 to 8. Instead, the lateral-directional data are referenced to sideslip angles which include a correction for the integrated average lateral-stream angle. Flow correction data are presented in appendix A.

Test Results

The test results are presented in the following figures, which are grouped in the order of discussion:

	Figure
Propeller characteristics:	
Aerodynamic characteristics of the propellers in presence of nacelles; $\alpha = 0^\circ$	17
Drag of stopped propeller at $\alpha = 0^\circ$	18
Drag of windmilling propeller at $\alpha = 0^\circ$	19
Drag cleanup:	
Effect of Reynolds number	20 and 21
Repeatability of data	22 and 23
Effect of leading-edge gloves and vortex generators	24 and 25
Effect of angle of attack on flow attachment for fully clean configuration	26 and 27
Effect of fairing over protuberances and installing fillets	28 and 29
Effect of wing trailing-edge modification	30 and 31
Effect of flap and spoiler leak paths	32
Effect of varying airflow through engine nacelles	33 and 34
Total effect of drag cleanup	35 and 36
Effect of drag cleanup on airplane efficiency	37
Effect of pressure belts and tufts	38 and 39
Winglets:	
Effect of winglet skew; cant, 20°	40 and 41
Effect of winglet skew; cant, 15°	42 and 43
Effect of winglet skew; cant, 10°	44
Effect of winglet skew; cant, 5°	45
Effect of winglet cant; skew, -5°	46
Summary of effect of winglets	47
Effect of winglet skew on span-load distribution	48

Figure

Stability and control:

Effect of power on longitudinal aerodynamics; $\delta_f = 0^\circ$ 49
Effect of power on longitudinal aerodynamics; $\delta_f = 10^\circ$ 50
Effect of power on longitudinal aerodynamics; $\delta_f = 20^\circ$ 51
Effect of power on longitudinal aerodynamics; $\delta_f = 30^\circ$ 52
Effect of power on longitudinal aerodynamics; $\delta_f = 37^\circ$ 53
Summary of effects of power and flap deflection on $C_{L,max}$, C_{L_α}, and dC_m/dC_L 54
Effect of stabilator deflection on longitudinal aerodynamics; $\delta_f = 0^\circ$ 55
Effect of stabilator deflection on longitudinal aerodynamics; $\delta_f = 10^\circ$ 56
Effect of stabilator deflection on longitudinal aerodynamics; $\delta_f = 20^\circ$ 57
Effect of stabilator deflection on longitudinal aerodynamics; $\delta_f = 30^\circ$ 58
Effect of stabilator deflection on longitudinal aerodynamics; $\delta_f = 37^\circ$ 59
Summary of effect of power and flap deflection on stabilator effectiveness 60
Effect of flap deflection on longitudinal aerodynamics with power off 61
Effect of flap deflection on static lateral-directional stability derivatives; power off 62
Effect of power on static lateral-directional stability derivatives . . . 63
Effect of winglets on static lateral-directional stability derivatives 64
Effect of sideslip angle on incremental wind axes drag coefficient for various flap-deflection angles 65
Effect of power, angle of attack, and flaps on spoiler effectiveness 66
Spoiler effectiveness comparison with 1/4-scale data 67
Effect of power on rudder effectiveness 68
Lateral-directional characteristics with right engine inoperative; $\delta_f = 0^\circ$ 69
Lateral-directional characteristics with right engine inoperative; $\delta_f = 20^\circ$ 70
Lateral-directional characteristics with right engine inoperative; $\delta_f = 37^\circ$ 71
Effect of asymmetric power on lift characteristics (simulated engine failure) 72

RESULTS AND DISCUSSION

Propeller Characteristics

The results of tests made to evaluate the installed propeller performance at 0° angle of attack are presented in figure 17. Although the propellers used on ATLIT normally operate as constant-speed propellers (where the blade angle varies with advance ratio and loading), propeller data were obtained in these tests with blade angles fixed for purposes of analysis. Results are presented for propeller blade angles (measured at 0.75 of the radius) of 16°, 18°, 20°, 22°, 24°, and 26°. As mentioned in the section "Tests and Apparatus," each blade angle was evaluated through the full range of engine power at three different tunnel velocities in order to cover the entire range of advance ratio of interest. The results of figure 17 for each individual blade setting are, therefore, curves faired through the data obtained at all three tunnel velocities.

Inasmuch as thrust and torque were measured on the propeller shaft in the presence of the engine nacelles, the coefficients and efficiencies presented correspond to "installed" propeller coefficients and efficiencies and are not the same as would be obtained with an "isolated" propeller. The efficiencies as measured here are not propulsive efficiencies, because thrust measured on the propeller shaft is not necessarily the net propulsive thrust (which could be either greater or less than shaft thrust). Details of measured propeller efficiency and propulsive efficiency are presented in appendix B.

The results (fig. 17) indicate peak propeller efficiencies of approximately 0.825 to 0.835 for blade angles of 20° to 26° for the range of advance ratio between 0.75 and 1.00. These values of installed propeller efficiency are 3 to 4 percent below the "propulsive" efficiencies of a two-bladed propeller with an activity factor of 90 tested at comparable conditions on a streamlined nacelle without a wing (fig. 3, ref. 9, generally referred to as the "Gray Charts"). Likewise, these measured propeller efficiencies are 3 to 4 percent lower than values quoted by the manufacturer.

During the propeller performance tests, drag measurements were also obtained from the propeller thrust balance for each of the six values of propeller blade angle with the propellers stopped. These results are presented in figure 18 in terms of two forms of drag coefficient: (1) the left-hand scale is a propeller drag coefficient based on propeller diameter; (2) the right-hand scale is the conventional drag coefficient based on the wing area of the subject airplane ($S = 14.40\ \text{m}^2$ $(155\ \text{ft}^2)$). In figure 18, the results of the present investigation are compared with the data of reference 10 and with an analytical approximation suggested by Hoerner in reference 11. Unfortunately, the present tests were limited to a small range of blade angles ($\beta_{.75} = 16^\circ$ to 26°) by the thrust balance installation, and no results were obtained with the propeller feathered. As the limited data of the present investigation agree reasonably well with the results of references 10 and 11, a rational estimate of the feathered-propeller drag of the propellers used on ATLIT can be obtained from the values of references 10 and 11 at $\beta_{.75} = 90^\circ$. These data emphasize the importance of feathering the propeller of the dead engine during an engine-out climb. For ATLIT, such feathering reduces the drag penalty attributable to a stopped propeller from $C_D = 0.0110$ to $C_D = 0.0008$.

During training flights, the evaluation of single-engine climb performance is often accomplished with the simulated dead engine throttled back to the low speed approximately equivalent to zero torque, which has been defined as the "windmilling propeller" state. The drag of a windmilling propeller is not equivalent to the drag of a feathered propeller; therefore, flight test single-engine climb performance obtained with the dead engine windmilling should be adjusted to account for the difference in drag between the "propeller windmilling" and the "feathered propeller" conditions. The results presented in figure 19 provide a basis for establishing this difference in propeller drag for the ATLIT airplane. In this figure, test results from the present investigation are compared with similar data from reference 10 for three parameters plotted as functions of propeller blade angle: the advance ratio for zero torque, the drag coefficient of the windmilling propeller, and the ratio of the windmilling-propeller drag to the stopped-propeller drag. The data of the present investigation are in excellent agreement with those of reference 10 for the blade angle versus advance ratio corresponding to zero torque. In other words, the present tests and the tests of reference 10 indicate that the windmilling-propeller state for any given blade angle occurs at a specific value of advance ratio. The drag of the windmilling propeller decreases with increasing blade angle, and the drag data of the present investigation agree reasonably well with those of reference 10. One of the general conclusions of reference 10 was that the drag of a windmilling propeller is greater than that of a stopped propeller for $\beta_{.75} < 15^\circ$ and less than that of a stopped propeller for $\beta_{.75} > 15^\circ$. Data from the present investigation tend to support this conclusion.

The effects of propeller drag on the engine-out climb performance of the ATLIT airplane may now be examined for three possible situations relating to the inoperative engine: (1) stopped propeller, (2) windmilling propeller, and (3) feathered propeller. The best rate-of-climb flight condition for ATLIT occurs at a free-stream velocity of 30.5 m/sec (87 knots) for a wing loading of 0.564 Pa (27 lbf/ft^2), as determined from data given in reference 1. The following table provides a comparison of the drag penalties associated with three possible propeller situations:

Engine characteristics	Inoperative engine		
	Stopped propeller	Windmilling propeller	Feathered propeller
Engine speed, rpm	0	1000	0
$\beta_{.75}$, deg	26	26	90
V/nD	---------	1.390	------
ΔC_D	0.0103	0.0021	0.0008
Difference in rate of climb (relative to feathered propeller), m/min (ft/min)	-29 (-95)	-4 (-13)	

For the operating engine: engine speed is 2700 rpm; $\beta_{.75} = 20^\circ$; V/nD = 0.515.

Drag Cleanup

Inasmuch as the climb and top-speed performance of ATLIT fell short of predictions (ref. 1), a part of the present wind-tunnel investigation was devoted to drag evaluation of the airplane as received and to the evaluation of various drag cleanup modifications. This part of the investigation was conducted with the propellers removed, winglets off, flaps retracted, horizontal tail on, and all control surfaces neutral.

The philosophy for the drag cleanup study was that careful attention to construction details could result in significant drag reductions. Reference 12 suggests the relative importance of various drag cleanup techniques applicable to current general-aviation airplanes. As shown in that study, drag improvement due to individual cleanup items is quite small, but a significant drag reduction can usually be achieved by combining the increments due to several cleanup items.

Reynolds number effects and data repeatability.- The maximum speed capability of the Langley Full-Scale Tunnel permits testing to a Reynolds number of about 3.28×10^6 per meter (1×10^6 per foot). However, airplane structural limitations impose additional restrictions on tunnel test speed, especially at the higher angles of attack when buffet is encountered. For the purpose of this study, the test Reynolds number should be as near full scale as possible and at least high enough that the drag coefficient of the GA(W)-1 airfoil is no longer sensitive to further reduction in Reynolds number. The effects of Reynolds number on the longitudinal characteristics of the airplane are presented in figures 20 and 21. (Throughout the drag cleanup discussion the overall longitudinal aerodynamics are presented as part (a) of each figure; the lift-drag polar is then presented with a greatly expanded drag-coefficient scale as part (b) of each figure.) Examination of the expanded lift-drag polars (figs. 20(b) and 21(b)) indicates that a test Reynolds number of 3.50×10^6 (based on $\bar{c}$) provided drag data nearly equal to that obtained at the maximum possible Reynolds number of 4.10×10^6. Drag data obtained at $R = 2.30 \times 10^6$ were higher than those measured at $R = 3.50 \times 10^6$. The trend of these Reynolds number effects agree with the results of two-dimensional tests of the 17-percent-thick GA(W)-1 airfoil presented in reference 13. Comparison of the results of figures 20 and 21 shows an increase in minimum drag at comparable values of Reynolds number which is attributable to unsealing the engine inlets. This drag increment is discussed in more detail in the section, "Engine Cooling Drag."

Results showing the repeatability of data at Reynolds numbers of 3.50×10^6 and 2.30×10^6 are presented in figures 22 and 23, respectively. Data for the higher Reynolds number were repeatable within ΔC_D values of 0.0005, an accuracy which corresponds to the published accuracy of the tunnel scale system.

Wing-root leading-edge gloves and vortex generators.- During the ATLIT flight investigation, one source of drag was identified as flow separation on the wing upper surface inboard of the nacelles and on the sides of the fuselage at values of C_L corresponding to the climb condition. (See ref. 1.) Two devices used during the flight investigation to alleviate the premature flow separation were the drooped-leading-edge gloves, or strakes, and the vortex generators placed on the upper surface of the wing inboard of the nacelles and on the sides of the fuselage above the wing. (See fig. 8.) A third device designed to alleviate this same problem was the wing-fuselage fillet used in the flight investigation. (Again see fig. 8.) For the present wind-tunnel investigation this wing-fuselage fillet was redesigned to provide better contouring with the refaired underside of the fuselage as shown in figure 10. During the wind-tunnel investigation, the effects of the wing-root leading-edge gloves and vortex generators in combination with the redesigned wing-fuselage fillets were determined. (Tests were not conducted to determine the effects of leading-edge gloves or vortex generators with the wing-fuselage fillets removed.)

The results presented in figures 24 and 25 indicate favorable effects caused by leading-edge gloves and vortex generators only at the highest angles of attack (values of $C_L > 1.0$). Each of these devices produced small drag penalties at values of lift coefficient corresponding to cruise. These results are what would be expected if the redesigned wing-fuselage fillets could completely solve the problem of premature flow separation.

Tuft studies conducted with the redesigned wing-fuselage fillets installed showed no flow separation on the wing upper surface inboard of the nacelles or on the sides of the fuselage at angles of attack below about 8° or for lift coefficients less than 1.10. (See figs. 26 and 27.) The conclusion is therefore drawn that the redesigned fillets solved the problem of premature flow separation. The effects of the redesigned fillets in relation to fillets removed are discussed in the next section.

Drag cleanup related to fairing over protuberances and installing fillets.- Certain features of the redesigned wing caused problems in mating the wing to the unmodified fuselage and to the essentially unmodified engine nacelles. For example, the redesigned wing was equipped with full-span Fowler flaps with external flap tracks. The wing juncture at the underside of the fuselage was built to accommodate the inboard flap tracks, but this installation resulted in an aerodynamically poor interface between the wing and fuselage. This interface consisted of a streamwise gap about 75 cm (3 in.) wide extending from the rear wing spar to the wing trailing edge, so that the wing had no lower-surface skin to join with the fuselage in this area. Also, the underside of the basic Seneca I fuselage had numerous protuberances consisting of external structural stiffeners and wing spar attachment brackets. (See fig. 11(a).) As part of the drag cleanup, this area of the fuselage bottom was covered with sheet metal and refaired with the underside of the wing at the wing-fuselage juncture. (See fig. 11(b).) The gap in the lower-surface skin at this juncture was eliminated by the refairing. Comparison of figures 9 and 10 shows how the wing-fuselage trailing-edge fillet was added so that both the upper and lower surface of the wing at this juncture were smoothly contoured.

Other protuberances were primarily on the wing. There were 16 poorly fitted fuel tank inspection hatches located along the bottom of the wing, roundhead rivets at the wing-nacelle juncture, exposed flap brackets, and external spoiler hinges on the wing upper surface. Although refairing or covering these protuberances offered a relatively small potential for drag reduction because most of the protuberances were probably submerged in the local boundary layer, each of these protuberances was either faired or rebuilt flush with the local surface.

The results of tests made to evaluate the effect of fairing over protuberances and installing the wing-fuselage fillets are presented in figures 28 and 29. The drag data obtained at $R = 3.50 \times 10^6$ (fig. 28(b)) are the most significant. These results indicate the overall drag reduction at cruise ($C_L \approx 0.40$) was very small ($\Delta C_D \approx 0.0005$), but drag reduction corresponding to climb ($C_L \approx 1.00$) was significant ($\Delta C_D \approx 0.0050$). Most of this improvement resulted from installation of the wing-fuselage fillets, which delayed the premature wing-root flow separation.

Modified wing trailing edge.- The original installation of the full-span Fowler flap resulted in considerable spanwise irregularity in airfoil trailing-edge profile, especially aft of the 70-percent-chord station. In order to evaluate the effect of these trailing-edge discrepancies, the Fowler flap was removed and a new wing trailing edge was fabricated to true GA(W)-1 airfoil coordinates. Figures 30 and 31 present results obtained with the refabricated wing trailing edge compared with the as-received wing with the Fowler flap nested. The differences in drag cannot be attributed totally to trailing-edge irregularities because the as-received wing also was subject to drag associated with flap and spoiler leakage. This source of drag is discussed in the next section. The only proper conclusion to be drawn from the data of figures 30 and 31 is that the effects of trailing-edge irregularity on drag were negligible at lift coefficients corresponding to cruise flight. The reduced drag with the refabricated trailing edge at higher values of C_L was probably related to elimination of flap and spoiler leakage rather than elimination of trailing-edge irregularities. (These data also suggest that drag due to leakage might be eliminated by a tightly sealed flap installation.)

Flap and spoiler leak paths.- Inasmuch as the previously discussed results suggest abnormally high drag at the higher values of C_L, possibly associated with leakage through the wing trailing edge, tests of the as-received configuration were conducted with all possible sources of leaks through the wing sealed with plastic tape. During the flight investigation (ref. 1), a flap leak path was sealed with foam rubber weatherstripping as indicated in figure 6(b). Wind-tunnel test results to evaluate the effect of leak paths are presented in figure 32. These results indicate taping the flap leading-edge gap alone produced no measurable change in drag throughout the lift-coefficient range, but taping both the flap leading-edge gap (on the bottom of the wing) and the spoiler gaps (on the wing upper surface) caused a pronounced reduction in drag at the higher values of C_L. Apparently, the spoiler leak path was subject to venting at other places, at the wing-fuselage juncture at the end of the Fowler flap cove and through the open wheel wells, for example. A possible solution for this leak-path problem would be to seal all possible vent paths associated with the retracted Fowler flap.

Engine cooling drag.- As mentioned previously, a significant increment of drag is related to internal flow through the nacelles. Figures 20 and 21 present data for engine inlets sealed and unsealed, respectively. The position of the engine cowl flaps also governs the quantity of internal flow. Figure 12 shows the cowl flaps closed as they would be for engine cooling in normal cruise flight. Figure 13 shows the cowl flap fully open as would be required for adequate engine cooling in a full-power climb. An approximation of the drag attributable to engine cooling requirements is therefore obtainable from tests varying the quantity of internal flow through the engine nacelles. This method of assessing engine cooling drag is not exact because propeller slipstream effects are not included (propellers were removed, therefore inlet flow was free stream), and thermodynamic effects on internal pressure drop were not simulated (engines were not operating). Past experience has indicated this method to be conservative, accounting for only about 75 percent of the total cooling drag.

Test results showing the effect of varying airflow through the engine nacelles are presented in figures 33 and 34. From these results the approximation for cooling drag for the cruise condition ($C_L \approx 0.38$) is $\Delta C_D = 0.0035$, the increment between inlets sealed, cowls closed, and inlets unsealed, cowls closed. Similarly, the approximation for cooling drag for the climb condition ($C_L \approx 1.00$) is $\Delta C_D = 0.0080$, the increment between inlets sealed, cowls closed, and inlets unsealed, cowls open. These values of cooling drag are conservative and, to be realistic, should be increased by about 33 percent. The resulting cooling drag magnitudes would then be

Flight condition	$\Delta C_{D,cooling}$ (two engines)	Percent $C_{D,airplane}$
Cruise	0.0059	15.3
Climb	.0107	15.0

Considerable performance improvements (both in cruise and climb) could result from refinement of the engine cooling system.

Overall drag cleanup.- Results comparing the longitudinal aerodynamics and drag of the ATLIT airplane as received and fully clean are presented in figures 35 and 36. These data were obtained with engine inlets sealed and cowl flaps closed and therefore do not include cooling drag. The effects of flap and spoiler leakage are in the data for the as-received configuration. These overall results show improvements in lift-curve slope as well as reduced drag, particularly for the climb condition ($C_L \approx 1.00$) where a drag reduction of $\Delta C_D = 0.0100$ was realized. Most of this drag reduction was related to the effects of the wing-fuselage fillets and the elimination of the spoiler leakage path.

The data of figure 35(b) have been used in figure 37 to show the overall effect of the drag cleanup on the airplane efficiency factor, which is a measure of induced drag. These results apply to the untrimmed power-off configuration and show an improvement in airplane efficiency of approximately 14 percent attributable to the drag cleanup; however, the potential for further improvement is evident because Oswald's airplane efficiency factor was only 0.734 for the fully clean configuration. The reason for this relatively low airplane efficiency is related to the nacelle interference effects on the span-load distribution, as is discussed in a later section.

Pressure instrumentation belts and tufts.- The effects of the pressure belts used to obtain surface-pressure distributions on the left wing and the wool tufts distributed over the right wing and fuselage are presented in figures 38 and 39 at Reynolds numbers of 3.50×10^6 and 2.30×10^6, respectively. These results indicate ΔC_D values of 0.0010 to 0.0015 attributable to either of these testing technique devices. Also, the results indicate no measurable effect of these devices on lift and pitching-moment coefficients.

Winglet Investigation

Investigation of the effect of winglets on drag was conducted with the airplane in the fully clean configuration. Most of the results were obtained with the propellers removed, cowl flaps closed, and engine inlets open. In addition to conventional force data, upper- and lower-surface pressure measurements were obtained to evaluate the effect of winglet variables on span-load distribution. Pressure belts were cemented to the wing surface to obtain the wing pressure distribution at spanwise stations of 17.0, 31.0, 50.0, 75.0, 91.0, and 96.0 percent of the wing semispan. Surface-pressure orifices were installed in the winglet to obtain the winglet pressure distribution from spanwise stations at 22.0, 50.0, and 78.0 percent of the winglet span. Details of the pressure-orifice locations for the wing and winglet are given in figures 16(a) and 16(b), respectively. Installation of the winglet and pressure belts on the left wing is shown in the photograph of figure 14.

Only one winglet size was evaluated. Each winglet had 0.279 m^2 (3.00 ft^2) of area corresponding to 1.94 percent of the wing area. The two variables were winglet cant angle (measured with respect to the wing-chord plane) and winglet skew angle (measured with respect to the airplane longitudinal body axis). Positive skew and cant angles are defined in figure 15(b).

Longitudinal aerodynamics and drag polars.- The effects of winglet skew and cant on the longitudinal aerodynamics of the airplane are presented in figures 40 to 46. Expanded lift-drag polars are presented as part (b) of each of these figures in order to compare the effects of winglet variables on drag coefficient with the data obtained with winglets removed (basic wing tip). The results show only minor effects of winglet variables on lift and pitching-moment coefficients. (See part (a) of figs. 40 to 46.) From the expanded lift-drag polars (part (b) of figs. 40 to 46), the data generally show higher drag with winglets on at the lower values of C_L and, for certain winglet variables, reduced drag with winglets on at the higher values of C_L. In order to examine the effects of winglet skew and cant on drag, the results at a Reynolds number of 3.50×10^6 are summarized in figure 47. The incremental drag due to the winglets $\Delta C_{D,winglet}$ is plotted against airplane lift coefficient. These results show drag penalties due to winglets at all values of C_L below 0.6 for the entire range of skew and cant investigated. In general, negative skew angles (toe in) produced favorable drag increments at C_L values above about 0.8. The most favorable effect at climb lift coefficient combined with one of the least detrimental effects at cruise lift coefficient was obtained with a cant angle of 20° and with a skew angle of -7.5°.

Span-load distribution.- To help explain the poor results obtained with winglets, selected span-load distributions as determined from surface pressures are presented in figure 48. Figure 48(a) shows the effect of winglet skew angle on span-load distribution at angles of attack corresponding to cruise ($\alpha = 0^{\circ}$) and with the winglet cant angle fixed at 20°. For the cruise condition, the span-load distribution of the basic wing was far from that predicted by theory; nacelle interference effects were drastic, and loading near the wing tip was very low. The low loading at the tip could have been influenced by the spanwise variations in tunnel flow presented in appendix A. Consequently, there was little or nothing in the nature of a wing-tip vortex flow for the winglet to operate on and thereby reduce drag. For the cruise condition, the winglets had no effect on loading at the wing tip with 5° skew (toe out) and produced only small increases in tip loading with 0° and -7.5° skew angle. Pressure distribution on the winglet itself indicates that it was essentially unloaded with a skew angle of 5° (toe out) and that favorable winglet loading developed with skew angles of 0° and -7.5°. These results suggest that although the winglets were producing the desired pressure distributions with zero and negative skew angles, no beneficial effects on drag were achieved because the airplane wing tip was essentially unloaded.

For the climb condition (fig. 48(b)), the span-load distribution for the basic wing was irregular and not at all representative of a desirable elliptical span loading. The winglets did produce increased loading on the wing tip; -7.5° skew produced the most favorable effect extending inboard to the 75-percent-semispan station. As indicated earlier, this particular combination of winglet variables (cant, 20°; skew, -7.5°) produced a modest reduction in drag ($\Delta C_{D,\text{winglets}} = -0.0023$; see fig. 47). The winglets used in this investigation should provide about twice the drag reduction achieved for the climb condition if the span-load distribution of the basic wing were more nearly elliptical. Also, small favorable drag increments in the cruise condition would be expected if the basic wing tip had developed sufficient loading to produce a strong tip vortex flow.

Stability and Control

As mentioned in "Tests and Apparatus," the stability and control portion of the investigation was conducted on the airplane as received. These tests included the determination of the effects of symmetrical and asymmetrical (one-engine-out) power on the stability and control characteristics of the airplane for various flap deflections. Although the blade angle of the propellers was fixed at one setting ($\beta_{.75} = 18^{\circ}$) during this part of the investigation, the power conditions selected (V/nD and C_T) were appropriate to represent cases corresponding to "power for level flight" or "excess power for climb or wave-off" for the various flap deflections tested. For convenience, the data presented in this section are keyed to the installed propeller coefficients of each propeller and the advance ratio ($C_{T,lt}$, $C_{T,rt}$, and V/nD) and to the propeller-shaft thrust coefficient C_T".

Effect of symmetrical power on longitudinal characteristics.- The results of tests to determine the effect of symmetrical power (equal thrust from left and right propellers) on the longitudinal characteristics are presented in figures 49 to 53 for flap-deflection angles of 0°, 10°, 20°, 30°, and 37°, respectively. Each set of data is presented for several fixed settings of the horizontal stabilator and with the horizontal tail removed. The pitching-moment curves are referenced to the most aft center-of-gravity position $(0.25\bar{c})$ unless otherwise specified.

Some of the significant results of figures 49 to 53 in terms of $C_{L,max}$, C_{L_α}, and dC_m/dC_L as affected by power and flap deflection are summarized in figure 54, where the total shaft thrust coefficient C_T'' (sum of left- and right-engine thrust) serves as a convenient correlating parameter. These summarized results show pronounced increases in $C_{L,max}$ and C_{L_α} resulting from increasing C_T'' for all flap deflections. These effects are partially due to direct thrust components, $\Delta L \doteq T_{shaft} \sin (\alpha + \delta_f + i_p)$, and partially due to propeller-slipstream-induced effects over the wings and flaps, which result in increased circulation lift. A point of interest shown in figure 54 is the increase in C_{L_α} due to flap deflection, which is attributable to the increased effective wing area resulting from translation of the full-span Fowler flaps. All lift coefficients are based on the reference wing area of 14.40 m^2 (155 ft^2) for the flap-retracted configuration, whereas the effective wing area increases by approximately 19 percent during the first 10° deflection of the Fowler flaps. (See fig. 5.)

The results summarized in figure 54 also show a pronounced reduction in static margin with increasing power for the tail-on conditions (fig. 54(a)) and very little effect of power on static instability for the tail-off condition (fig. 54(b)). Another point which deserves comment appears in these results. For the tail-off condition (fig. 54(b)), the level of static instability with $\delta_f = 0^\circ$ is about $0.24\bar{c}$ $(dC_m/dC_L = 0.24)$, whereas the configuration with flaps extended shows a level of static instability of about $0.12\bar{c}$ $(dC_m/dC_L = 0.12\bar{c})$. In effect, extension of the flap results in an aft shift of the aerodynamic center, as is expected because of the Fowler action which translates the flap rearward. For the tail-on conditions, the stabilizing effect of the Fowler flap translation was not realized. (See fig. 54(a).) The reason is probably related to rate of change of downwash at the tail $d\epsilon/d\alpha$, which is adversely affected by the increased downwash resulting from deflection of the full-span Fowler flaps.

Some significant results relating to longitudinal stability and trim cannot be properly assessed in the summary figures just discussed. Therefore, from the basic data, it is evident that the destabilizing effects of power are not serious for the cruise configuration $(\delta_f = 0^\circ)$ or for the smaller flap-deflection angles (figs. 49 to 51). But these power and flap effects become quite serious for the landing configurations $(\delta_f = 30^\circ$ or 37°; see figs. 52 and 53). In fact, for the most aft center-of-gravity location, the effects of power are serious enough to produce neutral or slightly negative static margin for typical near-trim conditions with the Fowler flaps deflected 30° or 37°. (See figs. 52(b) and 53(c).)

These poor longitudinal stability characteristics for the wave-off condition with full flap deflection are further complicated by the onset of tail stall, which is evident at the lower angles of attack with $\delta_{stab} = -8^{\circ}$. (See figs. 52(c) and 53(e).) This tail stall condition is caused by the severe downwash induced by the highly deflected full-span Fowler flaps with high power settings. It should be emphasized that the ATLIT horizontal tail is identical to the basic Seneca I tail; no provisions were made to increase the tail maximum lift coefficient or to otherwise adapt the tail to the more severe trim requirements imposed by the full-span Fowler flaps. The magnitude of the flap-induced diving moments which must be trimmed out by large deflections of the horizontal tail are evident when the tail-off pitching-moment curves of figures 49(d), 50(d), 51(d), 52(e), and 53(g) are compared for the full range of flap deflections. These results together with the tail-on data shown in figures 52(c) and 53(e) for the landing configurations ($\delta_f = 30^{\circ}$ or 37°) indicate that the down-load capability of the horizontal tail is saturated for angles of attack below 4° with $\delta_{stab} = -8^{\circ}$.

This tail stall problem is further complicated for landing conditions with more forward locations of the airplane center of gravity. Moving the center of gravity forward (to $0.15\bar{c}$, for example) further increases the flap-induced diving moments (compare figs. 53(g) and 53(h) for horizontal-tail-off data), thereby imposing even greater trim requirements for the horizontal tail. This condition results in a fully stalled horizontal tail at angles of attack below 4° for the exact stabilator setting required for trim ($\delta_{stab} = -8^{\circ}$; see fig. 53(f)). Under this condition the airplane is unstable at lift coefficients lower than about 2.4 and would probably experience a severe nose-down trim change (nose tuck) with an increase in power. Any effort to correct for nose tuck by application of more "back stick" would only further stall the tail and would not provide any nose-up trim.

In its present configuration, ATLIT should be limited to a flap angle of about 30° in order to avoid most of the problems associated with tail stall. In order to make full use of the high-lift capability of the full-span Fowler flaps, two design approaches are suggested. First, a T-tail configuration would place the horizontal stabilator in a region where the flap-induced downwash would be minimized; second, an inverted leading-edge slat on the present horizontal tail should increase both the tail maximum lift coefficient and the tail-deflection angle of stall onset. Either change should displace the tail stall problem outside the operational flight range.

Effect of horizontal-stabilator deflection on longitudinal control.- The results of tests to evaluate the longitudinal control characteristics of the airplane are presented in figures 55 to 59 for flap-deflection angles of 0°, 10°, 20°, 30°, and 37°, respectively. Data are presented in each figure for the power-off case (propellers stopped) and for two power-on conditions. Some of these results were discussed in the previous section on the effects of power on longitudinal stability and lift. In figures 55 to 59, longitudinal control is shown to be completely satisfactory except for the conditions when tail stall was encountered for near-trim conditions with the largest flap deflection. In this case ($\delta_f = 37^{\circ}$; see fig. 59), results are presented for both forward and aft center-of-gravity locations to illustrate the trim limitations imposed by tail stall as affected by center-of-gravity travel (for example, compare figs. 59(c) and 59(d)).

With the exception of flight conditions bordering the tail stall problem, the effects of power on longitudinal control effectiveness $C_{m_{\delta_{stab}}}$ are more readily seen in the summarized results of figure 60. In general, these results show that increasing power caused a substantial increase in longitudinal control effectiveness through some portion of the angle-of-attack range for all flap-deflection angles. These results indicate that the dynamic pressure at the tail due to propeller slipstream was to some extent altered by flap-deflection angle. Thus, a high-lift configuration tended to draw the slipstream downward so that its major effect on the tail was felt only at high angles of attack.

Effect of flap deflection on power-off longitudinal characteristics.- The longitudinal characteristics of the airplane as affected by deflection of the flaps is presented in figure 61 for three unpowered conditions: (1) propellers off, engine inlets sealed, and cowl flaps closed (fig. 61(a)); (2) propellers on and stopped with $\beta_{.75} = 18^\circ$, engine inlets unsealed, and cowl flaps open (fig. 61(b)); and (3) horizontal tail off with propellers stopped, inlets unsealed, and cowl flaps open (fig. 61(c)). The propellers-off data (fig. 61(a)) provide a set of lift-drag polars appropriate for performance analysis for the complete range of flap deflections. The lift curves are smooth and depict well-behaved stall characteristics for all flap angles. The pitching-moment curves show a relatively uniform level of static stability essentially unaffected by flap deflection throughout the usable lift range. The propellers-on data of figure 61(b) reflect the large increases in drag attributable to the combined effect of stopped propellers and free-stream flow through the nacelles (inlets unsealed and cowl flaps fully open). In addition, the presence of the stopped propellers apparently triggered earlier stall for the higher flap-deflection configurations, causing a reduction in $C_{L,max}$. The tail-off data of figure 61(c) indicate the large increase in diving moments caused by flap deflection which has been discussed previously.

Lateral-directional characteristics.- The results of tests to determine the static lateral-directional stability of the airplane are presented in figures 62 and 63 in terms of the derivatives C_{Y_β}, C_{n_β}, and C_{l_β} as functions of angle of attack. These derivatives were obtained from the average slopes of C_Y, C_n, and C_l versus sideslip angle over a range of β from -5° to 15° and are referred to the airplane body axes. (See fig. 1(c).) The effect of flap deflection on lateral-directional stability is shown in figure 62 for power-off conditions (propellers stopped). These results indicate the airplane was directionally stable and had positive effective dihedral for the entire range of flap deflections throughout the angle-of-attack range investigated. Flap deflection causes a modest reduction in directional stability for the middle angle-of-attack range and in general produced a large increase in effective dihedral. The decrease in directional stability probably resulted from some reduction in dynamic pressure over the vertical tail when the flaps were deflected. The increased effective dihedral is related to the higher lift-curve slopes for the flaps-deflected configurations. (See fig. 54.)

The effect of power on lateral-directional stability is shown in figure 63 for $\delta_f = 0^\circ$ and 37°. For the flaps-retracted case (fig. 63(a)) power had little or no effect on directional stability but did cause an increase in effective dihedral in the lower angle-of-attack range. This result is consistent with the increase in lift-curve slope caused by power. For the flaps-deflected case (fig. 63(b); $\delta_f = 37^\circ$), power reduced directional stability, although the airplane was still directionally stable throughout the angle-of-attack range. Power caused a reduction in effective dihedral below the angle of attack corresponding to power-off stall ($\alpha \approx 10^\circ$) and a large increase in effective dihedral at higher angles of attack. The cause of the reduced effective dihedral in the low angle-of-attack range is not clear, but the increased effective dihedral at the higher angles of attack is consistent with the large induced lift due to power with high flap-deflection angles.

In conjunction with the investigation of the effects of winglets on airplane performance (see "Winglet Investigation" in this report), tests were also conducted to evaluate the effects of winglets on the lateral-directional characteristics. The results of these tests are presented in figure 64 and show that the installation of the winglets had little effect on static directional stability but caused a significant increase in effective dihedral. This result is not unexpected, because the winglet cant angle, in effect, adds to the geometric dihedral of the wing.

During the tests made to evaluate the effects of sideslip on lateral-directional characteristics, data were also measured to evaluate the effect of sideslip on drag. These results would be useful for the determination of performance penalties associated with sideslipping the airplane into the dead-engine direction in order to obtain lateral trim during single-engine climb. These data are presented in figure 65 in terms of incremental wind-axis drag coefficients as functions of sideslip angle for the complete set of flap deflections. An appropriate range of C_L for each flap-deflection angle is shown and indicates that drag due to sideslip is relatively independent of δ_f and C_L.

Lateral-directional control.- The ATLIT airplane uses spoilers for lateral control and the standard Seneca I rudder for directional control. The spoiler lateral control system used on the ATLIT was the result of development tests conducted at Wichita State University and reported in references 14 and 15. The overall results of tests to determine the spoiler control characteristics on the full-scale ATLIT are presented in figure 66 for all five settings of the full-span Fowler flaps. These results also include some data on the effects of power on spoiler lateral control which had not been investigated during the development testing at Wichita State University. In the present tests, power conditions were selected which would correspond to "power for level flight" with both engines operating for the airplane at the appropriate angle of attack. These "trimmed-power" conditions are denoted by the solid symbols in figure 66.

The results presented in figure 66 indicate that with power off, the spoiler roll-control effectiveness was reasonably linear at 0° angle of attack. For the flaps-retracted case (fig. 66(a)), spoiler effectiveness decreased with increasing angle of attack, and at $\alpha \approx 16^\circ$ the first 20° of spoiler deflection produced no rolling moment whatsoever. This result indicates that the spoiler is located in a region of separated flow at this high angle-of-attack condition (corresponding to stall). For this case as well as for all of the lower flap angles, the effects of power on spoiler effectiveness were insignificant (figs. 66(a) to 66(d)); however, with $\delta_f = 37^\circ$ (fig. 66(e)) power increased spoiler effectiveness significantly at the higher angle of attack.

In figure 67 spoiler effectiveness obtained in the present investigation is compared with the results of reference 15 for several power-off cases at 0° angle of attack. The data of reference 15 were obtained with a 1/4-scale semispan model of the ATLIT wing. These results agree well with the flaps-retracted test (fig. 67(a)), but for all the flaps-deflected cases, the spoiler roll-control effectiveness on the full-scale airplane was lower than that obtained with the 1/4-scale semispan model. These results suggest that some details of the flap cove and gap may have been different on the model and the airplane.

Rudder effectiveness was determined only for the flaps-retracted condition. Results showing the effect of symmetrical power on rudder effectiveness are presented in figure 68. These results indicate that with power off, rudder effectiveness decreases about 35 percent as angle of attack is increased to 20°. This loss of rudder effectiveness, however, is partially offset by the effects of power.

Engine-out characteristics.- The effects of engine failure on the lateral-directional characteristics of the ATLIT airplane were evaluated with $\delta_f = 0^\circ$, 20°, and 37°. In each case engine failure was simulated by having the right engine stopped and the left engine operating at two different power levels. The lower of these two power levels represents the normal "power for level flight" condition which could exist prior to engine failure; the higher power level represents full power on the operating engine at the previously established trimmed level flight condition (when both engines were operating). Furthermore, this engine-failure situation represented the initial emergency; i.e., the stopped propeller was not feathered ($\beta_{.75} = 18^\circ$).

The results for the engine-out characteristics are presented in figures 69 to 71. Part (a) of each figure shows the lateral-directional asymmetry caused by the left engine operating with all controls neutral. Part (b) of each figure shows the effect of 10° of rudder deflection, which is intended to compensate for the asymmetric yawing moment due to engine failure. Part (c) of each figure shows the effect of spoiler deflection in combination with the 10° of rudder deflection, which is intended to compensate for both the asymmetric yawing and rolling moments due to engine failure.

The results presented in figure 69(a) for the flaps-retracted case indicate sizable asymmetric moments due to engine out both in yaw and roll. The rolling-moment asymmetry depends strongly on angle of attack and exceeds the yawing-moment asymmetry at the higher values of α. This rolling-moment asymmetry is associated with the loss in power-induced lift on the failed-engine side. This loss is discussed in more detail later. The yawing-moment asymmetry is primarily a function of the asymmetric thrust and the drag of the stopped propeller. A rudder deflection of 10° was adequate to trim out the yawing moment due to engine failure at the initial power condition ($C_T'' = 0.050$), but about 12° or 13° of rudder deflection would be required to compensate for the yawing-moment asymmetry due to full power on the operating engine (fig. 69(b)). The combined effects of 10° of rudder deflection and 20° of spoiler deflection for this case ($\delta_f = 0^\circ$) are shown in figure 69(c). The yawing-moment curves were about the same for the two left-engine power levels as with $\delta_r = 10^\circ$ and $\delta_{spl} = 0^\circ$ (compare with fig. 69(b)); however, the 20° of spoiler deflection produced large compensating rolling moments at low angles of attack and practically no changes in rolling moment at the upper end of the angle-of-attack range. This loss of spoiler effectiveness at high angle of attack was noted previously in the discussion of figure 66(a). The most significant result of the data presented in figure 69 is that for the simulated engine-failure situation corresponding to a single-engine full-power climb at $C_L = 1.00$ ($\alpha = 6.5^\circ$), the lateral-directional asymmetries due to engine failure would be trimmed out with $\delta_r = 12^\circ$ and $\delta_{spl} = 14^\circ$ at this 0° sideslip condition. It should be recognized that this is not the only way to trim out lateral asymmetries in an engine-out climb. For example, the use of spoiler deflection to counteract rolling moment due to engine failure would certainly introduce serious drag penalties. Therefore, a better method to trim for engine-out climb might be not to use spoiler deflection but to force the airplane into a small-sideslip condition by additional deflection of the rudder. This introduction of sideslip allows $-C_{l_\beta}$ to produce the corrective rolling moment. A comparison to determine which of these techniques would provide the best single-engine climb performance would involve an evaluation of drag due to spoiler deflection versus drag due to sideslip. The following table has been prepared from available data for the single-engine climb condition with $\delta_f = 0^\circ$, $C_L = 1.00$, and $\alpha = 6.5^\circ$ (well away from minimum control speed or stall considerations):

$\Delta C_{l_{required}} = -0.0160$	Figure 69(b)
$\beta_{required} = \dfrac{\Delta C_{l_{required}}}{C_{l_\beta}} = \dfrac{-0.0160}{-0.00135} = 12^\circ$	Figure 63(a)*
Alternately, $\delta_{spl,required} = 19^\circ$	Figure 69(c)

*The value of C_{l_β} used in this calculation is based on the average of measured data (for power off and symmetrical power) and is assummed to be valid for the asymmetrical power condition.

The drag penalty for each method is

Trim method	ΔC_D	Figure
$\beta = 12^\circ$	0.0150	65
$\delta_{spl} = 19^\circ$	.0025	66(a)

This brief analysis indicates that sideslipping the airplane into the dead engine would introduce a drag penalty 6 times greater than that obtained by leveling the wings with spoiler deflection.

The lateral-directional characteristics presented in figures 70 and 71 are applicable to engine failures under take-off and landing conditions, respectively. Under these conditions, the values for full-power shaft thrust coefficients are much higher than in figure 69 because of the lower dynamic pressures during take-off and landing compared with that for the flaps-retracted climb condition. Under these conditions, with flaps deflected, the asymmetric power-induced lift became quite large, especially above the power-off stall. (See fig. 72.) As a consequence, the lateral-directional asymmetries for the take-off and landing conditions are appreciably more severe than for the flaps-retracted condition. (Compare figs. 69(a), 70(a), and 71(a).) For $\delta_f = 37^\circ$, the rolling-moment asymmetry due to engine failure was extremely large at about $\alpha \approx 14^\circ$, or just above the power-off stall.

Figures 70(b) and 71(b) show that 10° of rudder deflection was totally inadequate to trim out the asymmetric yawing moment caused by full power on the operating engine. Figures 70(c) and 71(c) show that 30° of spoiler deflection was appreciably more than required to trim out the asymmetric rolling moments due to engine failure. These results suggest the following more appropriate control deflections to satisfy trim requirements for engine failure during take-off and during wave-off from landing approach conditions for $\alpha = 5^\circ$:

$$\delta_f = 20^\circ; \quad C''_{T,lt} = 0.146; \quad \delta_r = 13^\circ; \quad \delta_{spl} = 16^\circ$$

$$\delta_f = 37^\circ; \quad C''_{T,lt} = 0.219; \quad \delta_r = 18^\circ; \quad \delta_{spl} = 17^\circ$$

On the basis of the previous brief analysis concerning drag penalties associated with lateral trim requirements with $\delta_f = 0^\circ$, these control deflections should not introduce serious single-engine performance penalties during take-off and wave-off conditions.

CONCLUDING REMARKS

A full-scale wind-tunnel investigation has been conducted to evaluate the aerodynamic performance, stability, and control of the Advanced Technology Light Twin-Engine airplane (ATLIT). The following remarks relate to the most significant results of the investigation:

1. Aerodynamic performance was seriously degraded by excess drag at lift coefficients representative of climbing flight. Premature flow separation near the wing-fuselage juncture and leakage through the wing (as a result of the particular flap and spoiler installation) were the two most significant sources of this excess drag. Installation of a revised wing-fuselage fillet and elimination of the flap and spoiler leak paths provided significant reductions in drag at climb conditions but had little effect on drag at cruise conditions.

2. Airplane efficiency factor was relatively poor even for the "fully clean" configuration (Oswald's airplane efficiency factor of 0.734). This

result is attributable, in part, to nacelle interference effects on the wing span-load distributions.

3. Engine cooling drag (for both engines) amounted to approximately 15 percent of total airplane drag for both the climb and cruise conditions.

4. Measured installed propeller efficiencies were 3 to 4 percent lower than the propulsive efficiencies for a comparable propeller from the "Gray Charts" (NACA ARR No. 3125).

5. The effect of power on longitudinal stability was strongly destabilizing, especially for large deflections of the full-span Fowler flaps. Conditions of zero static margin could occur with a flap deflection of 37° with full power on both engines as for the wave-off condition.

6. Stalling of the horizontal tail was encountered as a result of trimming the large diving moments associated with high deflections of the full-span Fowler flaps. This tail stall problem produced static longitudinal instability at lift coefficient values below 2.4 with a flap deflection of 37° under conditions representative of a full-power wave-off.

7. The airplane was directionally stable and had positive effective dihedral throughout the entire angle-of-attack range for all flap deflections and for all power conditions.

8. The spoiler lateral-control system provided reasonably linear roll-control characteristics except for flap deflections of 0° at high angles of attack ($\alpha = 16^{\circ}$), where the first 20° of spoiler deflection was totally ineffective. Spoiler roll-control effectiveness increased with flap deflection, and there was no indication of control effectiveness reversal throughout the range of flap deflections.

9. Lateral-directional asymmetries resulting from a simulated engine failure were quite large but could be easily trimmed with reasonable deflections of spoilers and rudder. During an engine-out climb, performance penalties associated with lateral-trim requirements were minimized by using a spoiler to trim out rolling-moment asymmetry rather than by sideslipping the airplane into the dead engine.

Langley Research Center
National Aeronautics and Space Administration
Hampton, VA 23665
February 6, 1980

FLOW CORRECTIONS

Prior to mounting the airplane in the tunnel, flow surveys were conducted to determine average flow angularity and dynamic pressure across the width of the tunnel at a height corresponding to the wing height and at a test section station corresponding to the $0.25\bar{c}$ location of the wing. Similar surveys were conducted at two tunnel speeds corresponding approximately to the test conditions at Reynolds numbers of 2.30×10^6 and 3.50×10^6 reported here. The results of these flow surveys are presented as figure A1. From these data the integrated average values of $\Delta\alpha$, $\Delta\beta$, and q/q_{ref} across the 12-m (40-ft) span of the airplane were found to be (where q is the local dynamic pressure and q_{ref} is the dynamic pressure based on test chamber static pressure for this atmospheric wind tunnel).

q_{ref}		$\Delta\alpha$, deg	$\Delta\beta$, deg	q/q_{ref}
Pa	lbf/ft^2			
484	10.1	0.176	0.564	1.0486
1101	23.0	-.076	.541	1.0530

These stream-angle corrections and dynamic-pressure ratios are standard inputs to the data reduction program for tests of airplanes in the Langley Full-Scale Tunnel. Although the integrated average values of $\Delta\alpha$ were quite small, the survey data show the variation of $\Delta\alpha$ across the span of the airplane to vary from small upwash values near the center to small downwash values near the wing tips. In effect, this tunnel flow distortion imposes an effective increase in wing twist, or washout, which would not exist in free air. For the two cases surveyed, the effective increase in wing washout was about 1°; however, no corrections related to this increase in wing washout have been applied to the data reported here.

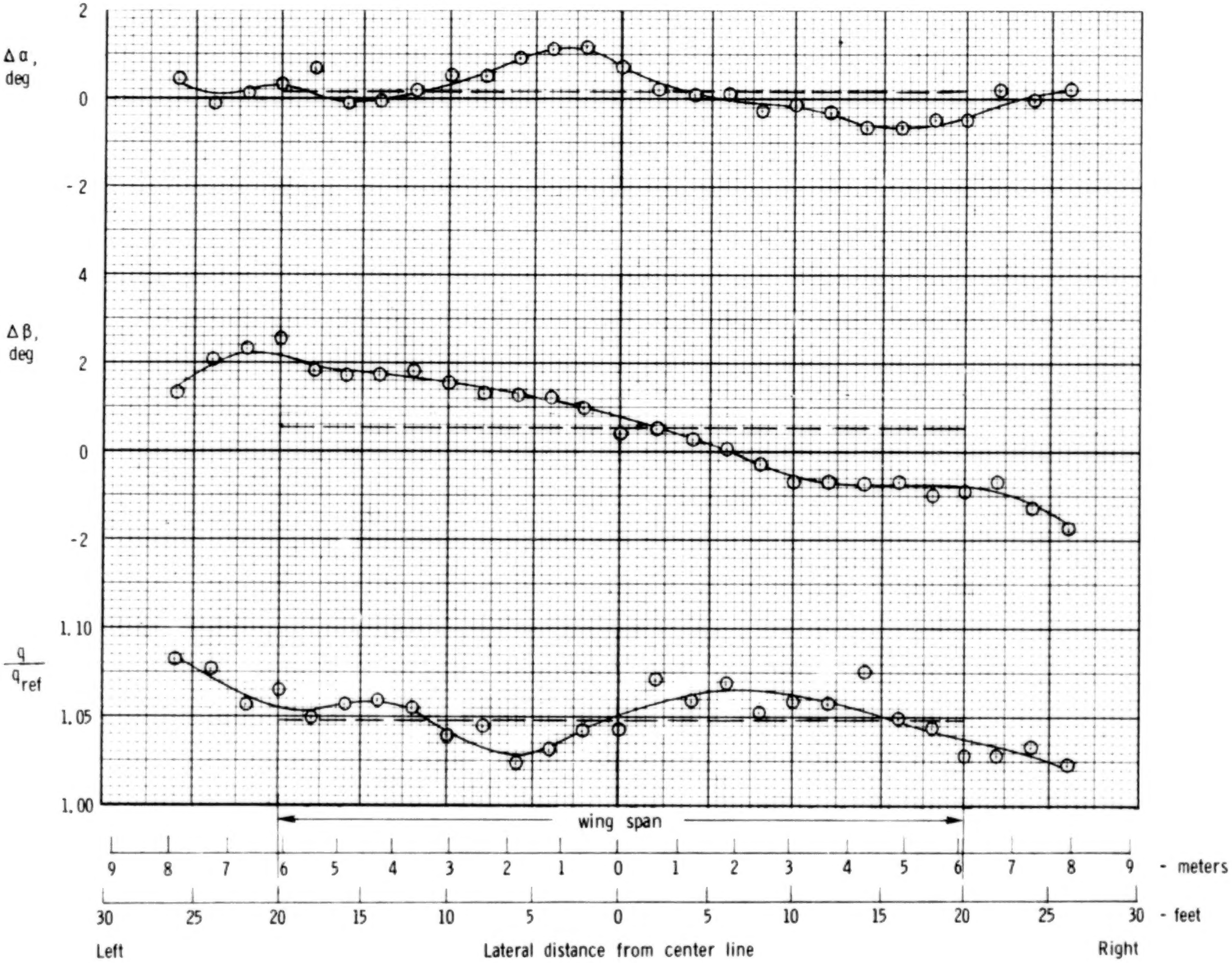

(a) q_{ref} = 484 Pa (10.1 lbf/ft^2).

Figure A1.- Lateral variation of airstream flow at wing location in tunnel. (Dashed lines are integrated average values across wing span.)

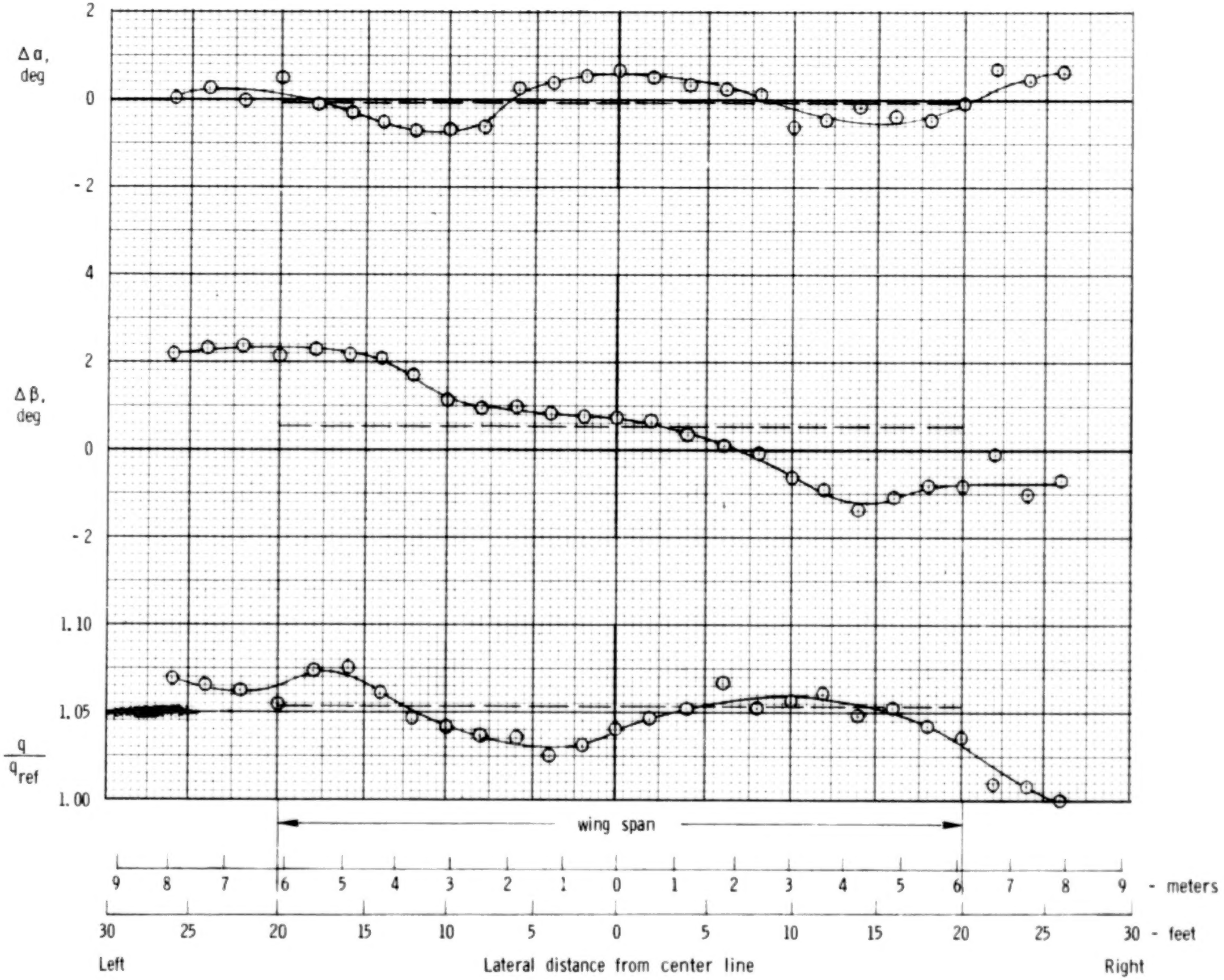

(b) q_{ref} = 1101 Pa (23.0 lbf/ft^2).

Figure A1.- Concluded.

APPENDIX B

METHOD OF PERFORMANCE EVALUATION

Fundamentally, the two factors necessary for airplane performance calculations are (1) power required as determined from lift-drag data and weight information for the airplane; and (2) power available as determined from the engine and propeller characteristics. The purpose of this appendix is to show how the data of the present investigation may be used to account for all major factors affecting the performance of the airplane with the flaps retracted.

Lift-Drag Characteristics

Power effects.- The power-on tests of the present investigation provide a basis for evaluating the effects of power on the lift-drag polar of the subject airplane. Figure B1 illustrates this effect of power for the flaps-retracted, "as-received" configuration with all controls neutral, cowl flaps open, and inlets unsealed at a Reynolds number of 2.30×10^6. Data are presented for four conditions: (1) propellers off; (2) propellers stopped (with the incremental drag of the stopped propellers subtracted out); (3) both engines operating at a power setting appropriate for cruise at $C_L = 0.35$ $(C_T'' = 0.033)$; and (4) both engines operating at a power setting appropriate for level flight at $C_L = 1.1$ $(C_T'' = 0.100)$. For cases (3) and (4) the direct components of thrust as determined from the propeller thrust balance have been subtracted from the lift and drag data, so that only the induced effects of propeller slipstream are left in these data. In relation to the power-off propellers-off polar, these results indicate that the effects of power produced a reduction in drag at the lower thrust coefficient, a slight increase in drag at the higher thrust coefficient, and a pronounced increase in maximum lift at either value of thrust coefficient. The reduction in drag at the lower value of thrust coefficient is attributable to the effect of the low-velocity propeller slipstream helping to clean up separated flow areas around the nacelles and wing-fuselage juncture. The small increase in drag at the higher value of thrust coefficient is attributable to scrubbing drag on the various airplane parts subjected to the high-dynamic-pressure region of the propeller slipstream. (At this higher value of thrust coefficient, the ratio of slipstream dynamic pressure to free-stream dynamic pressure would be about 1.25, from propeller momentum theory.) The increased $C_{L,max}$ with power is due to induced effects of the propeller slipstream on the wing, since the direct thrust components in lift have already been removed.

Trim effects.- The power-on polars of figure B1 were obtained from data with the horizontal stabilator set at 0° and are therefore generally untrimmed. A basis for establishing trim drag (in this case, for the aft center-of-gravity location $0.25\bar{c}$) is presented in figures B2 and B3 and with reference to figures 55(b) and 55(c) of the main text. The data of figures B2 and B3 are the thrust-removed polars for two values of δ_{stab} obtained at identical values of thrust coefficient used in figure B1. These results were then used to generate the trimmed polars of figure B4 ($C_m = 0$ throughout the C_L range). A separate curve is presented for each of the two values of thrust coefficient.

Inasmuch as these two levels of thrust ($C_T'' = 0.033$ and 0.100) were representative of power for level flight at cruise ($C_L = 0.35$) and of power for level flight at $C_L = 1.10$, respectively, then appropriate weighting of the two curves provides a single trimmed lift-drag polar representing the power for level flight conditions for all values of C_L between 0.35 and 1.10. This trimmed polar is presented as the solid curve of figure B5 and is strictly valid for C_L values between 0.35 and 1.10 and only at the Reynolds number of the test condition ($R = 2.30 \times 10^6$).

Reynolds number corrections.- The effects of Reynolds number on lift and drag were obtained only for unpowered conditions with the propellers removed (see figs. 20 and 21), where data were obtained at $R = 2.30 \times 10^6$, 3.50×10^6, and 4.10×10^6. Power-on tests were conducted only at $R = 2.30 \times 10^6$, from which the trimmed polar (including power effects) was established (solid curve of fig. B5). Therefore, the only means (based on experimental data) for correcting the trimmed polar, including power effects, to full-scale Reynolds number conditions must be based on appropriate incremental values of drag determined in the power-off tests. This procedure was used to establish the trimmed polar corrected to full-scale Reynolds number, shown as the dashed curve of figure B5. As indicated by the Reynolds number scale on the right margin of the figure, corrections for Reynolds number effects had to be extrapolated in the low lift-coefficient range because no data were available at $R > 4.10 \times 10^6$. These extrapolations were very minor since the effect of Reynolds number on C_L and C_D was quite small for values of R between 3.50×10^6 and 4.10×10^6. (See figs. 20 and 21.)

Cooling drag correction.- One additional correction is necessary to provide a trimmed lift-drag polar which includes power effects, is corrected to full-scale Reynolds number, and is appropriate to power required for level flight. This correction is related to proper accounting of cooling drag, which is dependent on cowl flap position. In normal level flight, engine cooling requirements are minimal, so that the cowl flaps would be fully closed. The lift-drag polars of figure B5 were derived from power-on tests of the airplane with cowl flaps fully open; a drag correction should, therefore, be made to conform with cowl flaps fully closed. This cooling drag correction is based on the data of figures 33 and 34, which indicate the following average incremental reductions of drag coefficient due to closing the cowl flaps:

C_L	ΔC_D (cowl flaps)
0	-0.0064
.2	-.0057
.4	-.0052
.6	-.0040
.8	-.0031
1.0	-.0027
1.2	-.0023

When these corrections are applied to the full-scale Reynolds number polar of figure B5, the final trimmed polar appropriate to power required for level flight is obtained. This fully corrected polar is compared in figure B6 with a polar obtained at a Reynolds number of 3.50×10^6 with the propellers removed, cowl flaps closed, and inlets sealed (from fig. 33(b)). This comparison shows that the results of the unpowered tests with propellers removed are in excellent agreement with the established full-scale Reynolds number polar (which was based on powered test results) for the lift-coefficient range up to about 1.0. It appears, therefore, that most performance problems can be evaluated accurately on the basis of the unpowered results at $R = 3.50 \times 10^6$.

Propeller Characteristics

Results presented in the "Propeller Characteristics" section of this paper relate to the "installed" propeller performance as obtained from thrust and torque data measured by the special propeller balance which was mounted on the engine propeller shaft, and these results are presented in figure 17. During these tests, a method of simultaneously measuring effective thrust was utilized. This effective thrust measurement was obtained from the tunnel scale system on which the airplane was mounted. Thus, the effective thrust was obtained from force-scale drag measurements and the following relation for the $\alpha = 0^\circ$ condition:

$$T_e = \text{Drag}_{\text{propellers removed}} - \text{Drag}_{\text{propellers operating}}$$

where the drag measurements in both cases were obtained at the same tunnel velocity (constant dynamic pressure). In coefficient form the effective thrust coefficient may be expressed as:

$$C_{T,e} = \frac{\text{Drag}_{\text{propellers removed}} - \text{Drag}_{\text{propellers operating}}}{\rho n^2 D^4}$$

All the results obtained during the propeller performance tests are presented in figure B7, where the effect of propeller blade angle on C_P, C_T, and $C_{T,e}$ is shown for three ranges of V/nD (each corresponding to a constant tunnel velocity). Figure 17 (discussed in "Propeller Characteristics" section of this paper) was prepared by fairing through the propeller balance data for all three tunnel velocities for each blade setting. Thus, parts (a) and (b) of figure B7 are the raw data from which figure 17 was derived and are referred to here as "installed propeller characteristics."

The effective thrust data of figure B7(c) are considerably different from the measured shaft thrust of figure B7(b). In general, for any given blade angle $C_{T,e}$ is less than C_T at the lower values of V/nD but slightly greater than C_T at the higher values of V/nD. This observation implies that an efficiency factor based on effective thrust would be appreciably lower than the installed propeller efficiency in the low V/nD range and higher than the installed propeller efficiency in the higher V/nD range. An explanation for the differences between C_T and $C_{T,e}$ may be the increased drag of airplane parts which are affected by the high dynamic pressure of the propeller slipstream and the reduced drag of areas which might otherwise have separated flow. These effects would be expected to be a function of propeller slipstream dynamic pressure. The ratio of slipstream dynamic pressure to free-stream dynamic pressure may be determined from the following equation (based on propeller momentum theory):

$$\frac{q_S}{q_\infty} = 1 + \frac{8}{\pi} \frac{C_T}{(V/nD)^2}$$

The increment of drag coefficient attributable to propeller slipstream effects is a function of the difference between C_T and $C_{T,e}$:

$$\begin{aligned} \Delta C_{D,S} &= (C_T - C_{T,e}) \frac{2D^2}{(V/nD)^2 S} \\ &= \frac{\Delta \text{Drag}_{\text{slipstream}}}{q_\infty S} \end{aligned}$$

Using these equations, sample calculations were made to evaluate the differences in efficiency as determined from C_T and $C_{T,e}$ and the consequential $\Delta C_{D,S}$. Results are presented in figure B8 for a propeller blade angle of 16° (appropriate for the full-power climb condition) and in figure B9 for a blade angle of 24° (appropriate for a partial power cruise condition). Efficiency is shown as a function of V/nD on the upper half of each figure and $\Delta C_{D,S}$ is shown as a function of q_S/q_∞ on the lower half of each figure.

The results of figure B9 for $\beta_{.75} = 16^\circ$ primarily apply to take-off and climb conditions, where the constant-speed propellers would essentially be in the flat pitch mode and the engines would be operating at full power (approximately 2700 rpm). Thus, for a climb speed of 87 knots $V/nD = 0.52$ and the efficiency based on propeller thrust coefficient, C_T is 0.735, whereas the efficiency based on effective thrust coefficient $C_{T,e}$ is only 0.690. At this value of V/nD the ratio of slipstream dynamic pressure to free-stream dynamic pressure was about 1.57, for which $\Delta C_{D,S} = 0.0075$. The significance of the differences in efficiency as based on shaft thrust and effective thrust now becomes apparent. If power available is computed using the efficiency based on propeller thrust C_T, then the airplane lift-drag polar must be penalized by twice the $\Delta C_{D,S}$ value determined above for $V/nD = 0.52$ for the full-power climb condition with both engines operating. In other words, drag due to slipstream (or scrubbing drag) must be charged to the airframe; conversely, if power available is computed using the efficiency based on effective thrust, then the airplane lift-drag polar should not be penalized because the thrust losses attributable to scrubbing drag are already accounted for by the lower value of efficiency.

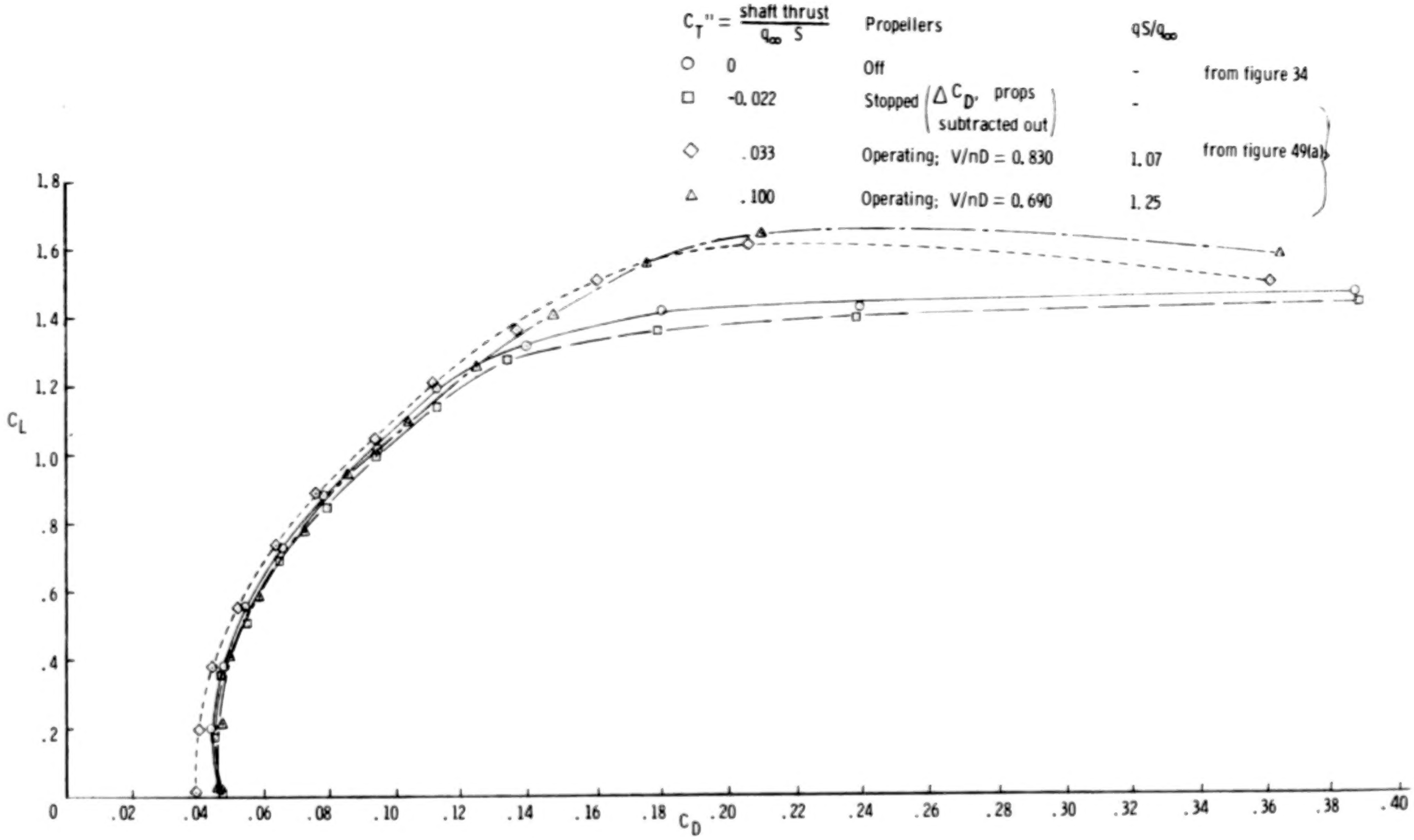

Figure B1.- Effect of power on "thrust-removed" lift-drag polars. $\delta_f = 0^\circ$; $\delta_{stab} = 0^\circ$; cowl flaps open; inlets unsealed; $R = 2.30 \times 10^6$; airplane "as received."

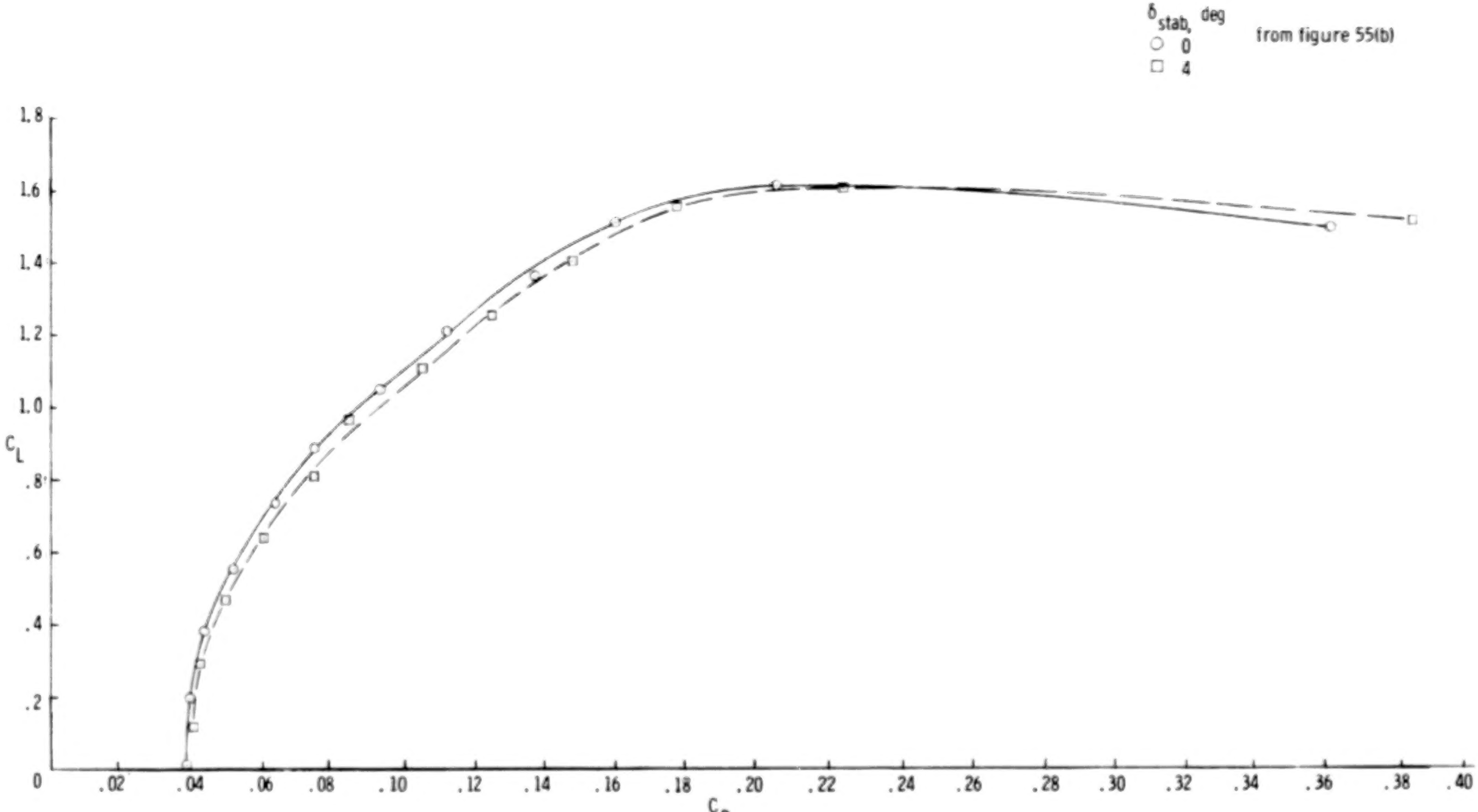

Figure B2.- Effect of δ_{stab} on "thrust-removed" lift-drag polars based on data at $C_T'' = 0.033$. $\delta_f = 0^\circ$; cowl flaps open; inlets unsealed; $R = 2.30 \times 10^6$; airplane "as received."

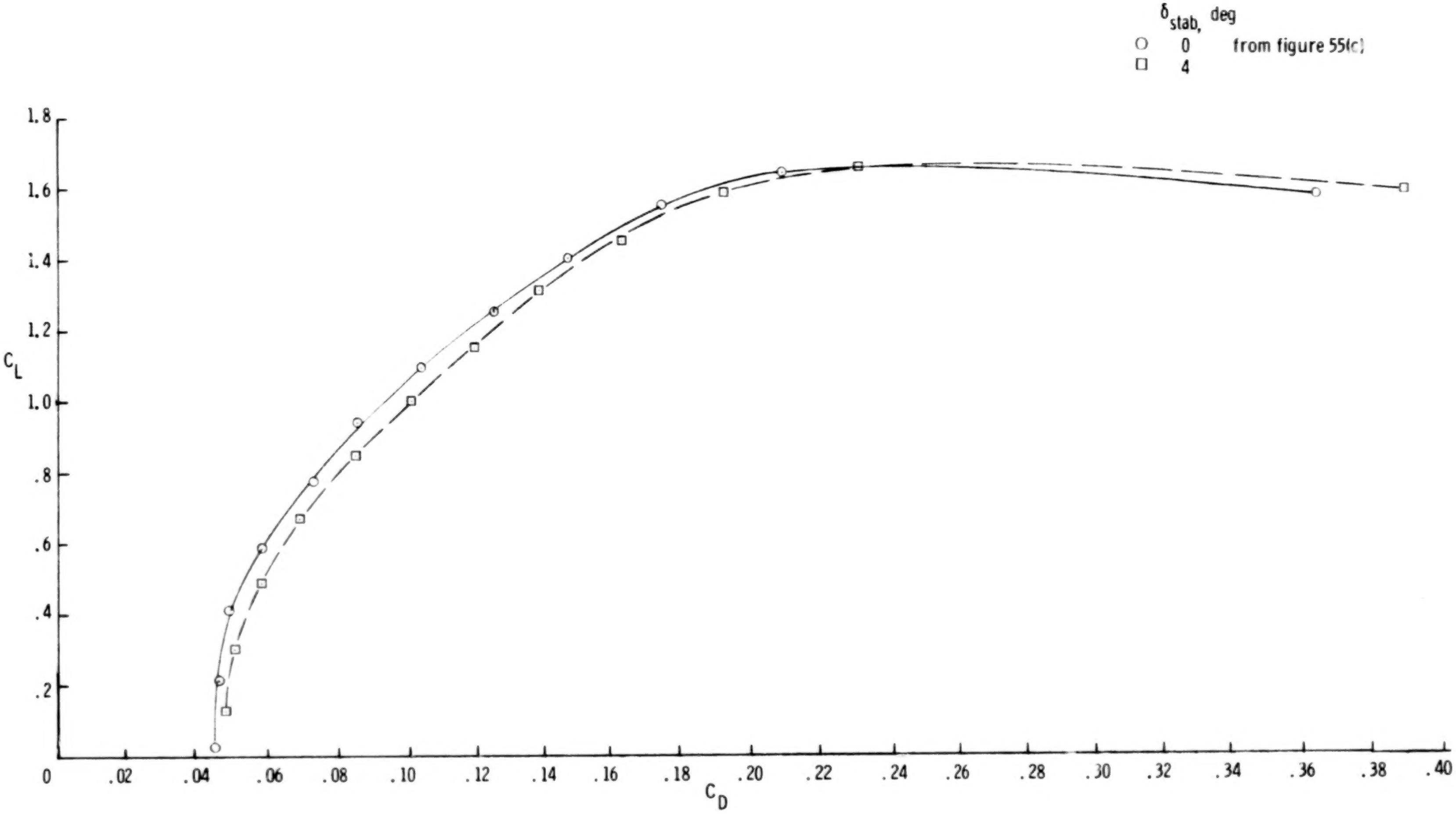

Figure B3.- Effect of δ_{stab} on "thrust-removed" lift-drag polars based on data at $C_T" = 0.100$. $\delta_f = 0^\circ$; cowl flaps open; inlets unsealed; $R = 2.30 \times 10^6$; airplane "as received."

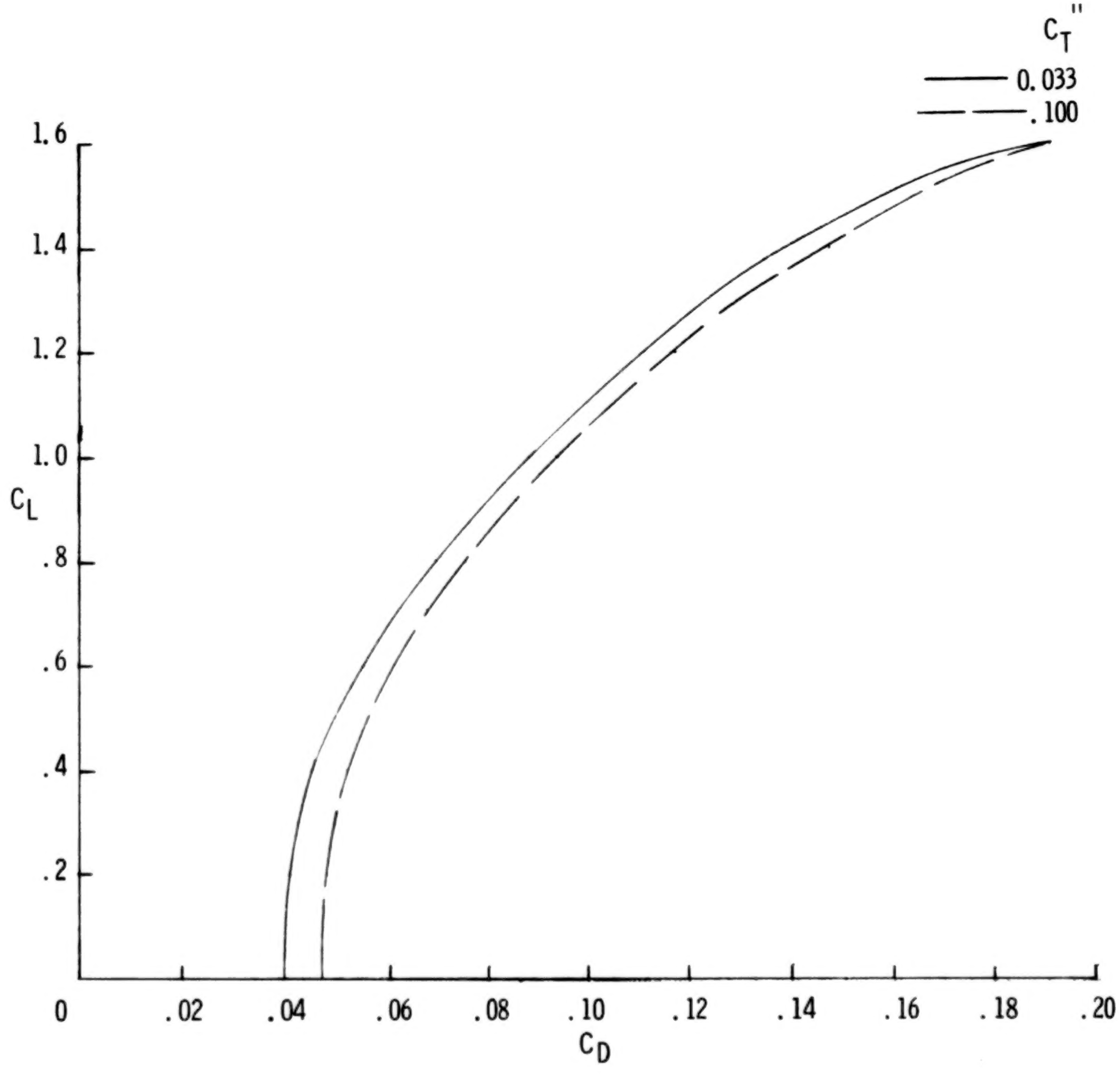

Figure B4.- Lift-drag polars based on two levels of C_T'' adjusted to account for stabilator trim drag with center of gravity at $0.25\bar{c}$. $\delta_f = 0^\circ$; cowl flaps open; inlets unsealed; $R = 2.30 \times 10^6$; airplane "as received."

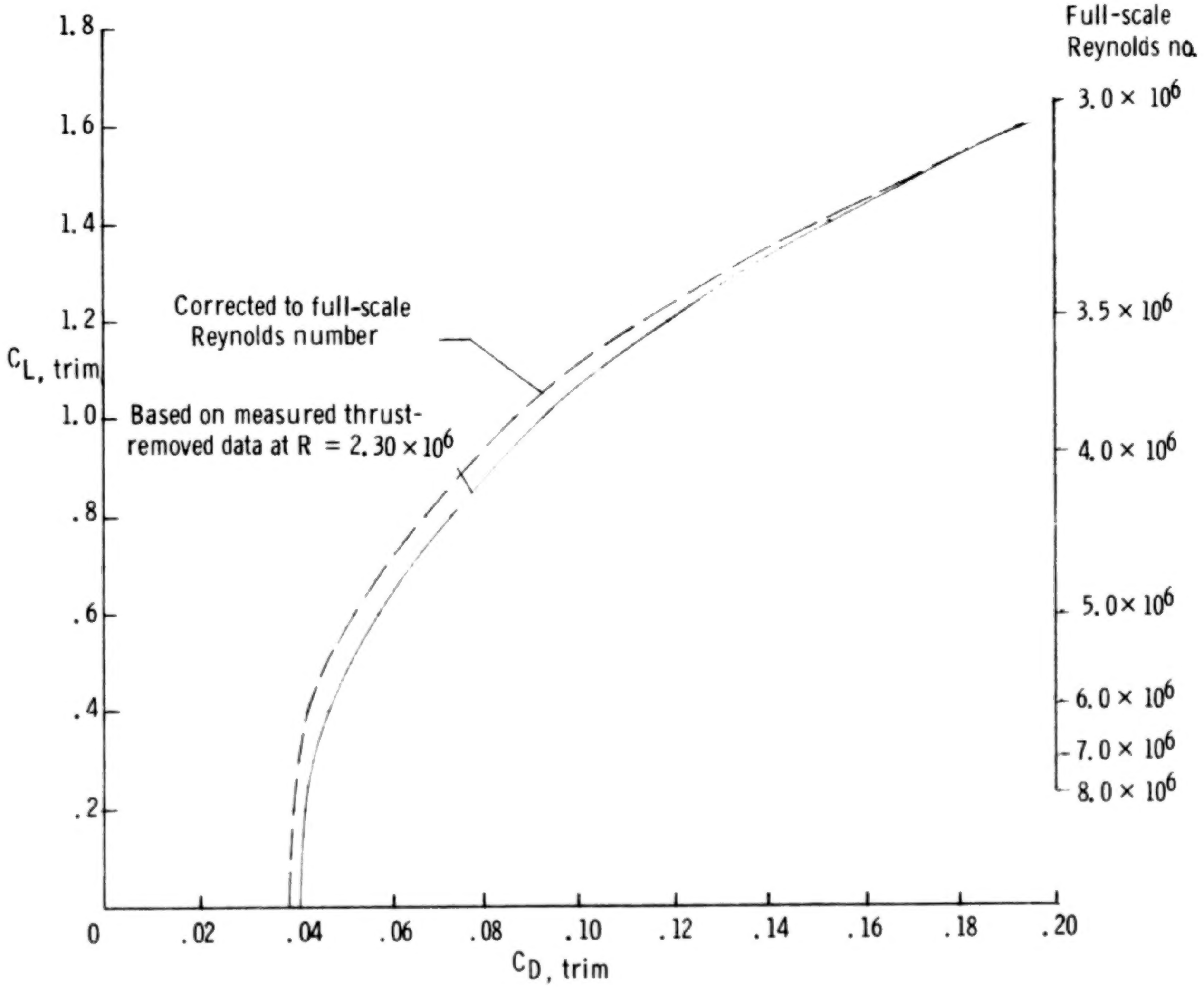

Figure B5.- Lift-drag polar adjusted to account for thrust required for level flight and stabilator trim drag; these polars then corrected to full-scale Reynolds number. $\delta_f = 0^\circ$; cowl flaps open; inlets unsealed; airplane "as received."

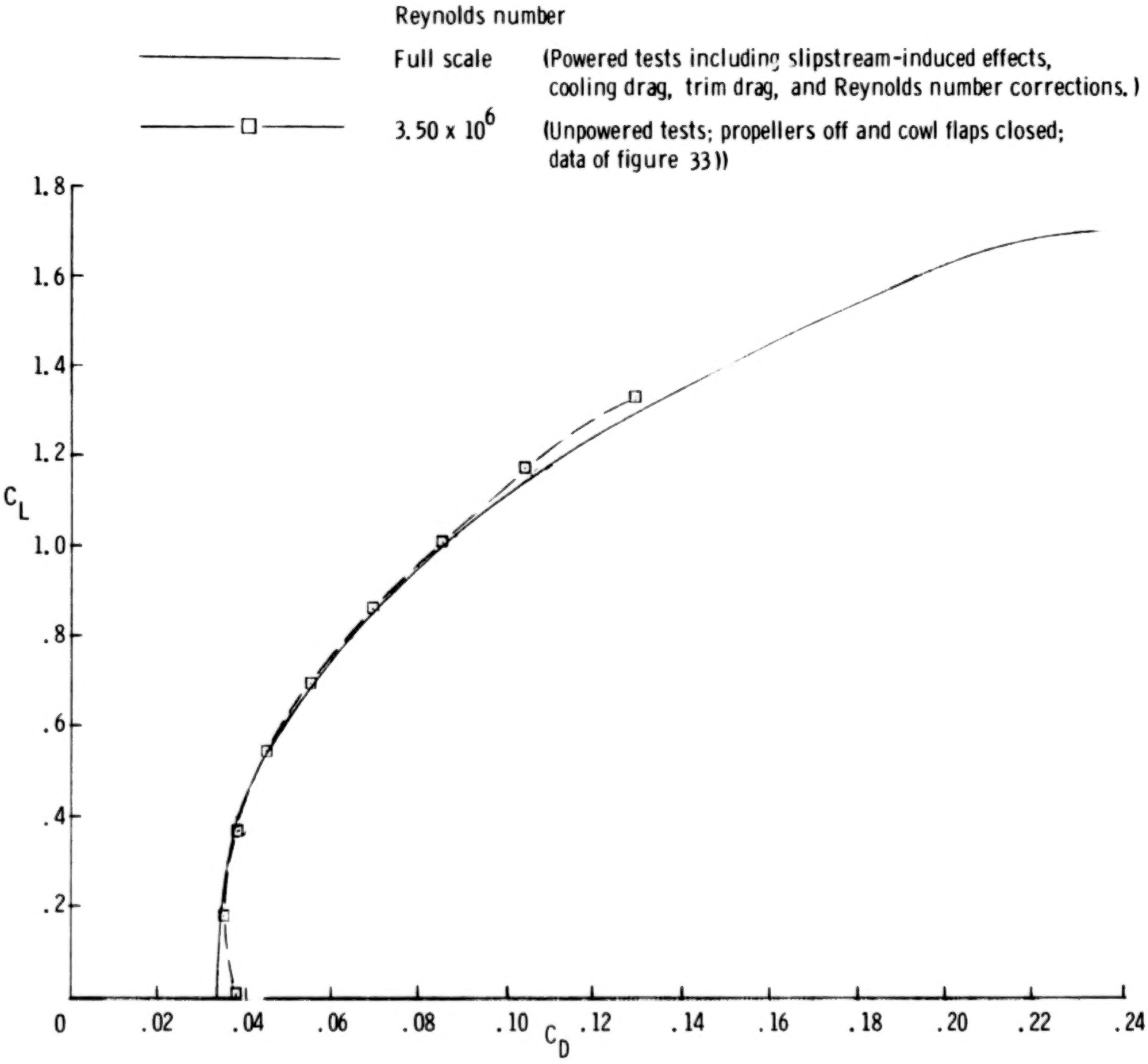

Figure B6.- Comparison of fully corrected lift-drag polar (based on powered tests) with unpowered data obtained with propellers removed. $\delta_f = 0^\circ$; cowl flaps closed; inlets unsealed.

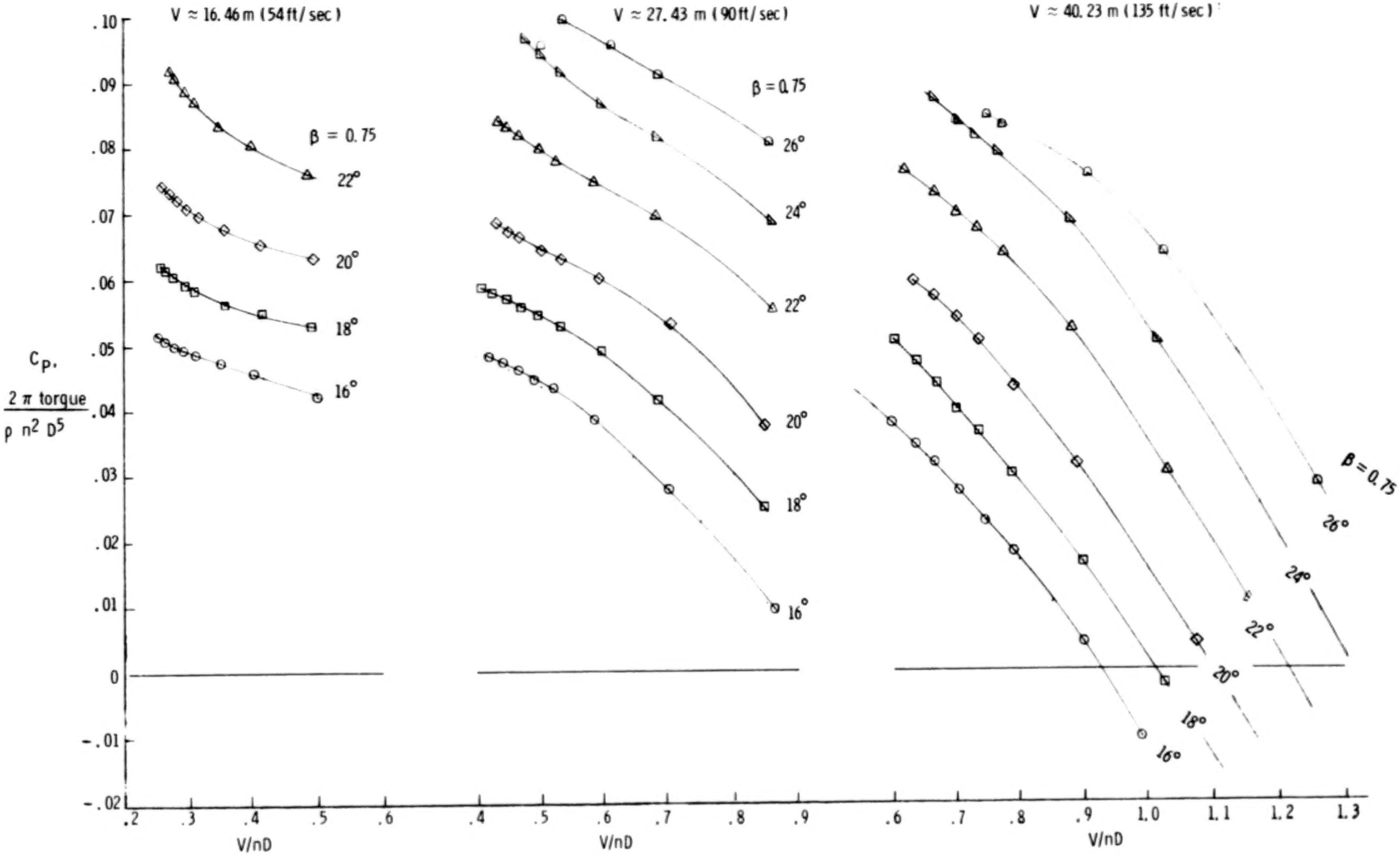

(a) C_P vs. V/nD (C_P based on torque measured on propeller shaft).

Figure B7.- Effect of propeller blade angle on propeller coefficients. $\alpha = 0^{\circ}$.

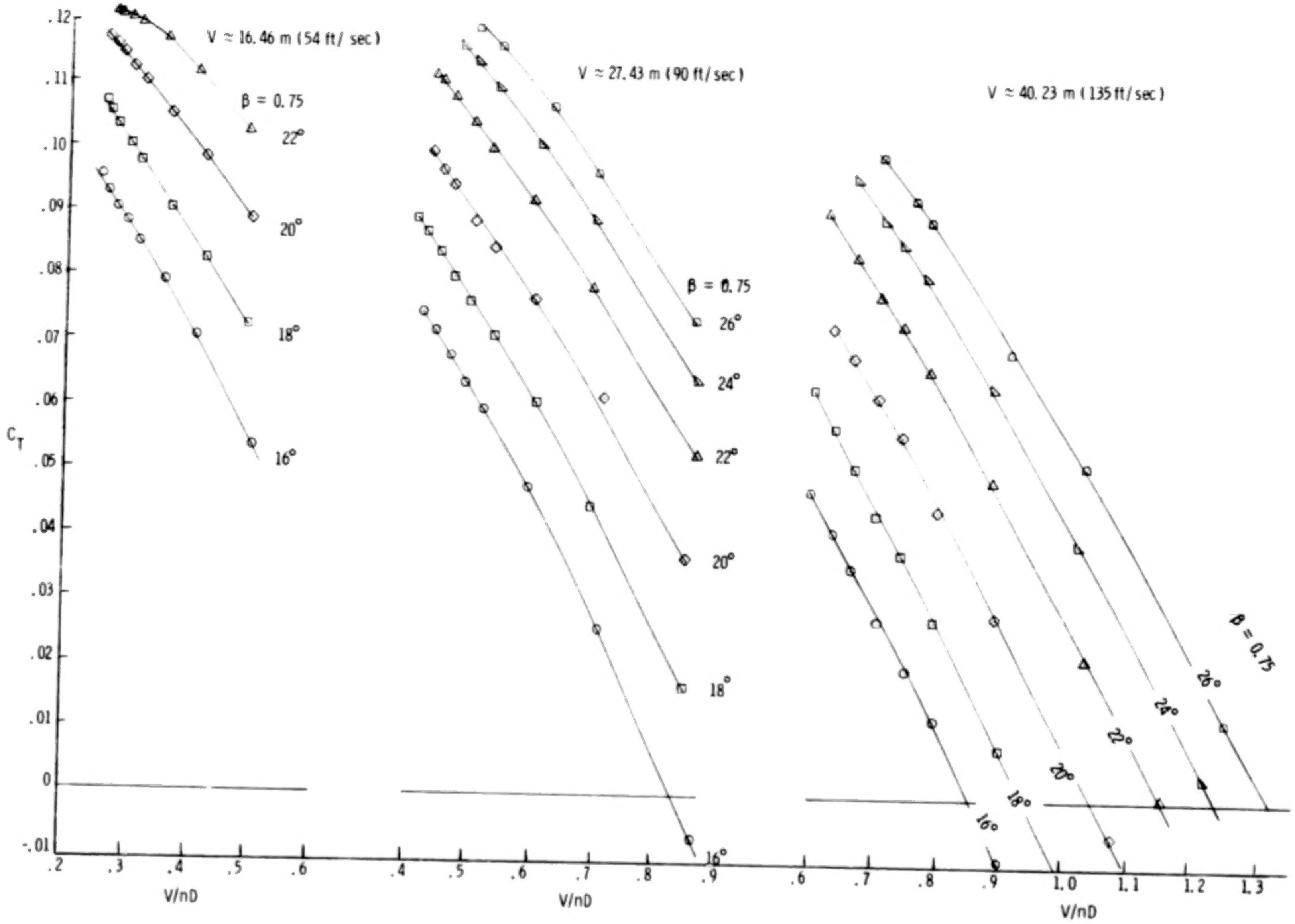

(b) C_T vs. V/nD (C_T based on thrust measured on propeller shaft).

Figure B7.- Continued.

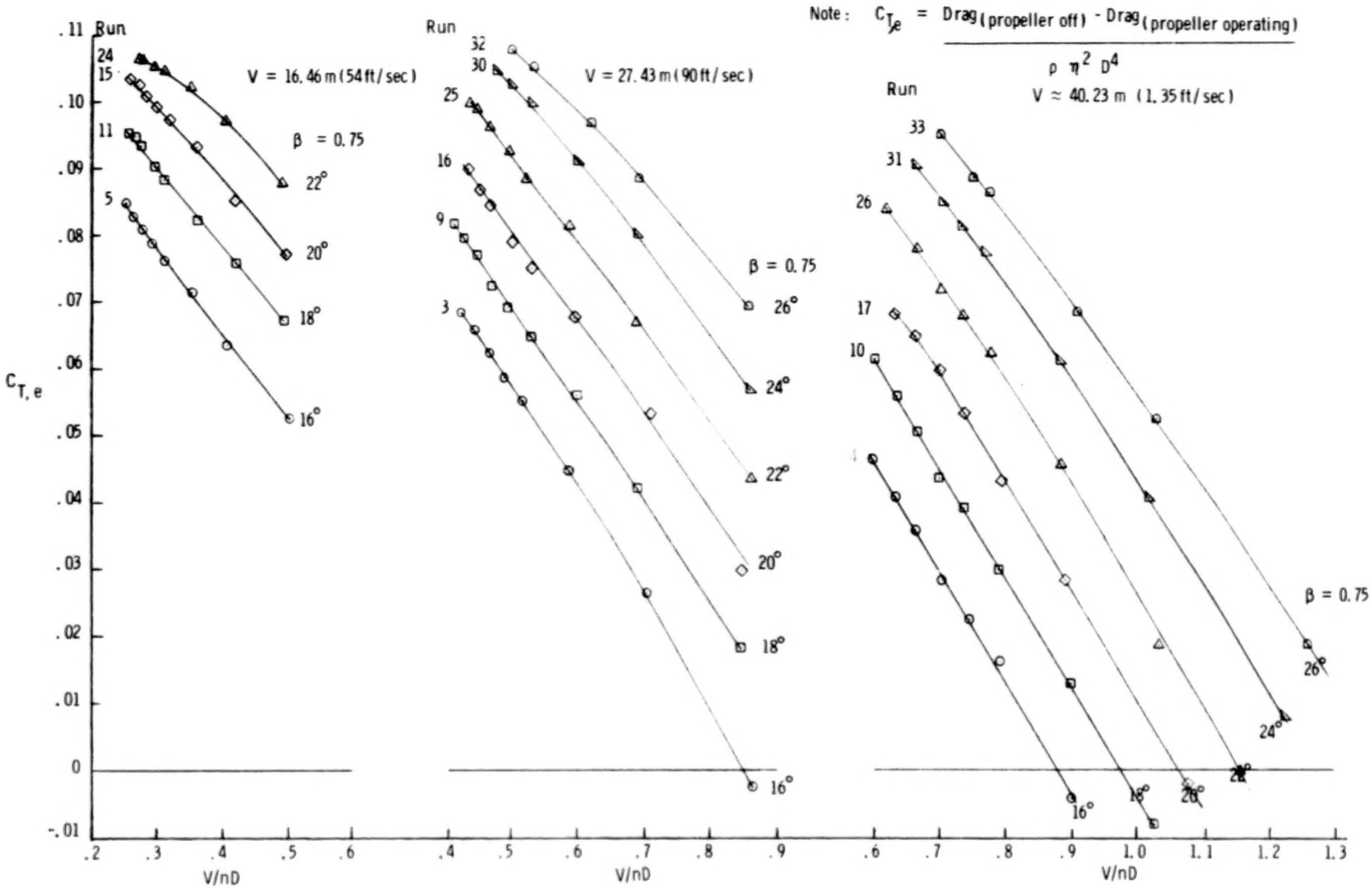

(c) $C_{T,e}$ vs. V/nD ($C_{T,e}$ from drag measurements on tunnel scale system).

Figure B7.- Concluded.

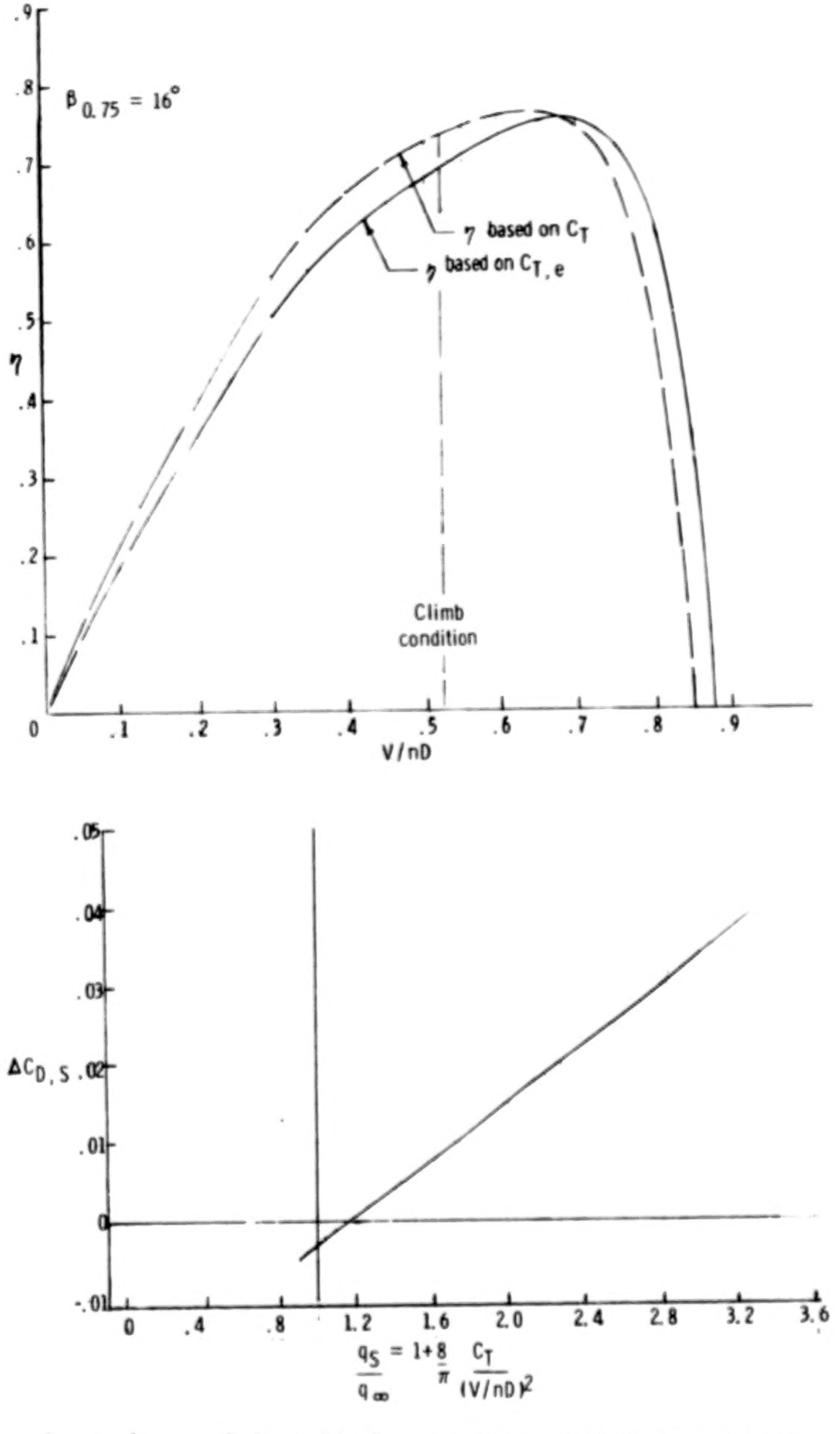

Figure B8.- Comparison of installed propeller efficiency (based on C_T) with efficiency based on effective thrust $C_{T,e}$ for $\beta_{.75} = 16°$ (appropriate for climb).

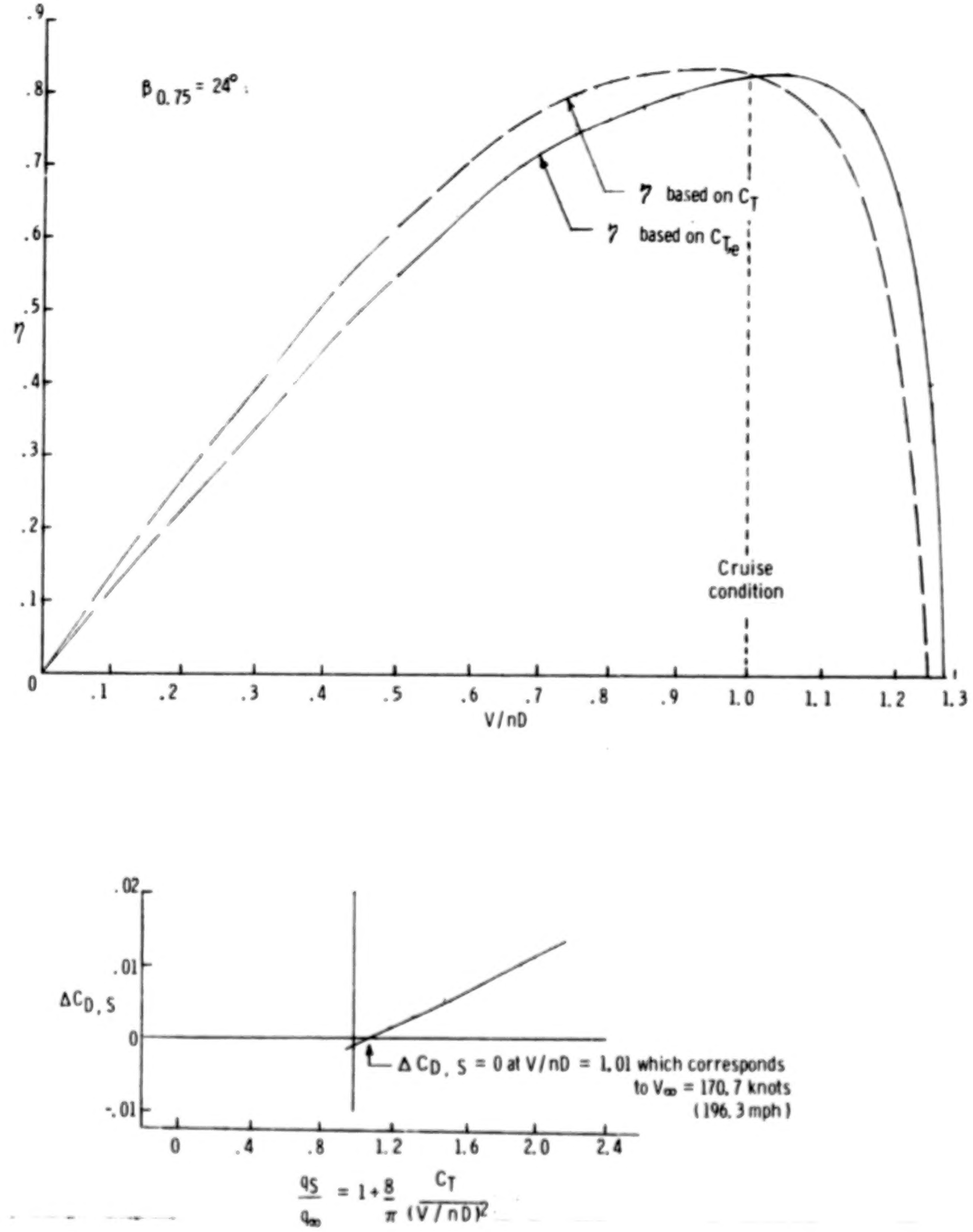

Figure B9.- Comparison of installed propeller efficiency (based on C_T) with efficiency based on effective thrust $C_{T,e}$ for $\beta_{.75} = 24^\circ$ (appropriate for high-speed cruise).

REFERENCES

1. Holmes, Bruce J.: Flight Evaluation of an Advanced Technology Light Twin-Engine Airplane (ATLIT). NASA CR-2832, 1977.

2. Yip, Long P.: Comparison of Wing Pressure Distributions and Boundary-Layer Characteristics for the Advanced Technology Light Twin-Engine Airplane (ATLIT) With Two-Dimensional Section Data for the GA(W)-1 Airfoil. Advanced Technology Airfoil Research - Volume II, NASA CP-2046, 1979, pp. 33-44.

3. Standard for Metric Practice. E 380-76, American Soc. Testing & Mater., 1976.

4. Heyson, Harry H.: Use of Superposition in Digital Computers To Obtain Wind-Tunnel Interference Factors for Arbitrary Configurations, With Particular Reference to V/STOL Models. NASA TR R-302, 1969.

5. Heyson, Harry H.: FORTRAN Programs for Calculating Wind-Tunnel Boundary Interference. NASA TM X-1740, 1969.

6. Fink, Marvin P.; and Freeman, Delma C., Jr.: Full-Scale Wind-Tunnel Investigation of Static Longitudinal and Lateral Characteristics of a Light Twin-Engine Airplane. NASA TN D-4983, 1969.

7. Fink, Marvin P.; Freeman, Delma C., Jr.; and Greer, H. Douglas: Full-Scale Wind-Tunnel Investigation of the Static Longitudinal and Lateral Characteristics of a Light Single-Engine Airplane. NASA TN D-5700, 1970.

8. Shivers, James P.; Fink, Marvin P.; and Ware, George M.: Full-Scale Wind-Tunnel Investigation of the Static Longitudinal and Lateral Characteristics of a Light Single-Engine Low-Wing Airplane. NASA TN D-5857, 1970.

9. Gray, W. H.; and Mastrocola, Nicholas: Representative Operating Charts of Propellers Tested in the NACA 20-Foot Propeller-Research Tunnel. NACA WR L-286, 1943. (Formerly NACA ARR 3I25.)

10. Hartman, Edwin P.: Negative Thrust and Torque Characteristics of an Adjustable-Pitch Metal Propeller. NACA Rep. 464, 1933.

11. Hoerner, Sighard F.: Fluid-Dynamic Drag. Publ. by the author (148 Busteed Drive, Midland Park, New Jersey 07432), 1965.

12. Coe, Paul L., Jr.: Review of Drag Cleanup Tests in Langley Full-Scale Tunnel (From 1935 to 1945) Applicable to Current General Aviation Airplanes. NASA TN D-8206, 1976.

13. McGhee, Robert J.; and Beasley, William D.: Low-Speed Aerodynamic Characteristics of a 17-Percent-Thick Airfoil Section Designed for General Aviation Applications. NASA TN D-7428, 1973.

14. Wentz, W. H., Jr.: Effectiveness of Spoilers on the GA(W)-1 Airfoil With a High Performance Fowler Flap. NASA CR-2538, 1975.

15. Wentz, W. H., Jr.; and Volk, C. G., Jr.: Reflection-Plane Tests of Spoilers on an Advanced Technology Wing With a Large Fowler Flap. NASA CR-2696, 1976.

TABLE I.- COMPARISON OF GEOMETRIC CHARACTERISTICS OF ATLIT AND SENECA I

	ATLIT	Seneca I
Wing:		
Area, m^2 (ft^2)	14.40 (155.0)	19.40 (208.7)
Span, m (ft)	12.19 (40.00)	11.85 (38.88)
Mean aerodynamic chord, m (ft)	1.225 (4.018)	1.60 (5.25)
Root chord, m (ft)	1.575 (5.167)	1.880 (6.167)
Tip chord, m (ft)	0.787 (2.583)	1.60 (5.25)
Aspect ratio	10.32	7.25
Taper ratio	0.50	1.00
Thickness ratio	0.17	0.15
Wing incidence (root), deg	0.20	0.75
Dihedral angle, deg	7	7
Washout angle, deg	2.7	3.00
Leading-edge sweep angle, deg	3.67	0
Trailing-edge sweep angle, deg	-3.67	0
Airfoil	GA(W)-1	65_2-415
Flap:		
Type	Fowler	Plain
Area (total), m^2 (ft^2)	3.56 (38.3)	2.13 (23.0)
Span (per side), m (ft)	5.15 (16.91)	1.44 (4.72)
Span, percent wing span	88	50
Chord, percent wing chord	30	20
Inboard wing station, m (ft)	0.71 (2.33)	0.71 (2.33)
Maximum deflection, deg	40	40
Spoiler (or aileron on Seneca I):		
Type	Vented gap upper surface	Plain
Area (total), m^2 (ft^2)	0.488 (5.25)	1.173 (12.63)
Span (per side), m (ft)	3.226 (10.58)	1.631 (5.35)
Span, percent wing span	52.9	27.5
Chord, m (ft)	0.076 (0.248)	0.360 (1.18)
Hinge line, percent wing chord	70	78
Inboard wing station, m (ft)	2.565 (8.417)	3.673 (12.050)

TABLE I.- Concluded

	ATLIT	Seneca I
Horizontal tail (stabilator):		
Area (including tab), m^2 (ft^2)	3.60 (38.7)	3.60 (38.7)
Area, percent wing area	24.97	18.54
Span, m (ft)	4.133 (13.56)	4.133 (13.56)
Span, percent wing span	33.9	34.9
Chord, m (ft)	0.871 (2.86)	0.871 (2.86)
Aspect ratio	4.75	4.75
Taper ratio	1.00	1.00
Thickness ratio	0.10	0.10
Stabilator hinge line, percent chord	26.6	26.6
Airfoil	NACA 0010	NACA 0010
Stabilator tab area, m^2 (ft^2)	0.54 (5.8)	0.54 (5.8)
Stabilator tab span, m (ft)	3.023 (9.917)	3.023 (9.917)
Stabilator chord, m (ft)	0.178 (0.583)	0.178 (0.583)
Tab hinge line, percent chord	79.6	79.6
Vertical tail (including rudder):		
Area, m^2 (ft^2)	1.90 (20.4)	1.90 (20.4)
Area, percent wing area	13.16	9.77
Span, m (ft)	1.56 (5.12)	1.56 (5.12)
Span, percent wing span	12.80	13.17
Aspect ratio	1.285	1.285
Taper ratio	0.423	0.423
Thickness ratio	0.090	0.090
Mean aerodynamic chord, m (ft)	1.282 (4.206)	1.282 (4.206)
Leading-edge sweep angle, deg	39.92	39.92
Airfoil	NACA 0009	NACA 0009
Rudder area, m^2 (ft^2)	0.706 (7.6)	0.706 (7.6)
Rudder span, m (ft)	1.52 (5.00)	1.52 (5.00)
Rudder chord, m (ft)	0.449 (1.474)	0.449 (1.474)

TABLE II.- GA(W)-1 AIRFOIL COORDINATES

Upper surface		Lower surface	
x/c	z/c	x/c	z/c
0	0	0	0
.00200	.01300	.00200	-.00930
.00500	.02040	.00500	-.01380
.01250	.03070	.01250	-.02050
.02500	.04170	.02500	-.02690
.03750	.04965	.03750	-.03190
.05000	.05589	.05000	-.03580
.07500	.06551	.07500	-.04210
.10000	.07300	.10000	-.04700
.12500	.07900	.12500	-.05100
.15000	.08400	.15000	-.05430
.17500	.08840	.17500	-.05700
.20000	.09200	.20000	-.05930
.25000	.09770	.25000	-.06270
.30000	.10160	.30000	-.06450
.35000	.10400	.35000	-.06520
.40000	.10491	.40000	-.06490
.45000	.10445	.45000	-.06350
.50000	.10258	.50000	-.06100
.55000	.09910	.55000	-.05700
.57500	.09668	.57500	-.05400
.60000	.09371	.60000	-.05080
.62500	.09006	.62500	-.04690
.65000	.08599	.65000	-.04280
.67500	.08136	.67500	-.03840
.70000	.07634	.70000	-.03400
.72500	.07092	.72500	-.02940
.75000	.06513	.75000	-.02490
.77500	.05907	.77500	-.02040
.80000	.05286	.80000	-.01600
.82500	.04646	.82500	-.01200
.85000	.03988	.85000	-.00860
.87500	.03315	.87500	-.00580
.90000	.02639	.90000	-.00360
.92500	.01961	.92500	-.00250
.95000	.01287	.95000	-.00260
.97500	.00609	.97500	-.00400
1.00000	-.00070	1.00000	-.00800

TABLE III.- AIRFOIL COORDINATES FOR WINGLETS

x/c	z/c for -	
	Upper surface	Lower surface
0	0	0
.0020	.0077	-.0032
.0050	.0119	-.0041
.0125	.0179	-.0060
.0250	.0249	-.0077
.0375	.0296	-.0090
.0500	.0333	-.0100
.0750	.0389	-.0118
.1000	.0433	-.0132
.1250	.0469	-.0144
.1500	.0499	-.0154
.1750	.0525	-.0161
.2000	.0547	-.0167
.2500	.0581	-.0175
.3000	.0605	-.0176
.3500	.0621	-.0174
.4000	.0628	-.0168
.4500	.0627	-.0158
.5000	.0618	-.0144
.5500	.0599	-.0122
.5750	.0587	-.0106
.6000	.0572	-.0090
.6250	.0554	-.0071
.6500	.0533	-.0052
.6750	.0508	-.0033
.7000	.0481	-.0015
.7250	.0451	.0004
.7500	.0419	.0020
.7750	.0384	.0036
.8000	.0349	.0049
.8250	.0311	.0060
.8500	.0270	.0065
.8750	.0228	.0064
.9000	.0184	.0059
.9250	.0138	.0045
.9500	.0089	.0021
.9750	.0038	-.0013
1.0000	-.0020	-.0067

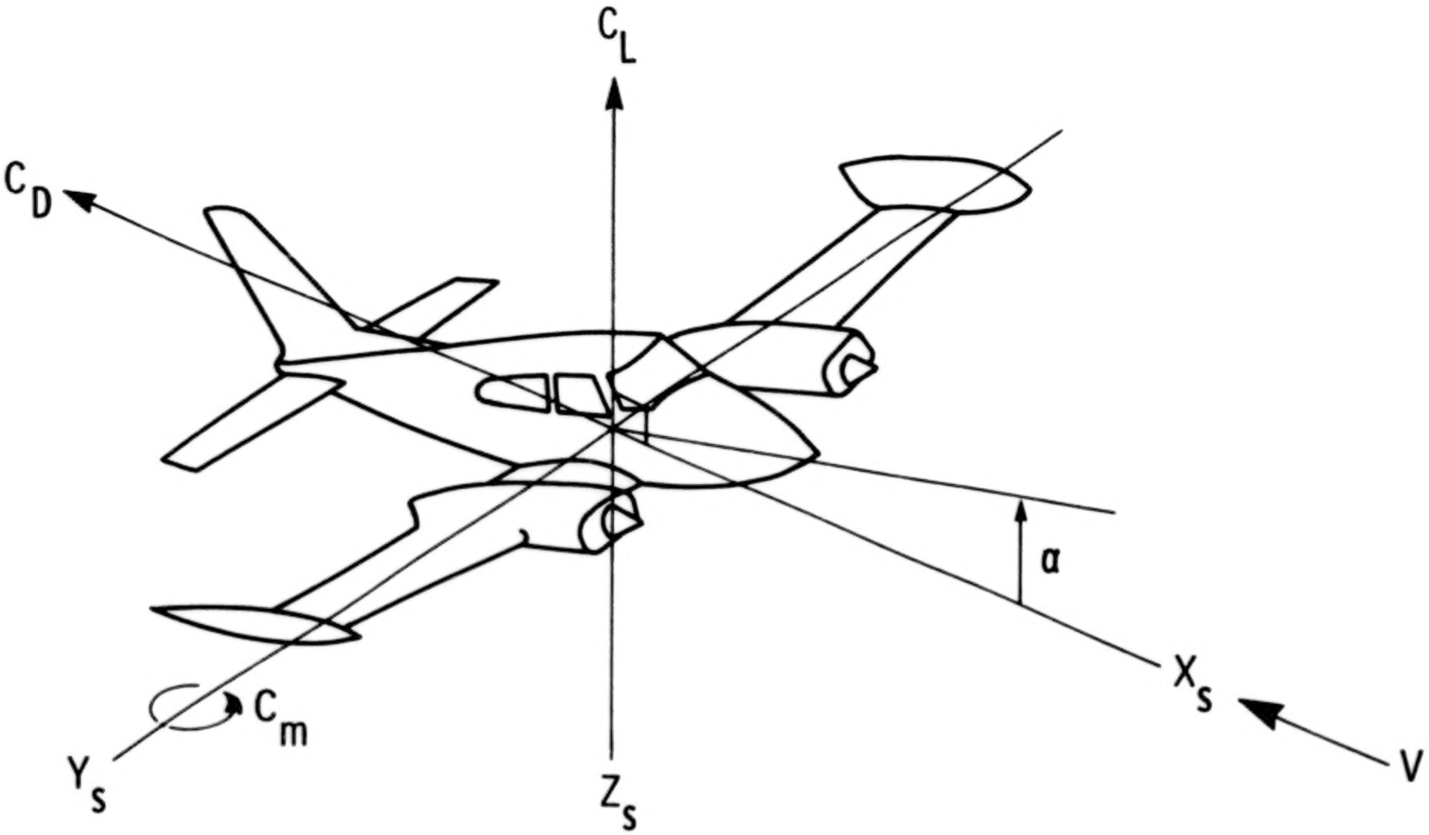
C_L
C_D
α
X_s
V
C_m
Y_s
Z_s

(a) Stability axes and positive sense of angles, forces, and moments (used for all longitudinal data unless specified otherwise).

Figure 1.- Systems of axes used in investigation.

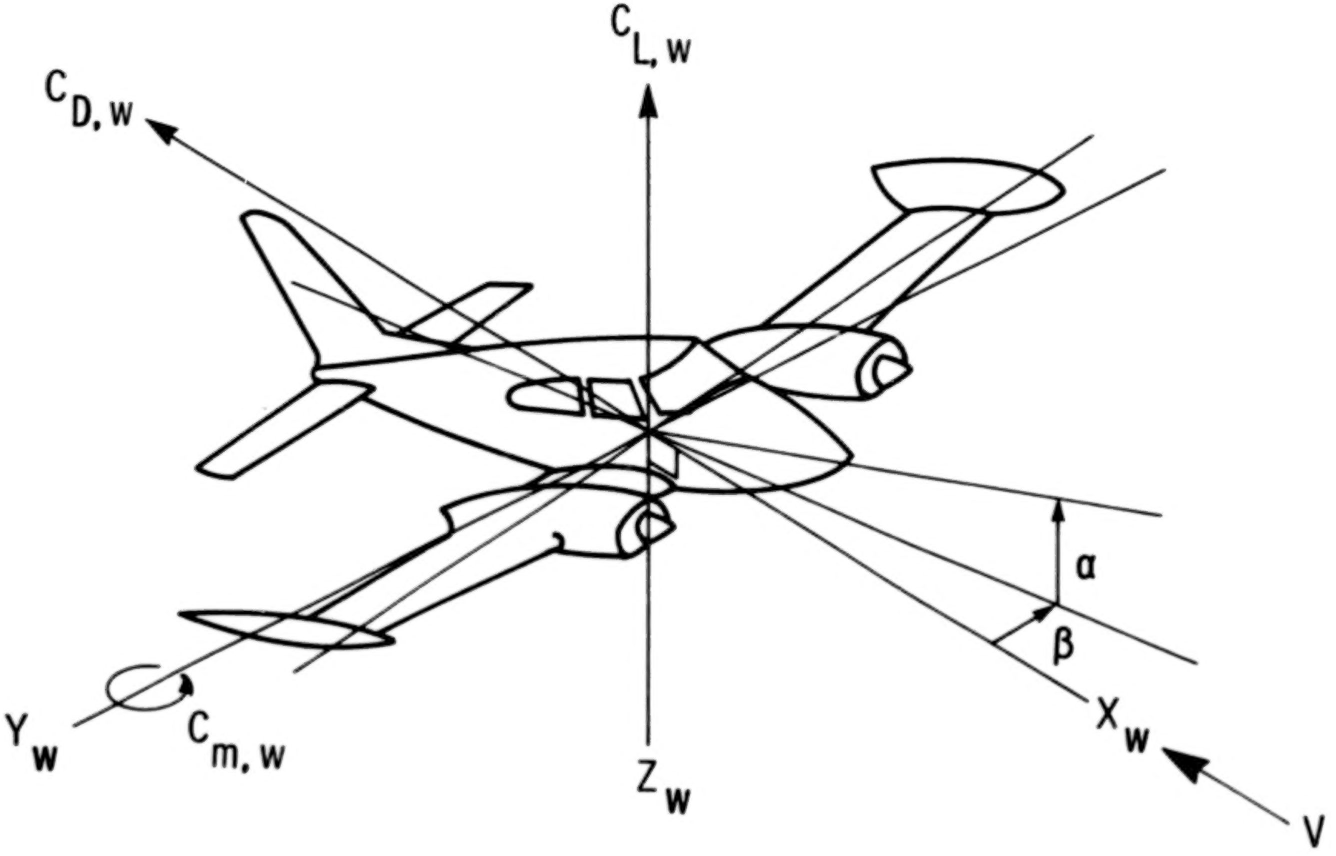
$C_{L,w}$
$C_{D,w}$
α
β
Y_w
$C_{m,w}$
Z_w
X_w
V

(b) Wind axes and positive sense of angles, forces, and moments (used for longitudinal data with airplane at sideslipped conditions).

Figure 1.- Continued.

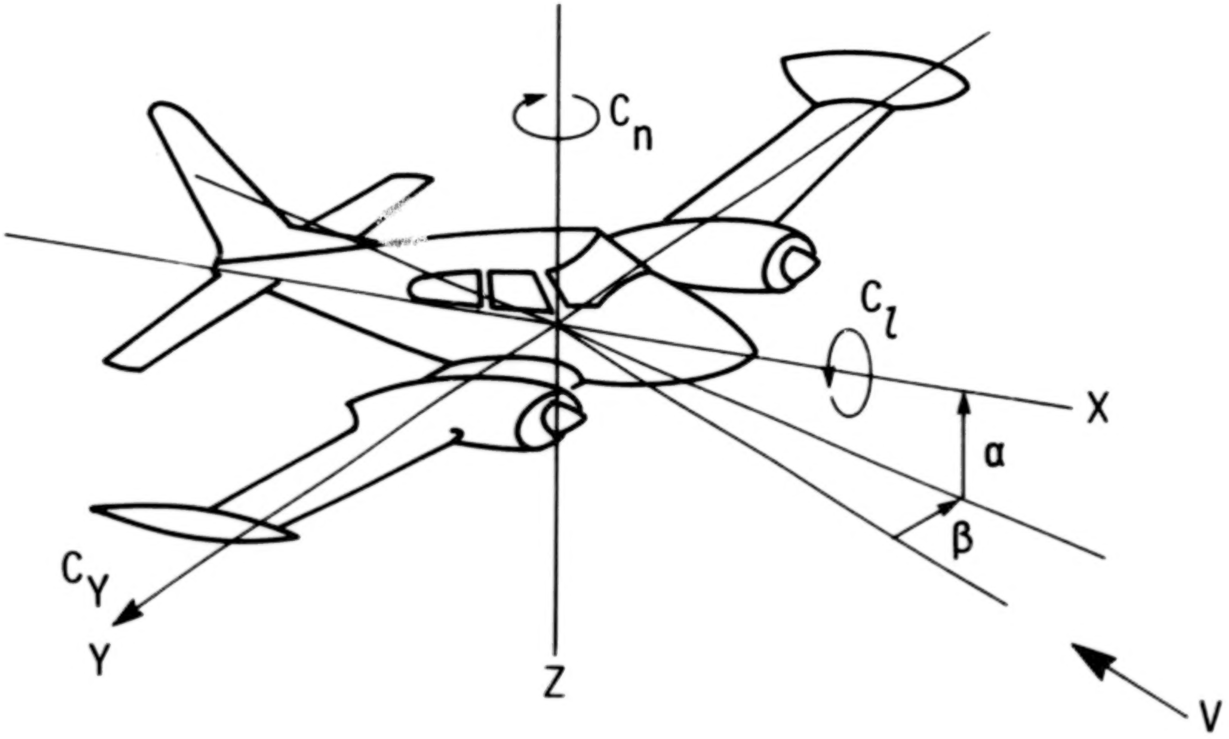

C_n
C_l
X
α
β
C_Y
Y
Z
V

(c) Body axes and positive sense of angles, forces, and moments (used for lateral-directional data only).

Figure 1.- Concluded.

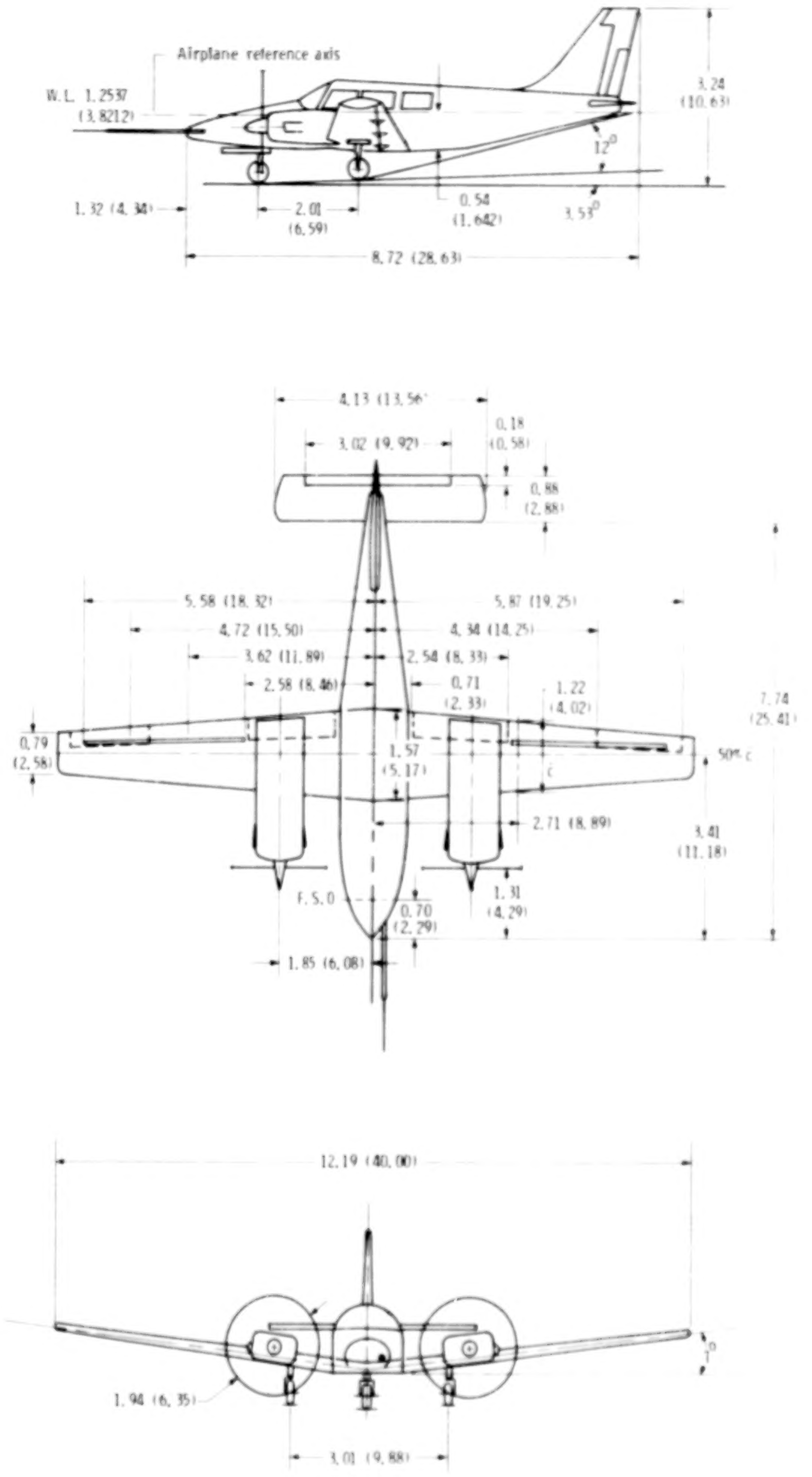
Airplane reference axis
W.L. 1.2537
(3.8212)
3.24
(10.63)
12°
1.32 (4.34)
2.01
(6.59)
0.54
(1.642)
3.53°
8.72 (28.63)
4.13 (13.56)
0.18
(0.58)
3.02 (9.92)
0.88
(2.88)
5.58 (18.32)
5.87 (19.25)
4.72 (15.50)
4.34 (14.25)
3.62 (11.89)
2.54 (8.33)
2.58 (8.46)
0.71
(2.33)
1.22
(4.02)
7.74
(25.41)
0.79
(2.58)
1.57
(5.17)
50% c
c
2.71 (8.89)
3.41
(11.18)
F.S. 0
1.31
(4.29)
0.70
(2.29)
1.85 (6.08)
12.19 (40.00)
7°
1.94 (6.35)
3.01 (9.88)

(a) Three-view sketch of ATLIT.

Figure 2.- Sketches of airplane. Dimensions given in meters (feet).

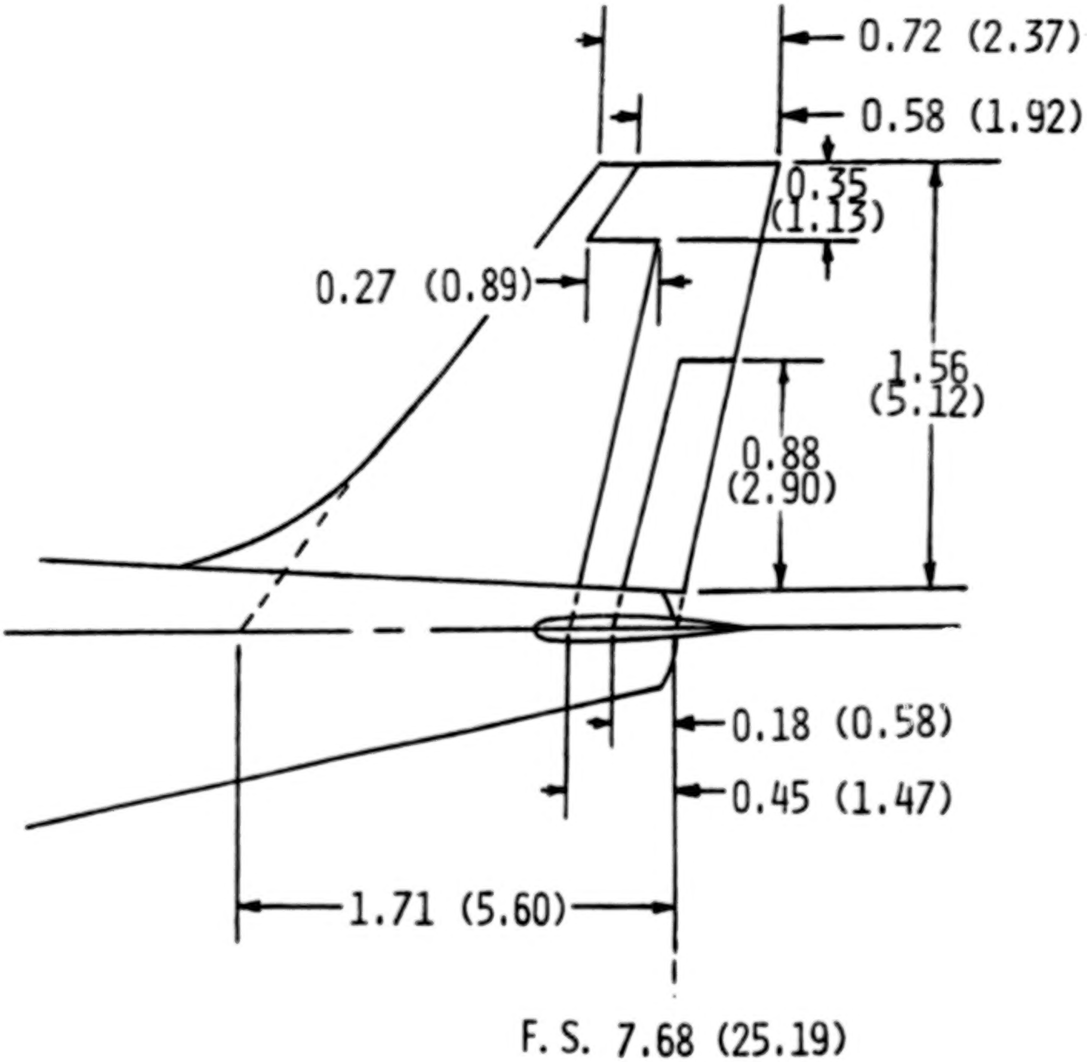
0.72 (2.37)
0.58 (1.92)
0.35 (1.13)
0.27 (0.89)
1.56 (5.12)
0.88 (2.90)
0.18 (0.58)
0.45 (1.47)
1.71 (5.60)
F.S. 7.68 (25.19)

(b) Vertical stabilizer details.

Figure 2.- Concluded.

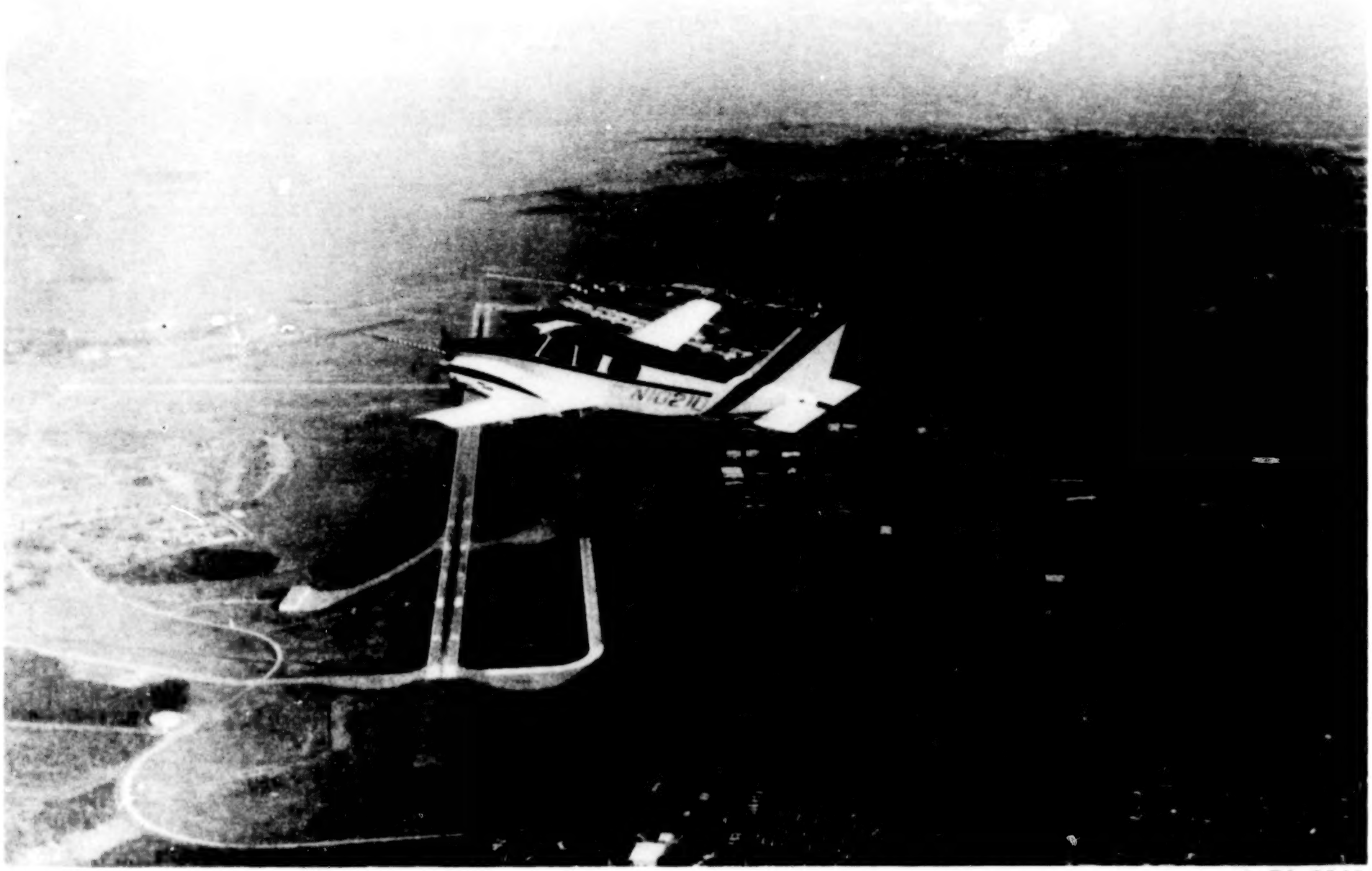

L-74-8245

(a) ATLIT in flight.

Figure 3.- Photographs of Advanced Technology Light Twin-Engine airplane (ATLIT).

58

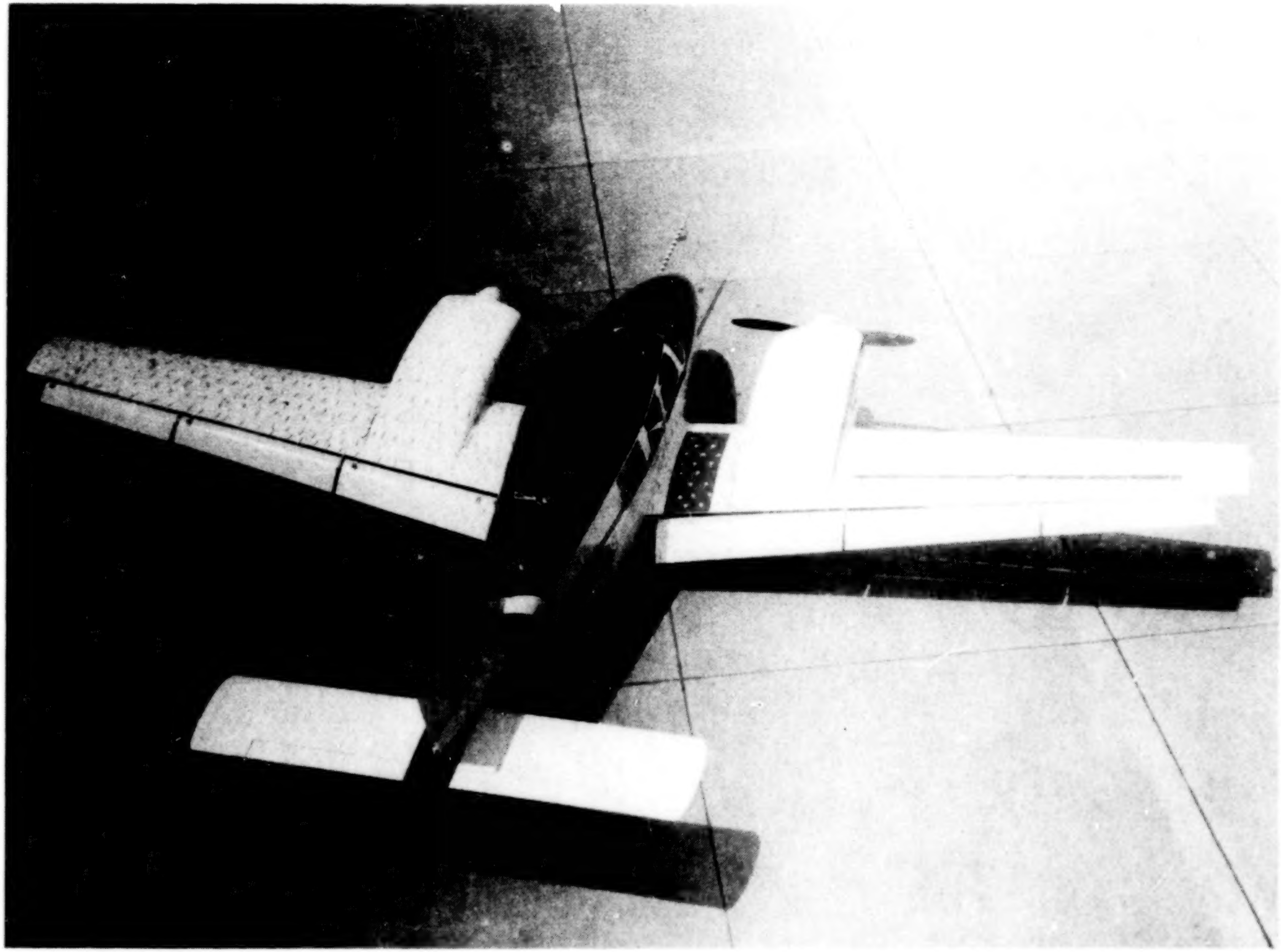

L-75-5904

(b) Top view of ATLIT showing Fowler flaps extended and right spoiler deflected.

Figure 3.- Continued.

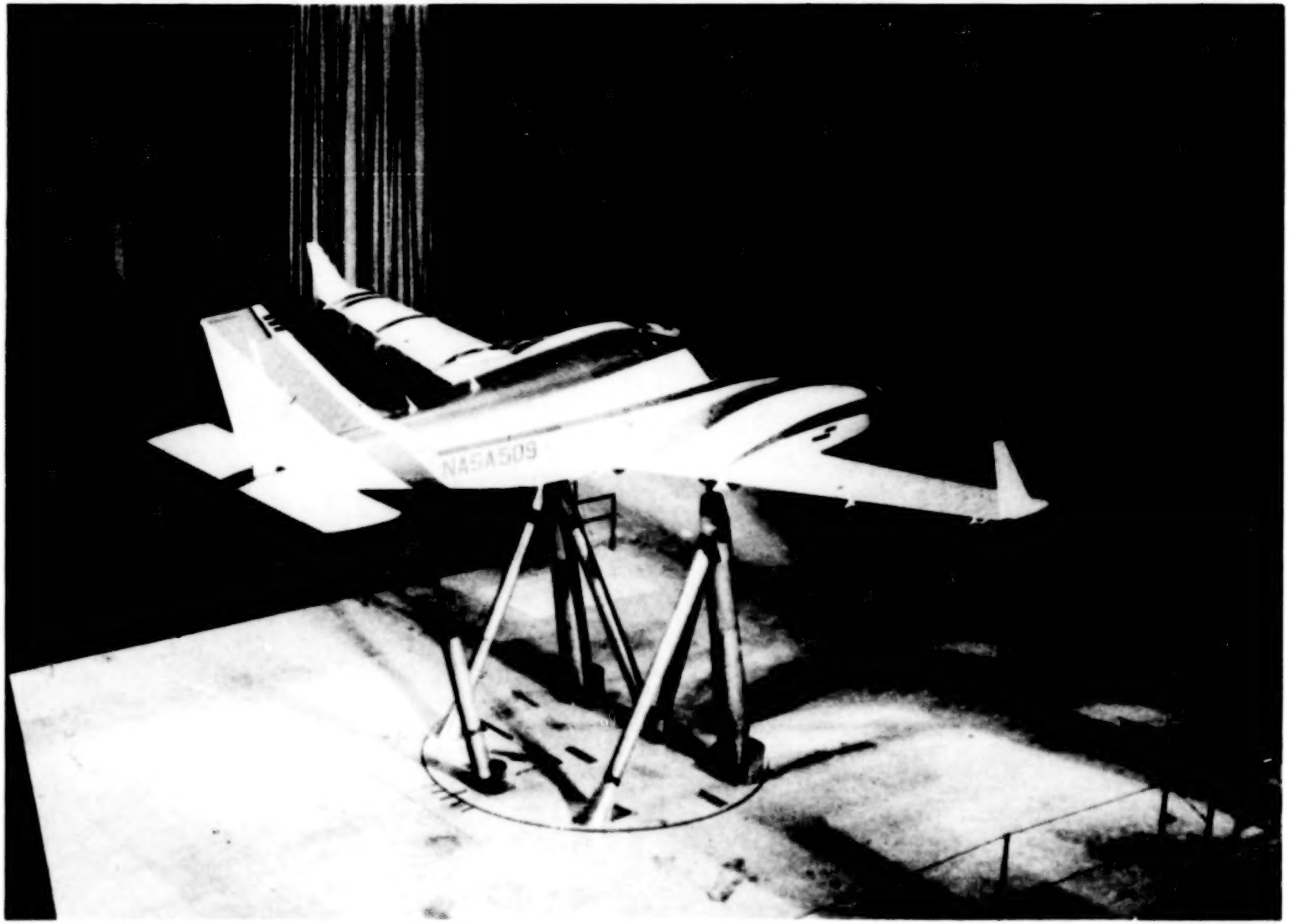

L-77-2768

(c) ATLIT in Langley Full-Scale Tunnel with winglets installed.

Figure 3.- Concluded.

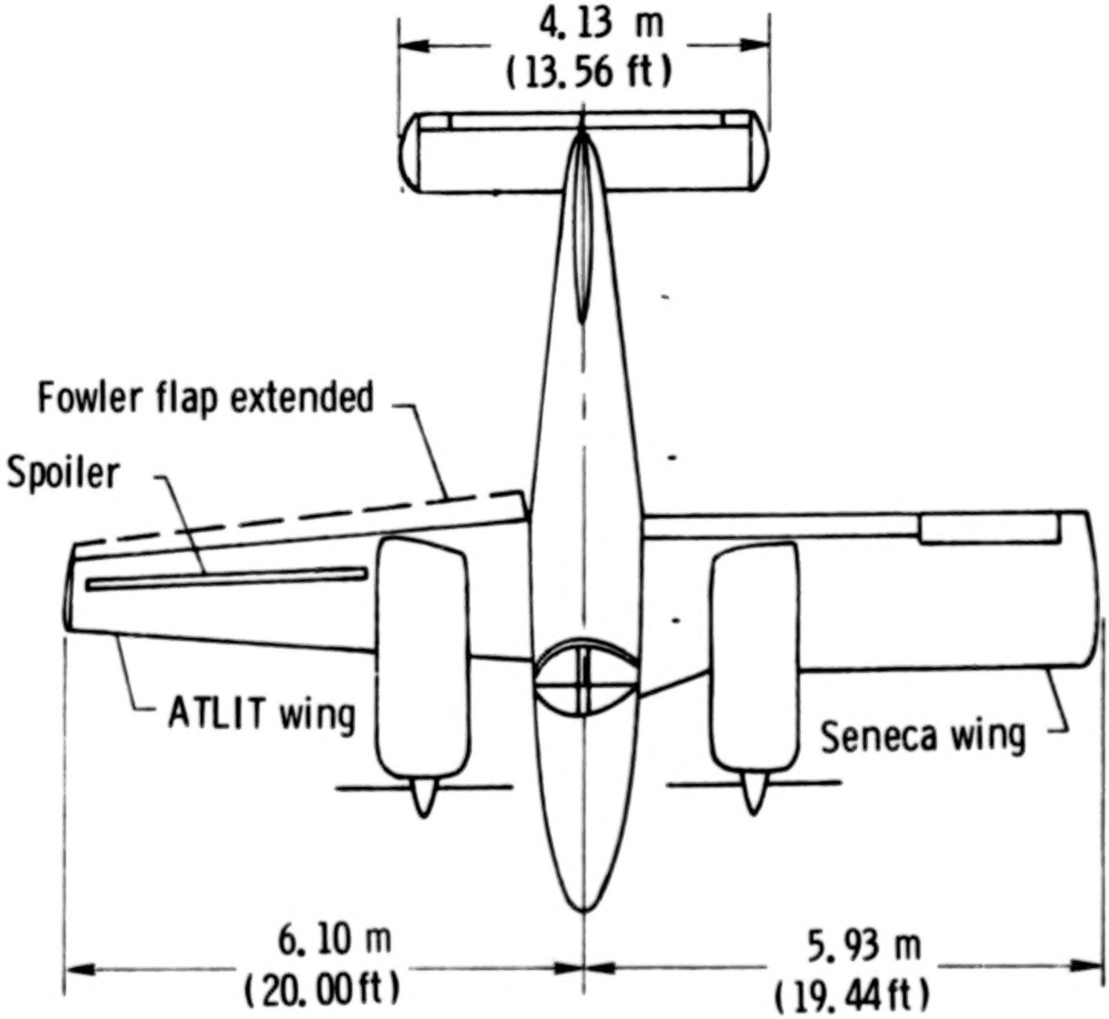
4.13 m
(13.56 ft)
Fowler flap extended
Spoiler
ATLIT wing
Seneca wing
6.10 m
(20.00 ft)
5.93 m
(19.44 ft)

(a) Overall plan view modifications.

Figure 4.- Geometric comparison of ATLIT and unmodified Seneca I.

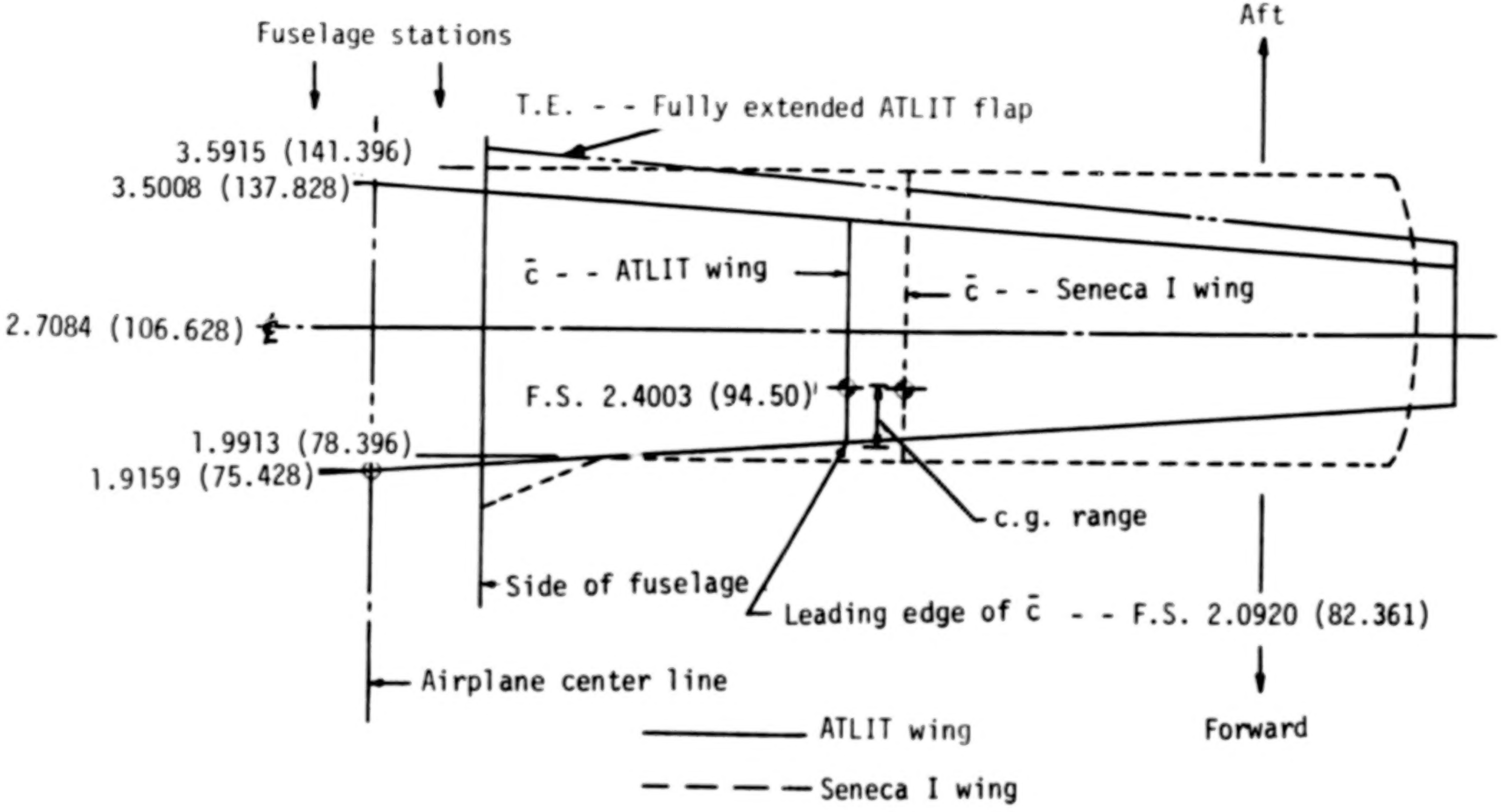
Fuselage stations
Aft
T.E. - - Fully extended ATLIT flap
3.5915 (141.396)
3.5008 (137.828)
$\bar{c}$ - - ATLIT wing
$\bar{c}$ - - Seneca I wing
2.7084 (106.628) ℄
F.S. 2.4003 (94.50)
1.9913 (78.396)
1.9159 (75.428)
c.g. range
Side of fuselage
Leading edge of $\bar{c}$ - - F.S. 2.0920 (82.361)
Airplane center line
Forward
ATLIT wing
Seneca I wing

(b) Detailed comparison of wing planforms. (See fig. 2(a) for fuselage station 0; stations given in meters (inches).)

Figure 4.- Concluded.

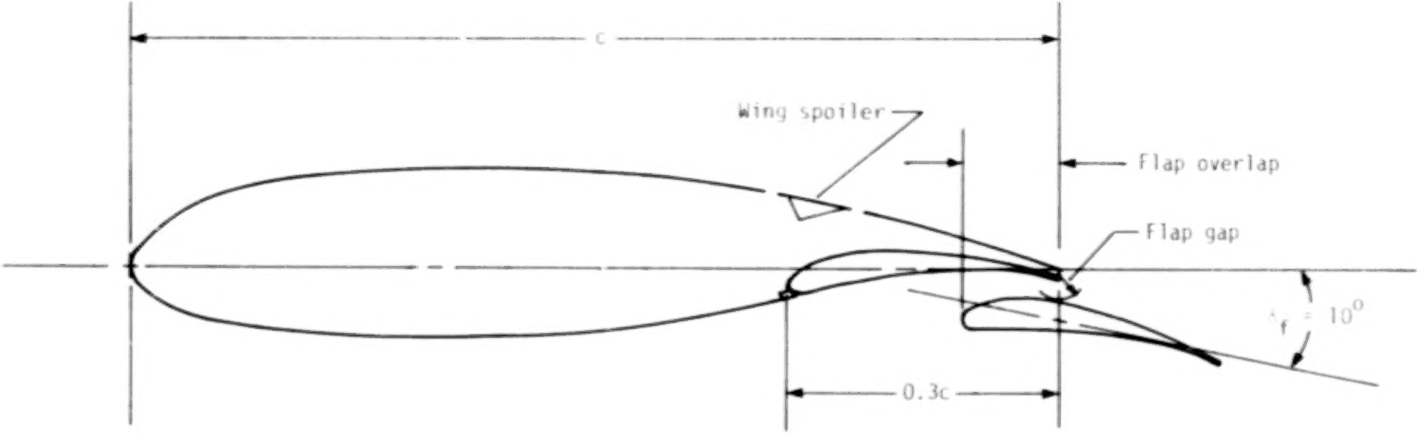

30 percent chord Fowler flap coordinates		
	Upper surface	Lower surface
X/c	Z/c	Z/c
0.000	-0.01920	-0.01920
0.025	0.00250	-0.02940
0.050	0.01100	-0.02490
0.075	0.01630	-0.02040
0.100	0.01900	-0.01600
0.125	0.01950	-0.01200
0.150	0.01820	-0.00860
0.175	0.01670	-0.00580
0.200	0.01330	-0.00360
0.225	0.00950	-0.00250
0.250	0.00530	-0.00260
0.275	0.00100	-0.00400
0.300	-0.00435	-0.00800

L.E. radius = 0.0122c

30 percent chord Fowler flap geometry		
Flap Deflection	Gap, percent chord	Overlap, percent chord
0°	0.00	30.00
5°	3.41	13.31
10°	3.66	10.94
20°	3.66	7.13
30°	3.66	2.85
37°	3.06	0.00
40°	3.15	-1.90

Figure 5.- Coordinates and geometry of Fowler flap.

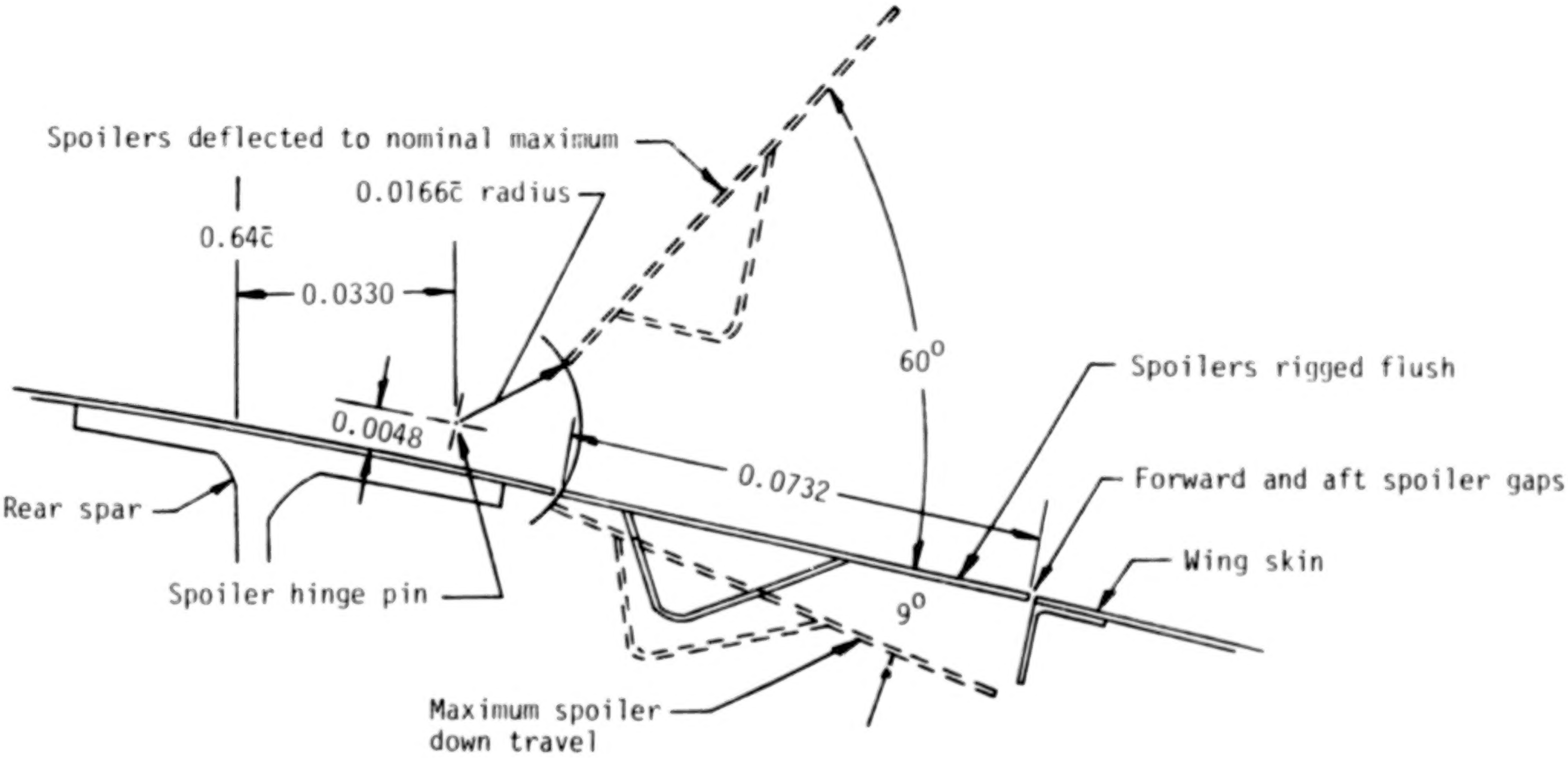
Spoilers deflected to nominal maximum
0.0166c̄ radius
0.64c̄
0.0330
0.0048
60°
Spoilers rigged flush
0.0732
Forward and aft spoiler gaps
Rear spar
Wing skin
9°
Spoiler hinge pin
Maximum spoiler down travel

(a) Spoiler installation detail.

Figure 6.- Spoiler system used for lateral control.

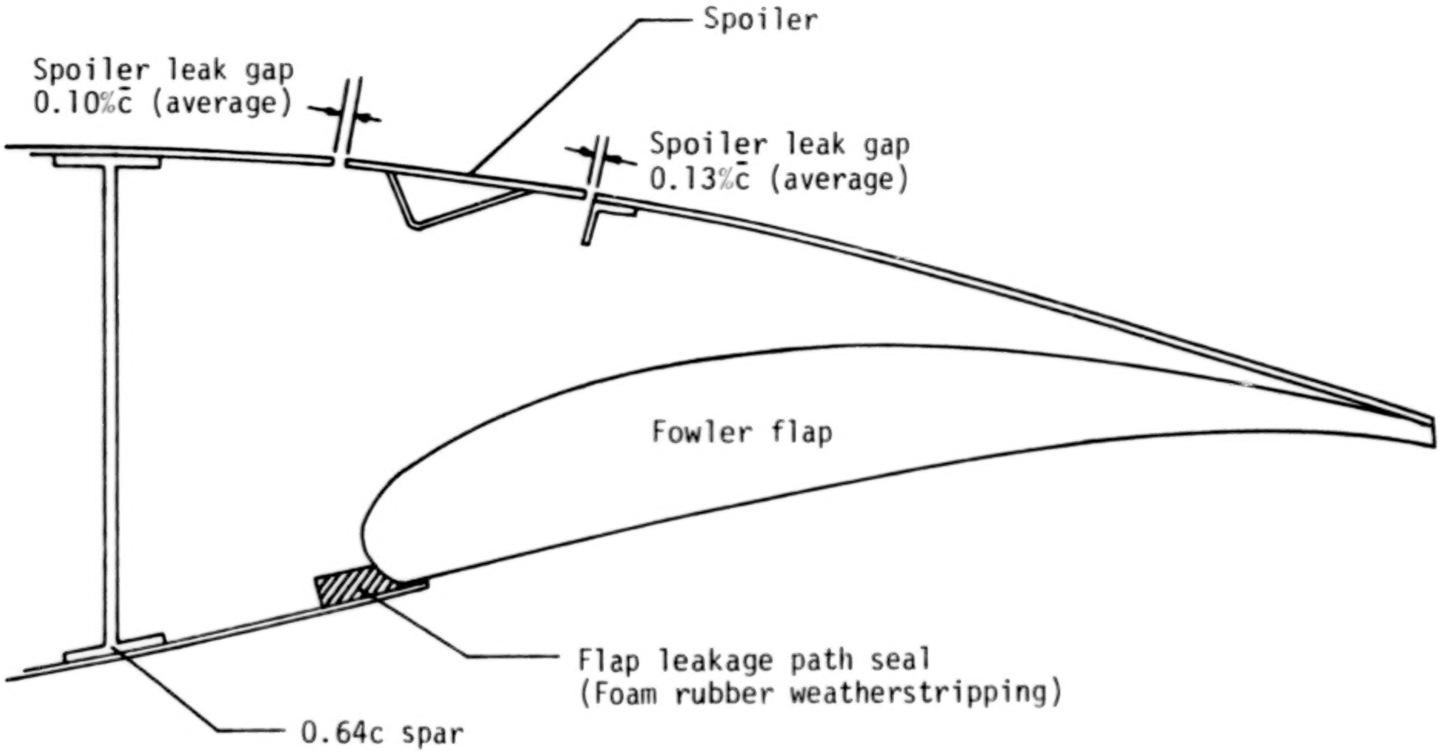
Spoiler
Spoiler leak gap
0.10%c̄ (average)
Spoiler leak gap
0.13%c̄ (average)
Fowler flap
Flap leakage path seal
(Foam rubber weatherstripping)
0.64c spar

(b) Flap and spoiler leak paths and method used to seal leakage during flight tests.

Figure 6.- Concluded.

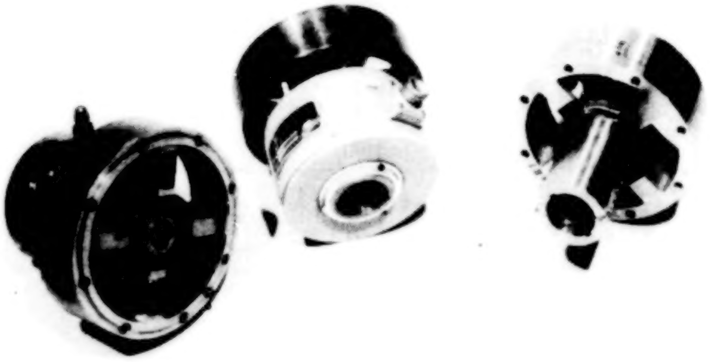

L-77-7876

(a) Propeller thrust-torque balances and slipring assemblies.

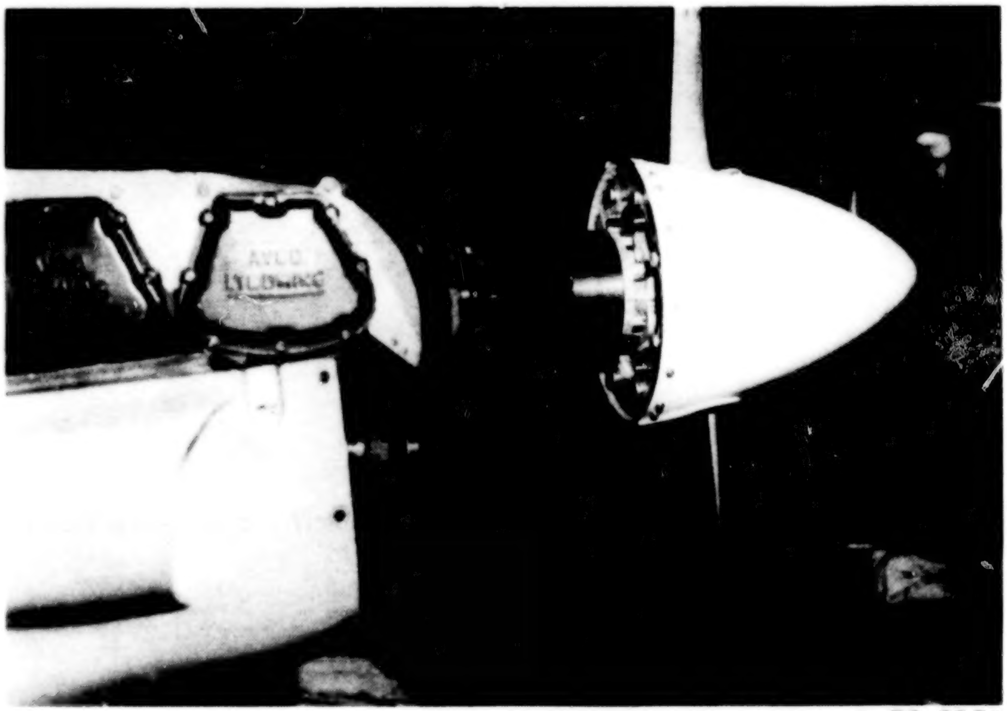

L-76-8151

(b) Installation on engine propeller shaft.

Figure 7.- Instrumentation for measurement of propeller thrust and torque.

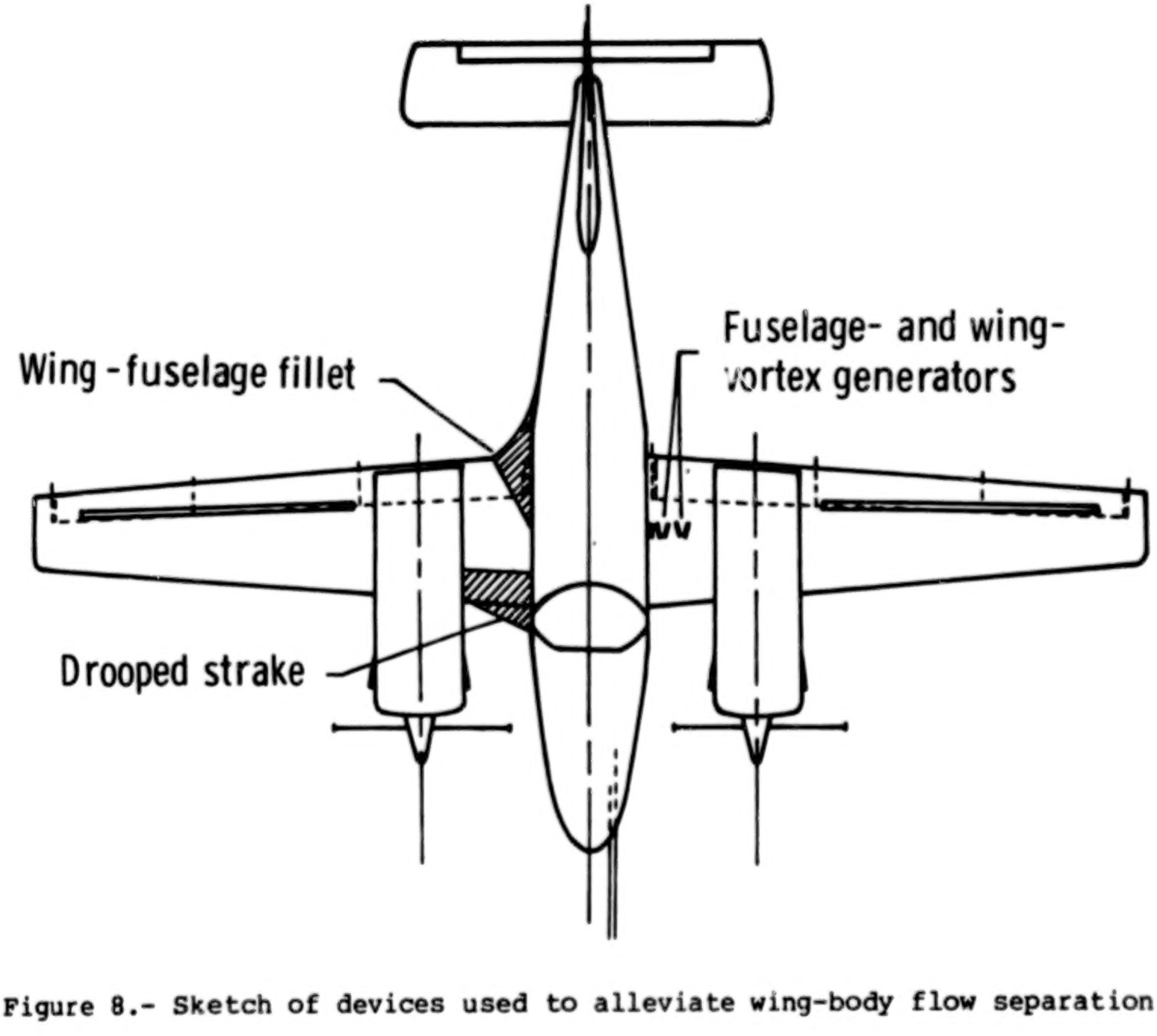
Wing - fuselage fillet
Fuselage- and wing-vortex generators
Drooped strake

Figure 8.- Sketch of devices used to alleviate wing-body flow separation.

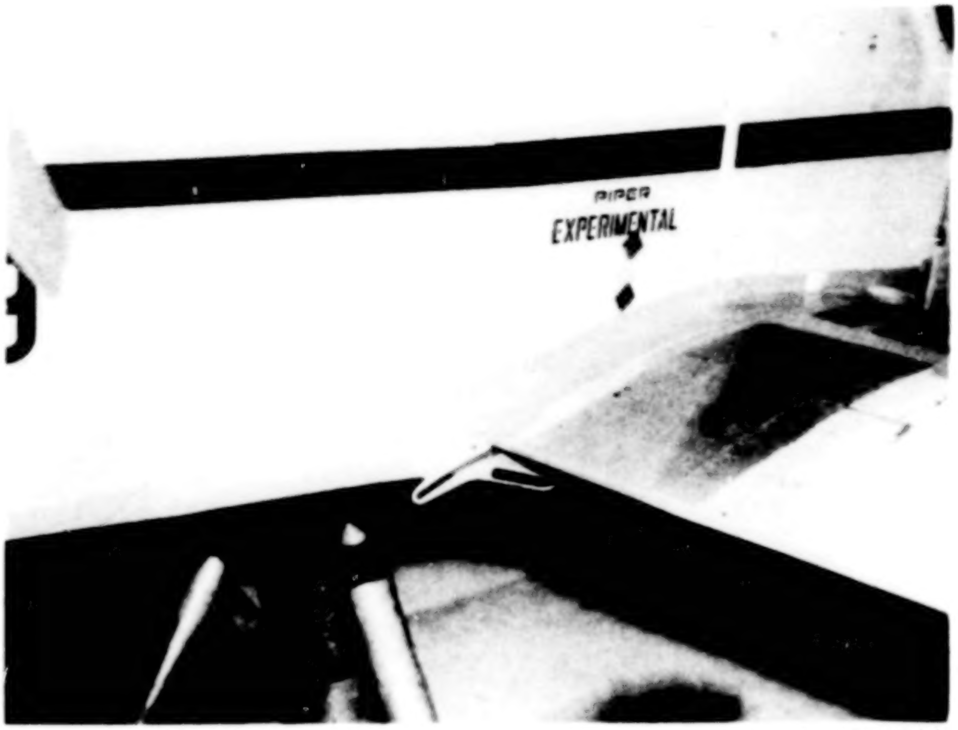
PIPER
EXPERIMENTAL

L-77-3858

(a) Top view.

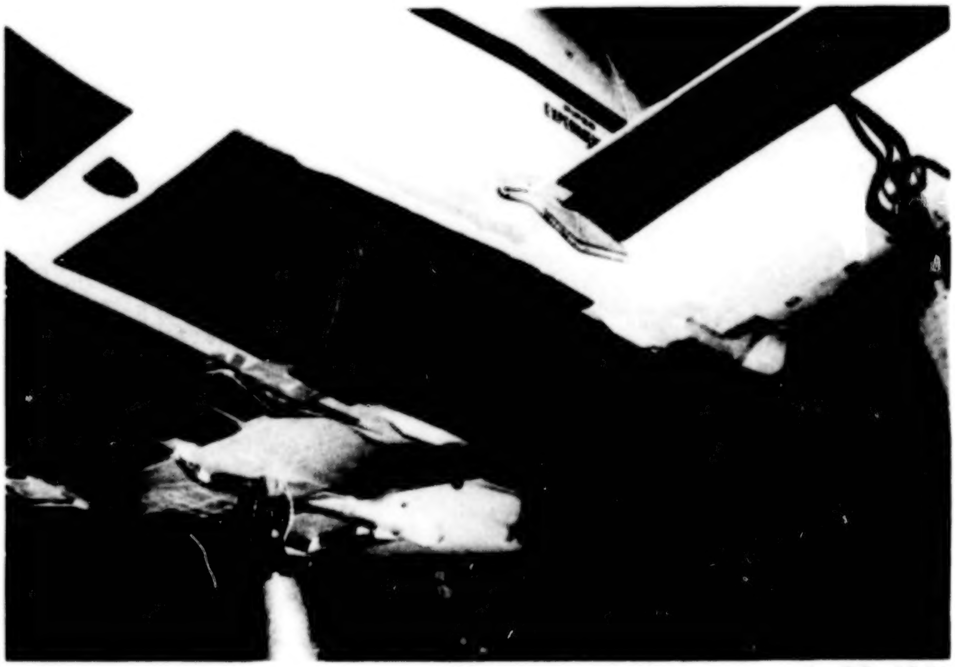

L-77-3855

(b) Bottom view.

Figure 9.- Wing-fuselage juncture without wing-fuselage fillet.

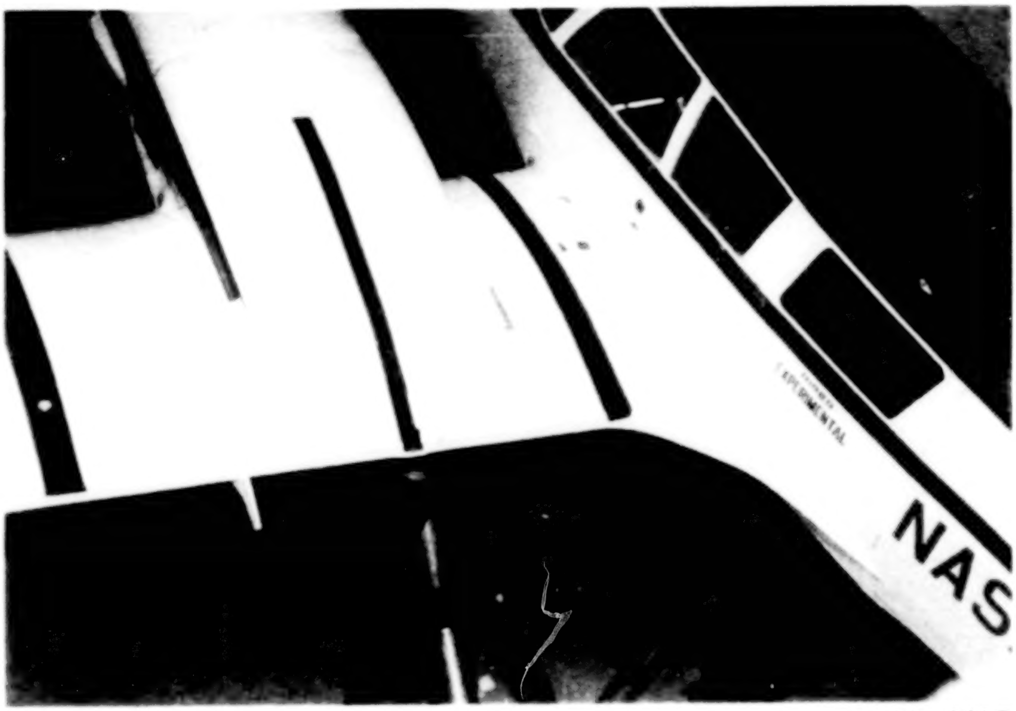
EXPERIMENTAL
NAS

L-77-3017

(a) Top view.

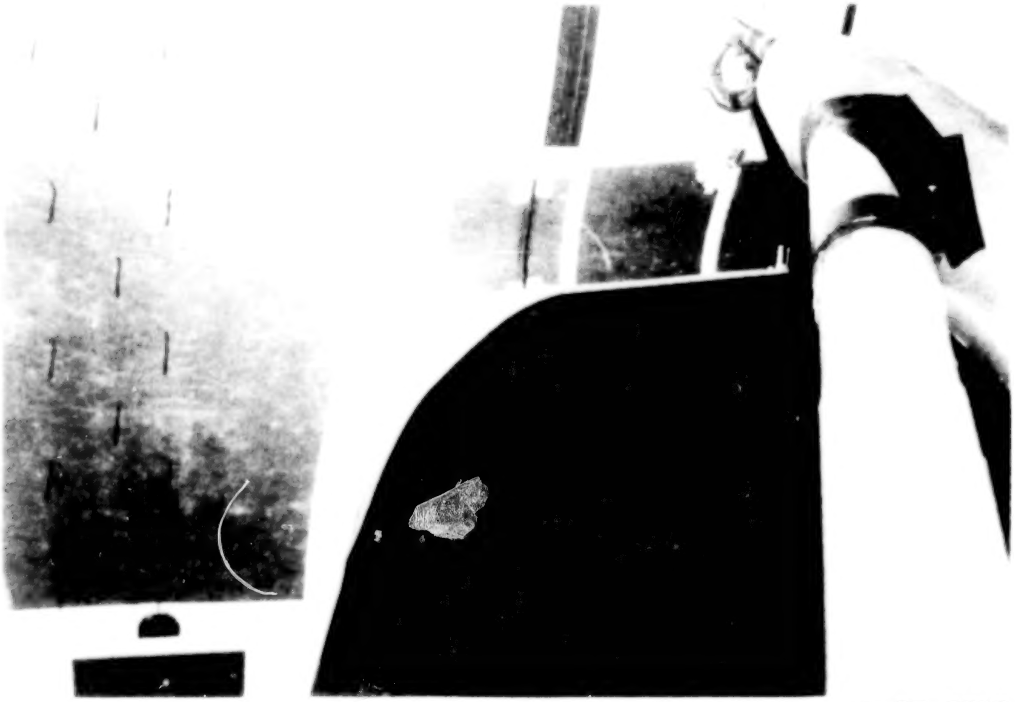

L-77-3018

(b) Bottom view.

Figure 10.- Wing-fuselage juncture with wing-fuselage fillet installed.

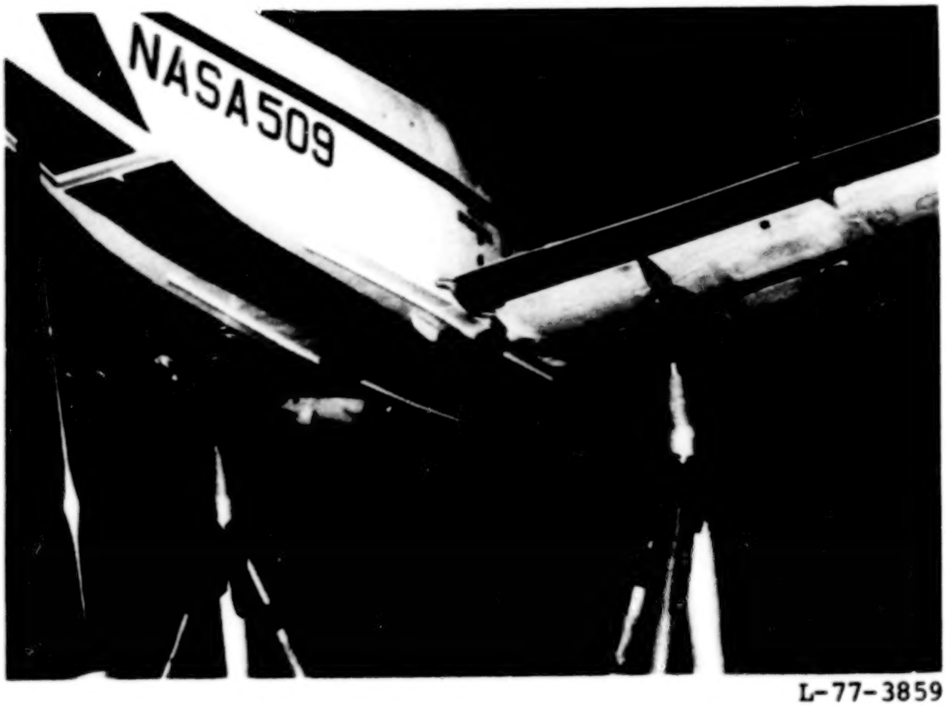

L-77-3859

(a) Fuselage bottom as received.

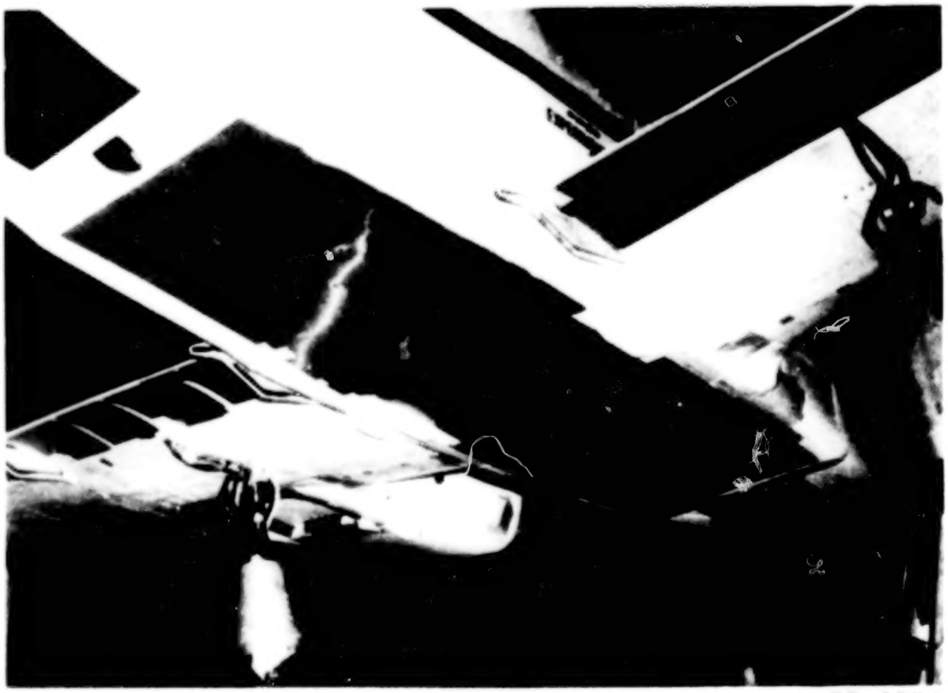

L-77-3854

(b) Fuselage bottom refaired.

Figure 11.- Modification to bottom of fuselage.

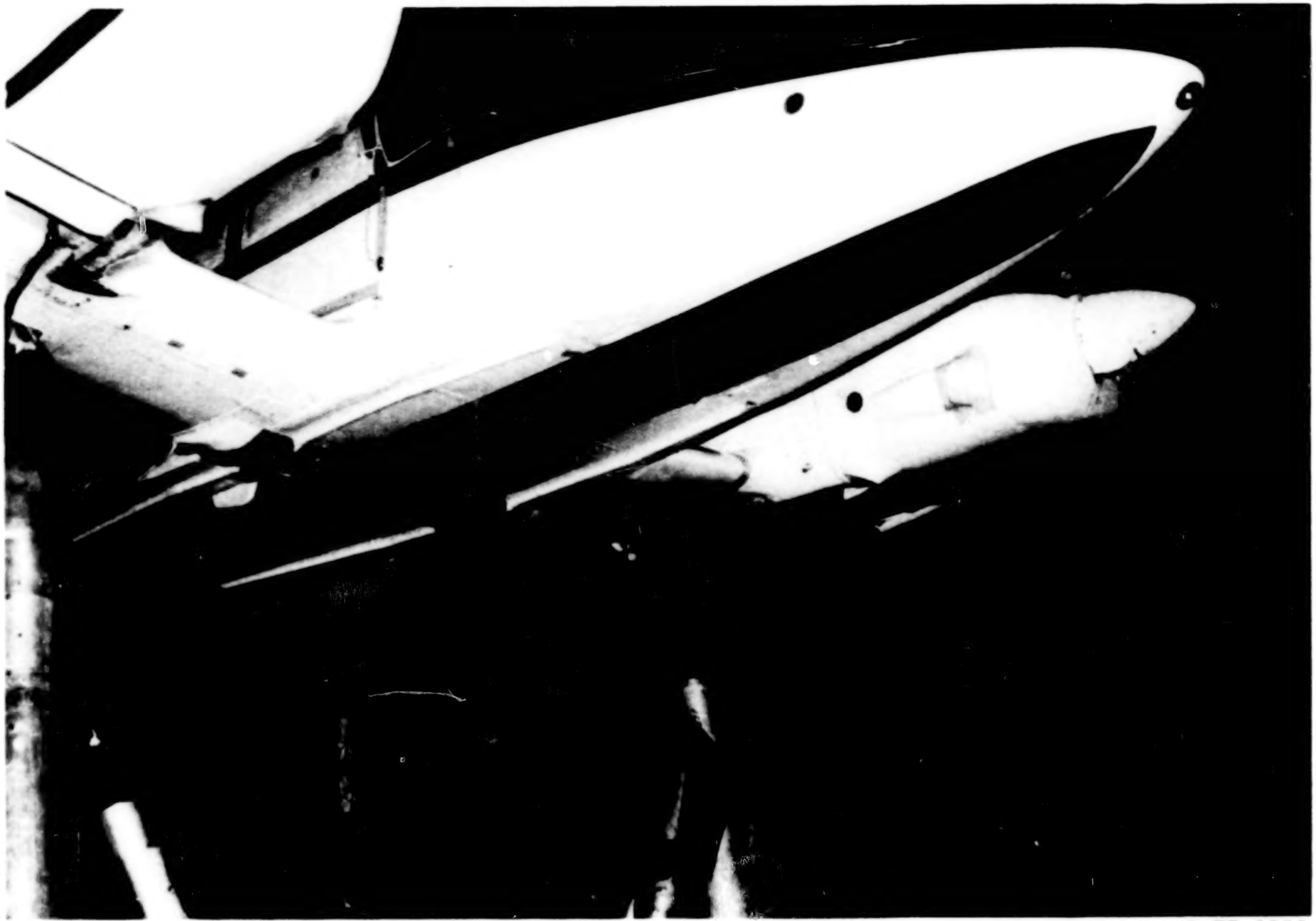

L-77-3850

Figure 12.- Airplane configuration with propellers removed, engine inlets sealed, and cowl flaps closed.

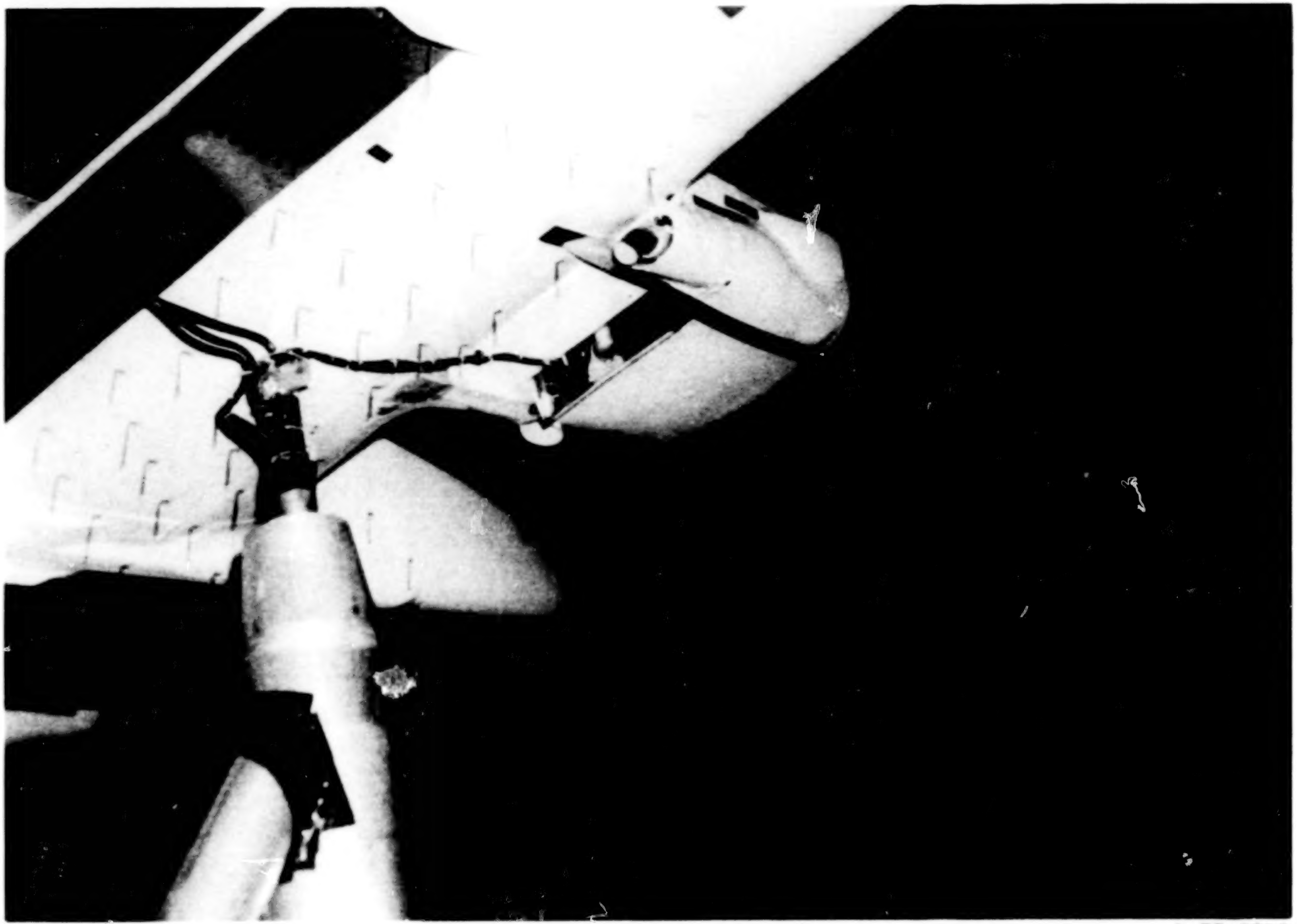

L-77-3016

Figure 13.- Airplane configuration with engine cowl flaps fully open.

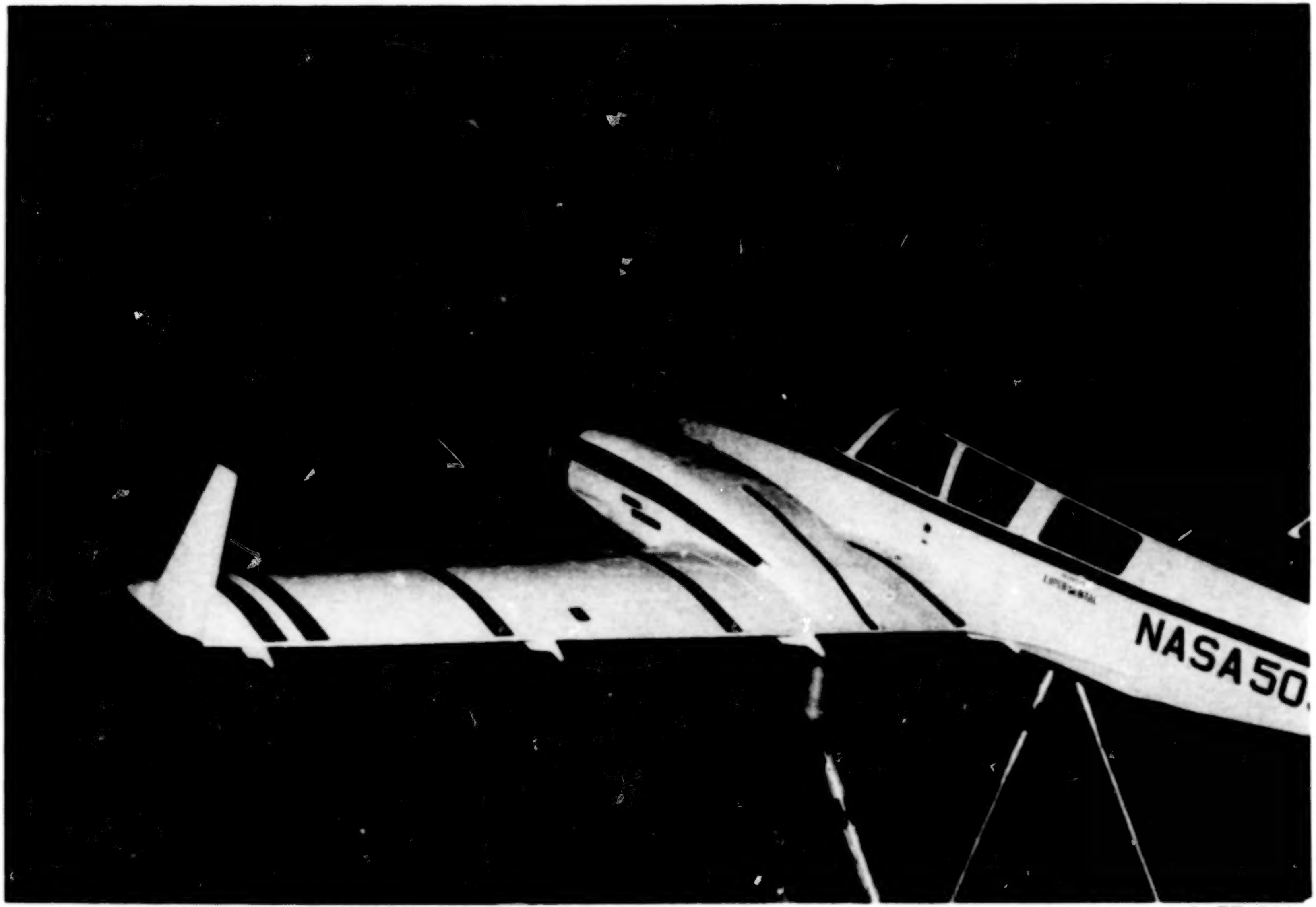

L-77-3023

Figure 14.- Installation of winglet and pressure belts (for wing surface-pressure measurements).

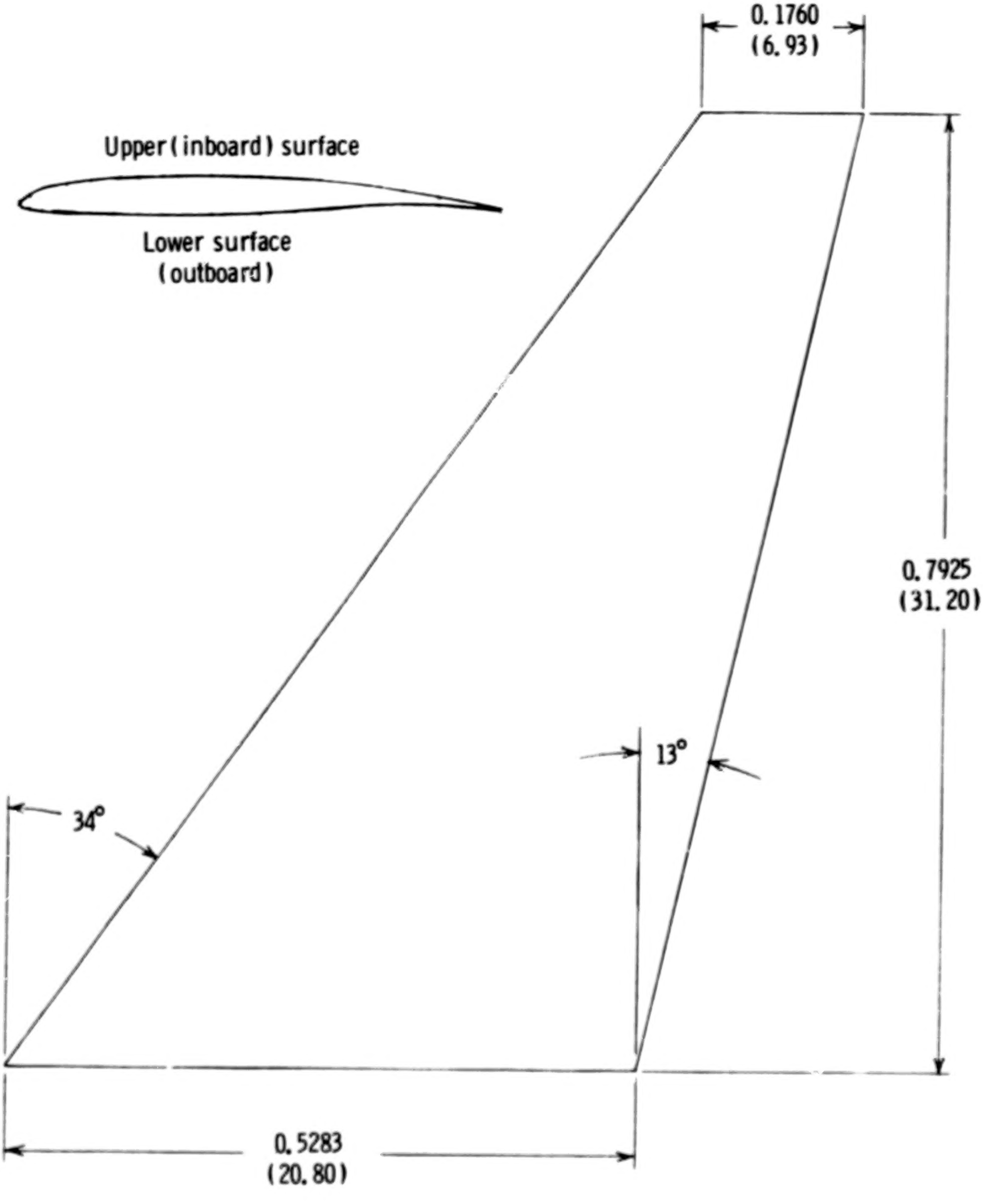
0.1760
(6.93)
Upper (inboard) surface
Lower surface
(outboard)
0.7925
(31.20)
13°
34°
0.5283
(20.80)

(a) Planform geometry.

Figure 15.- Sketch of winglet. Dimensions given in meters (inches).

NAS 1.60:1591

FULL-SCALE WIND-TUNNEL INVESTIGATION OF THE ADVANCED
TECHNOLOGY LIGHT TWIN-ENGINE AIRPLANE (ATLIT) ...
NASA TECHNICAL PAPER 1591... NATIONAL AERONAUTICS
AND SPACE ADMINISTRATION... MAY 1980

2 OF 4
24X
SUPTDOCS
GPO

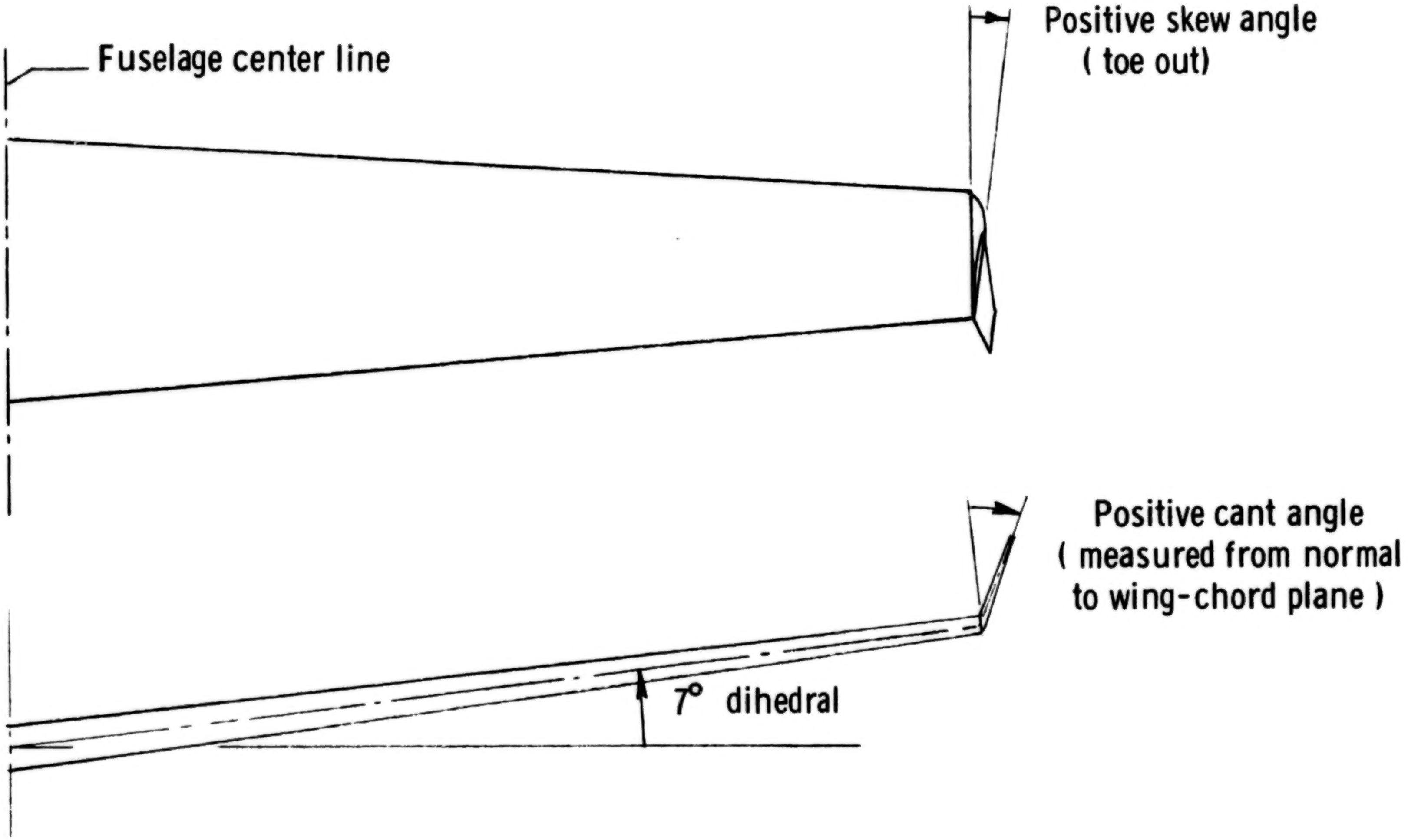
Fuselage center line
Positive skew angle
(toe out)
Positive cant angle
(measured from normal
to wing-chord plane)
7° dihedral

(b) Definitions of winglet skew and cant angles.

Figure 15.- Concluded.

Upper surface orifices x/c	Lower surface orifices x/c
0	
.025	.025
.050	.050
.075	
.100	.100
.150	
.200	
.250	.250
.350	
.450	.400
.550	
.650	.650
.750	
.850	.800
.950	.950

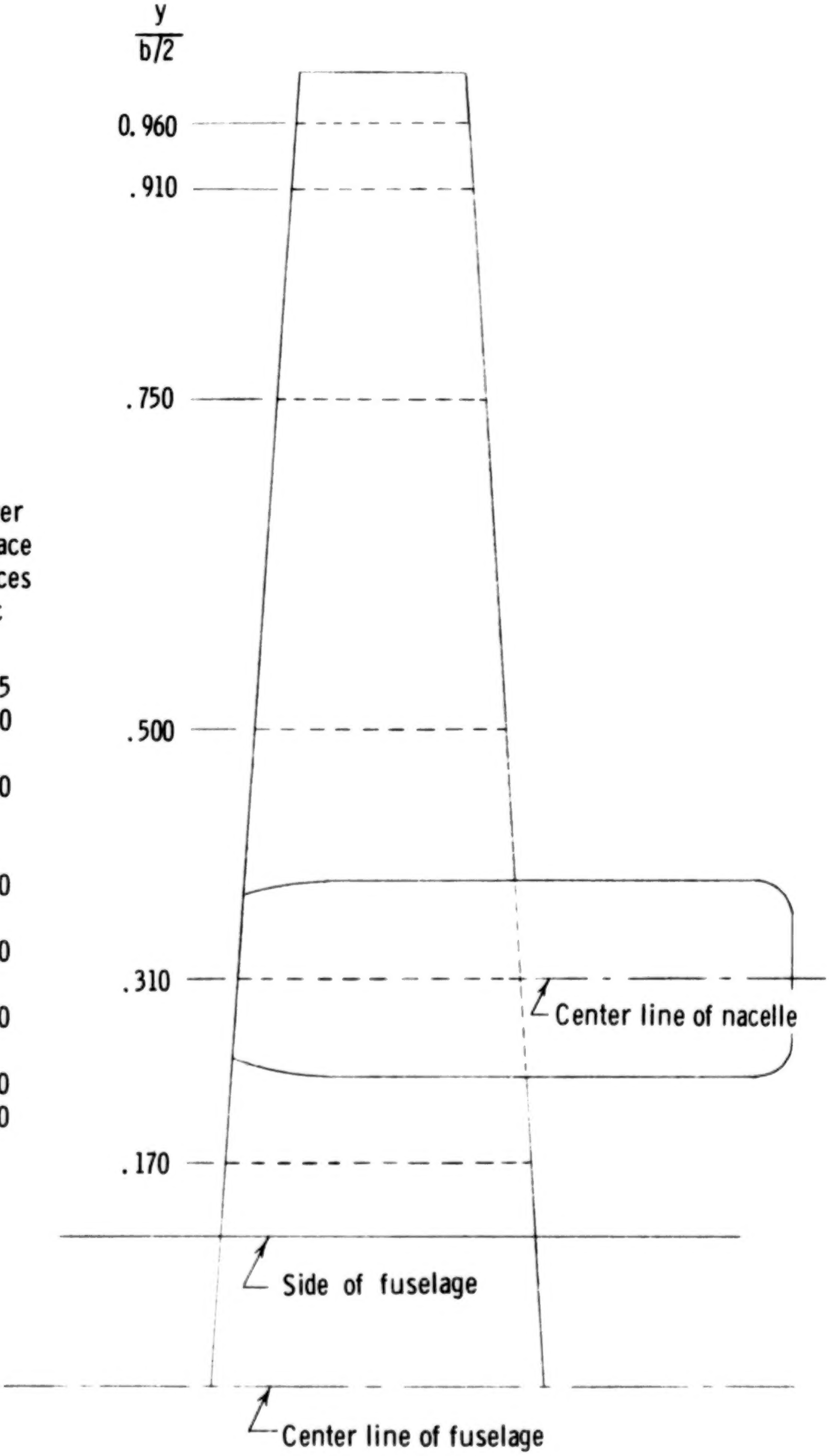
$\frac{y}{b/2}$
0.960
.910
.750
.500
.310
.170
Center line of nacelle
Side of fuselage
Center line of fuselage

(a) Pressure belts on wing.

Figure 16.- Location of surface-pressure belts and orifices.

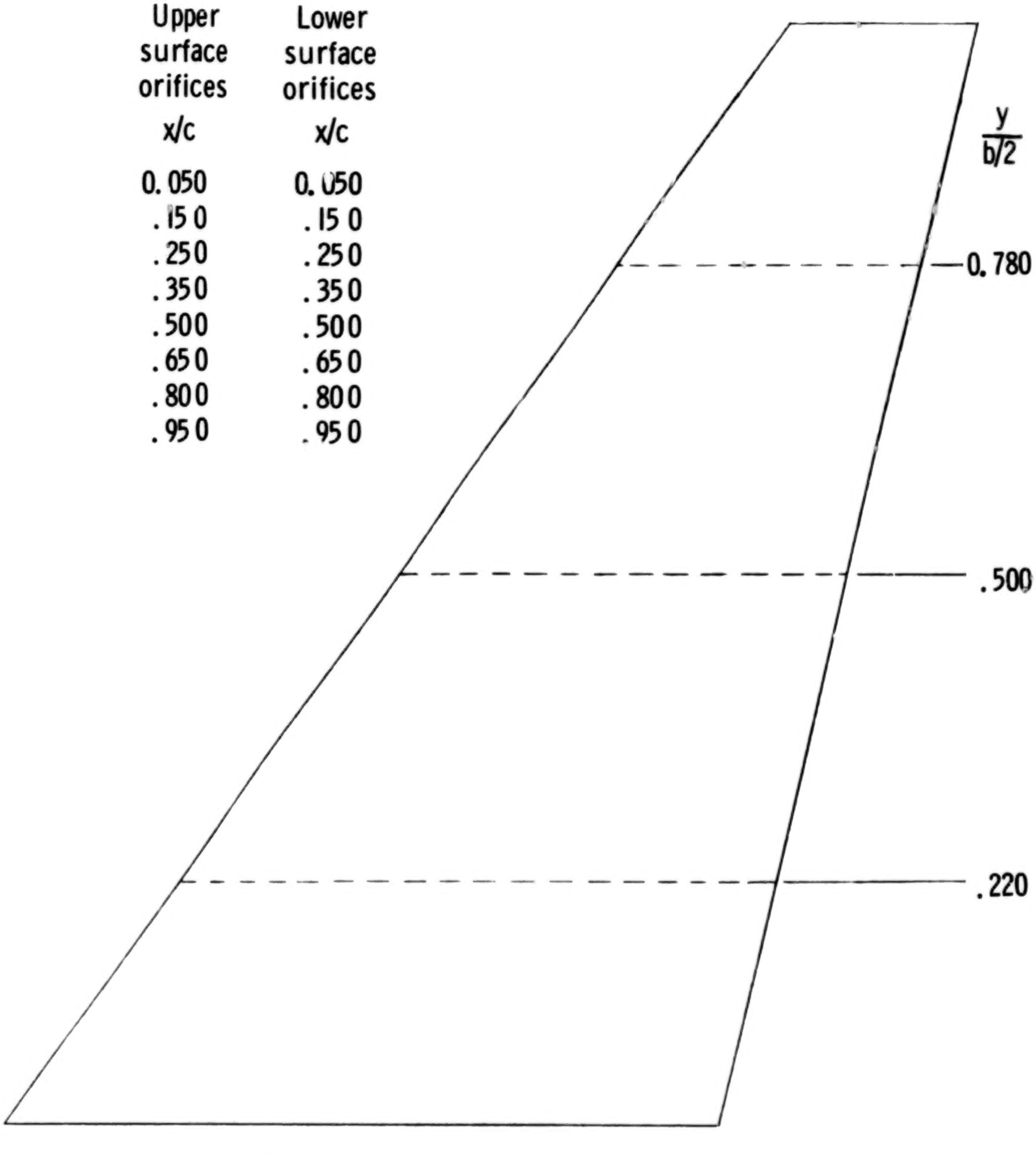

Upper surface orifices x/c	Lower surface orifices x/c
0.050	0.050
.150	.150
.250	.250
.350	.350
.500	.500
.650	.650
.800	.800
.950	.950

$\frac{y}{b/2}$
0.780
.500
.220

(b) Embedded pressure orifices on winglet.

Figure 16.- Concluded.

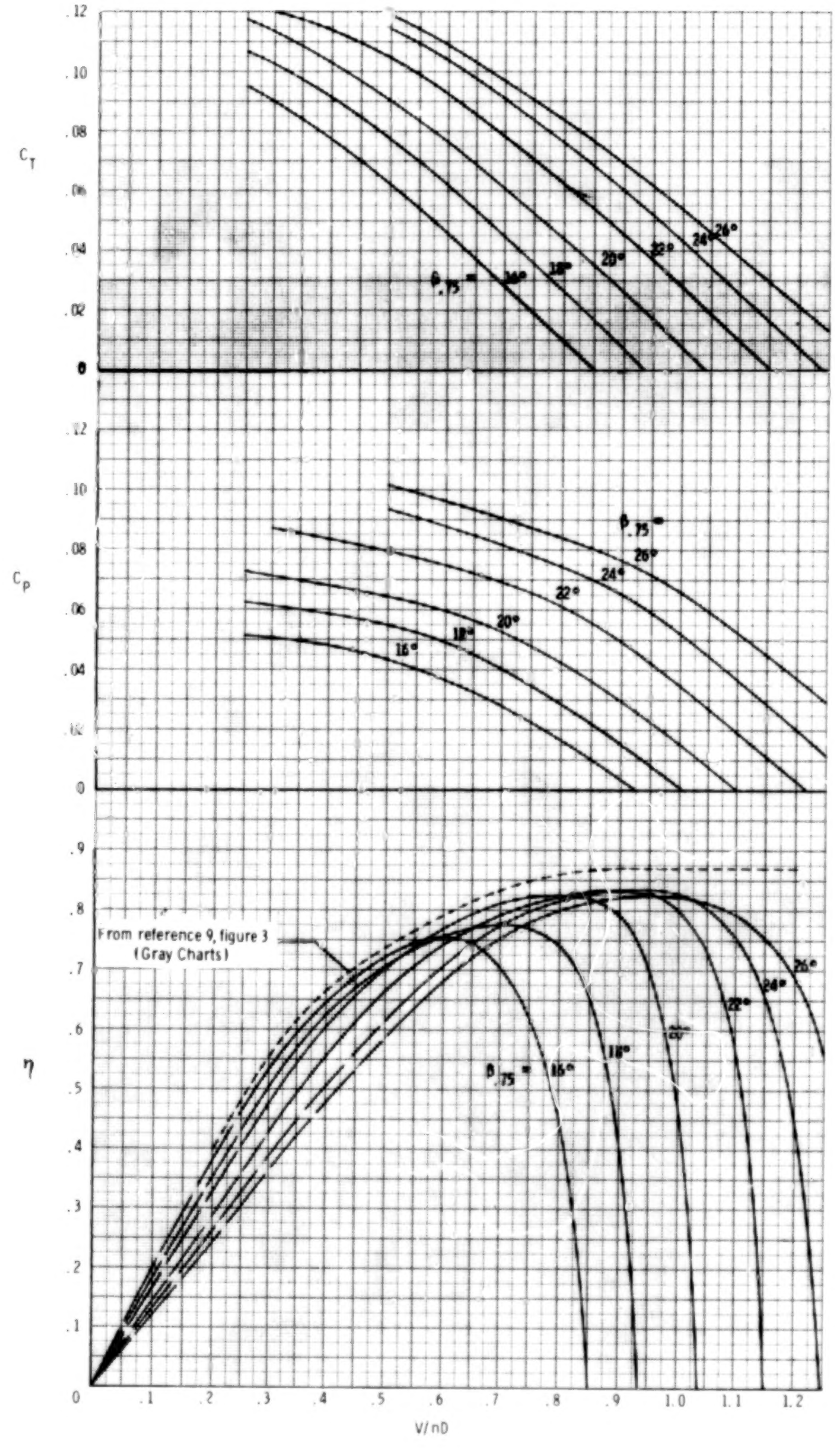

Figure 17.- Installed propeller characteristics at $\alpha = 0^\circ$.

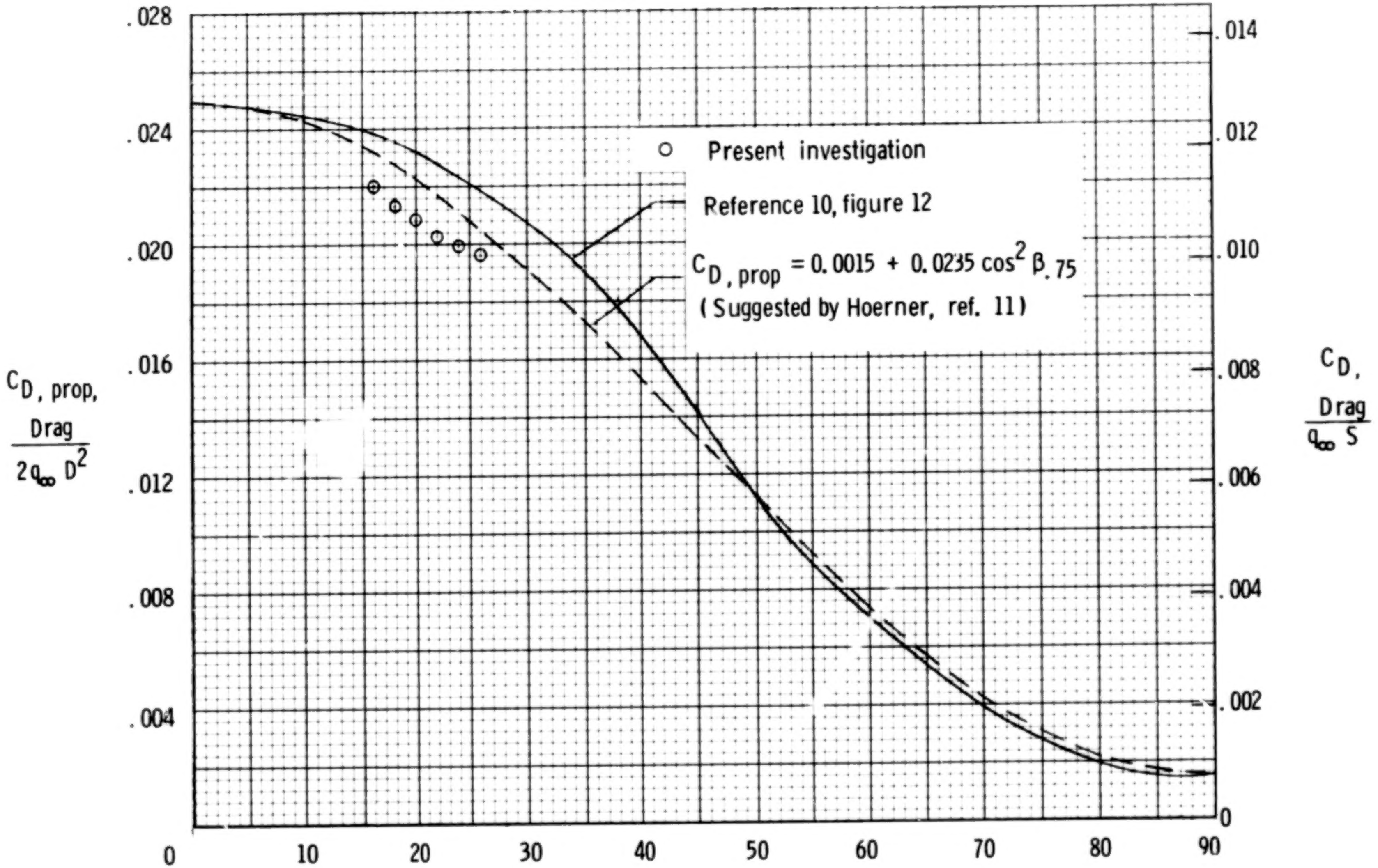

Figure 18.- Drag of stopped propeller at $\alpha = 0^\circ$.

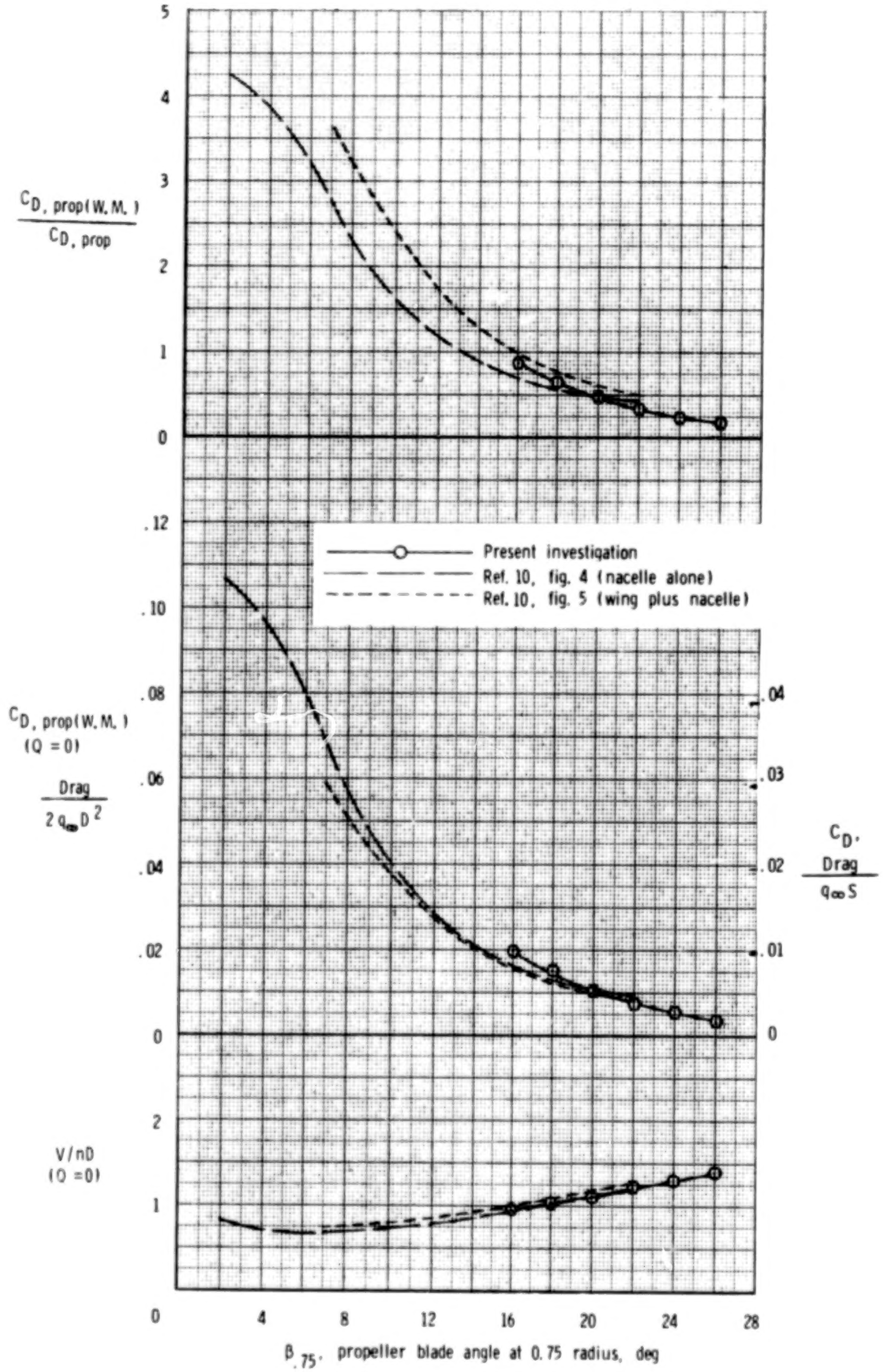

Figure 19.- Drag of windmilling propeller at $\alpha = 0^{\circ}$. (Q = 0 defines windmilling condition.)

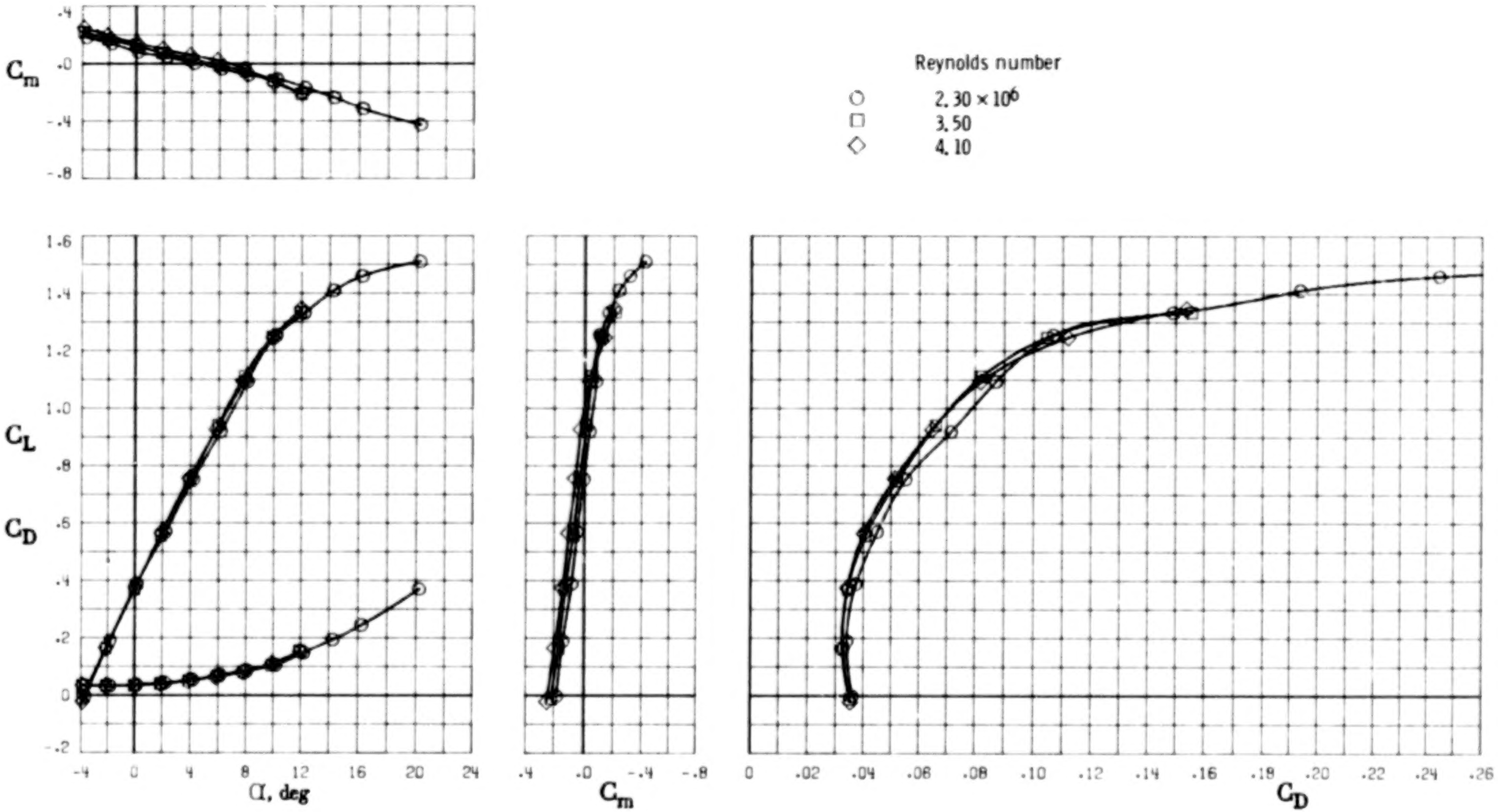

(a) Longitudinal characteristics.

Figure 20.- Effect of Reynolds number with engine inlets sealed and cowl flaps closed (fully clean configuration with pressure belts and tufts installed).

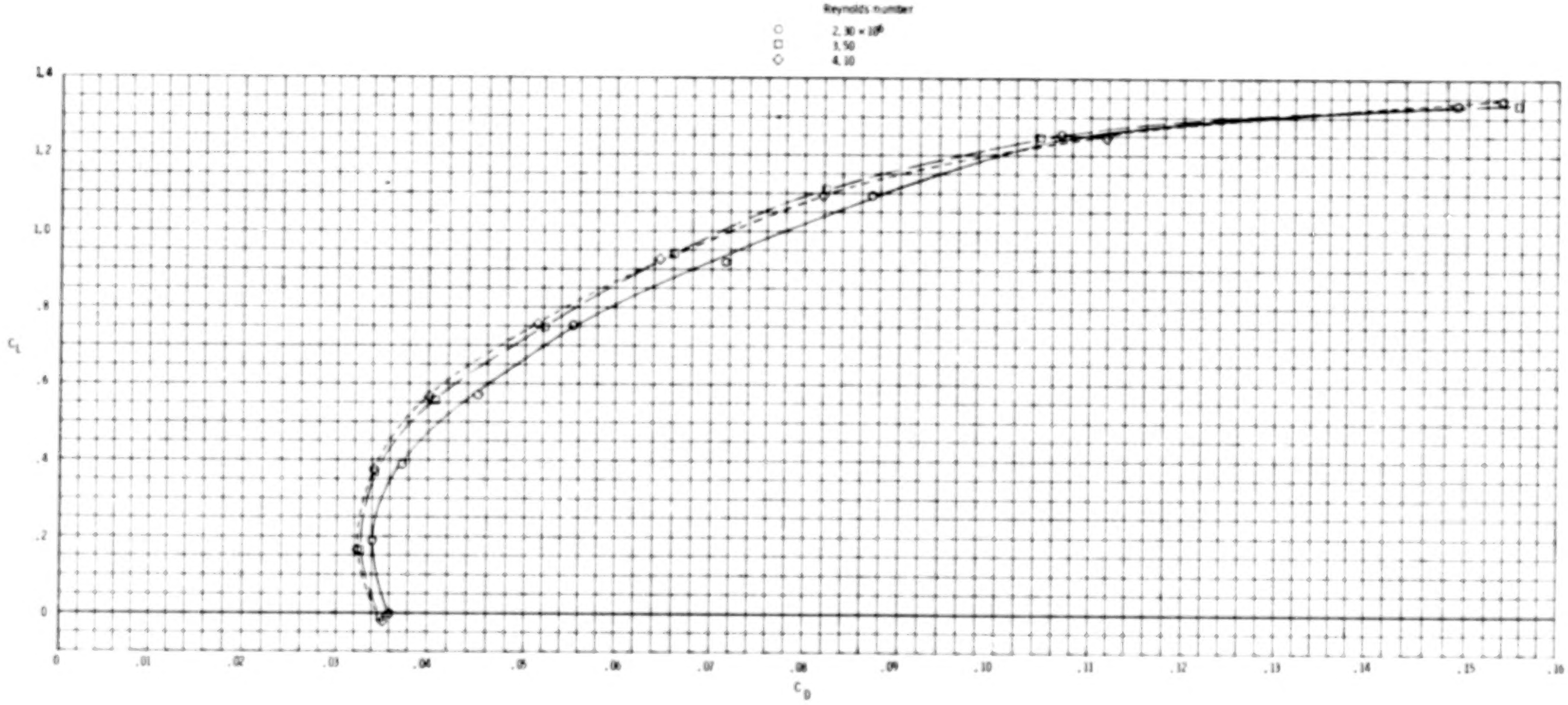

(b) Expanded lift-drag polars.

Figure 20.- Concluded.

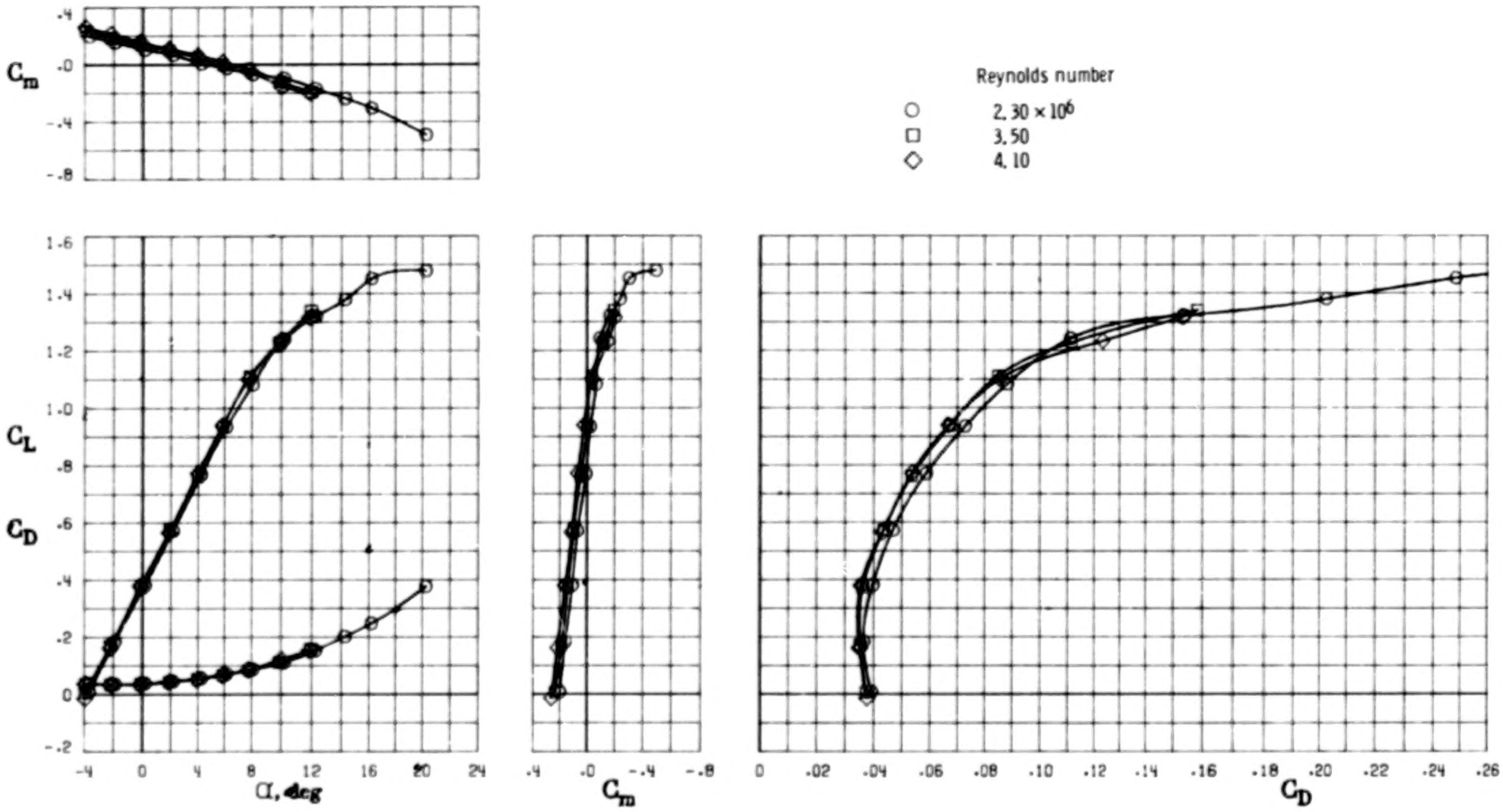

(a) Longitudinal characteristics.

Figure 21.- Effect of Reynolds number with engine inlets open and cowl flaps closed (fully clean configuration with pressure belts and tufts installed).

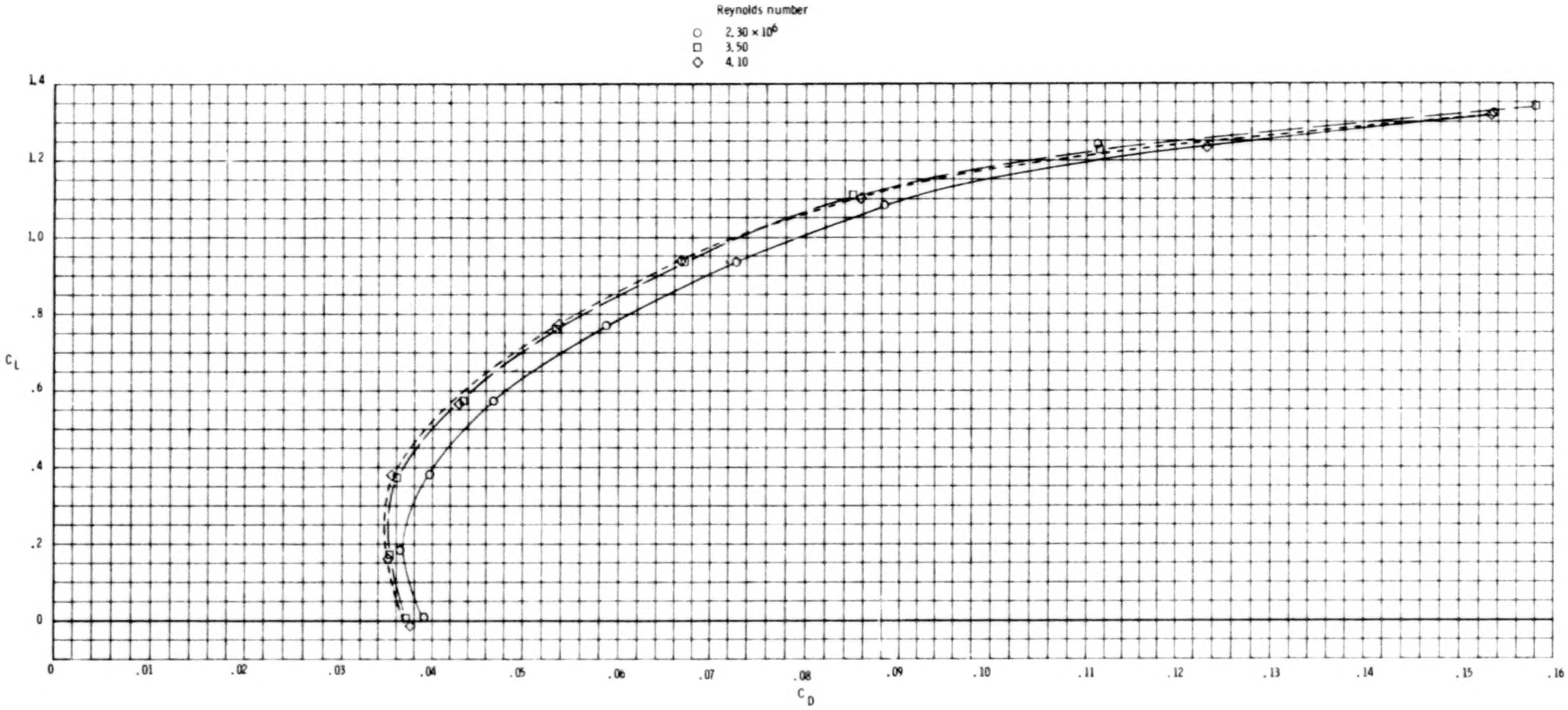

(b) Expanded lift-drag polars.

Figure 21.- Concluded.

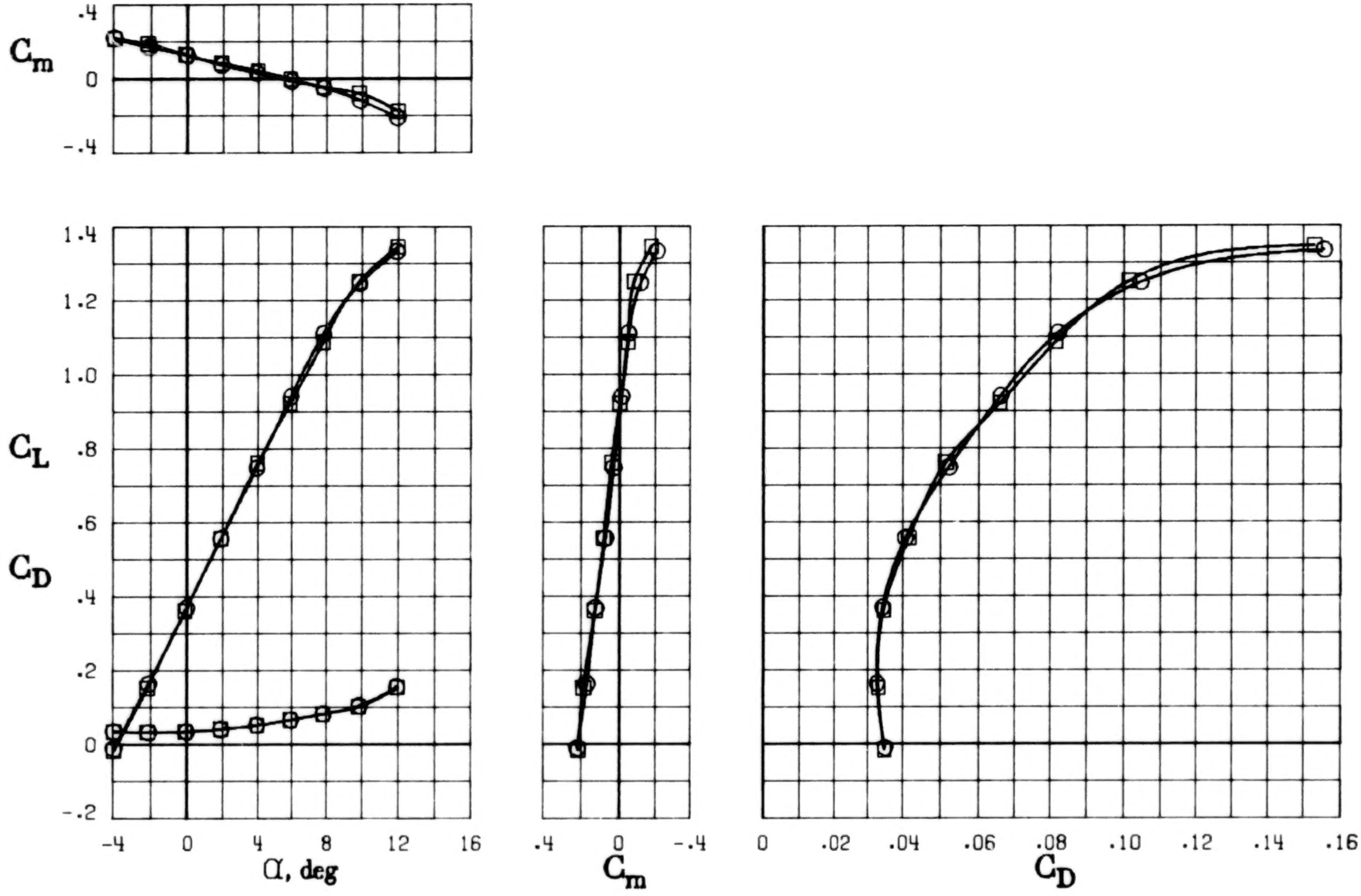

(a) Longitudinal characteristics.

Figure 22.- Repeatability of aerodynamic data at $R = 3.50 \times 10^6$ with engine inlets sealed and cowl flaps closed. Different symbols denote repeat runs.

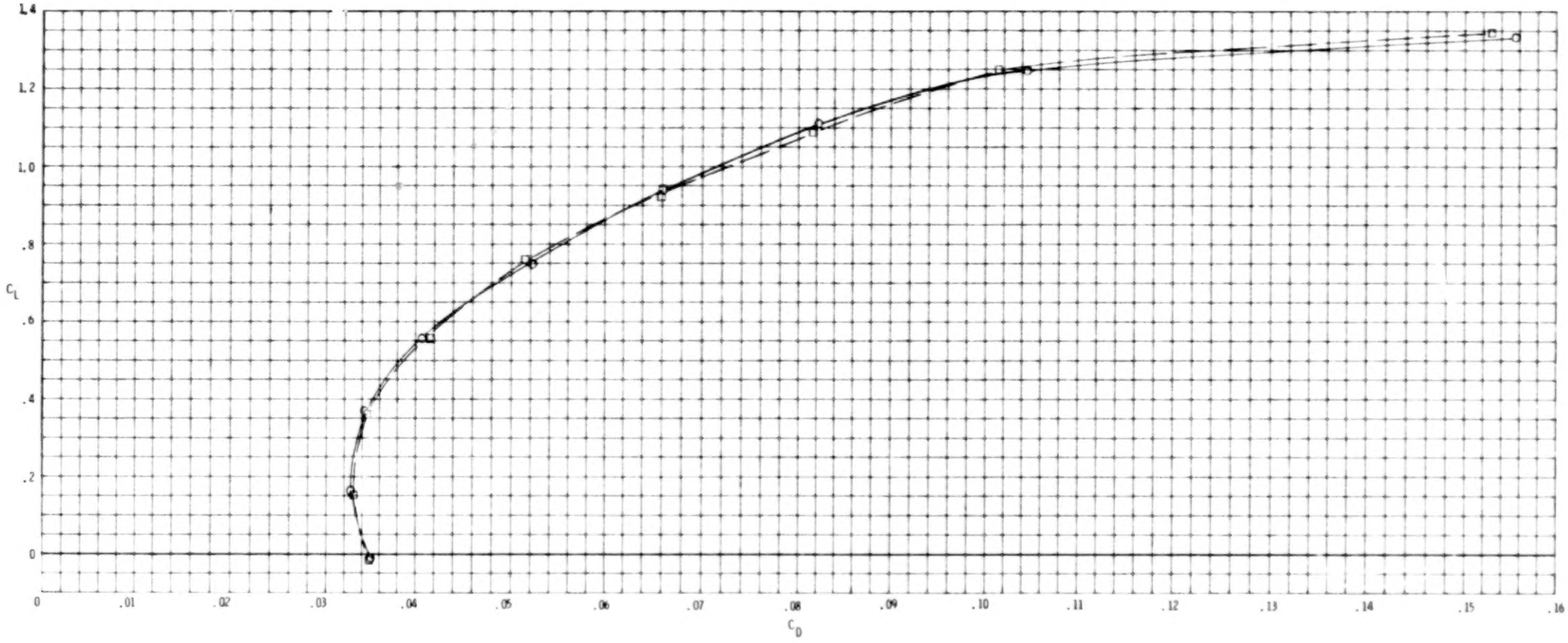

(b) **Expanded lift-drag polars.**

Figure 22.- Concluded.

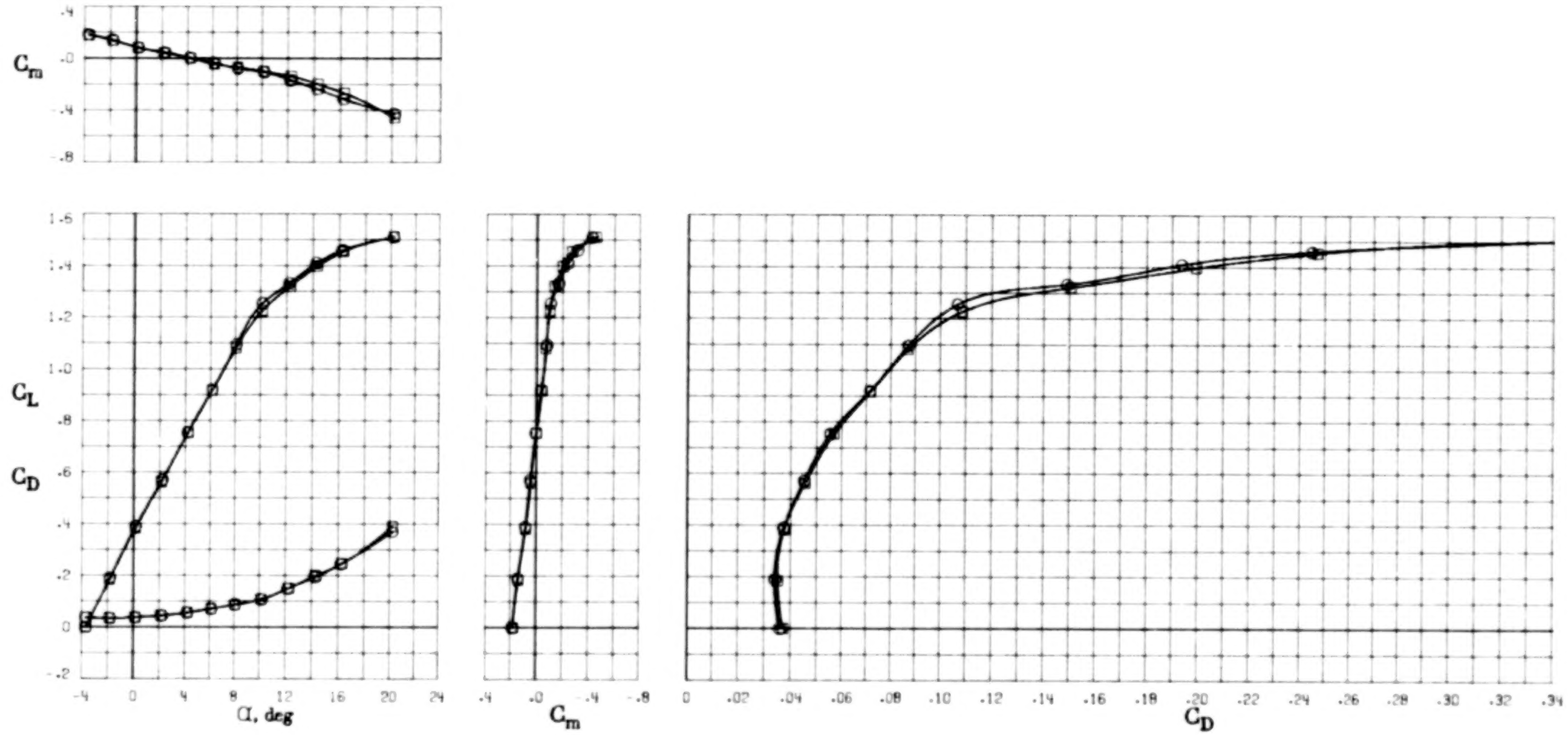

(a) Longitudinal characteristics.

Figure 23.- Repeatability of aerodynamic data at $R = 2.30 \times 10^6$ with engine inlets sealed and cowl flaps closed. Different symbols denote repeat runs.

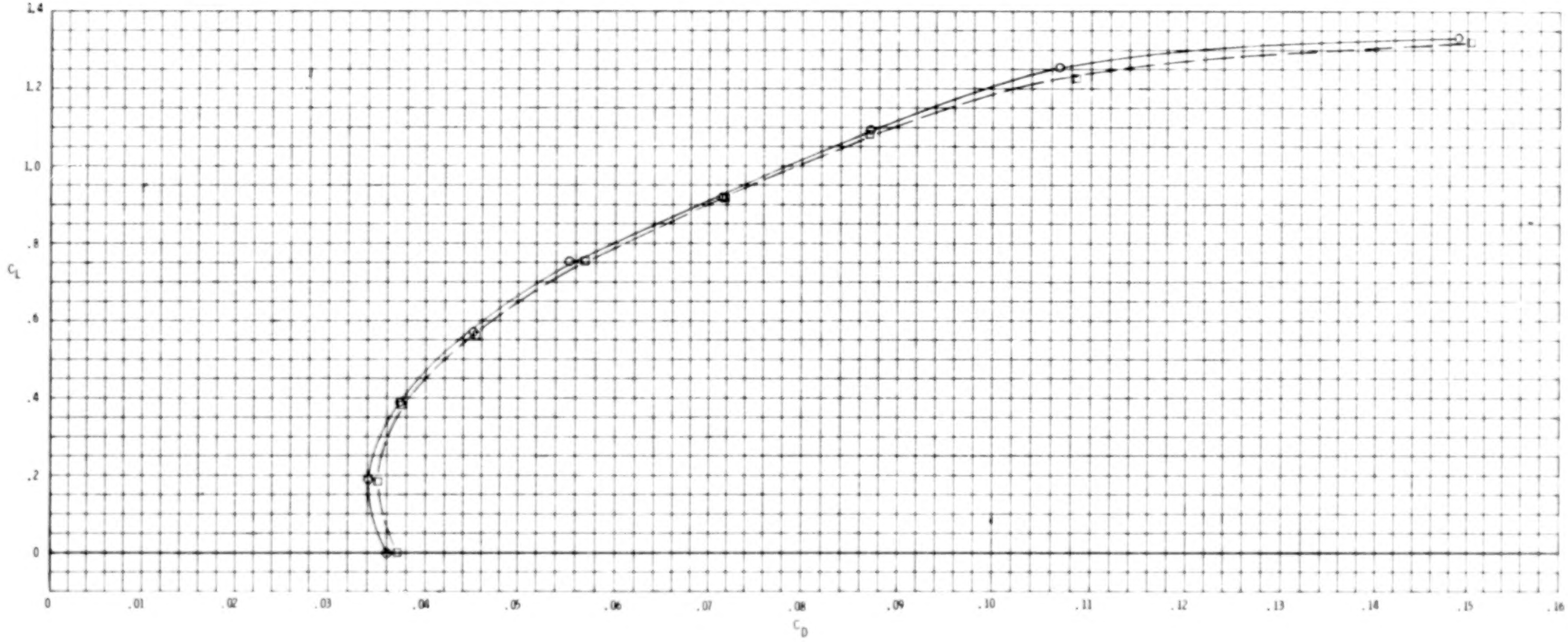

(b) Expanded lift-drag polars.

Figure 23.- Concluded.

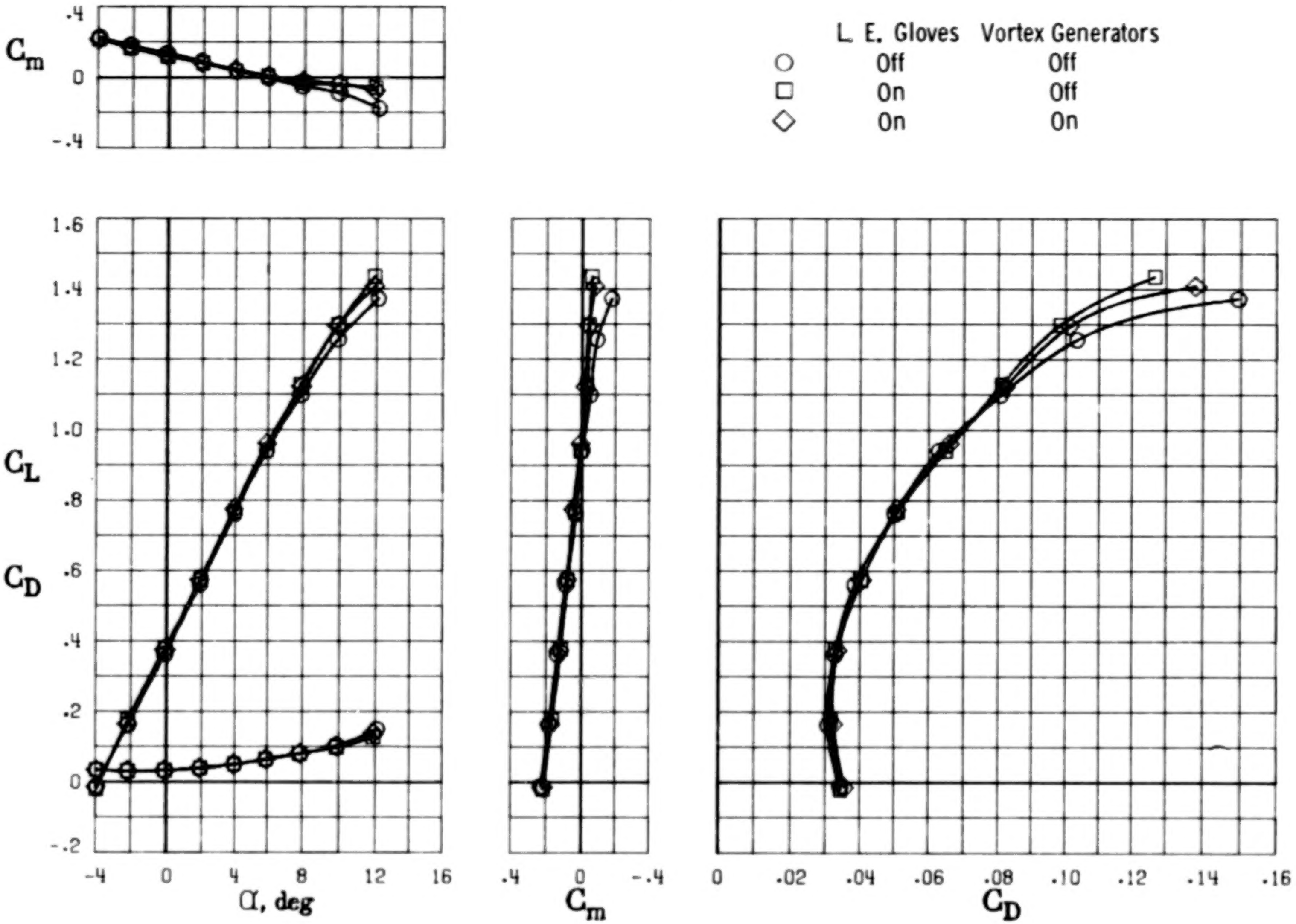

(a) Longitudinal characteristics.

Figure 24.- Effect of wing-root leading-edge gloves and vortex generators at $R = 3.50 \times 10^6$ with engine inlets sealed and cowl flaps closed (fully clean configuration; tufts and pressure belts removed).

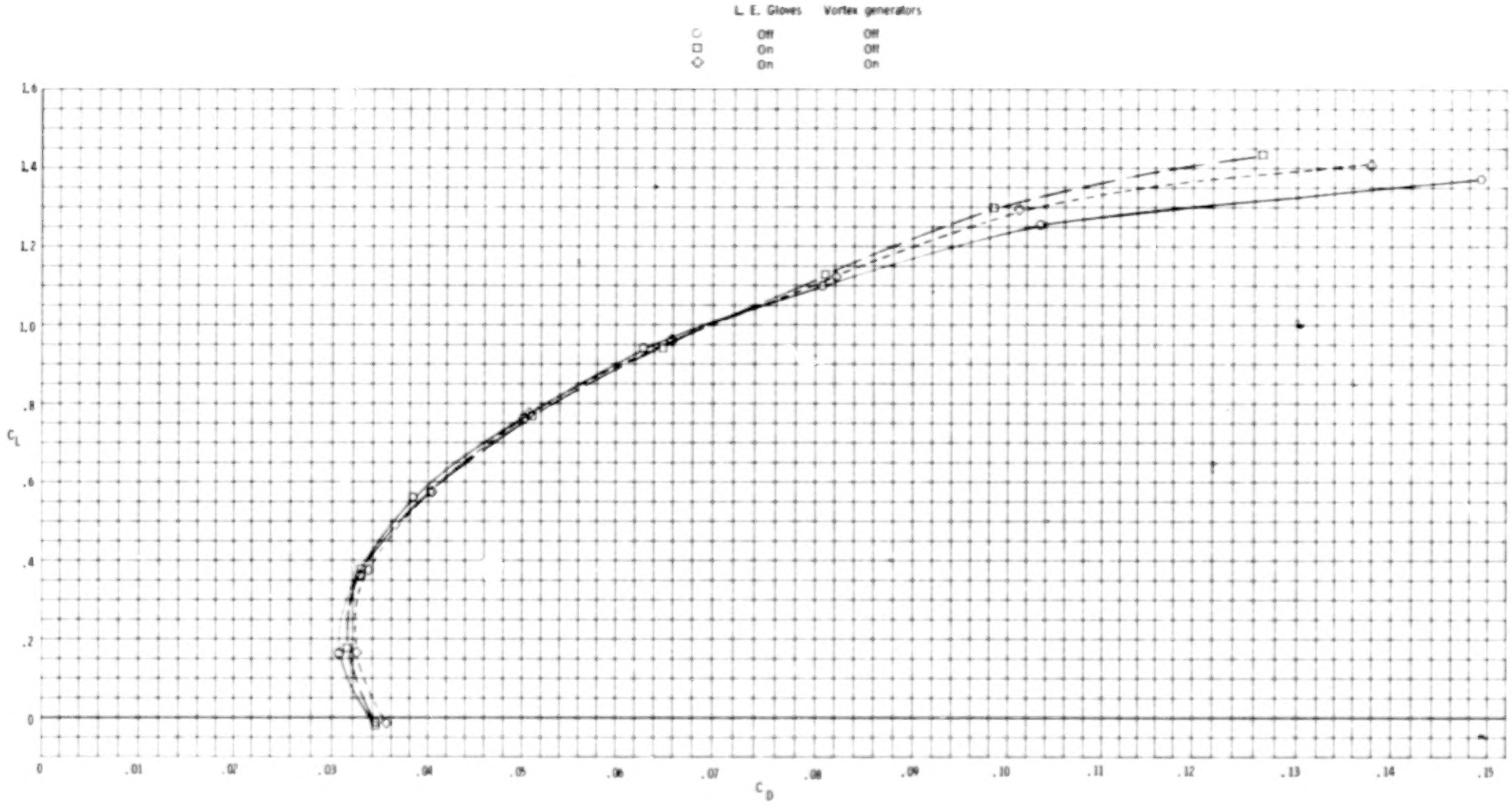

(b) Expanded lift-drag polars.

Figure 24.- Concluded.

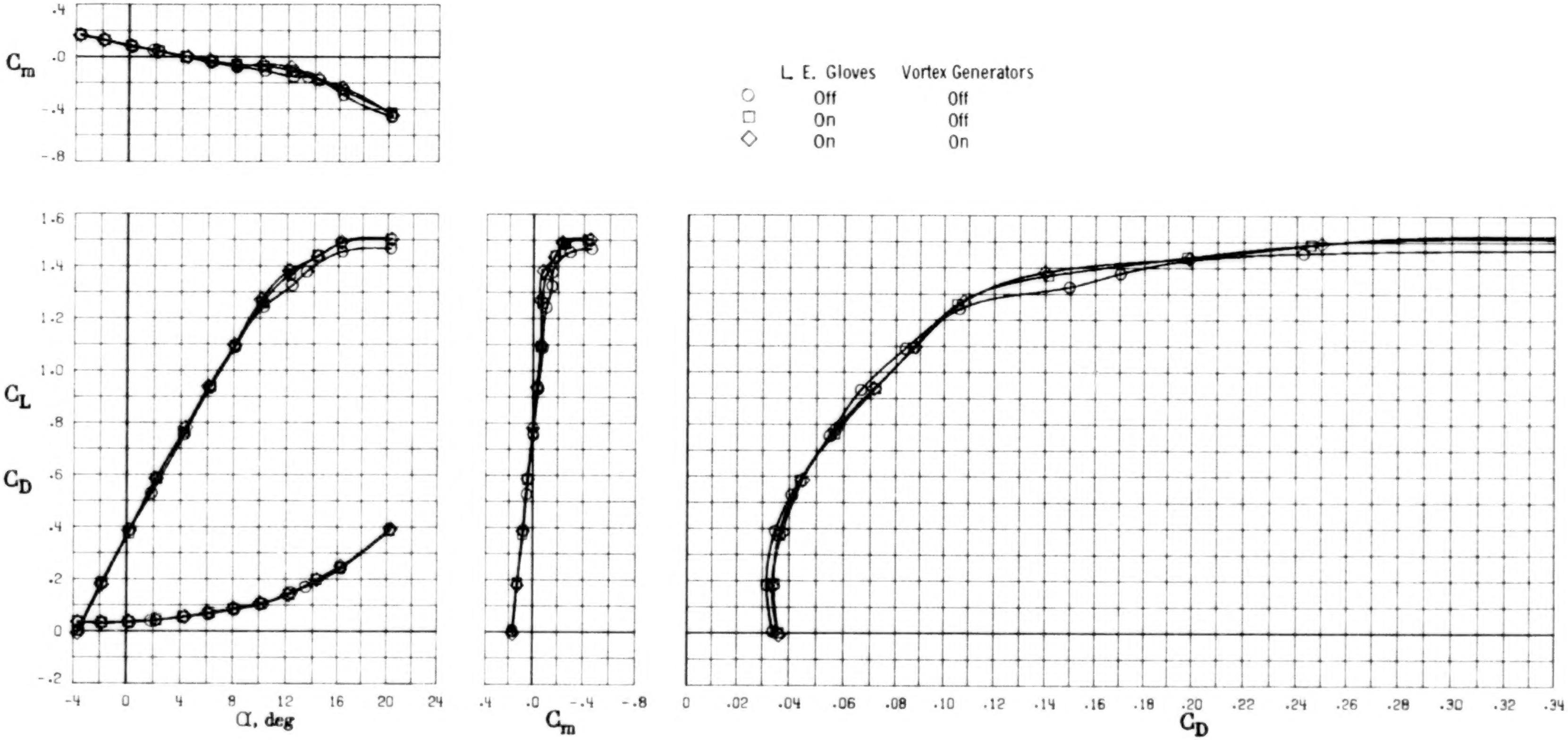

(a) Longitudinal characteristics.

Figure 25.- Effect of wing-root leading-edge gloves and vortex generators at $R = 2.30 \times 10^6$ with engine inlets sealed and cowl flaps closed (fully clean configuration; tufts and pressure belts removed).

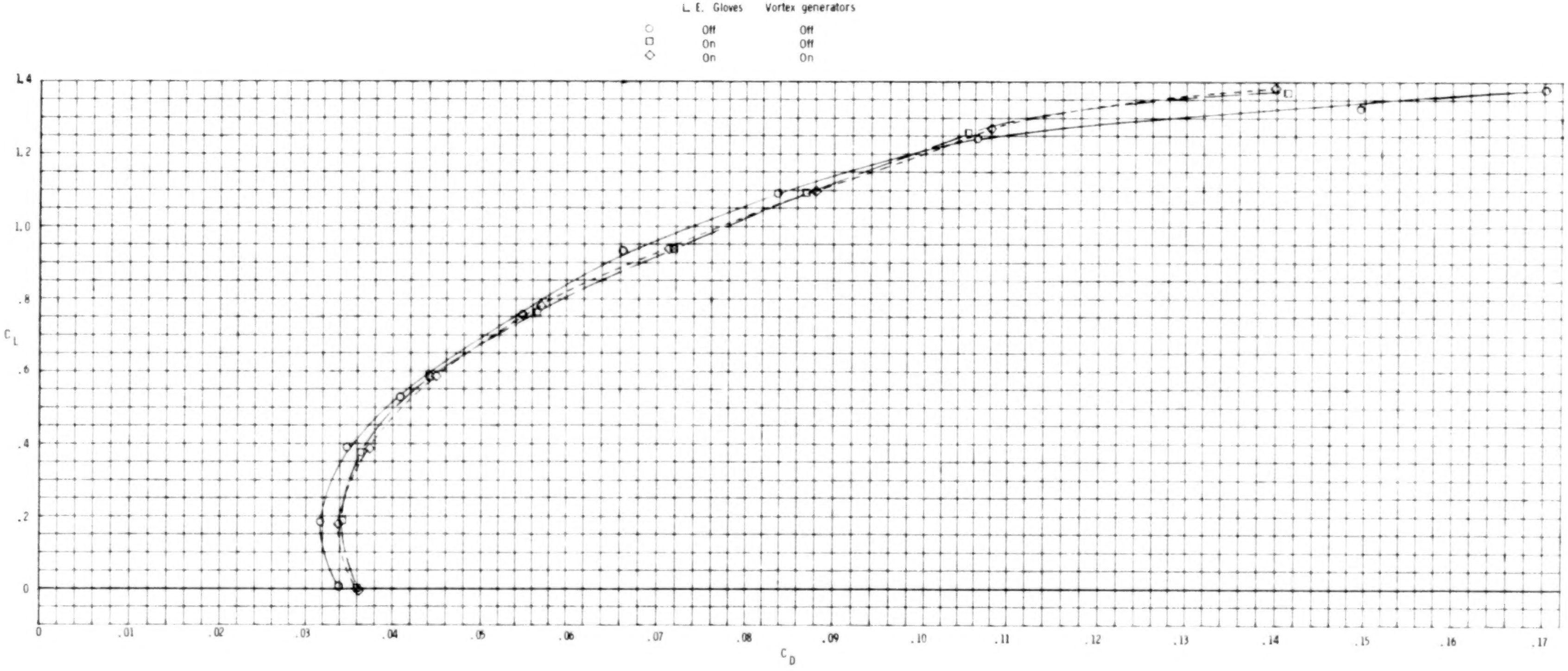

(b) Expanded lift-drag polars.

Figure 25.- Concluded.

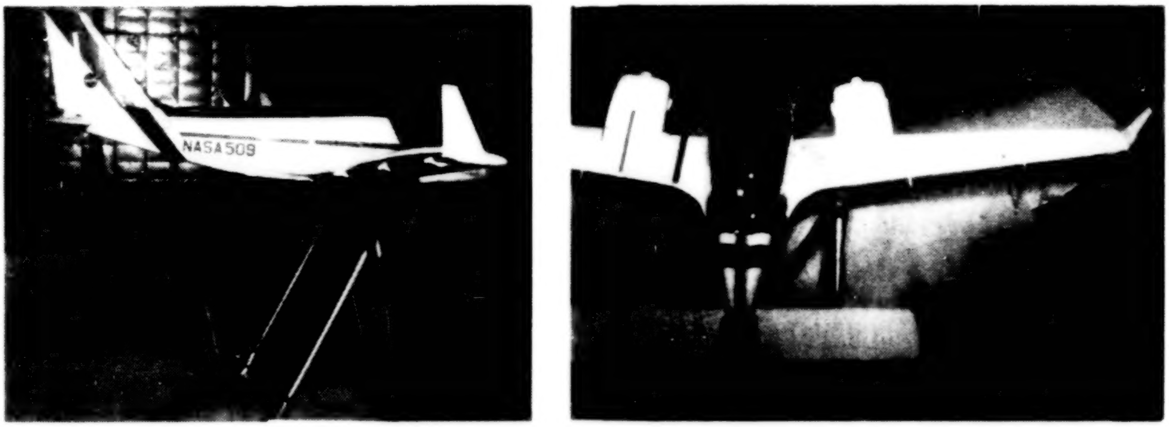

(a) $\alpha = -1.9^\circ$; $C_L = 0.229$.

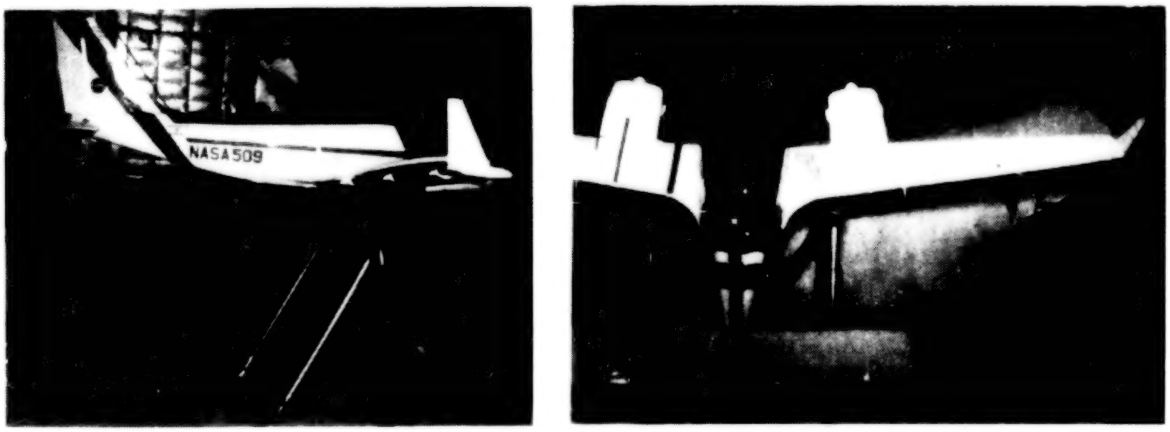

(b) $\alpha = 0.2^\circ$; $C_L = 0.429$.

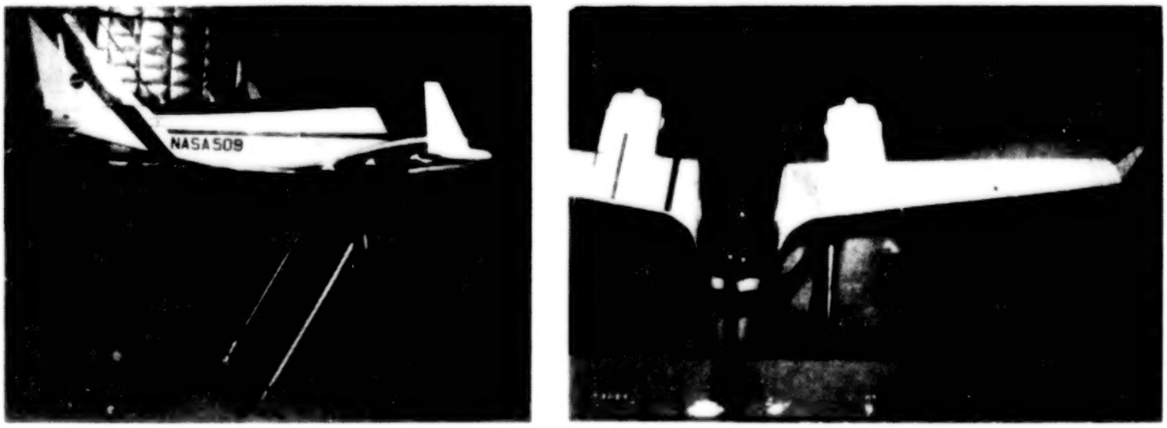

(c) $\alpha = 2.1^\circ$; $C_L = 0.628$. L-80-103

Figure 26.- Effect of angle of attack on flow attachment for fully clean configuration with winglets. Propellers off; engine inlets open; cowl flaps open; winglet cant, 20°; winglet skew, 2.5°.

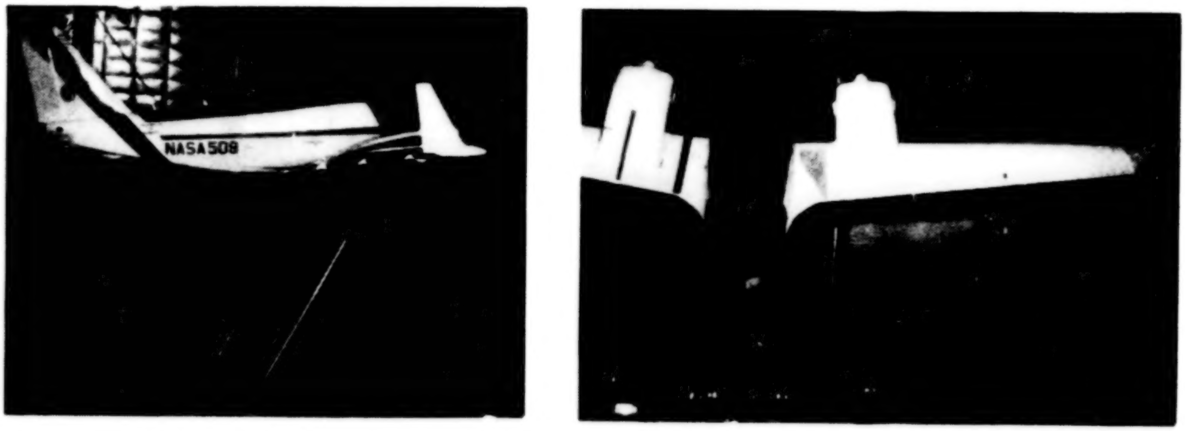

(d) $\alpha = 4.2^{\circ}$; $C_L = 0.818$.

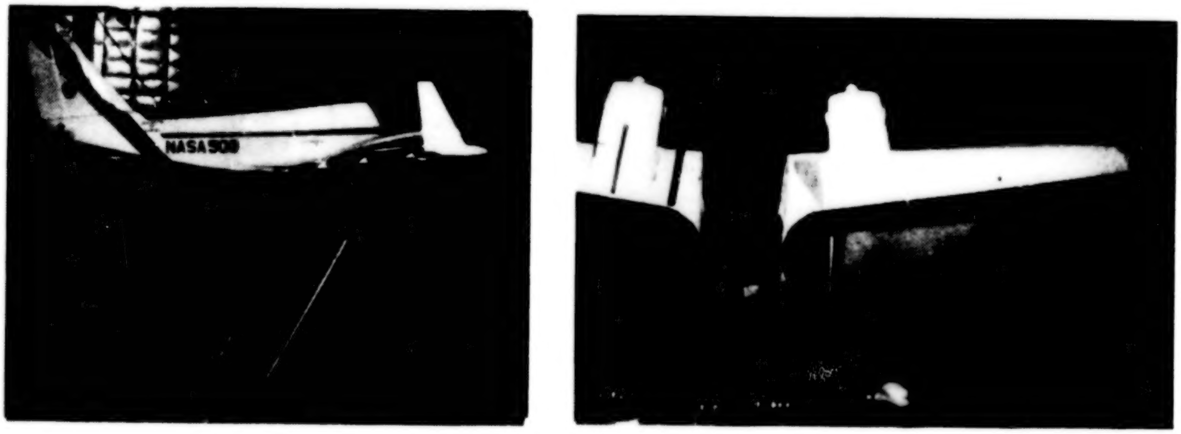

(e) $\alpha = 5.1^{\circ}$; $C_L = 0.901$.

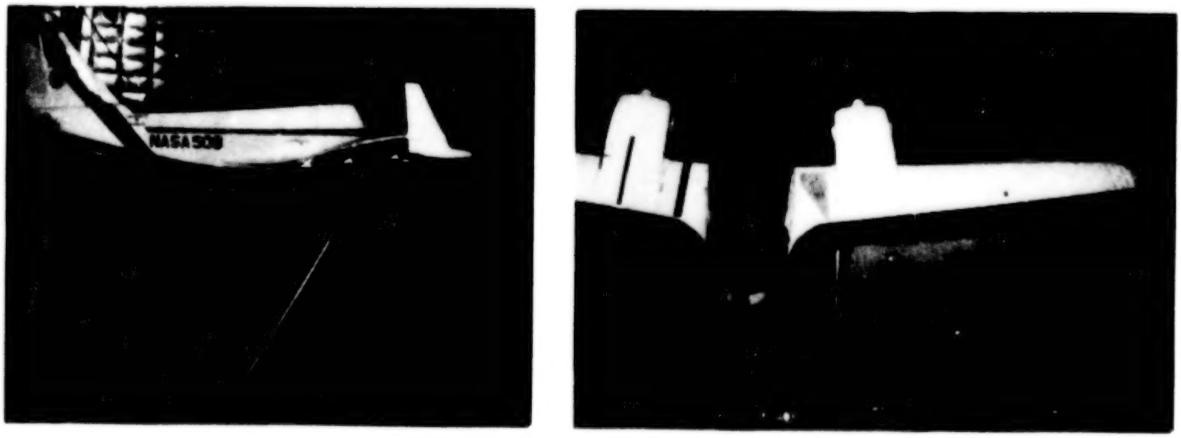

(f) $\alpha = 6.1^{\circ}$; $C_L = 0.999$.

L-80-104

Figure 26.- Continued.

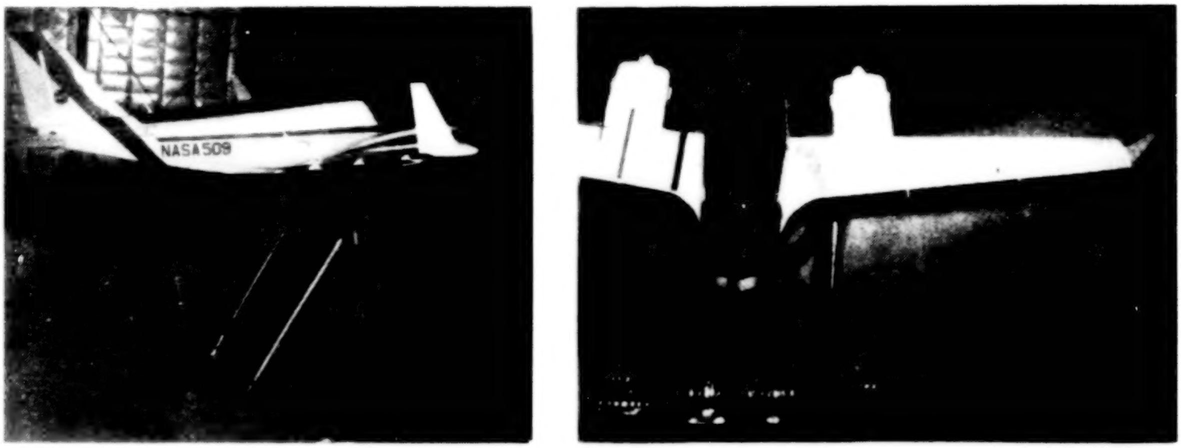

(g) $\alpha = 7.1^\circ$; $C_L = 1.082$.

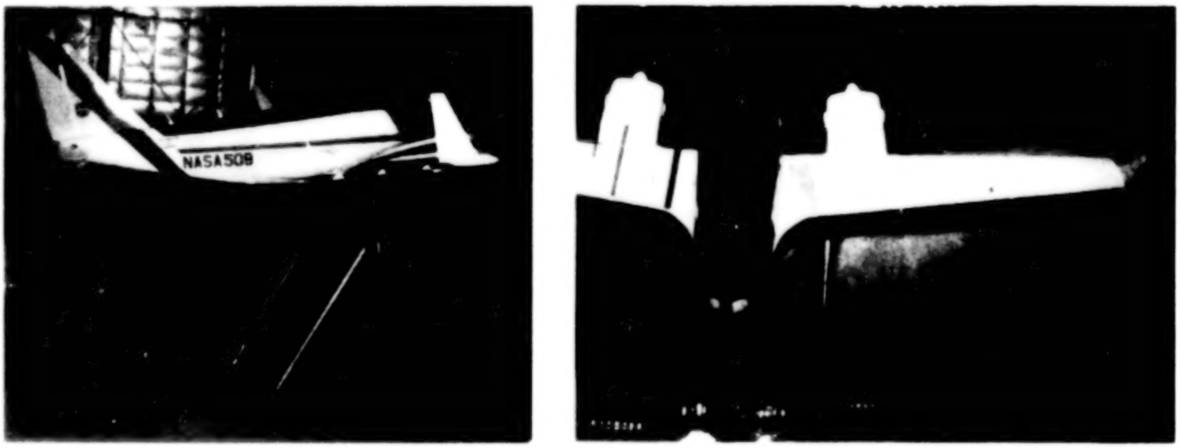

(h) $\alpha = 8.0^\circ$; $C_L = 1.157$.

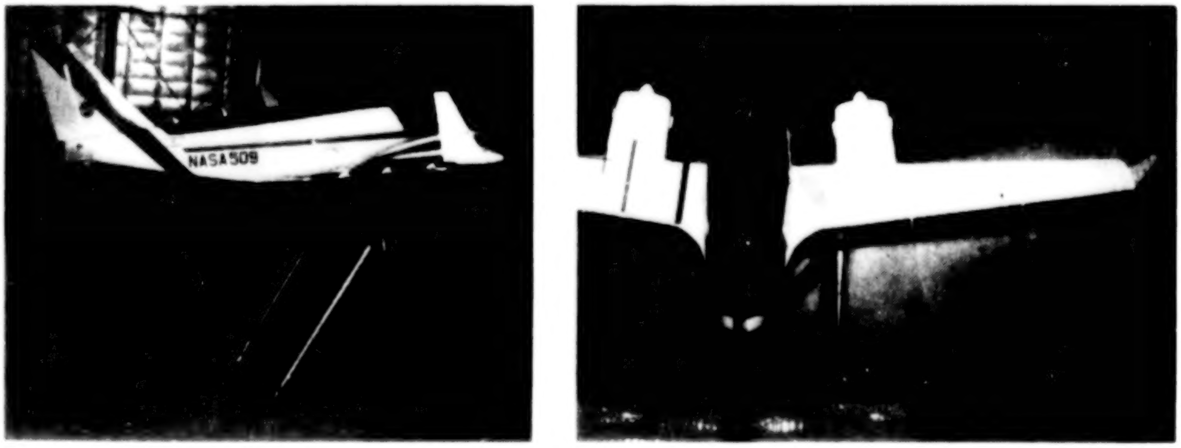

(i) $\alpha = 9.1^\circ$; $C_L = 1.225$.

L-80-105

Figure 26.- Continued.

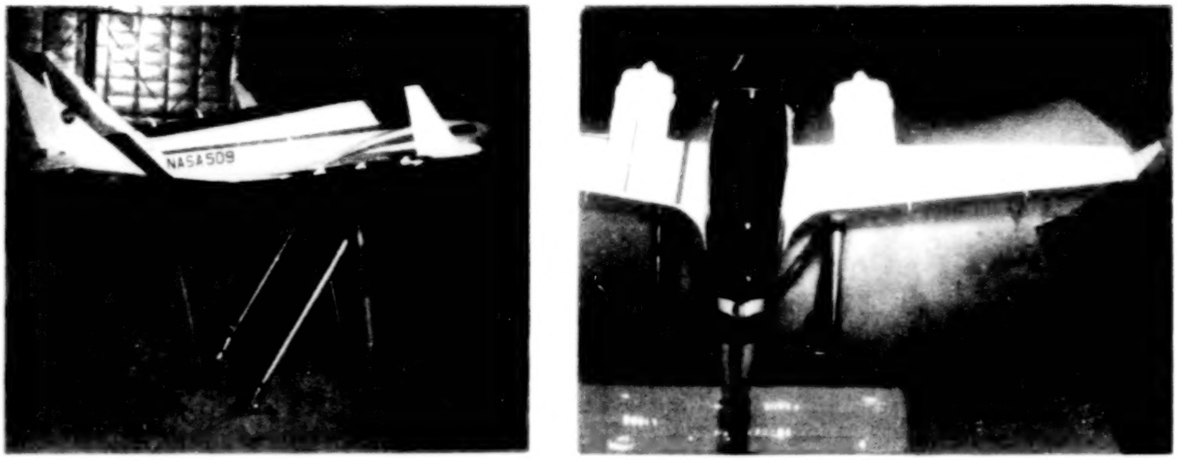

(j) $\alpha = 10.2^{\circ}$; $C_L = 1.282$.

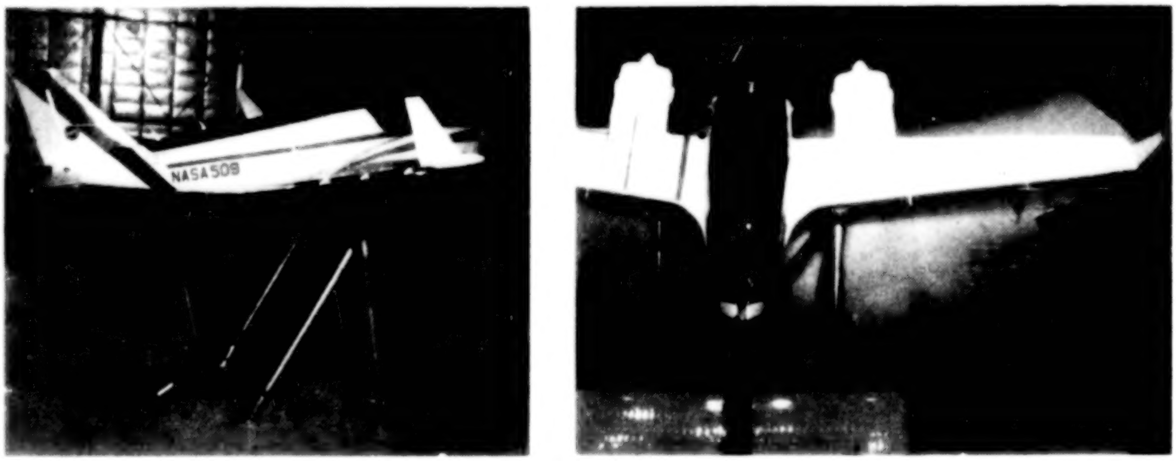

(k) $\alpha = 12.1^{\circ}$; $C_L = 1.380$.

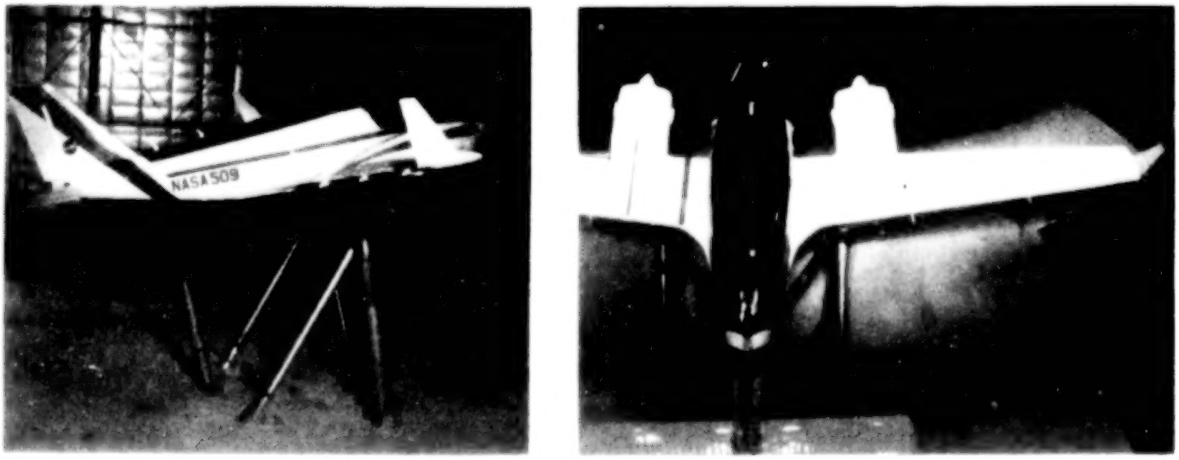

(l) $\alpha = 14.3^{\circ}$; $C_L = 1.449$.

L-80-106

Figure 26.- Continued.

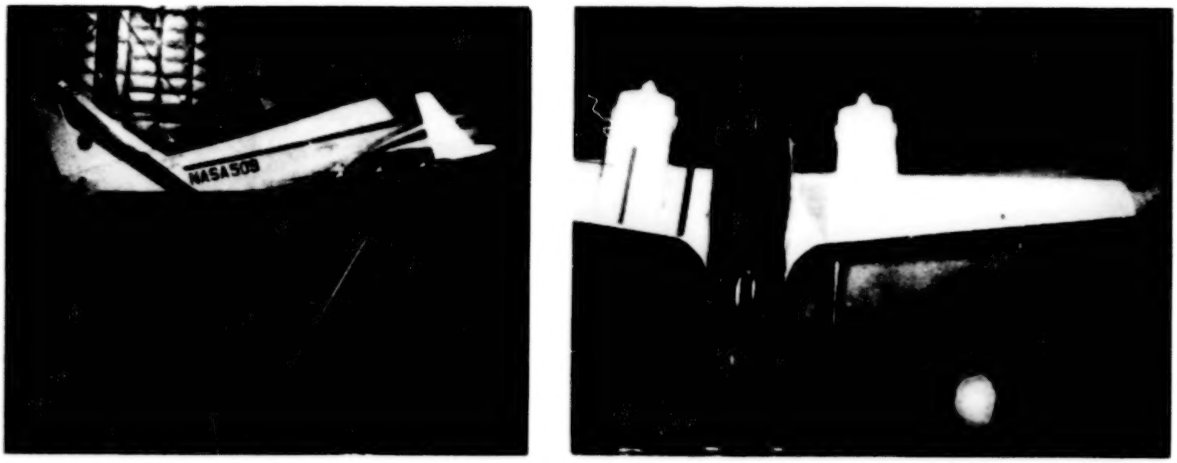

(m) $\alpha = 16.3^{\circ}$; $C_L = 1.519$.

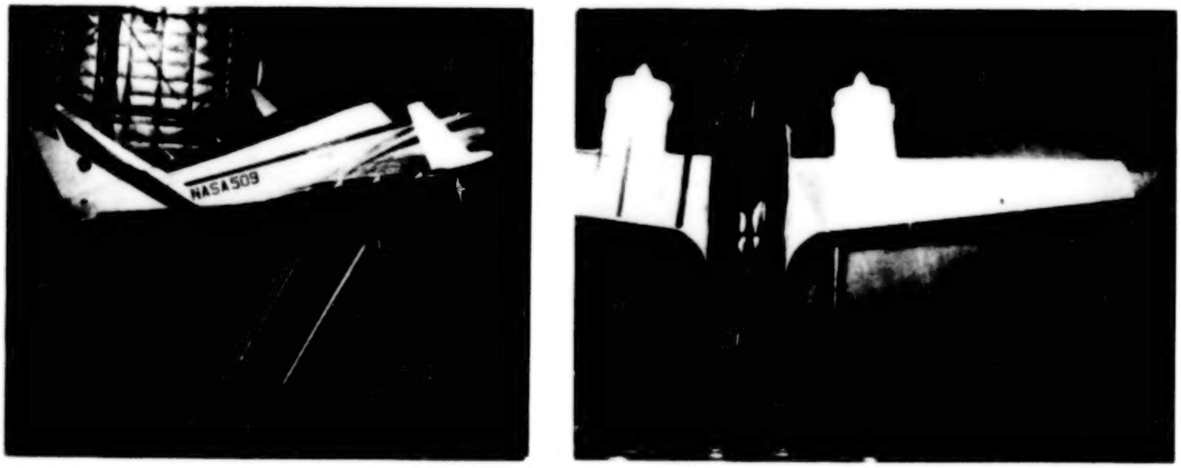

(n) $\alpha = 20.1^{\circ}$; $C_L = 1.553$.

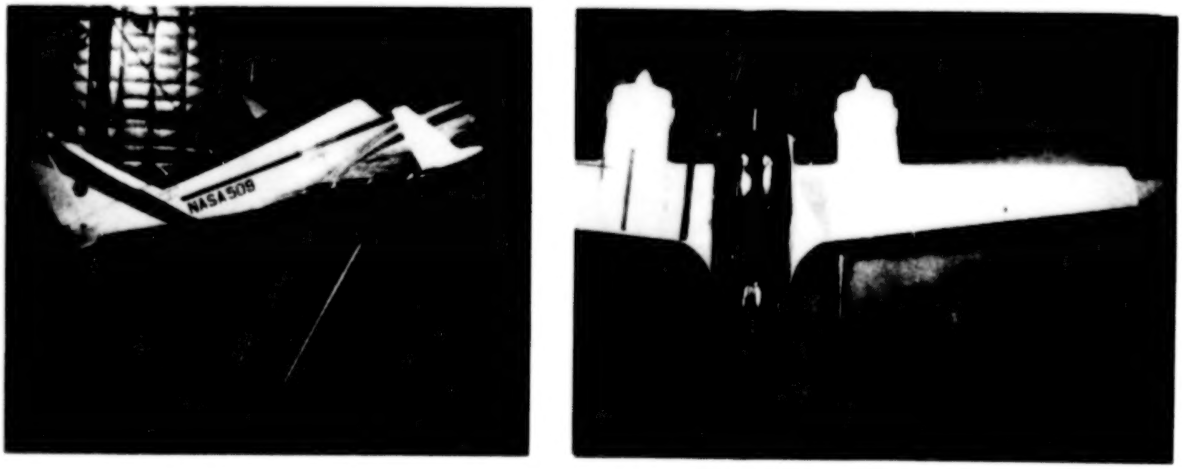

(o) $\alpha = 24.2^{\circ}$; $C_L = 1.430$.

L-80-107

Figure 26.- Concluded.

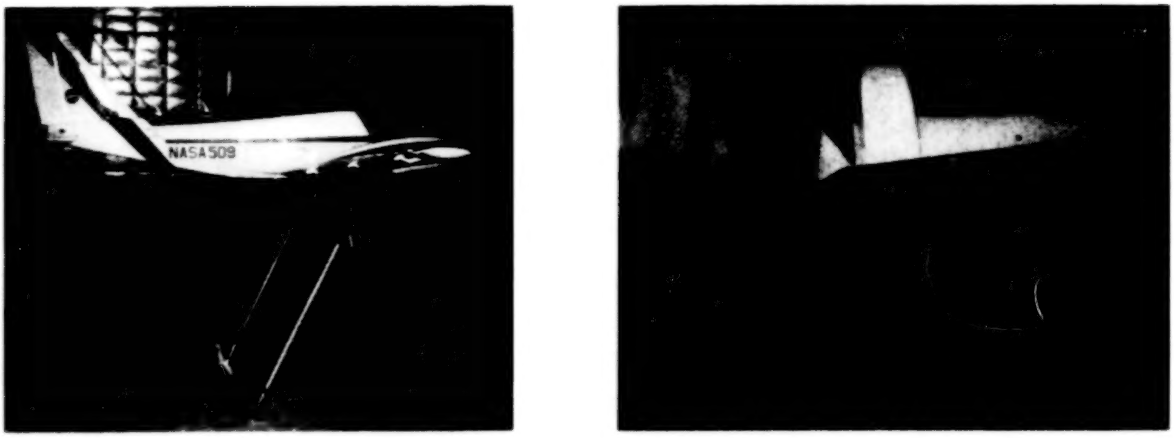

(a) $\alpha = 0^\circ$; $C_L = 0.421$.

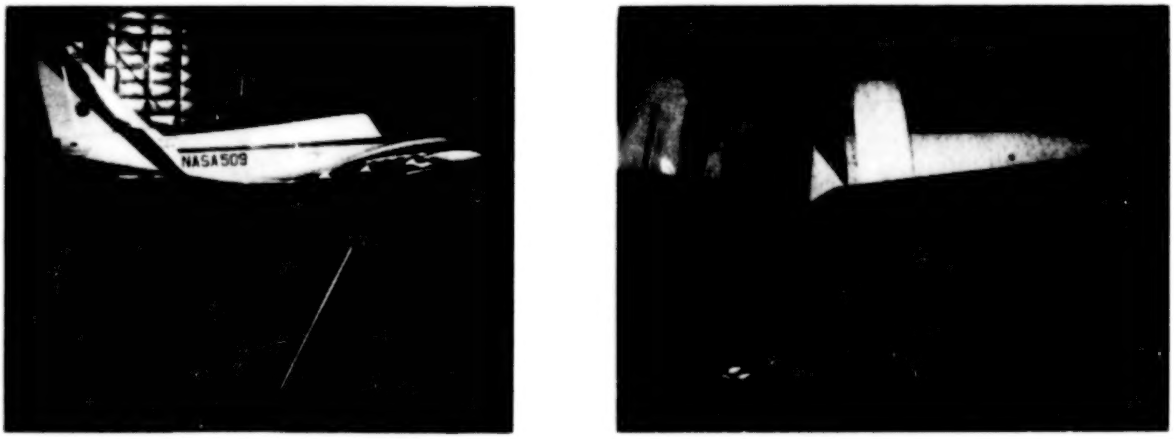

(b) $\alpha = 2.1^\circ$; $C_L = 0.634$.

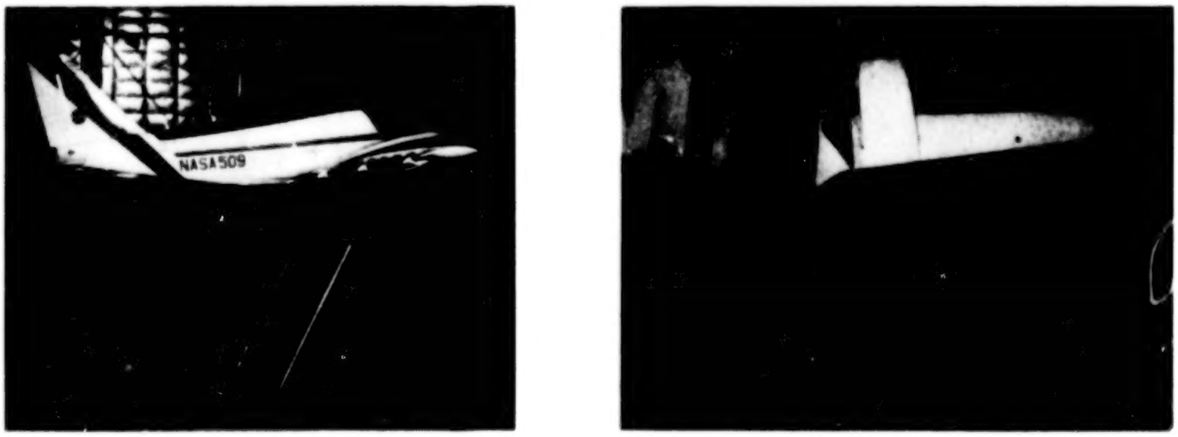

(c) $\alpha = 4.2^\circ$; $C_L = 0.857$.

L-80-108

Figure 27.- Effect of angle of attack on flow attachment for fully clean configuration with winglets off and propellers operating at climb power. $V/nD = 0.572$; $\beta_{.75} = 18^\circ$; $C_{T,lt} = C_{T,rt} = 0.066$.

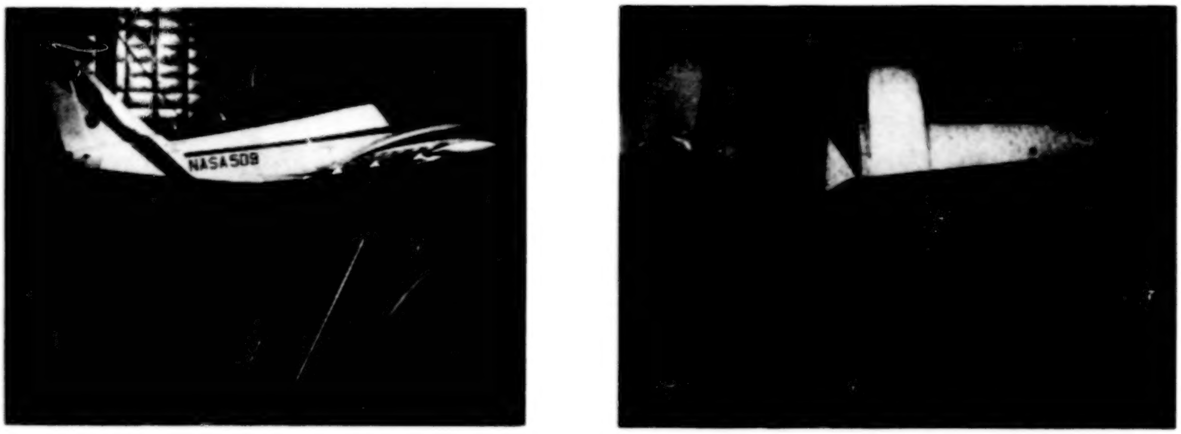

(d) $\alpha = 6.1^\circ$; $C_L = 1.059$.

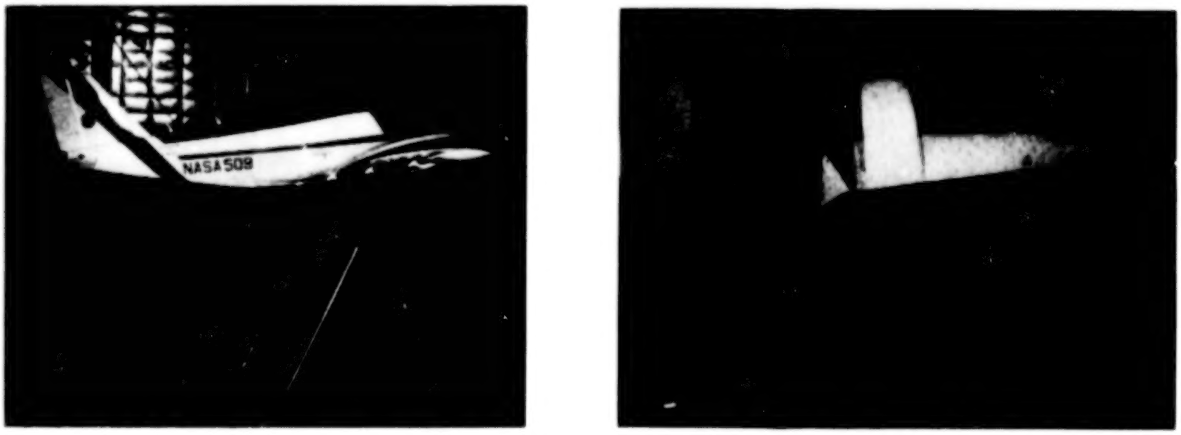

(e) $\alpha = 7.1^\circ$; $C_L = 1.146$.

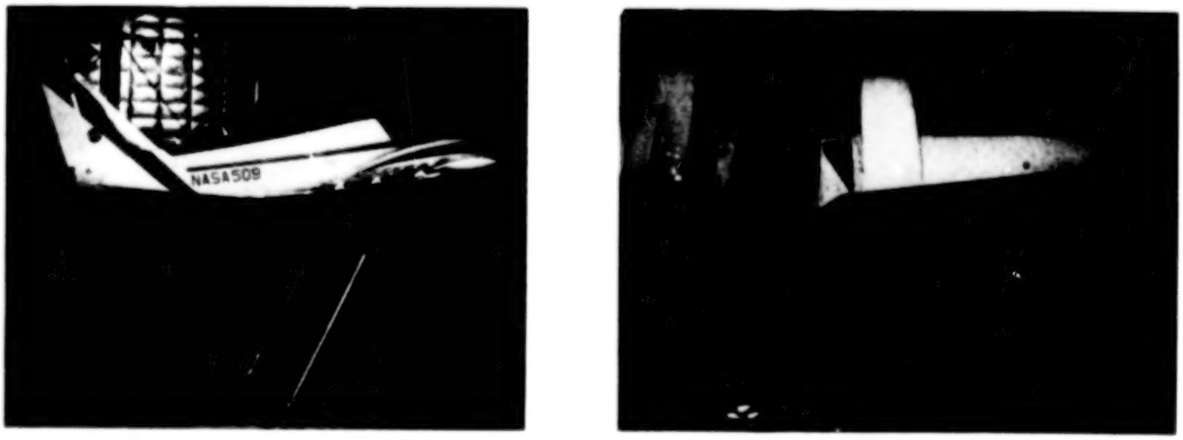

(f) $\alpha = 8.1^\circ$; $C_L = 1.233$.

L-80-109

Figure 27.- Continued.

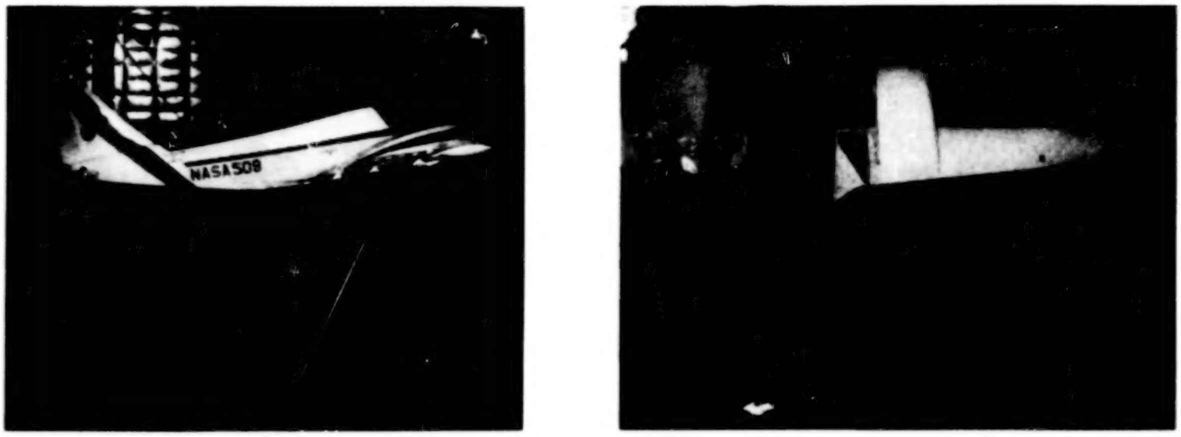

(g) $\alpha = 9.1^\circ$; $C_L = 1.313$.

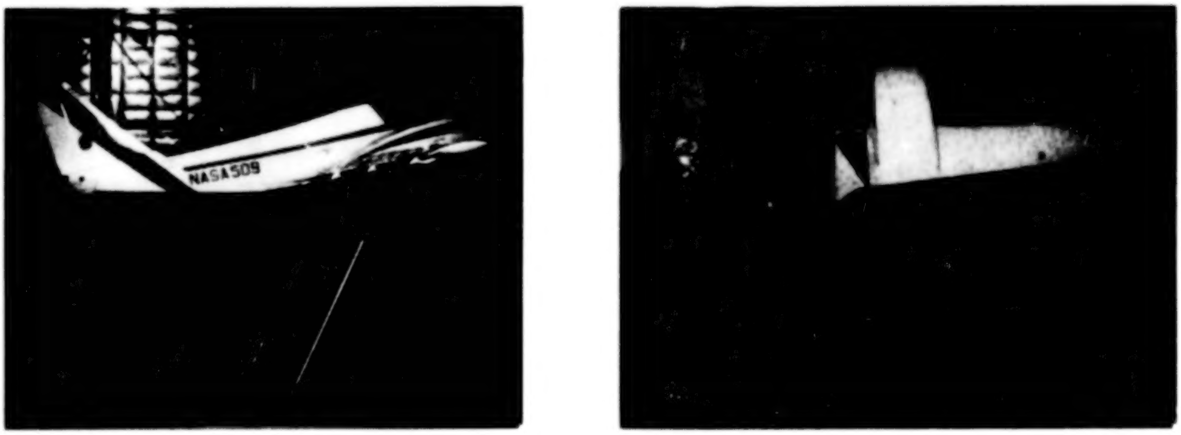

(h) $\alpha = 10.0^\circ$; $C_L = 1.392$.

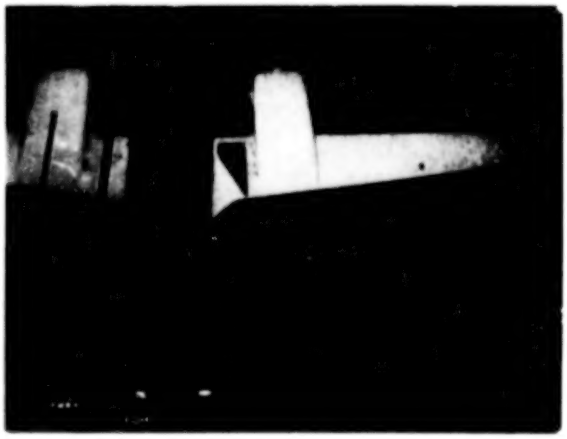

(i) $\alpha = 12.2^\circ$; $C_L = 1.542$.

L-80-110

Figure 27.- Continued.

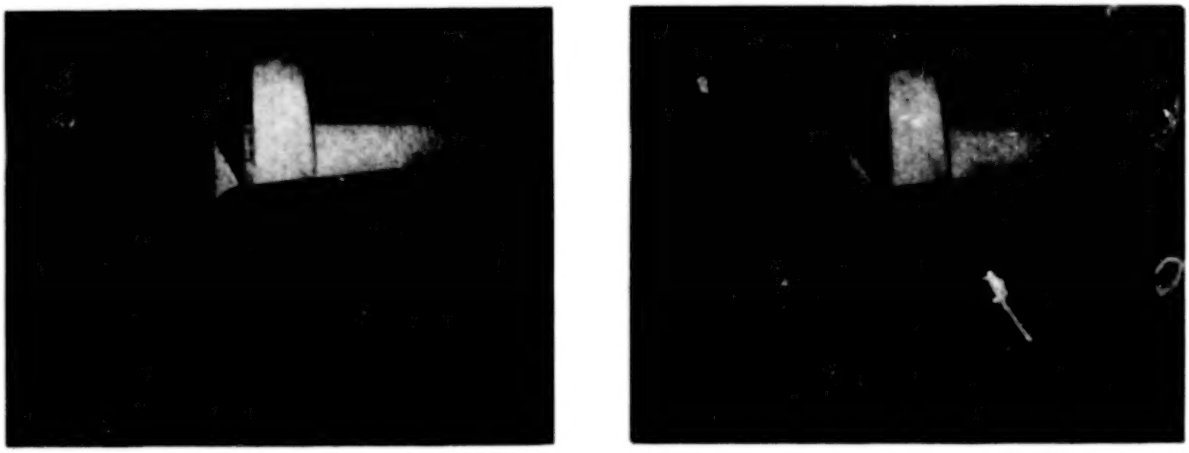

(j) $\alpha = 14.3^{\circ}$; $C_L = 1.645$.   (k) $\alpha = 16.2^{\circ}$; $C_L = 1.716$.

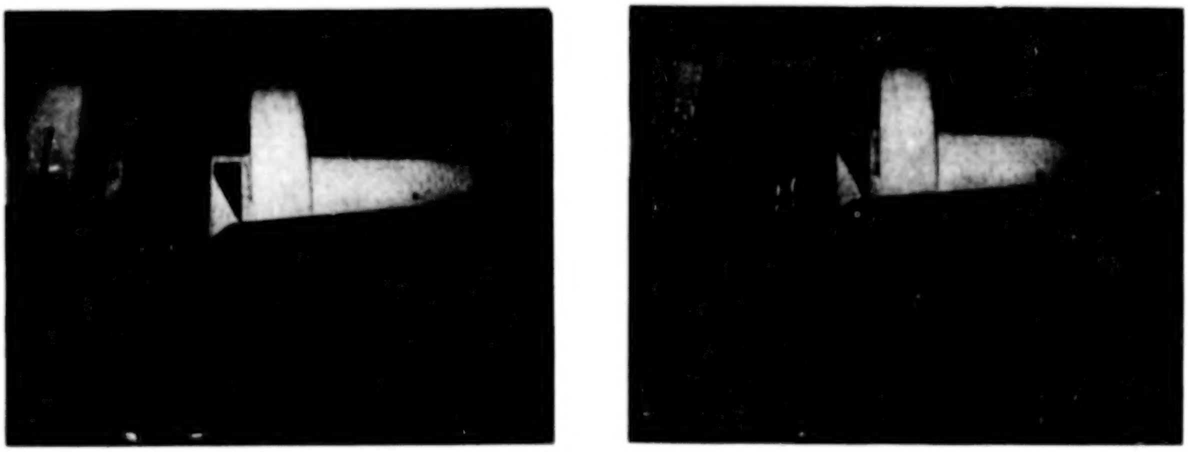

(l) $\alpha = 18.2^{\circ}$; $C_L = 1.725$.   (m) $\alpha = 20.2^{\circ}$; $C_L = 1.734$.

Figure 27.- Concluded.   L-80-111

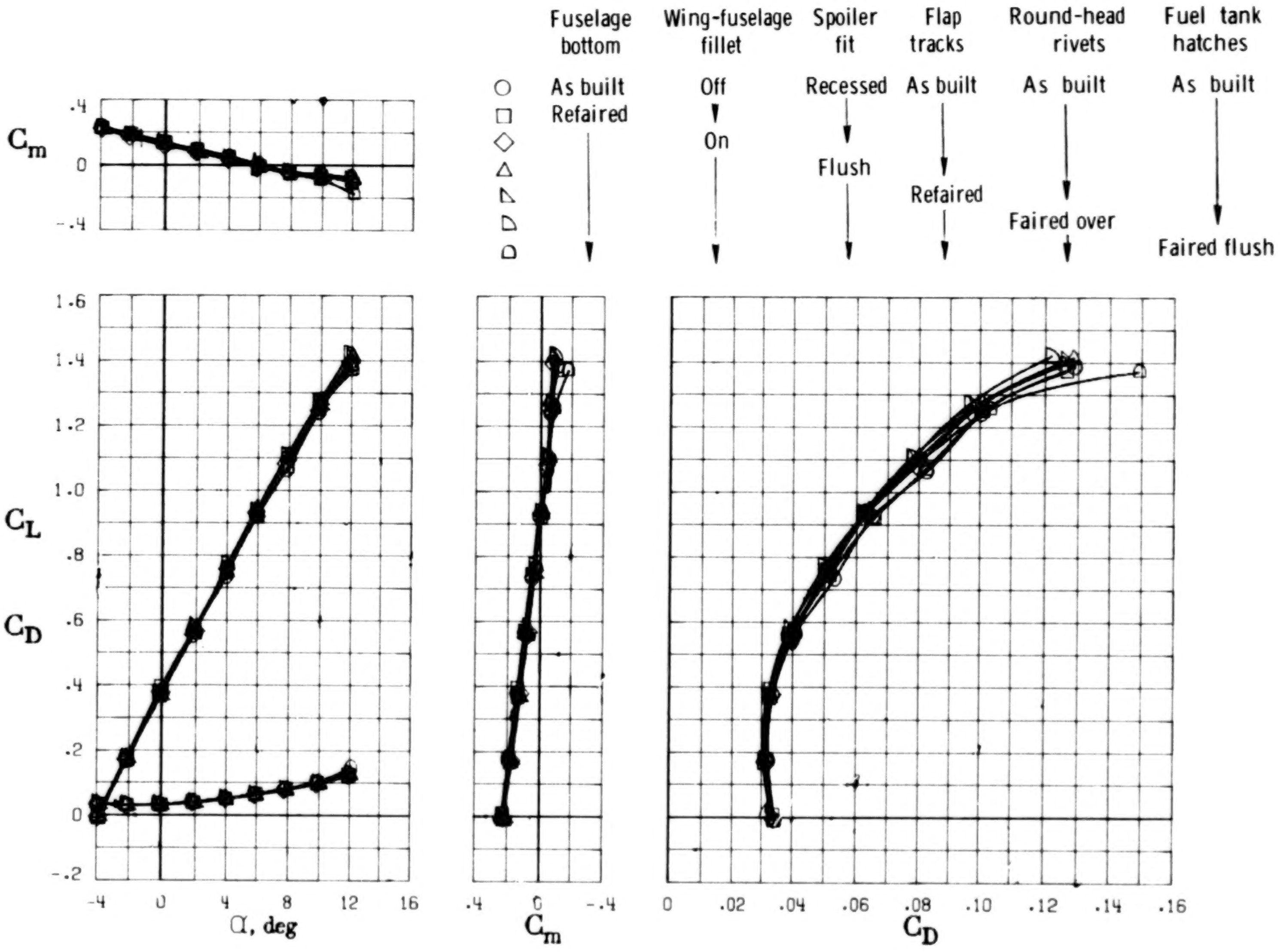

(a) Longitudinal characteristics.

Figure 28.- Effect of fairing over protuberances and installing fillets at $R = 3.50 \times 10^6$. Engine inlets sealed; cowl flaps closed; pressure belts, tufts, L.E. gloves, and vortex generators removed.

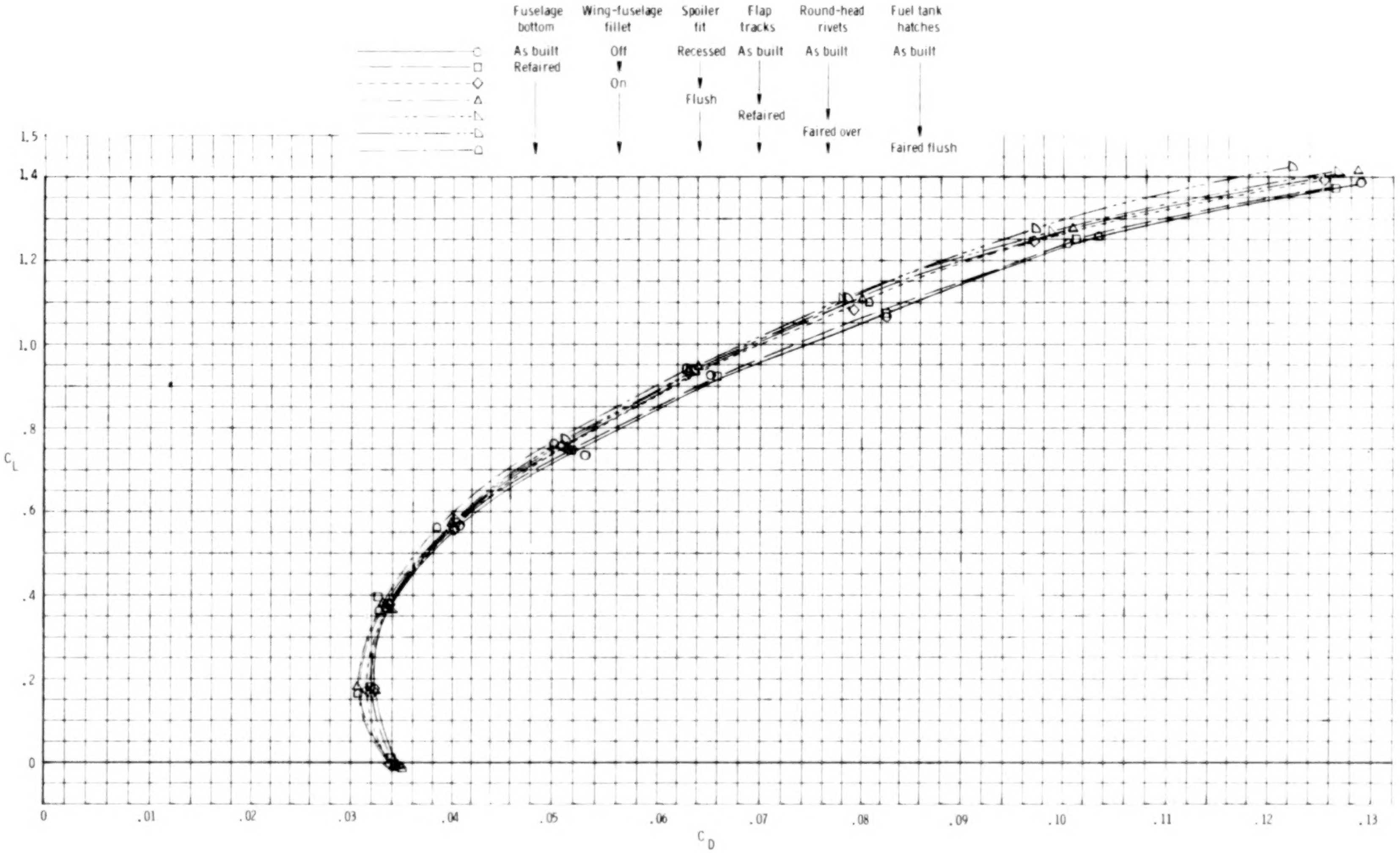

(b) Expanded lift-drag polars.

Figure 28.- Concluded.

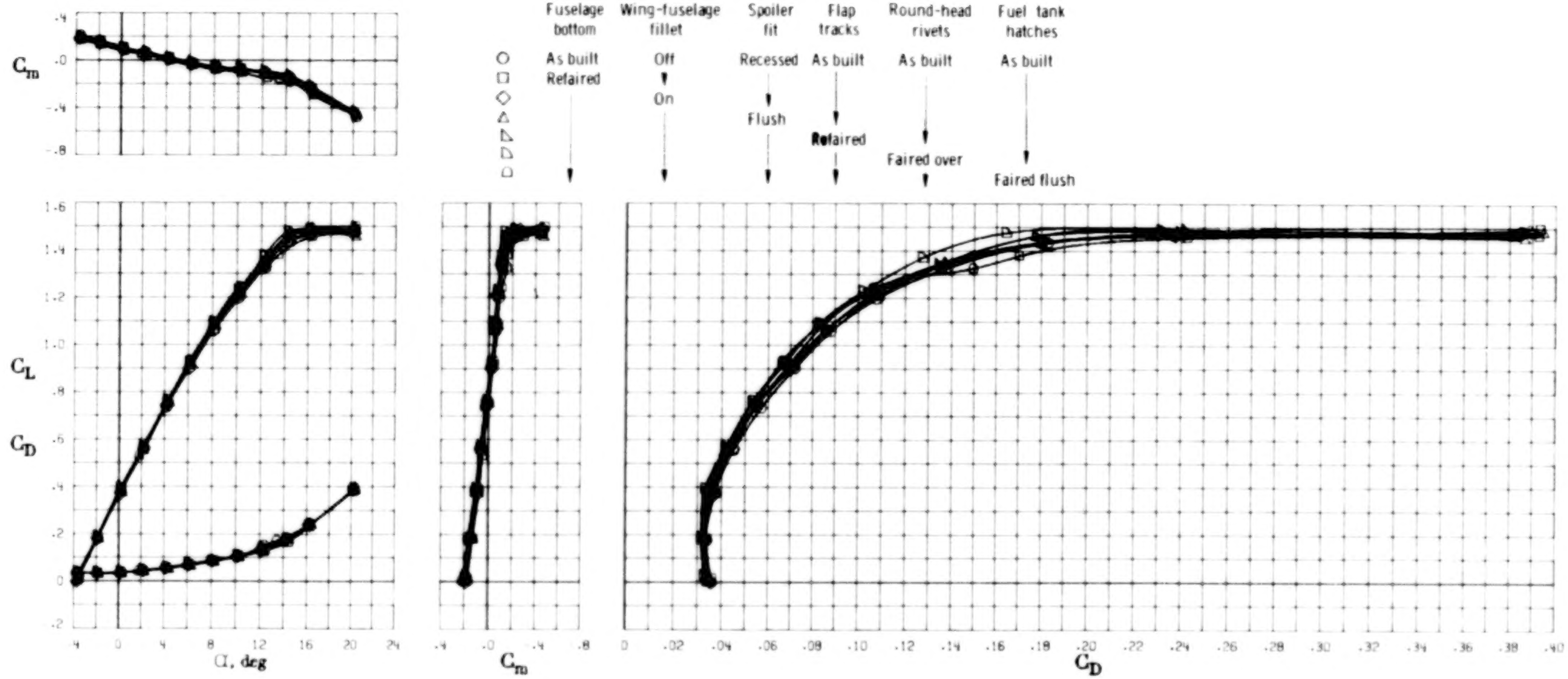

(a) Longitudinal characteristics.

Figure 29.- Effect of fairing over protuberances and installing fillets at $R = 2.30 \times 10^6$. Engine inlets sealed; cowl flaps closed; pressure belts, tufts, L.E. gloves, and vortex generators removed.

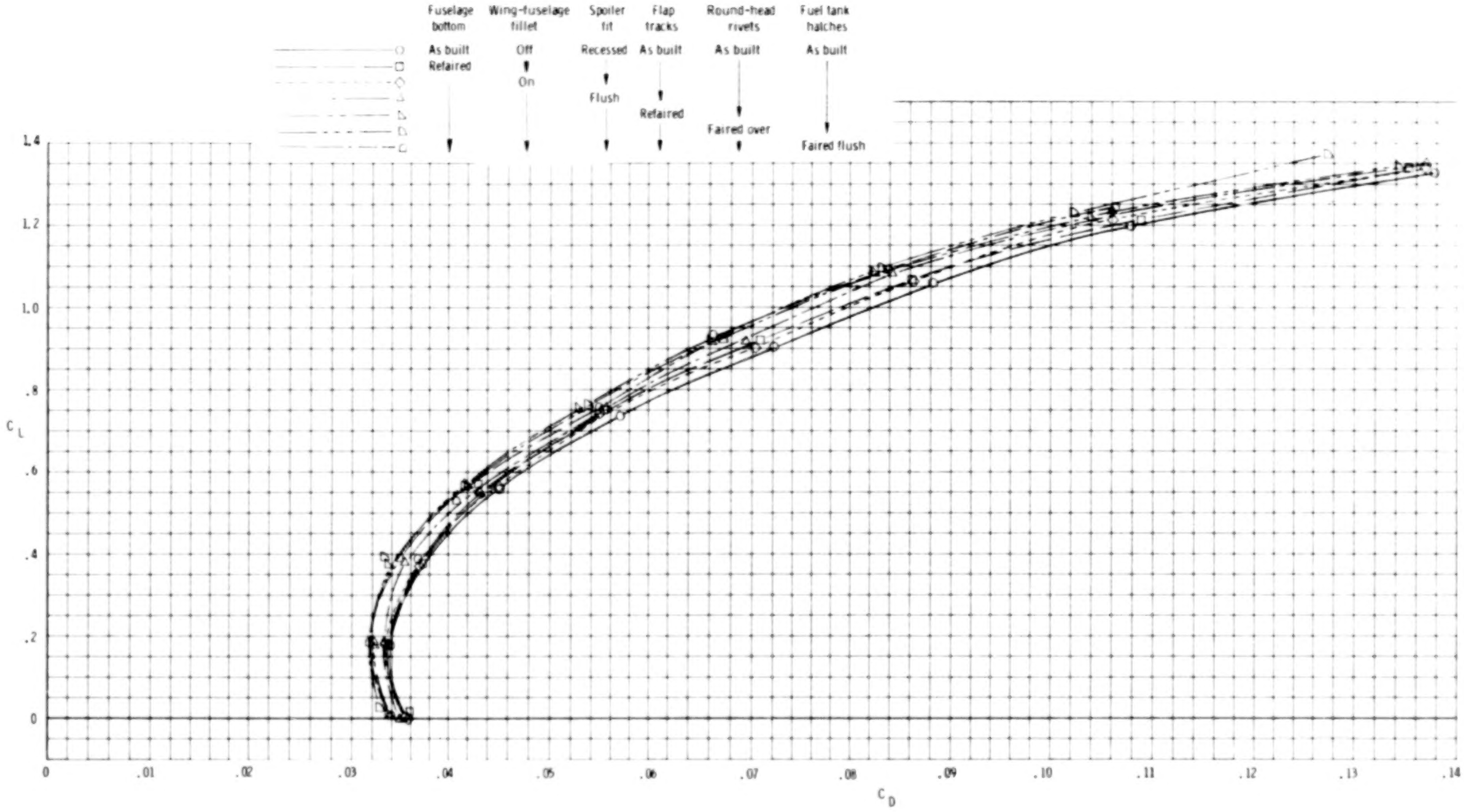

(b) Expanded lift-drag polars.

Figure 29.- Concluded.

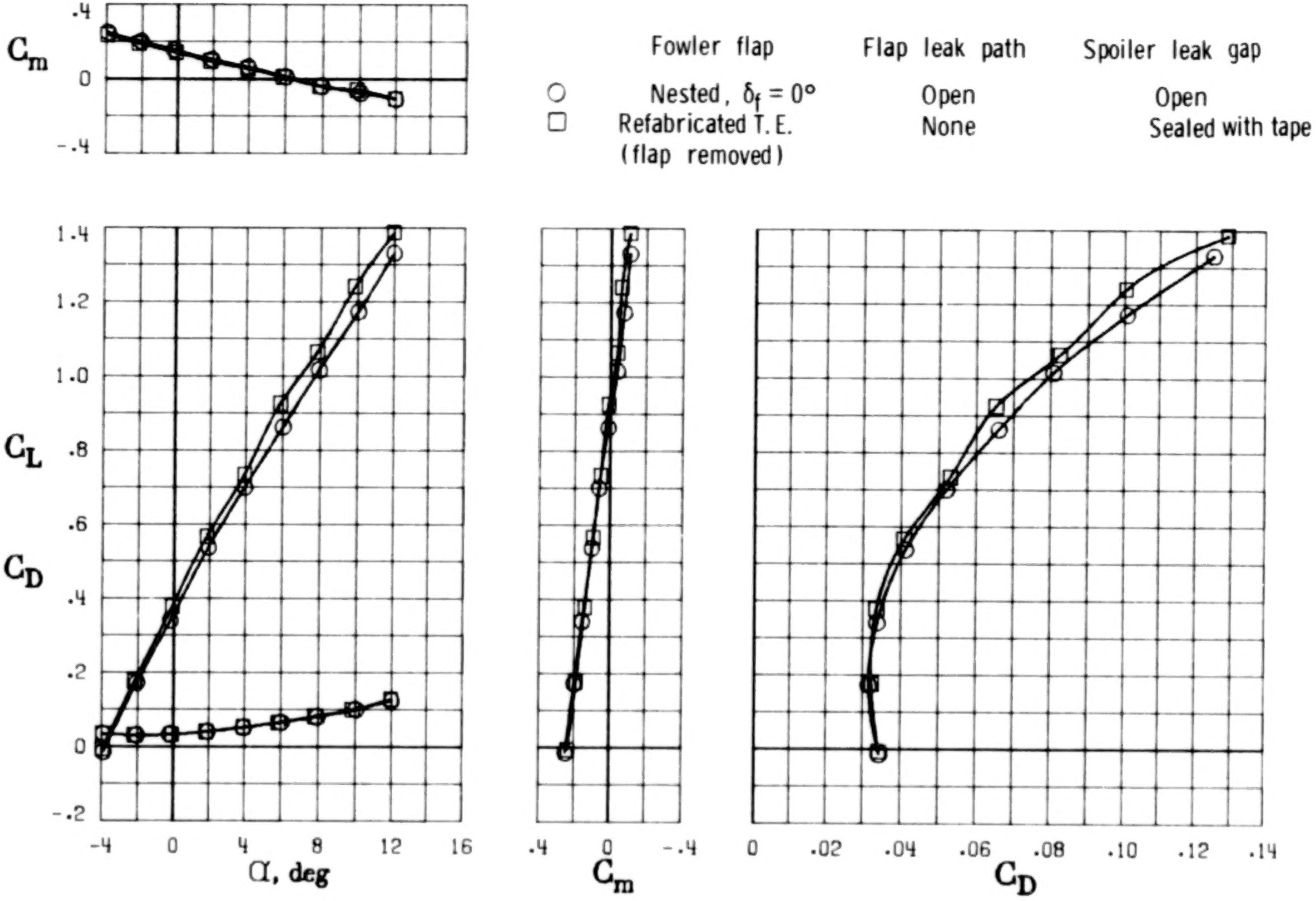

(a) Longitudinal characteristics.

Figure 30.- Effect of wing trailing-edge modification at $R = 3.50 \times 10^6$ with engine inlets sealed and cowl flaps closed.

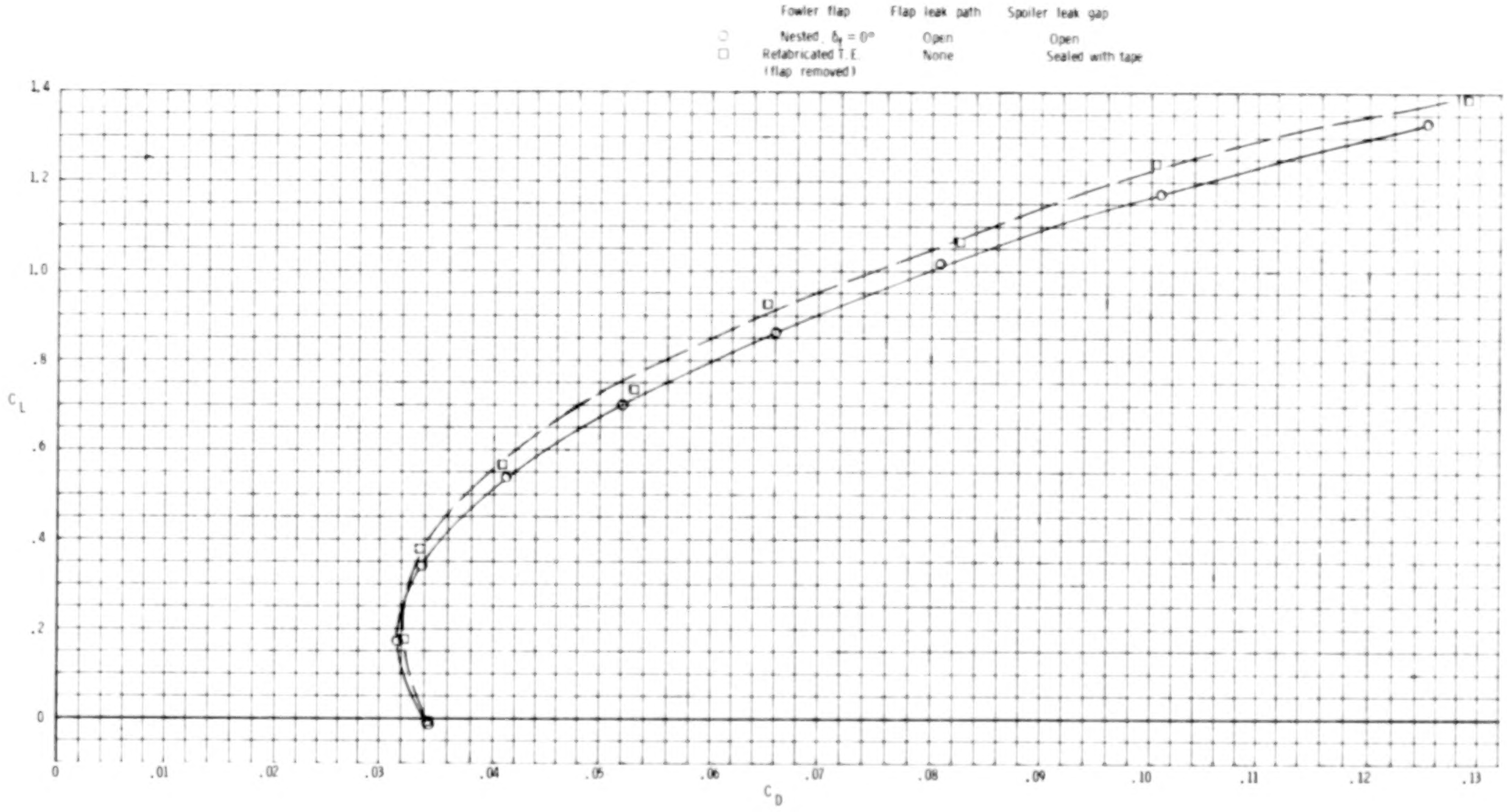

(b) Expanded lift-drag polars.

Figure 30.- Concluded.

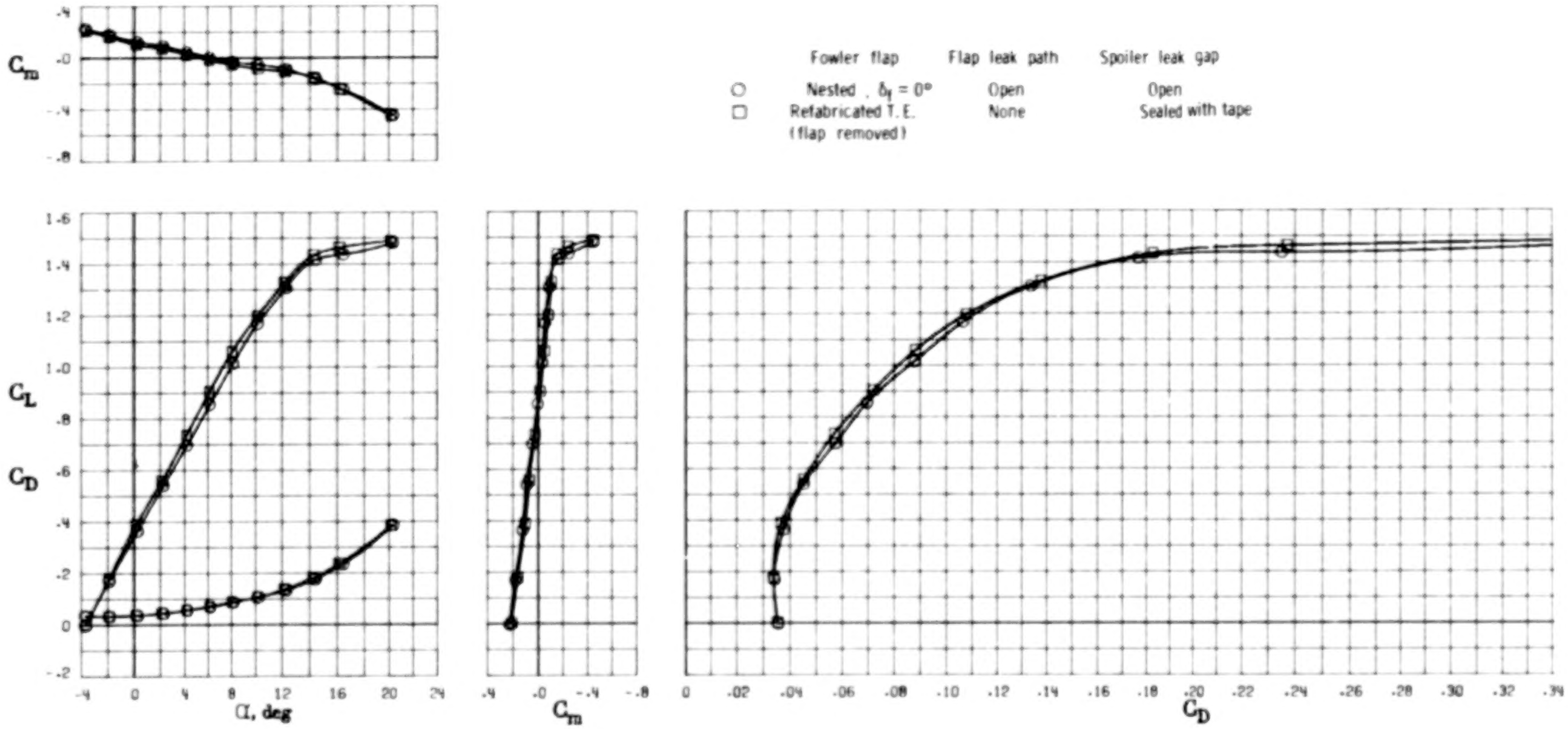

(a) Longitudinal characteristics.

Figure 31.- Effect of wing trailing-edge modification at $R = 2.30 \times 10^6$ with engine inlets sealed and cowl flaps closed.

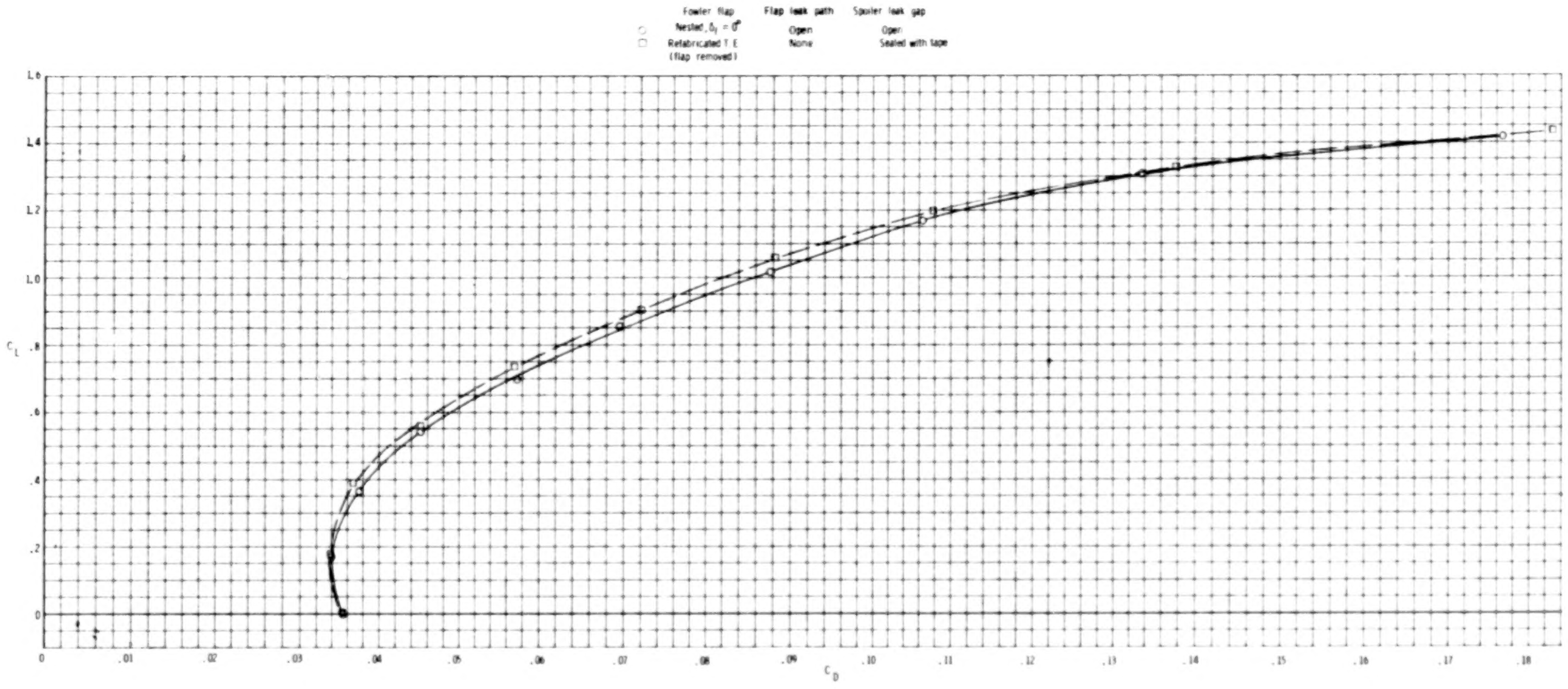

(b) Expanded lift-drag polars.

Figure 31.- Concluded.

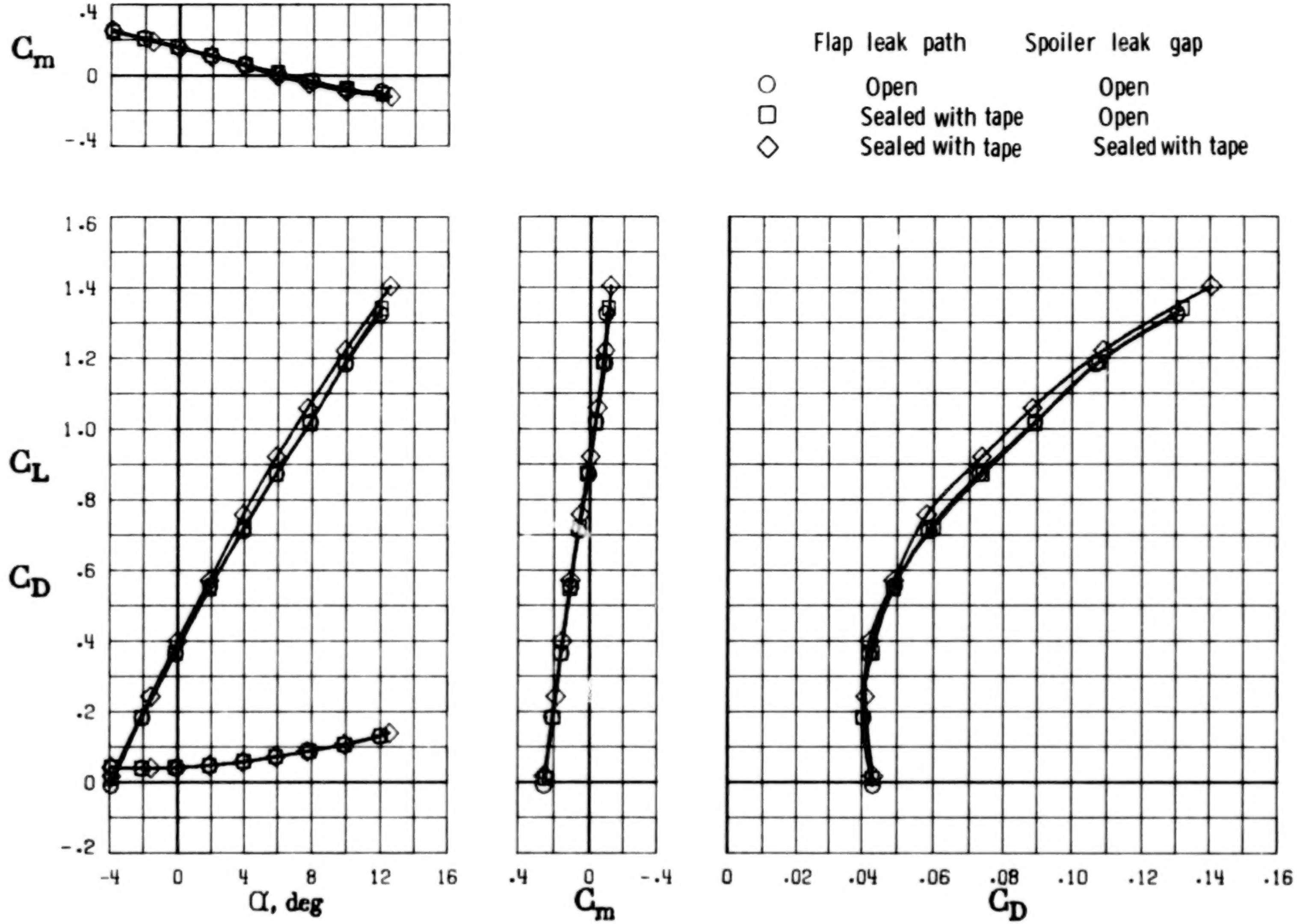

(a) Longitudinal characteristics.

Figure 32.- Effect of flap and spoiler leak paths for as-received climb configuration at $R = 3.50 \times 10^6$. $\delta_f = 0^\circ$; engine inlets open; cowl flaps open.

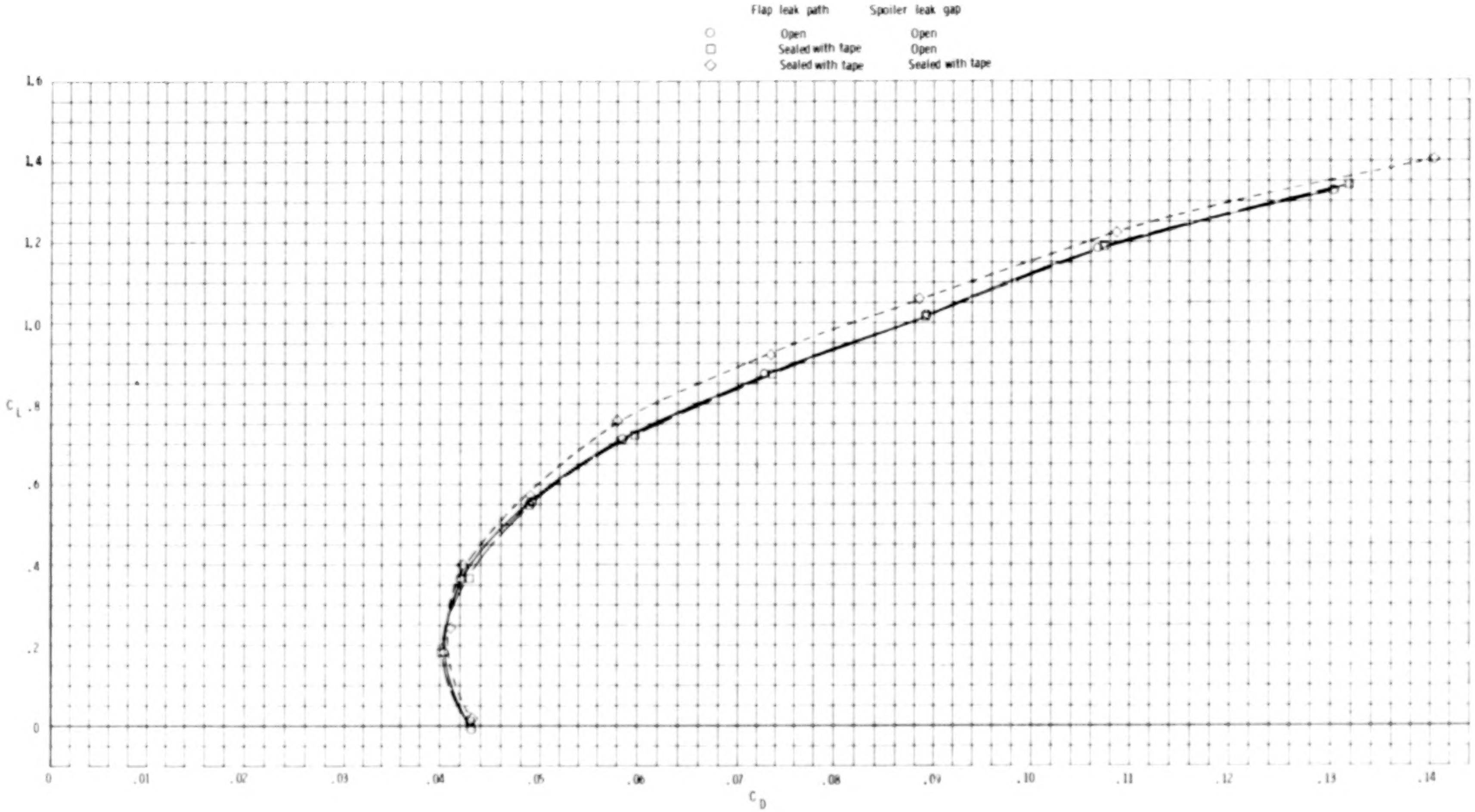

(b) Expanded lift-drag polars.

Figure 32.- Concluded.

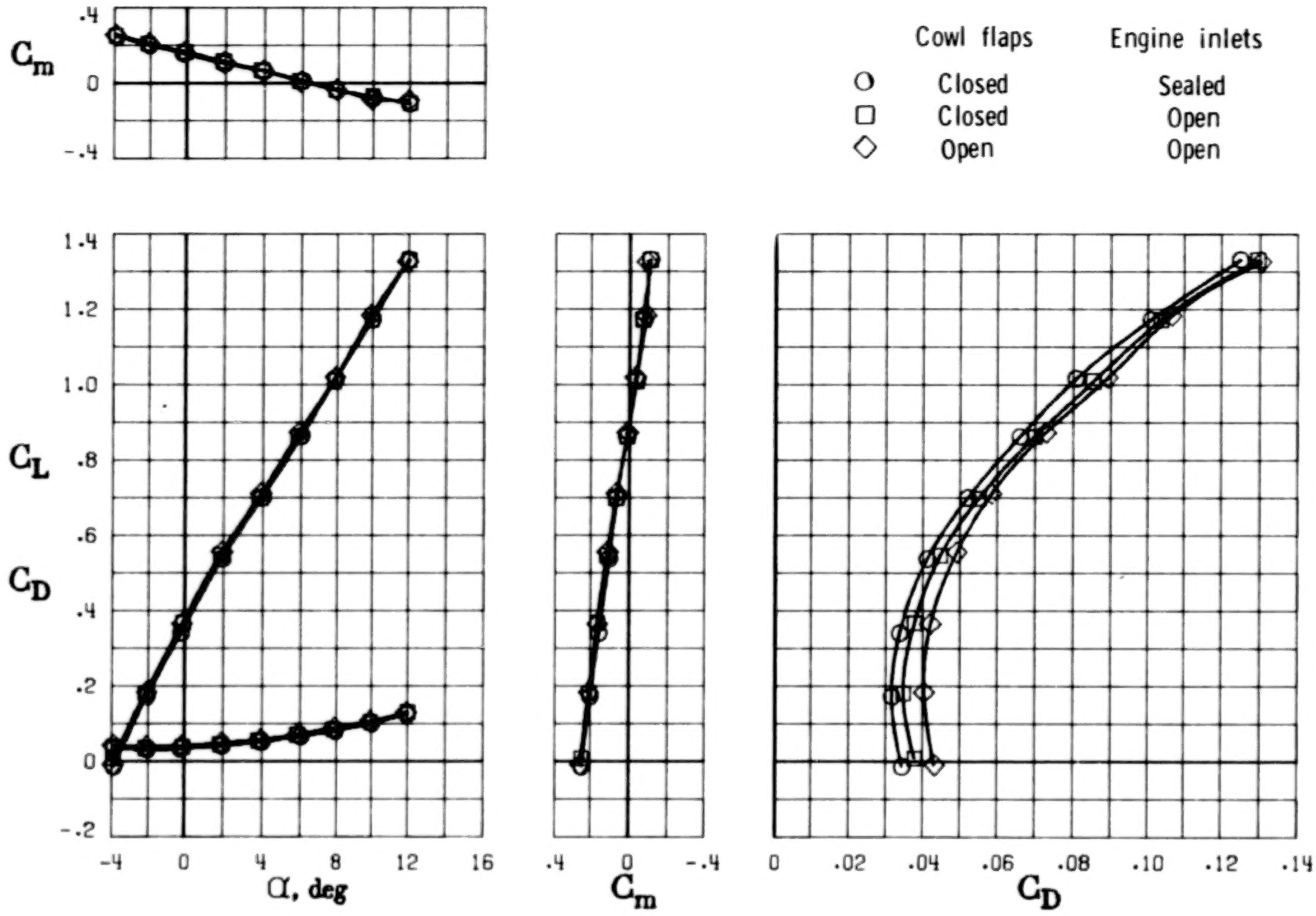

(a) Longitudinal characteristics.

Figure 33.- Effect of varying airflow through engine nacelles with propellers off at $R = 3.50 \times 10^6$. $\delta_f = 0^\circ$; flap and spoiler leak paths open.

1

111

112

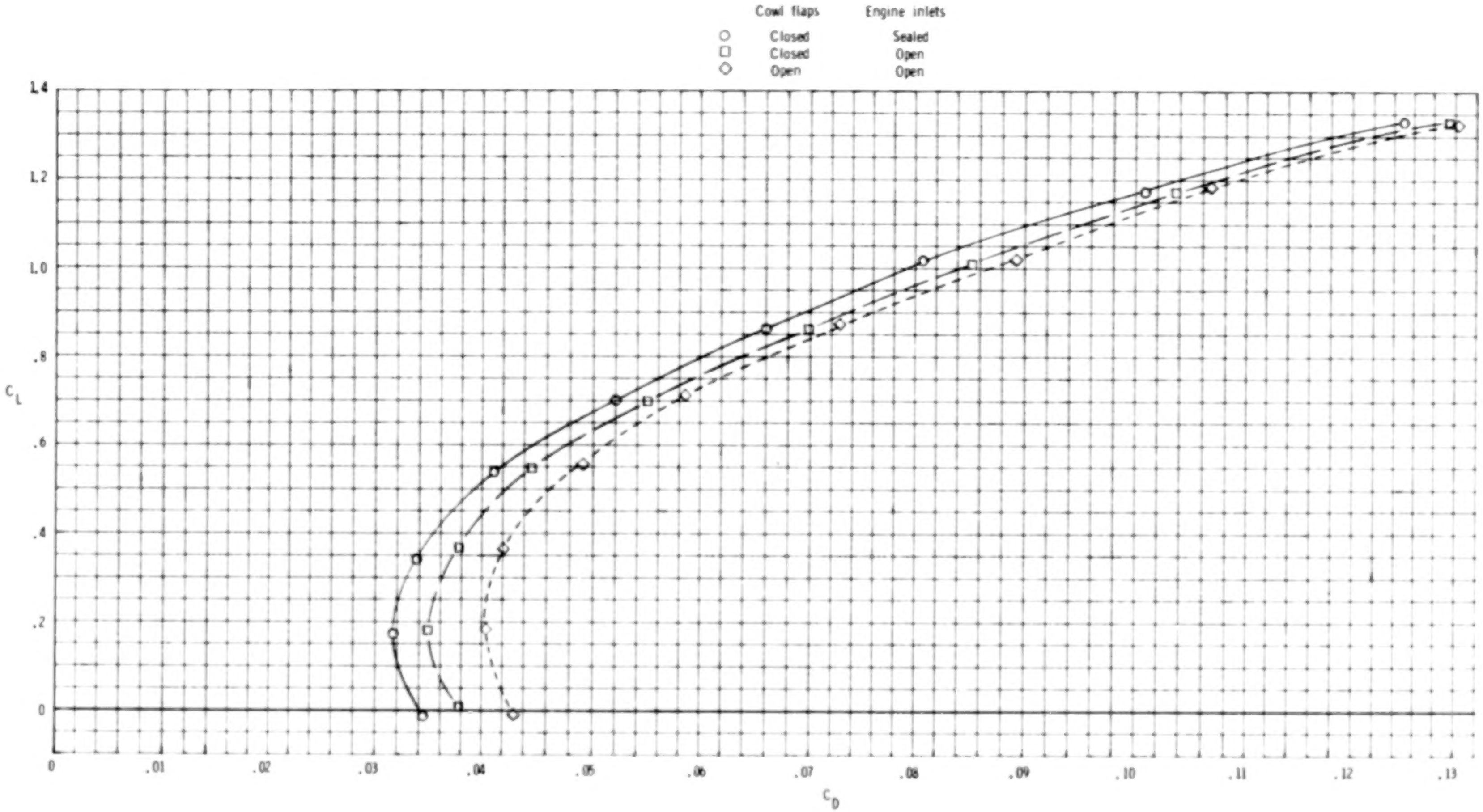

(b) Expanded lift-drag polars.

Figure 33.- Concluded.

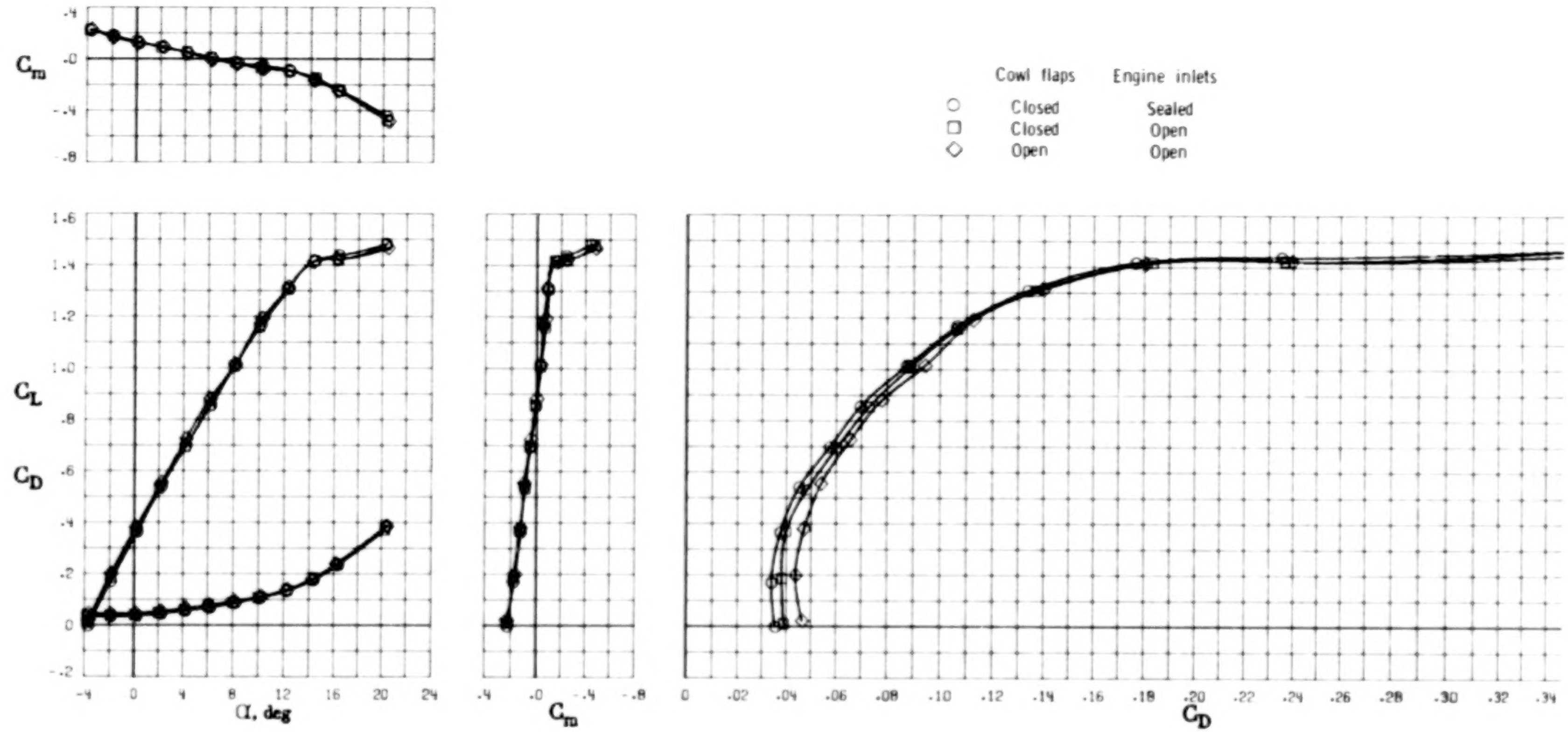

(a) Longitudinal characteristics.

Figure 34.- Effect of varying airflow through engine nacelles with propellers off at $R = 2.30 \times 10^6$. $\delta_f = 0^\circ$; flap and spoiler leak paths open.

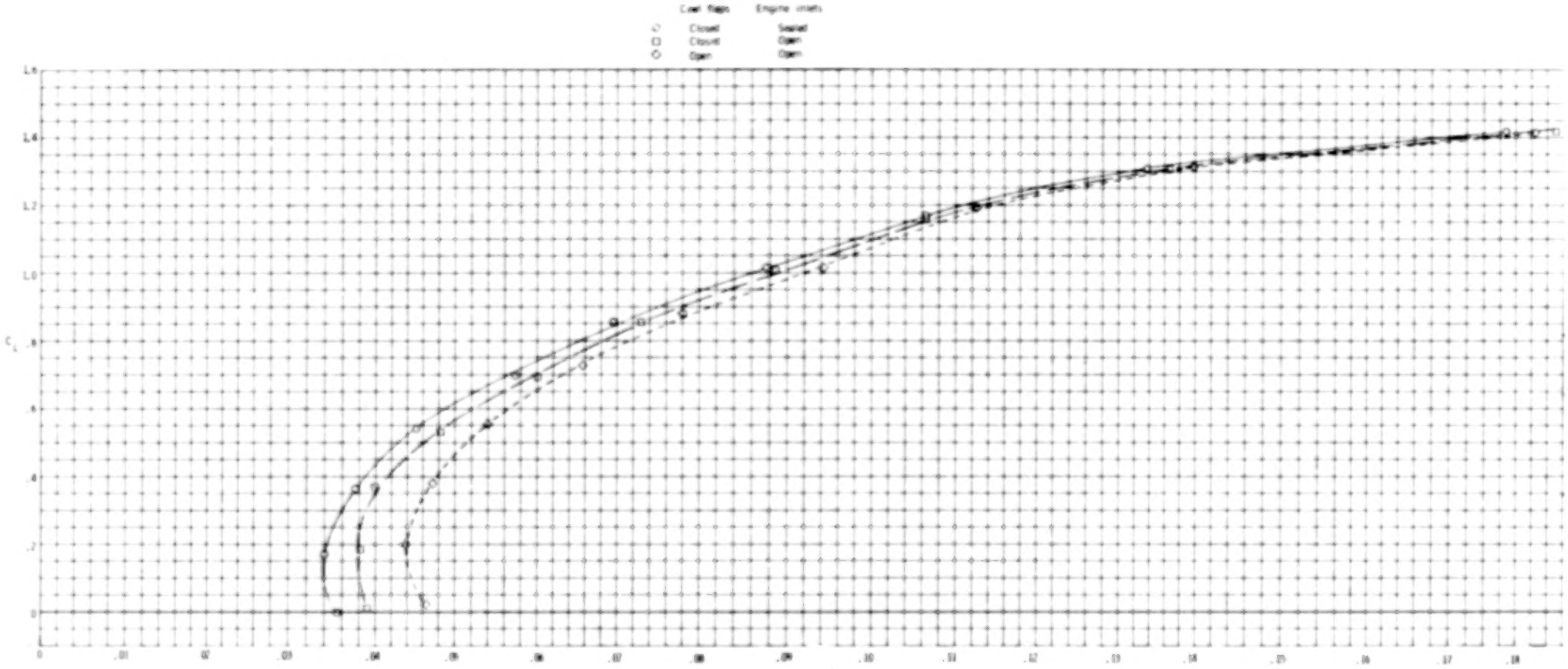

(b) Expanded lift-drag polars.

Figure 34.- Concluded.

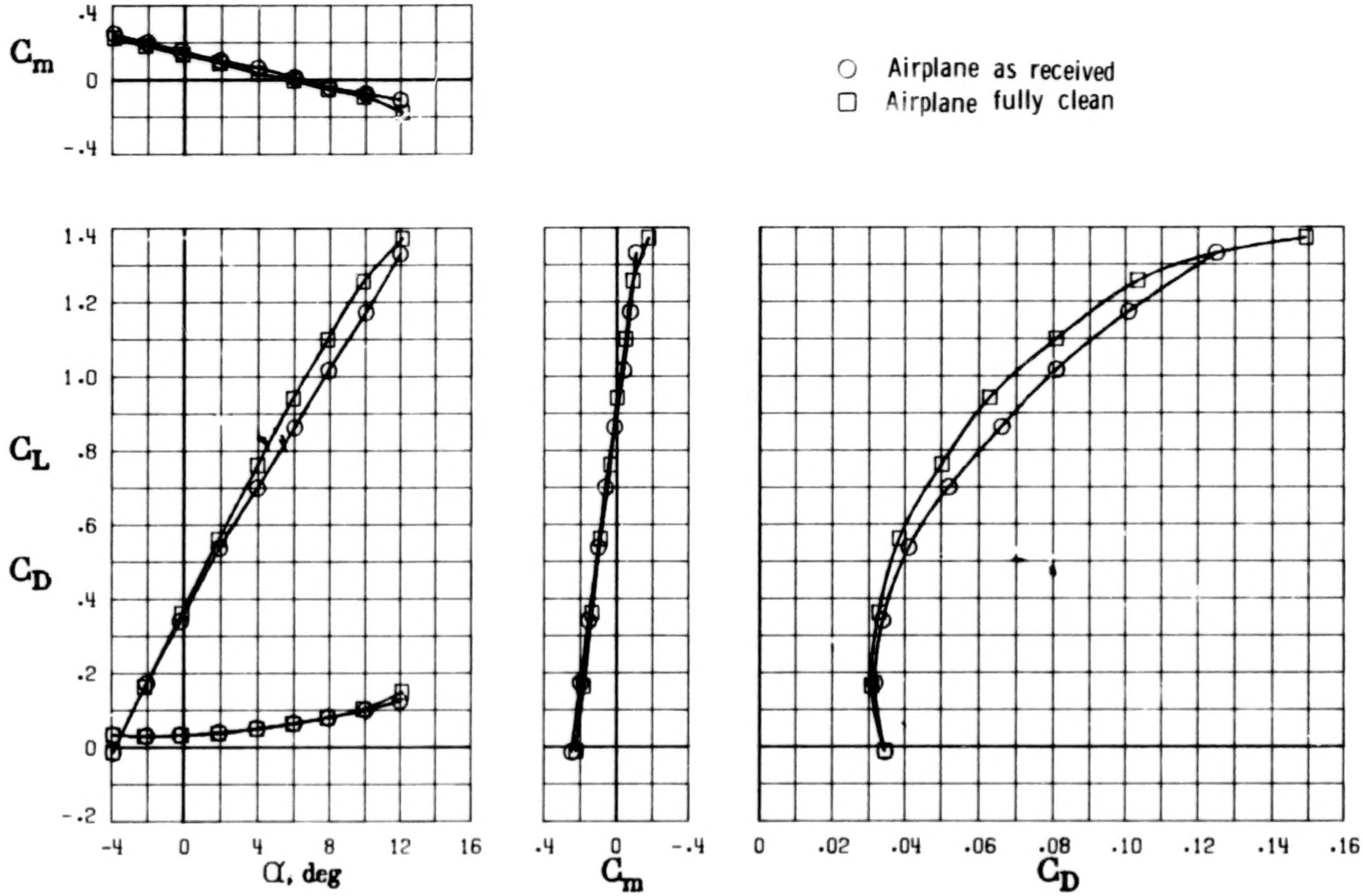

(a) Longitudinal characteristics.

Figure 35.- Total effect of drag cleanup at R = 3.50×10^6. $\delta_f = 0^\circ$; cowl flaps closed and engine inlets sealed; $\delta_{stab} = 0^\circ$.

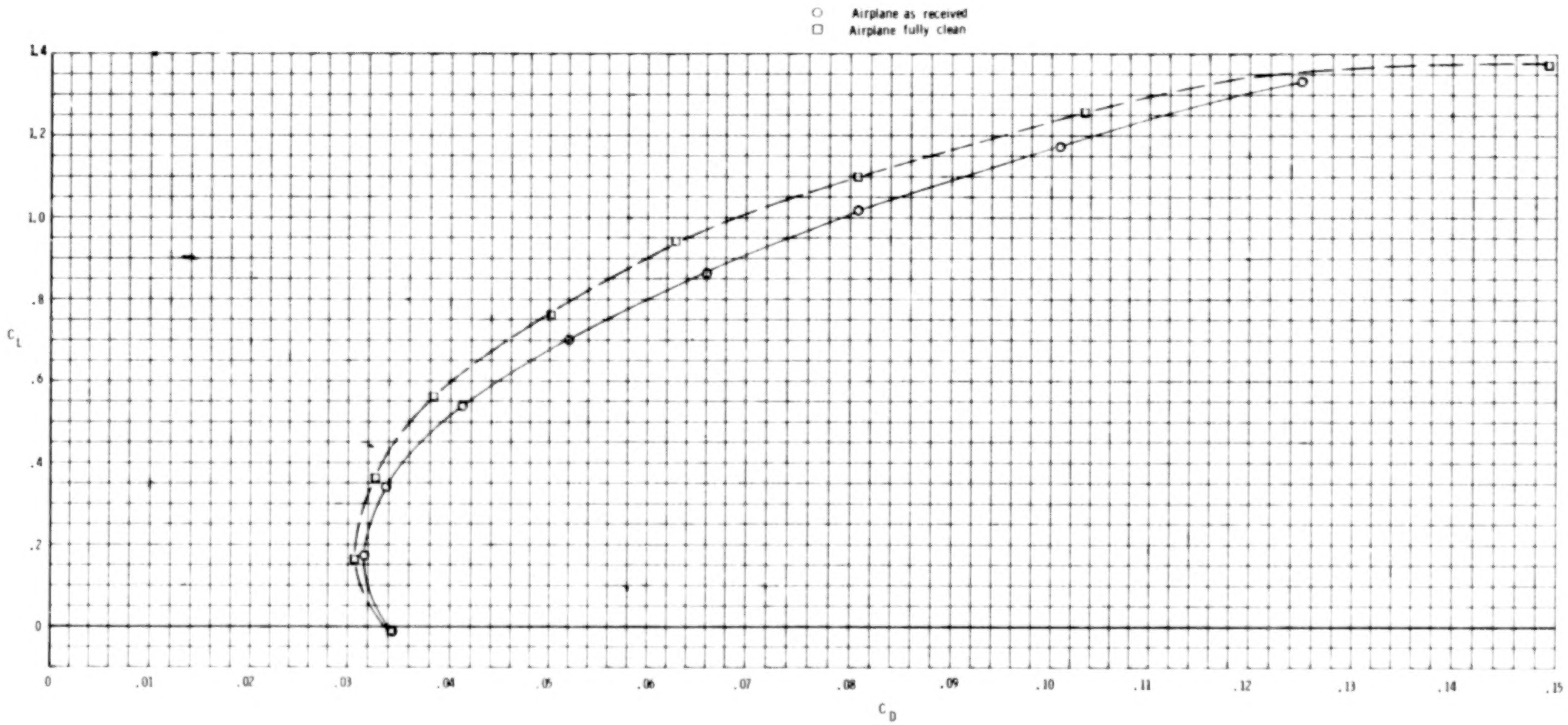

(b) Expanded lift-drag polars.

Figure 35.- Concluded.

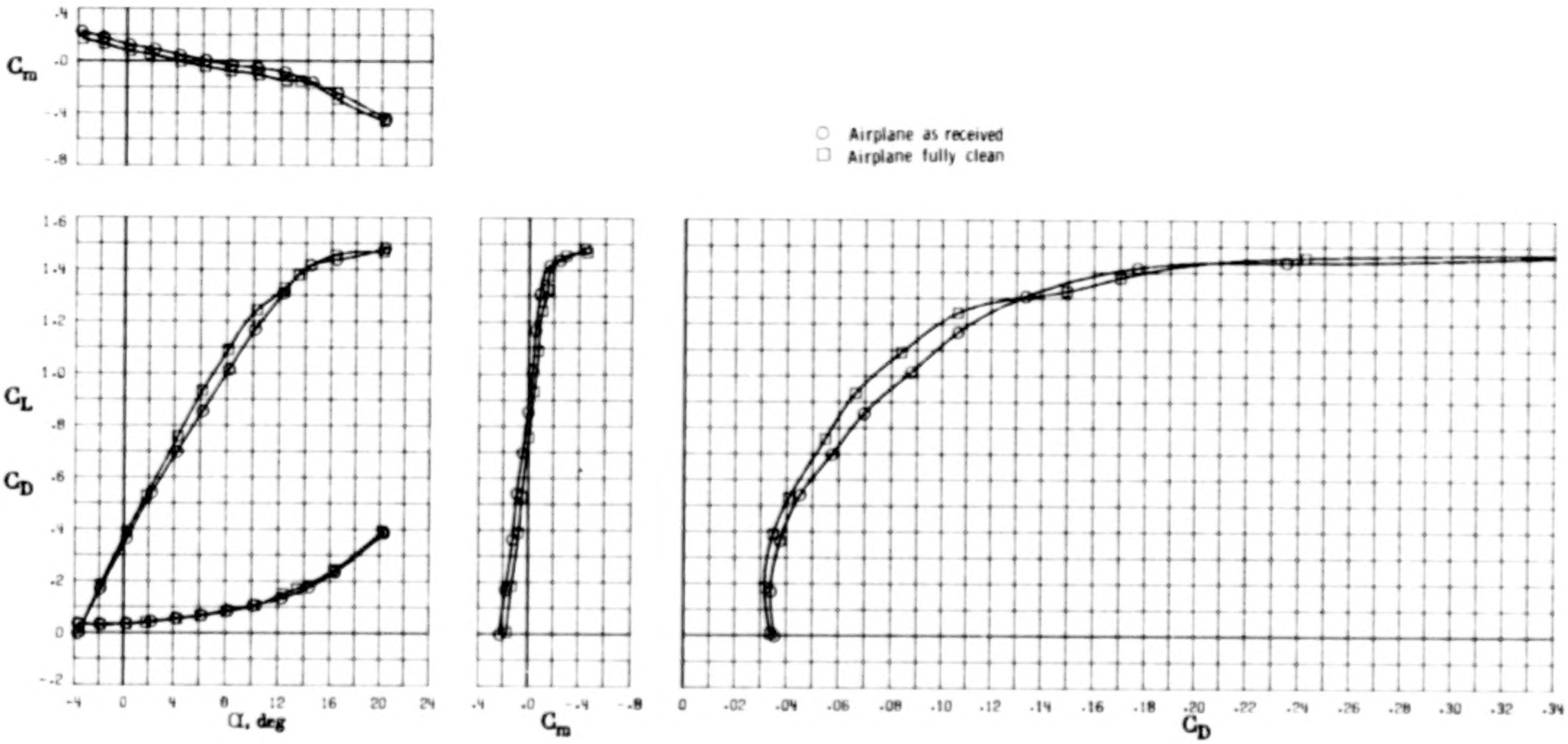

(a) Longitudinal characteristics.

Figure 36.- Total effect of drag cleanup at $R = 2.30 \times 10^6$. $\delta_f = 0^\circ$; cowl flaps closed and engine inlets sealed; $\delta_{stab} = 0^\circ$.

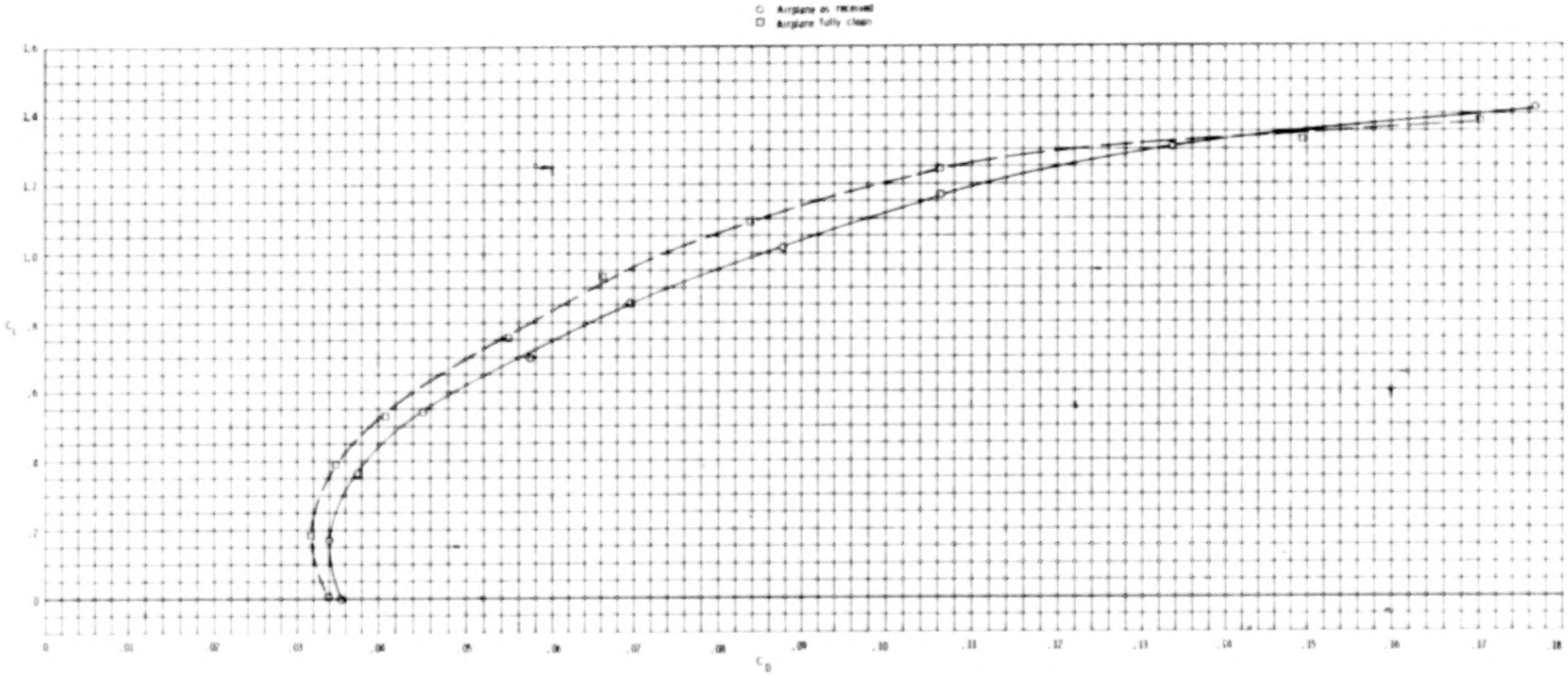

(b) Expanded lift-drag polars.

Figure 36.- Concluded.

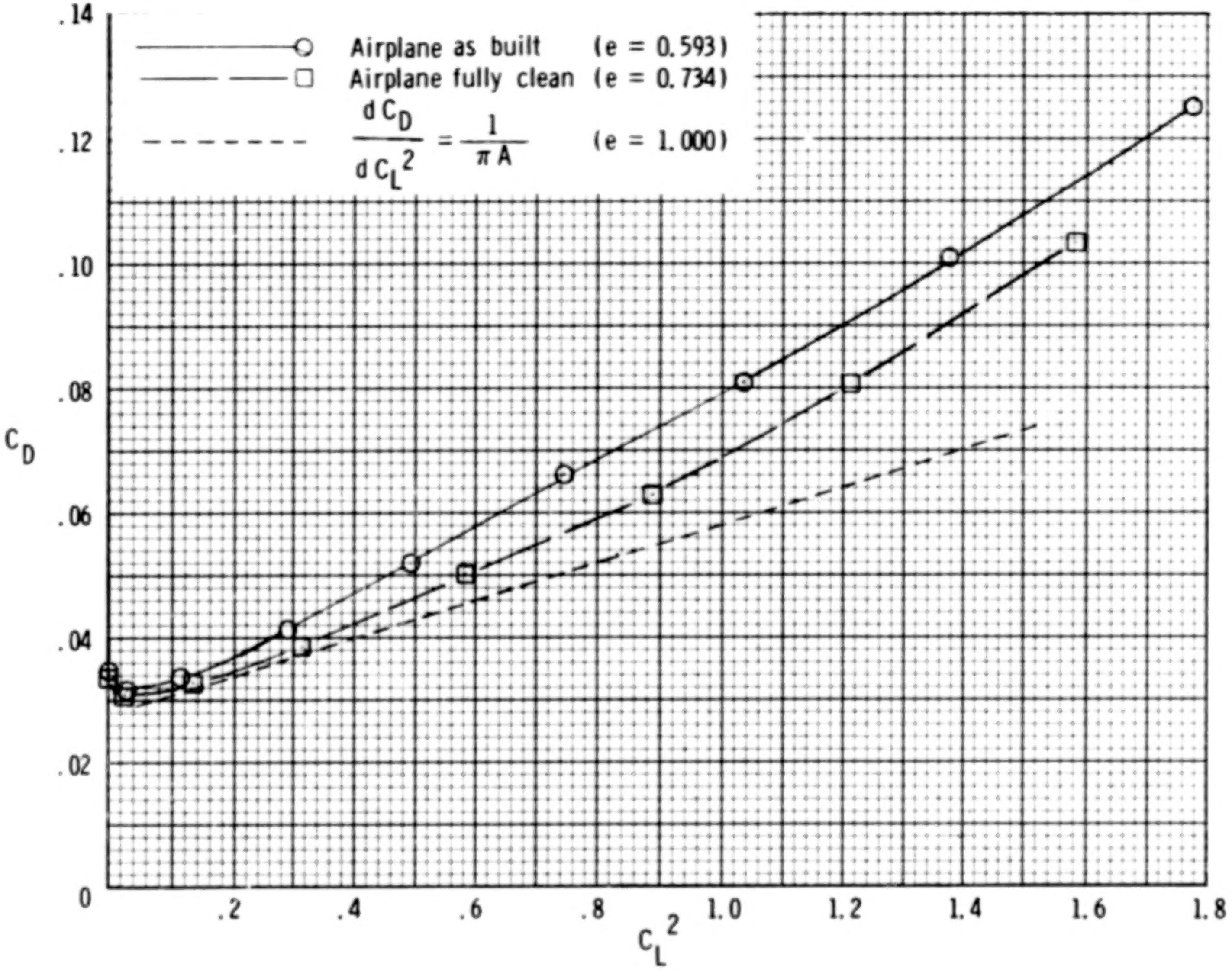

Figure 37.- Total effect of drag cleanup on power-off airplane efficiency factor. R = 3.50 × 10^6.

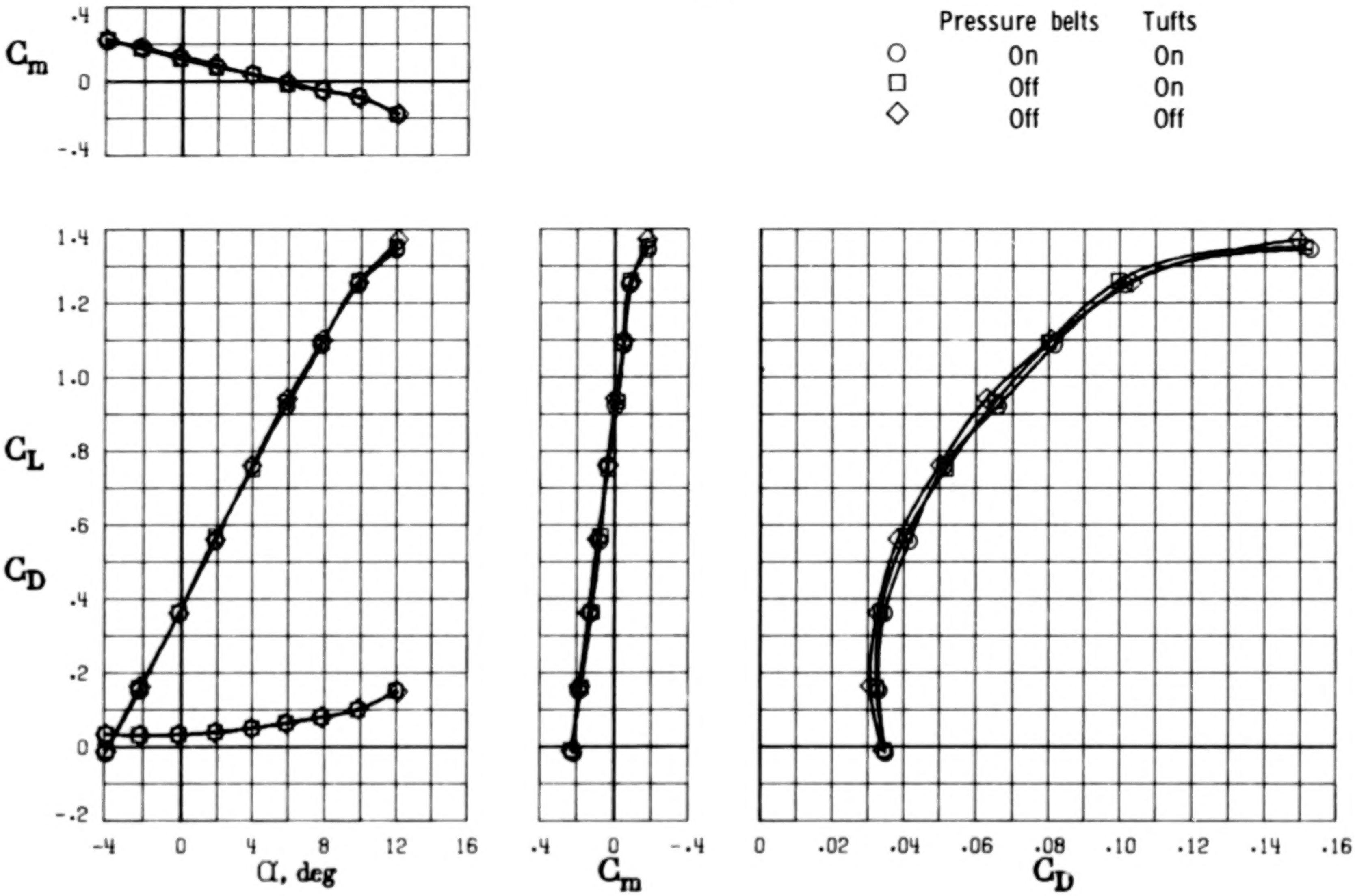

(a) Longitudinal characteristics.

Figure 38.- Effect of pressure belts and tufts at $R = 3.50 \times 10^6$ with engine inlets sealed and cowl flaps closed.

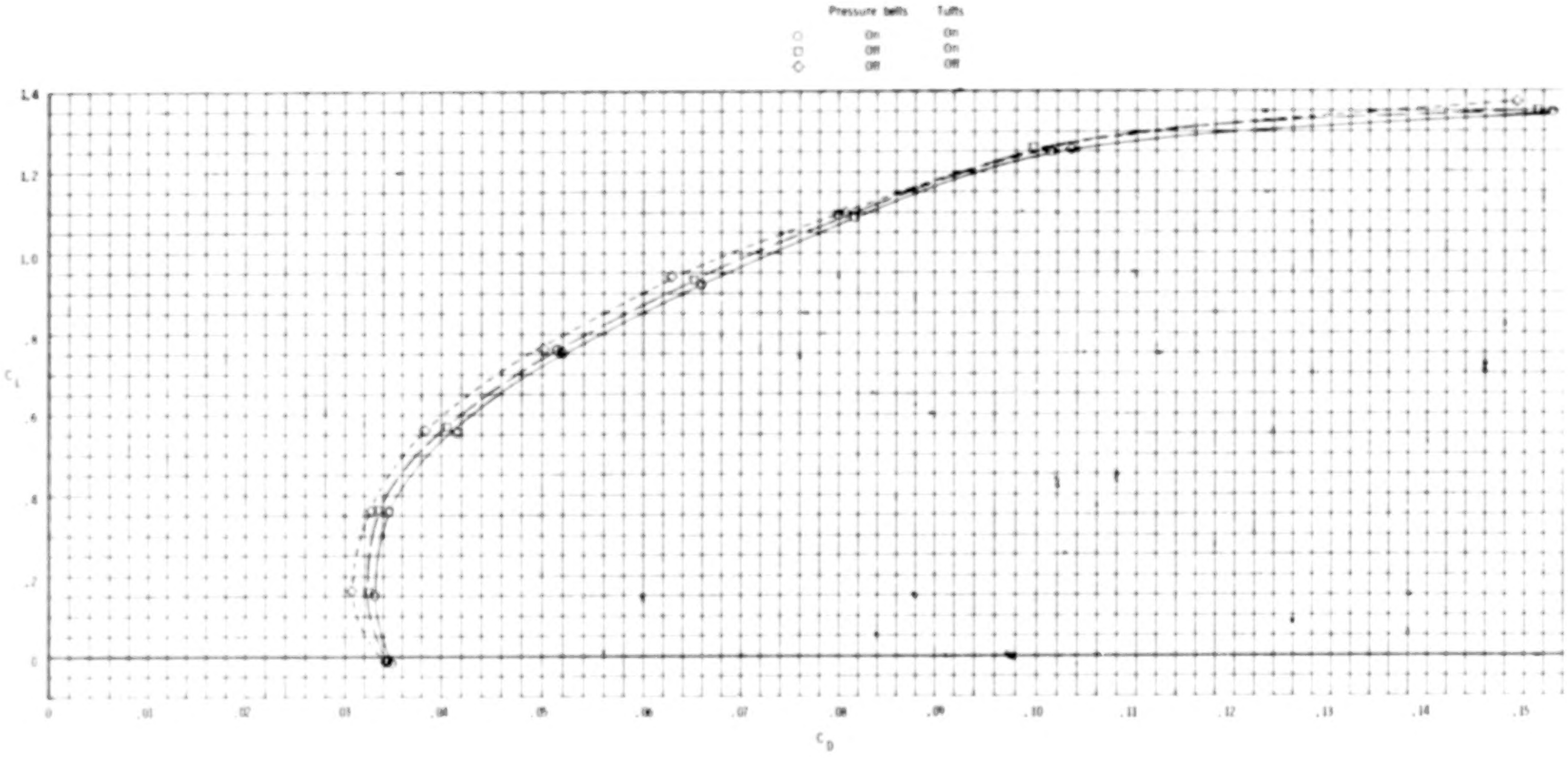

(b) Expanded lift-drag polars.

Figure 38.- Concluded.

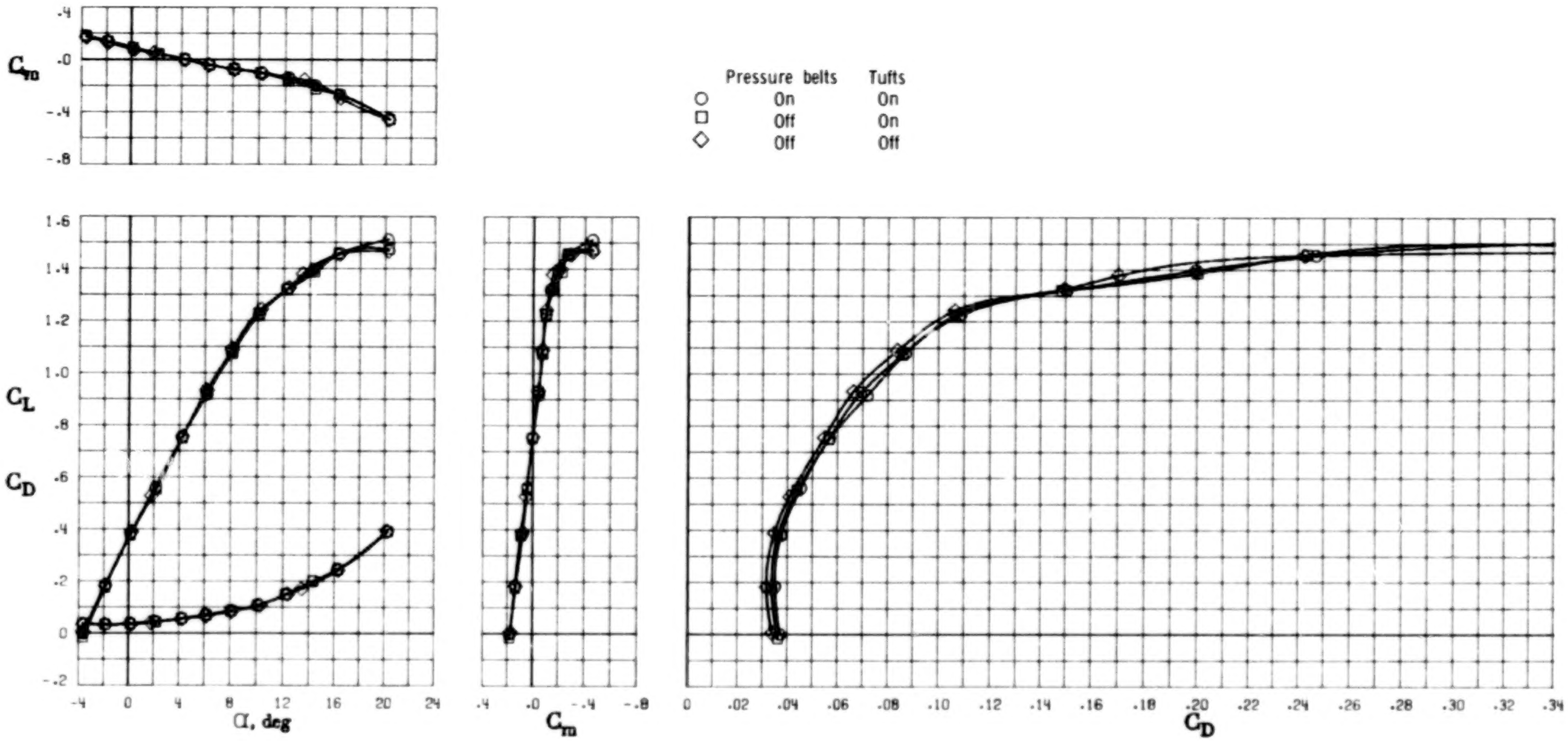

(a) Longitudinal characteristics.

Figure 39.- Effect of pressure belts and tufts at $R = 2.30 \times 10^6$ with engine inlets sealed and cowl flaps closed.

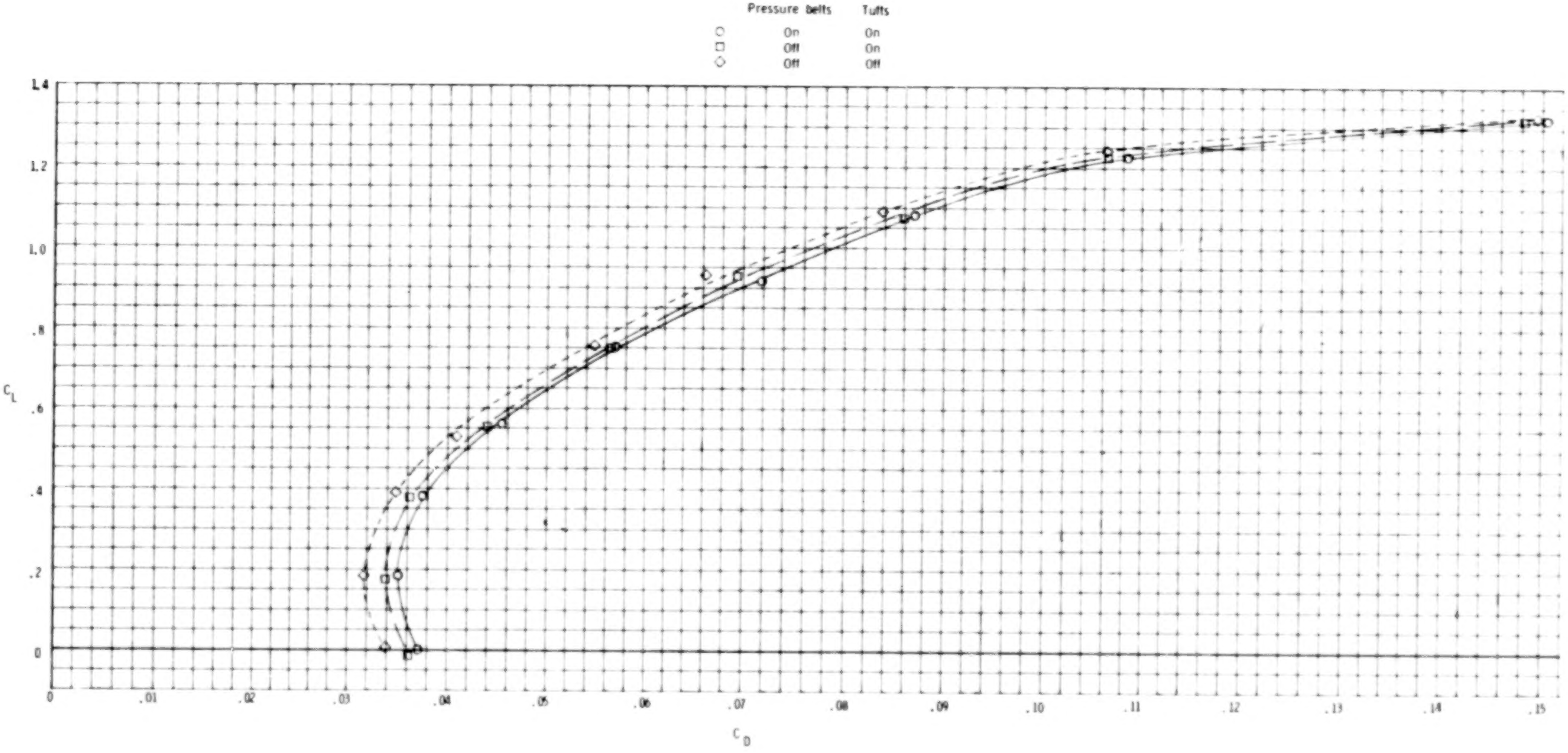

(b) Expanded lift-drag polars.

Figure 39.- Concluded.

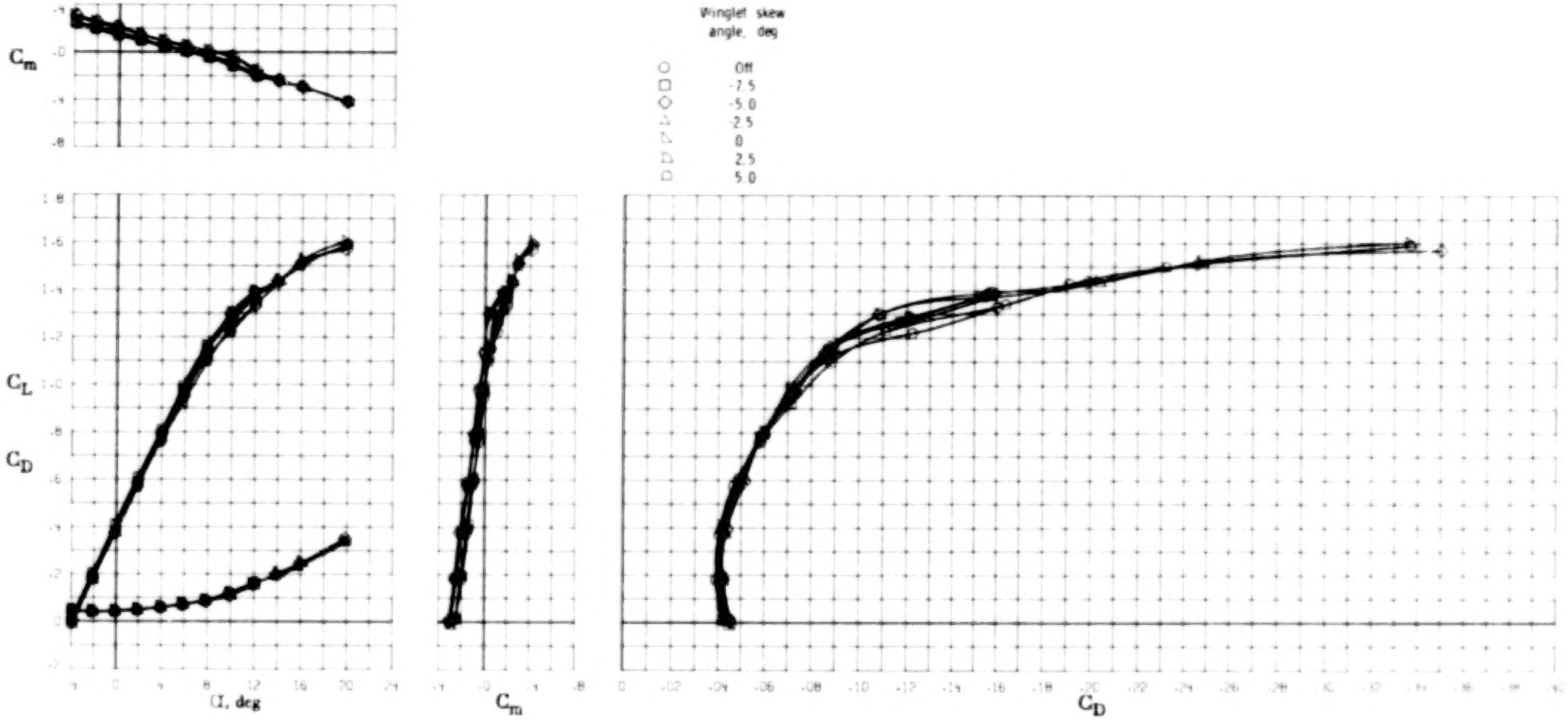

(a) Longitudinal characteristics.

Figure 40.- Effect of winglet skew angle for winglet cant angle of 20° at $R = 3.50 \times 10^6$.

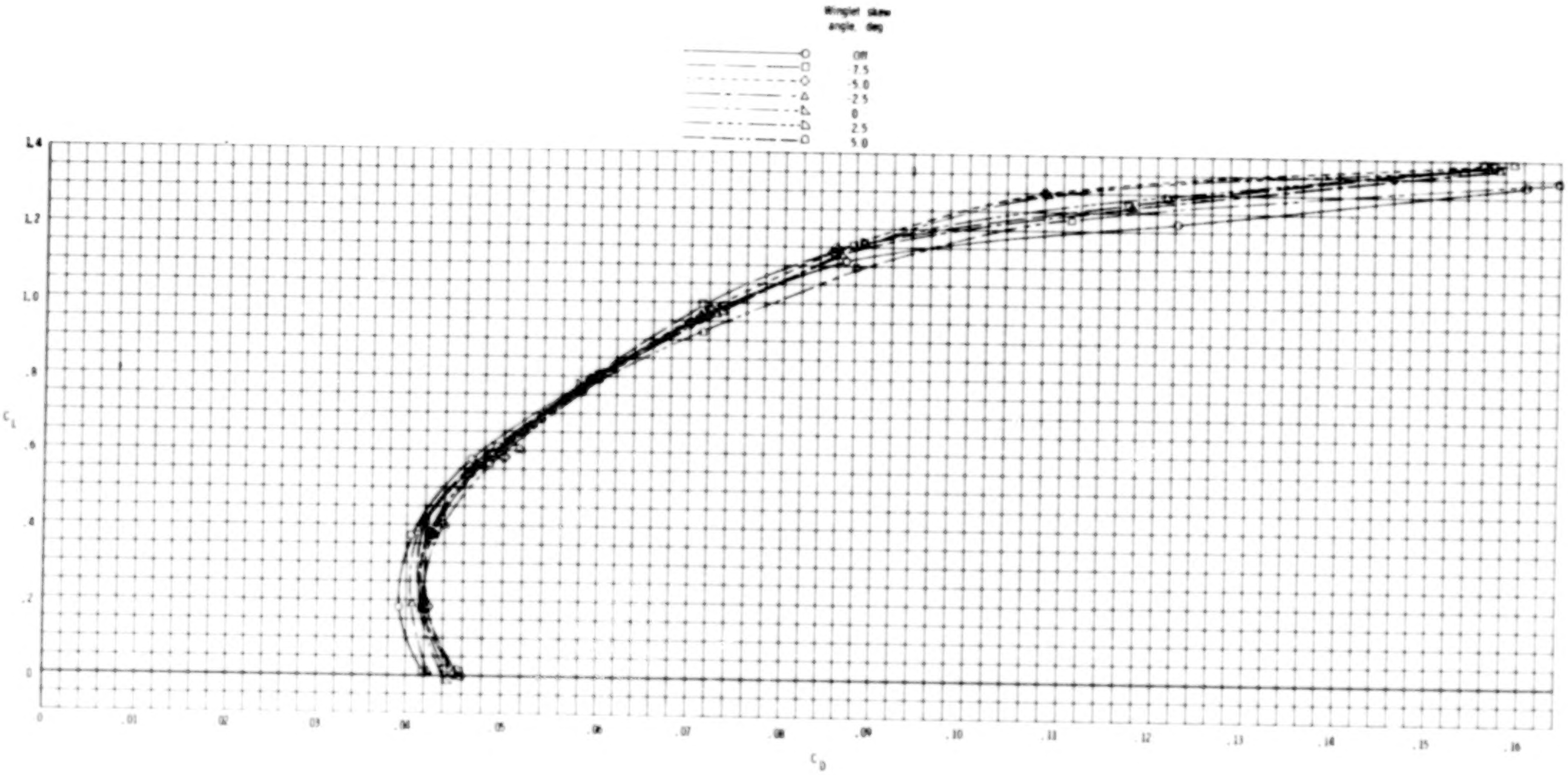

(b) Expanded lift-drag polars.

Figure 40.- Concluded.

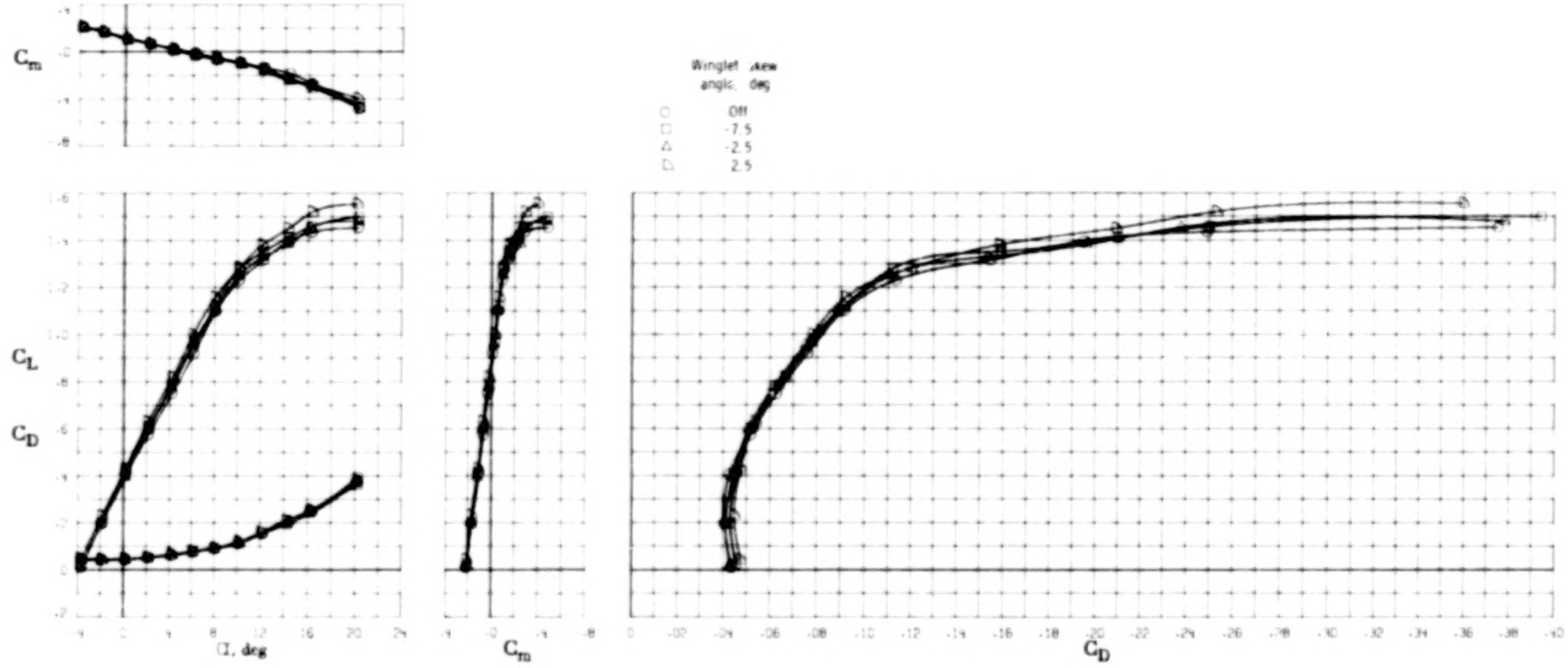

(a) Longitudinal characteristics.

Figure 41.- Effect of winglet skew angle for winglet cant angle of 20° at $R = 2.30 \times 10^6$.

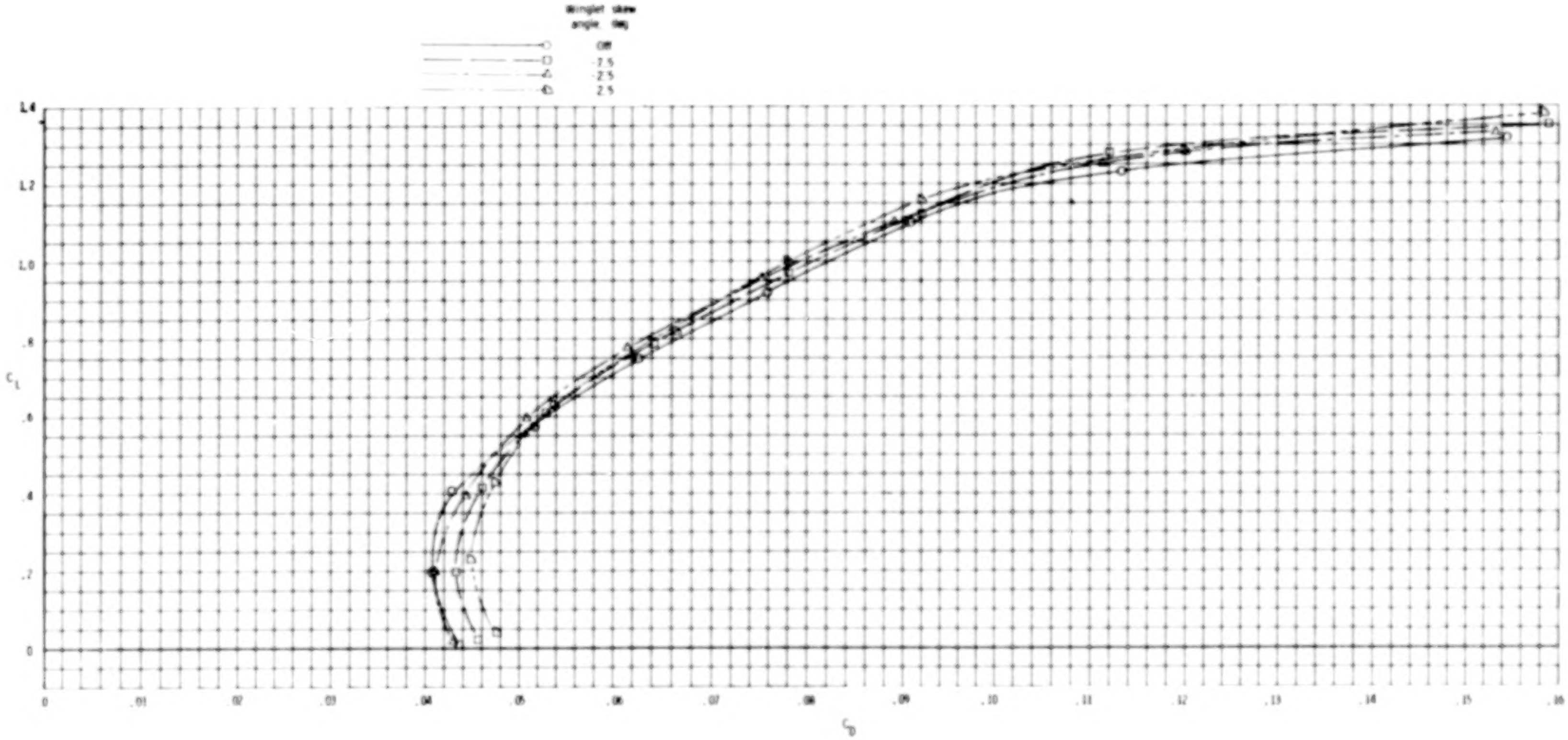

(b) Expanded lift-drag polars.

Figure 41.- Concluded.

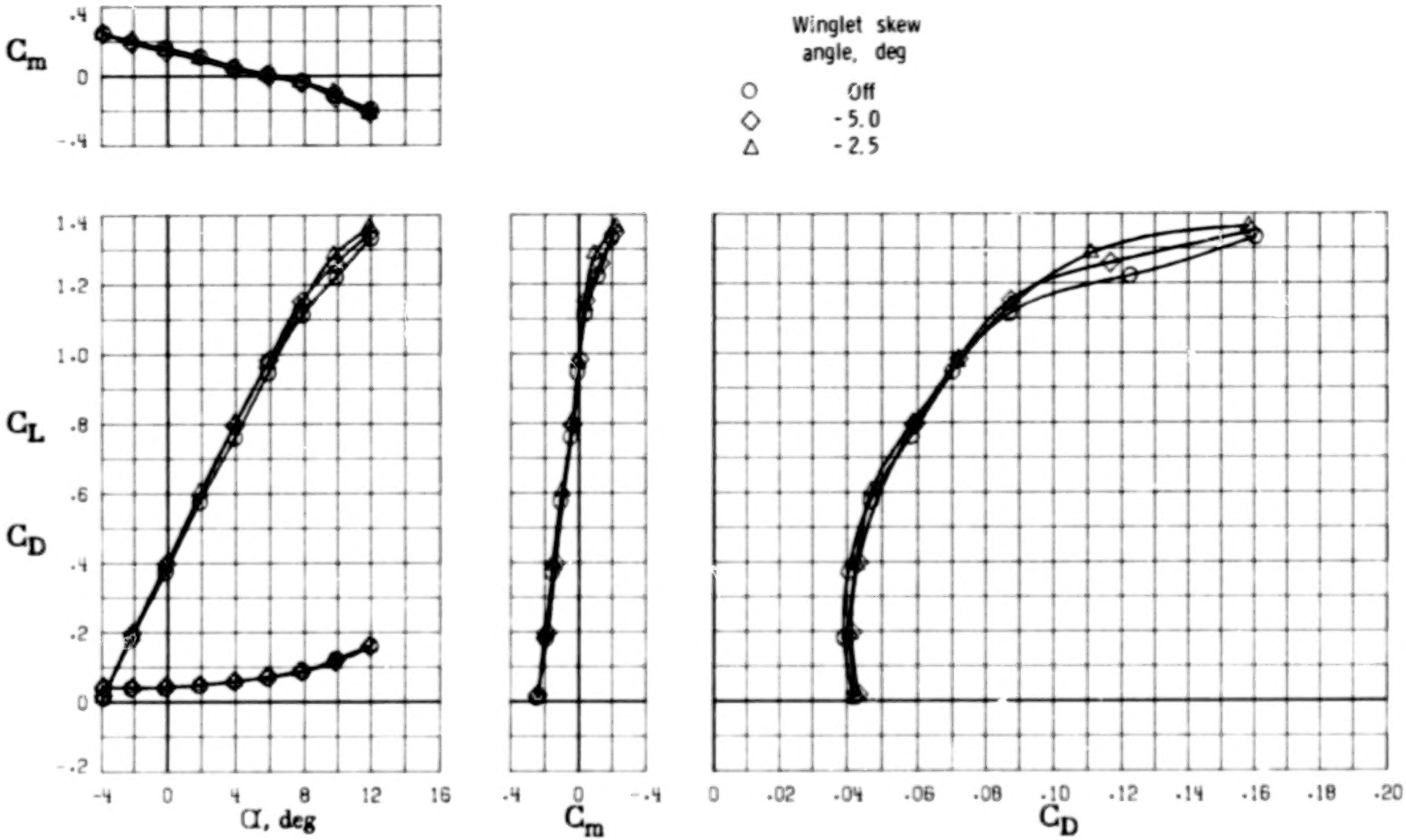

(a) Longitudinal characteristics.

Figure 42.- Effect of winglet skew angle for winglet cant angle of 15° at $R = 3.50 \times 10^6$.

NAS 1.60:1591

FULL-SCALE WIND-TUNNEL INVESTIGATION OF THE ADVANCED
TECHNOLOGY LIGHT TWIN-ENGINE AIRPLANE (ATLIT) ...
NASA TECHNICAL PAPER 1591... NATIONAL AERONAUTICS
AND SPACE ADMINISTRATION... MAY 1980

3 OF 4
24X
SUPTDOCS
GPO

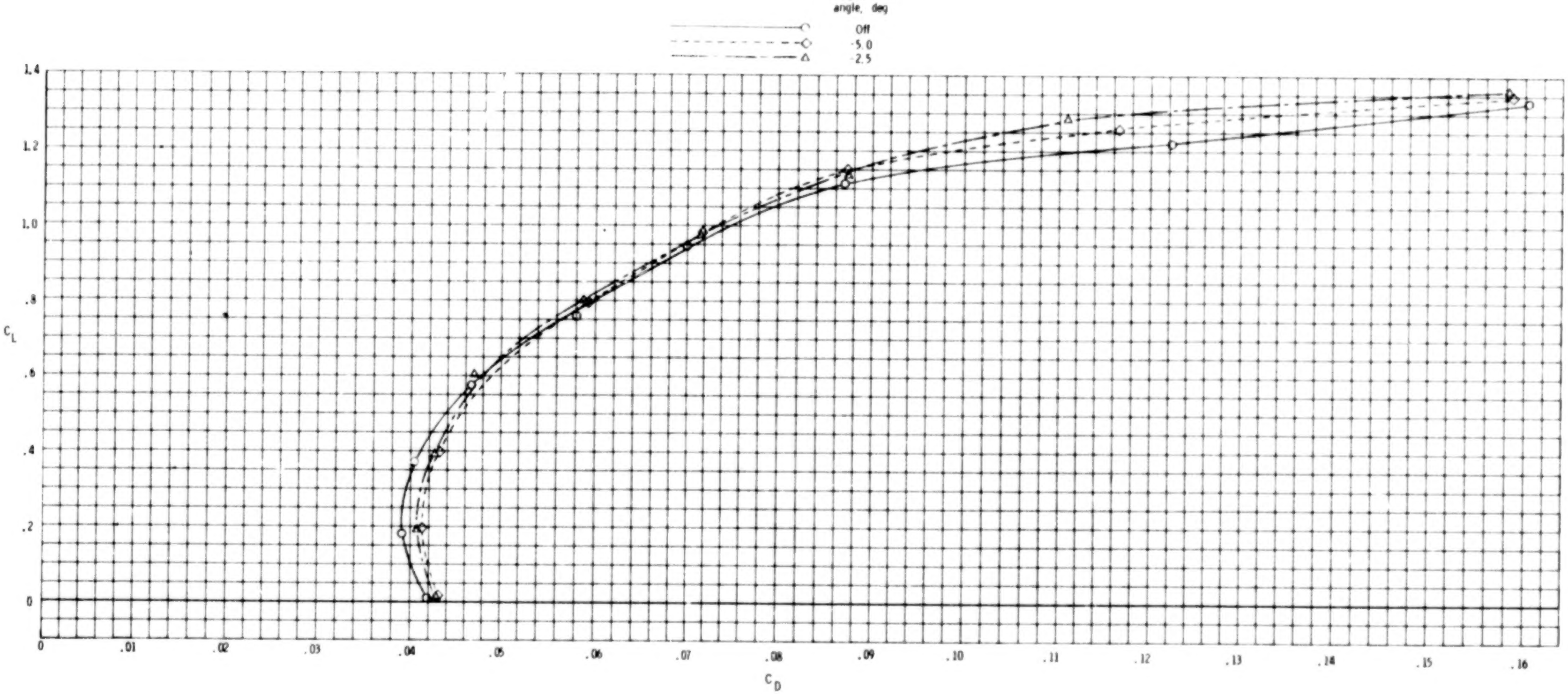

(b) Expanded lift-drag polars.

Figure 42.- Concluded.

130

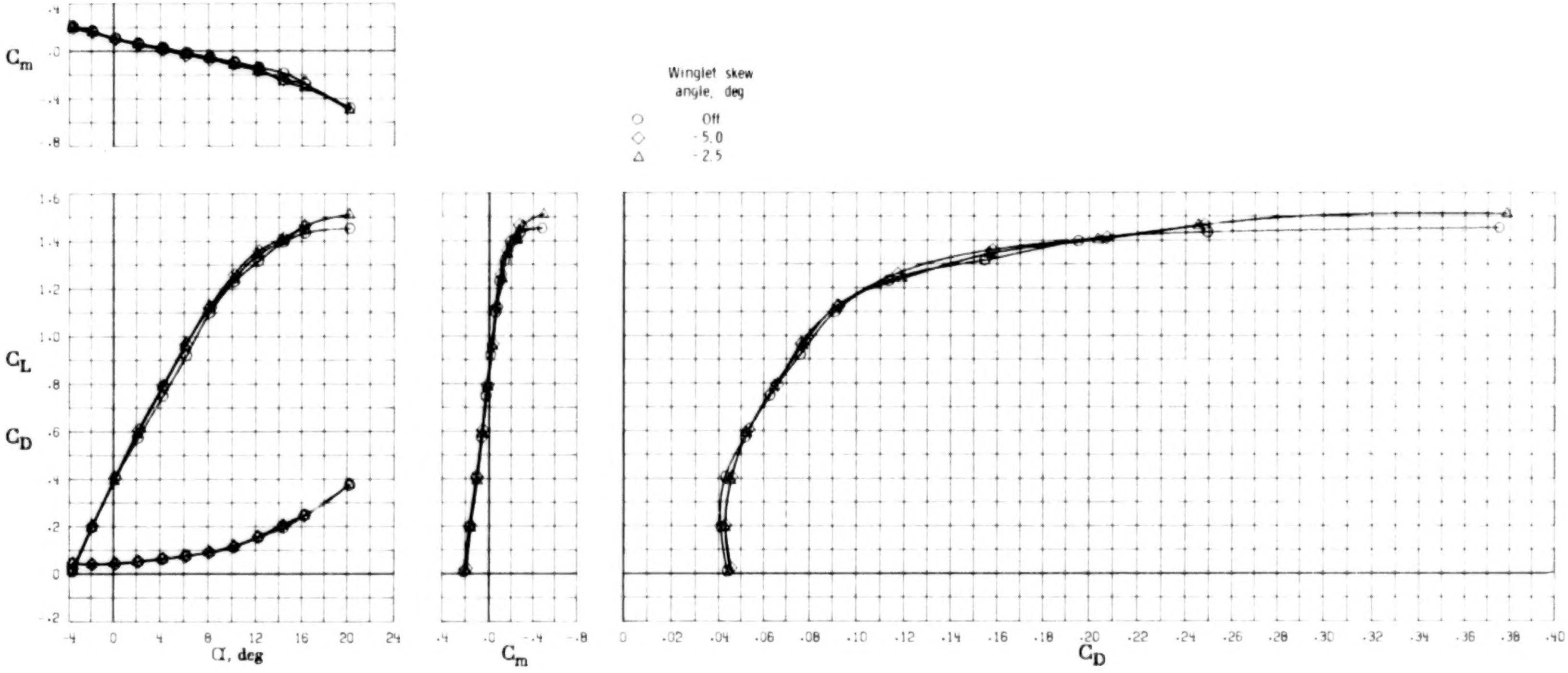

(a) Longitudinal characteristics.

Figure 43.- Effect of winglet skew angle for winglet cant angle of 15° at R = 2.30 × 10^6.

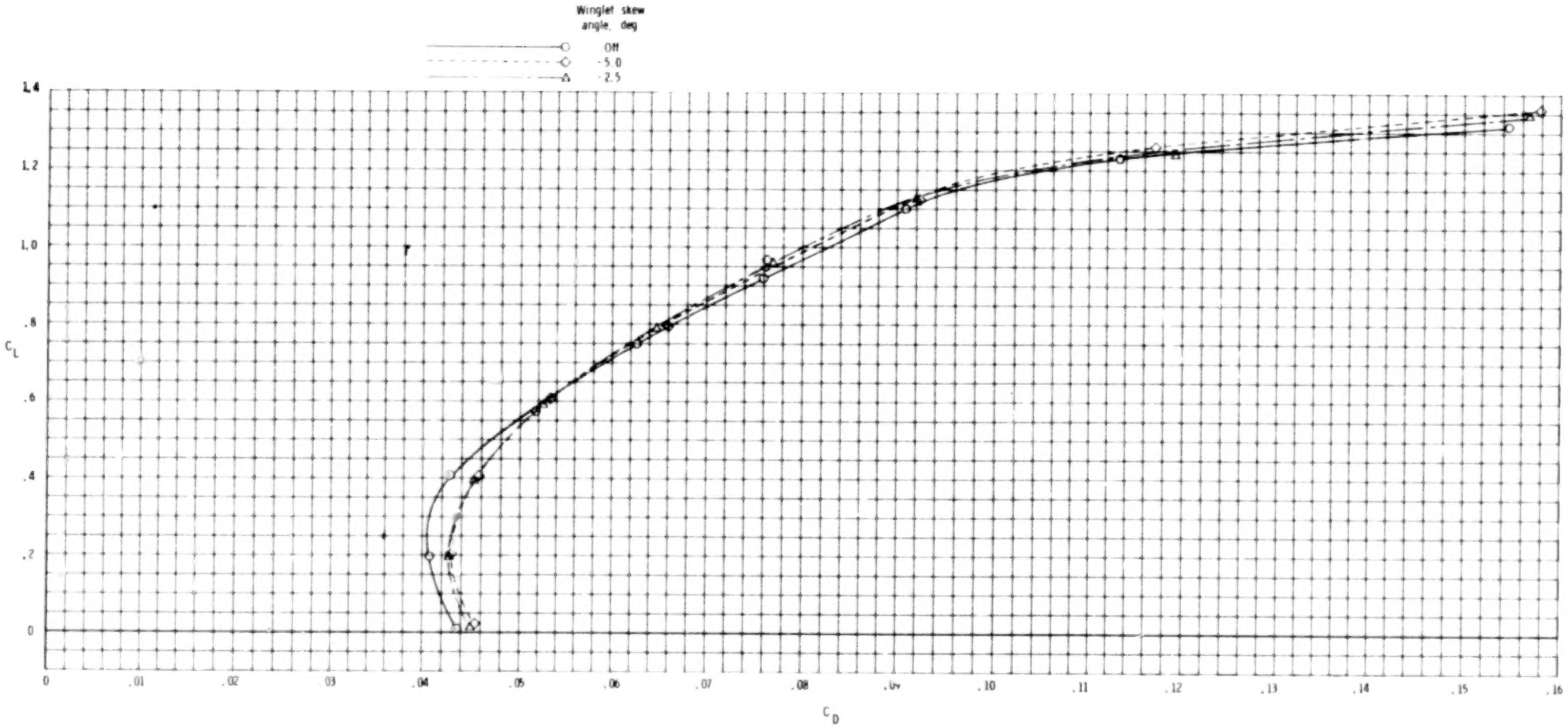

(b) Expanded lift-drag polars.

Figure 43.- Concluded.

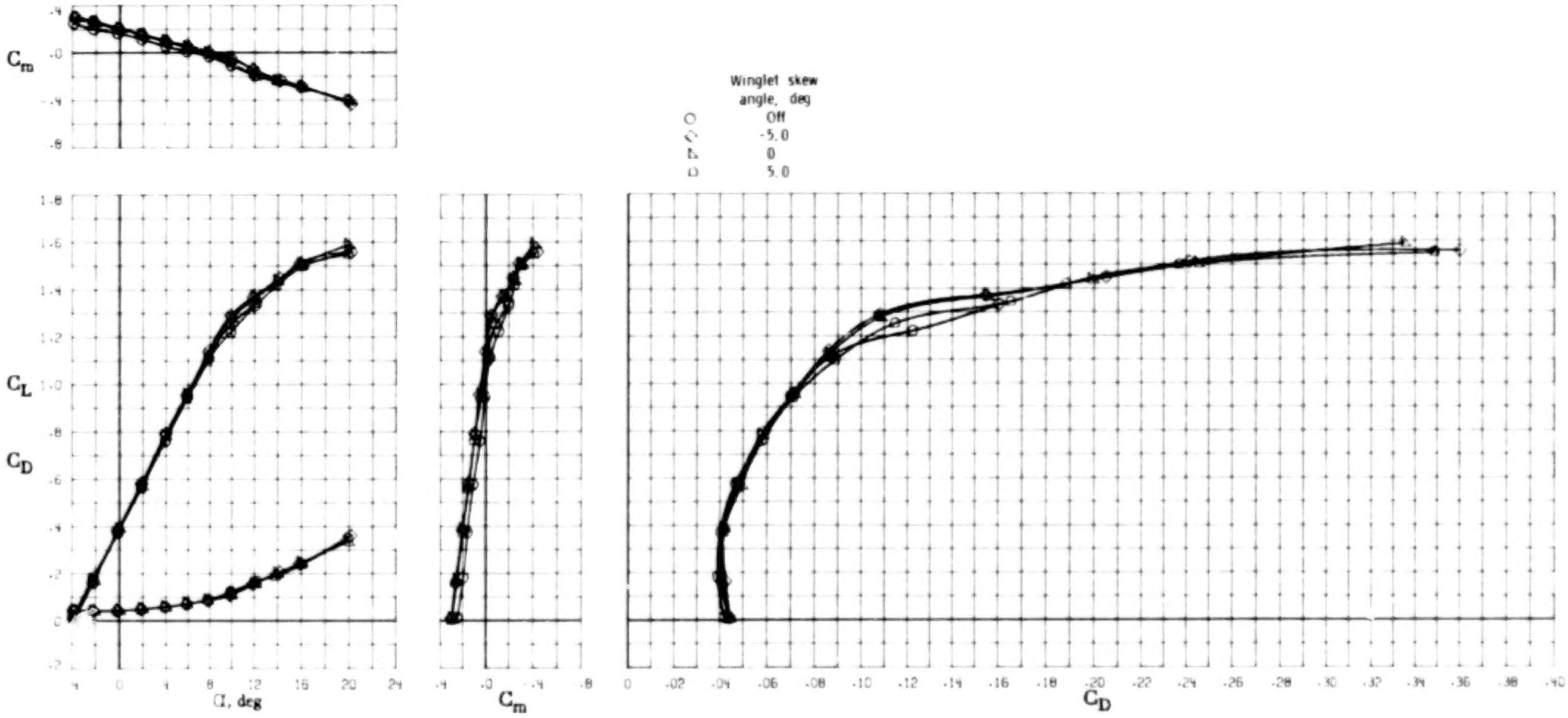

(a) Longitudinal characteristics.

Figure 44.- Effect of winglet skew angle for winglet cant angle of 10° at $R = 3.50 \times 10^6$.

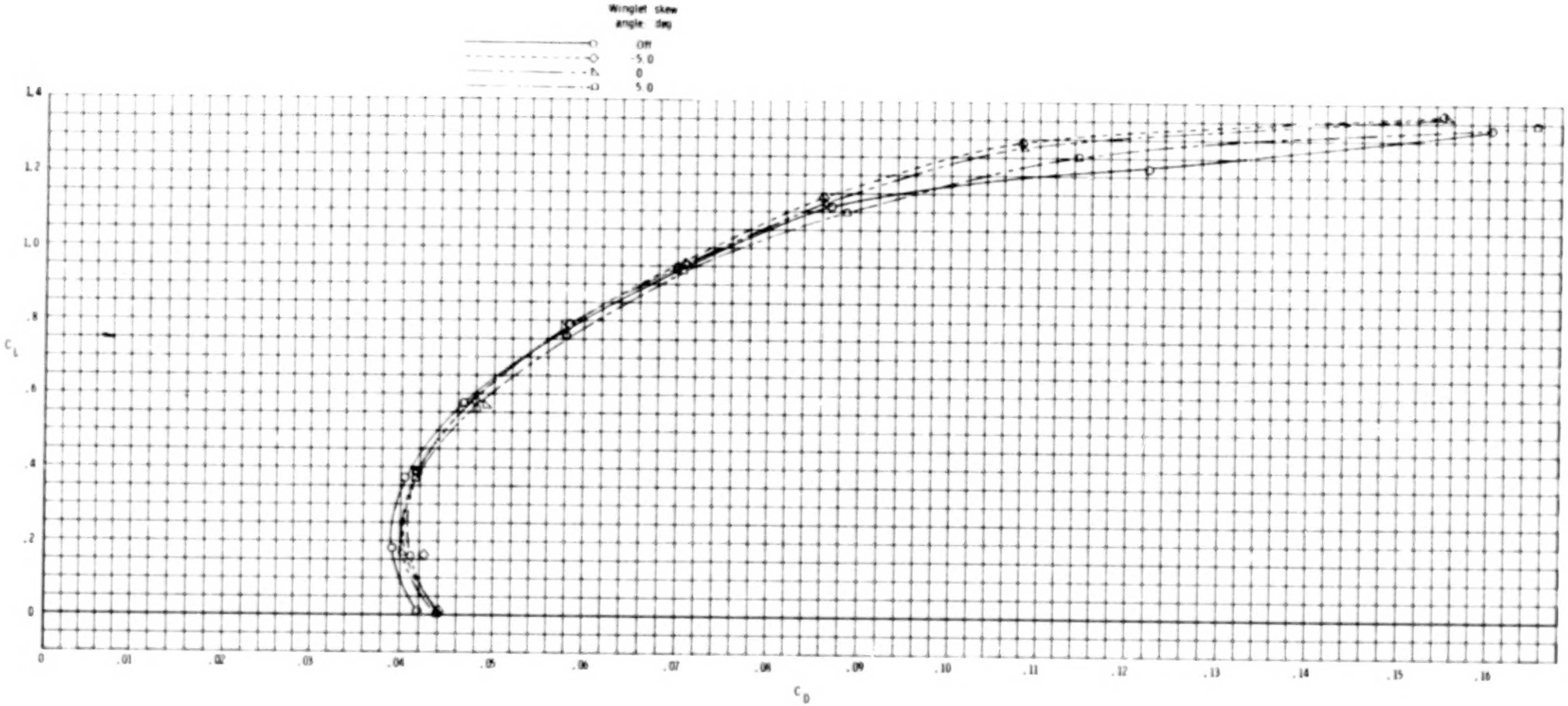

(b) Expanded lift-drag polars.

Figure 44.- Concluded.

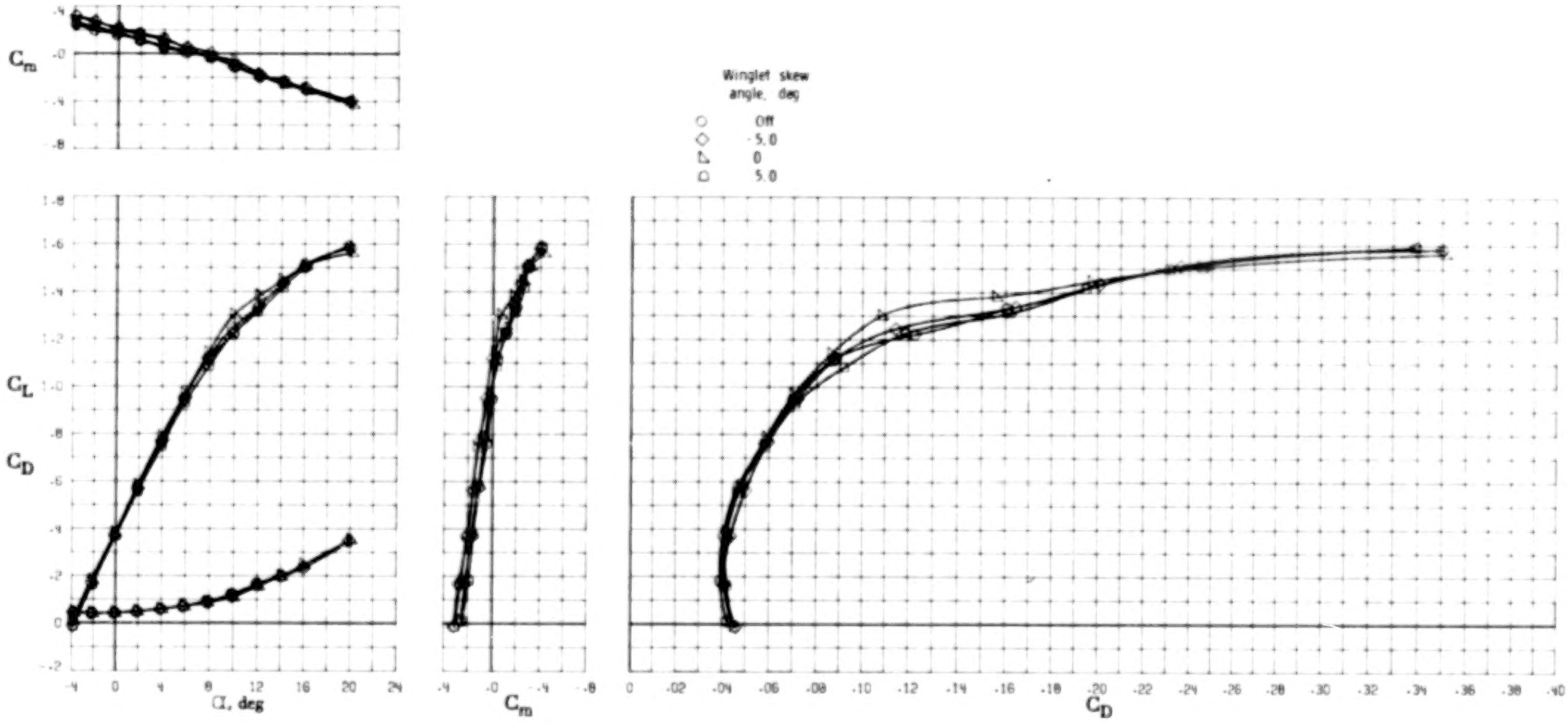

(a) Longitudinal characteristics.

Figure 45.- Effect of winglet skew angle for winglet cant angle of 5° at $R = 3.50 \times 10^6$.

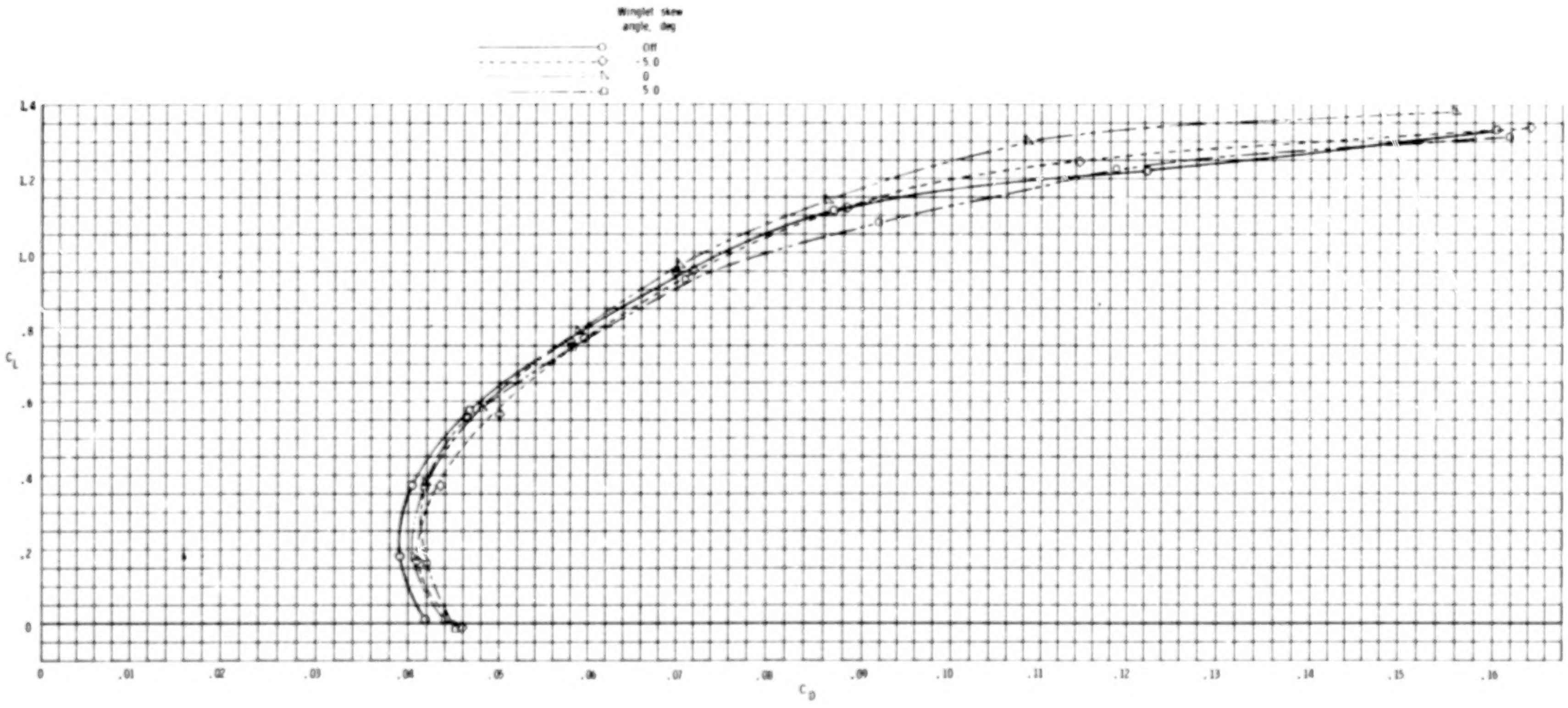

(b) Expanded lift-drag polars.

Figure 45.- Concluded.

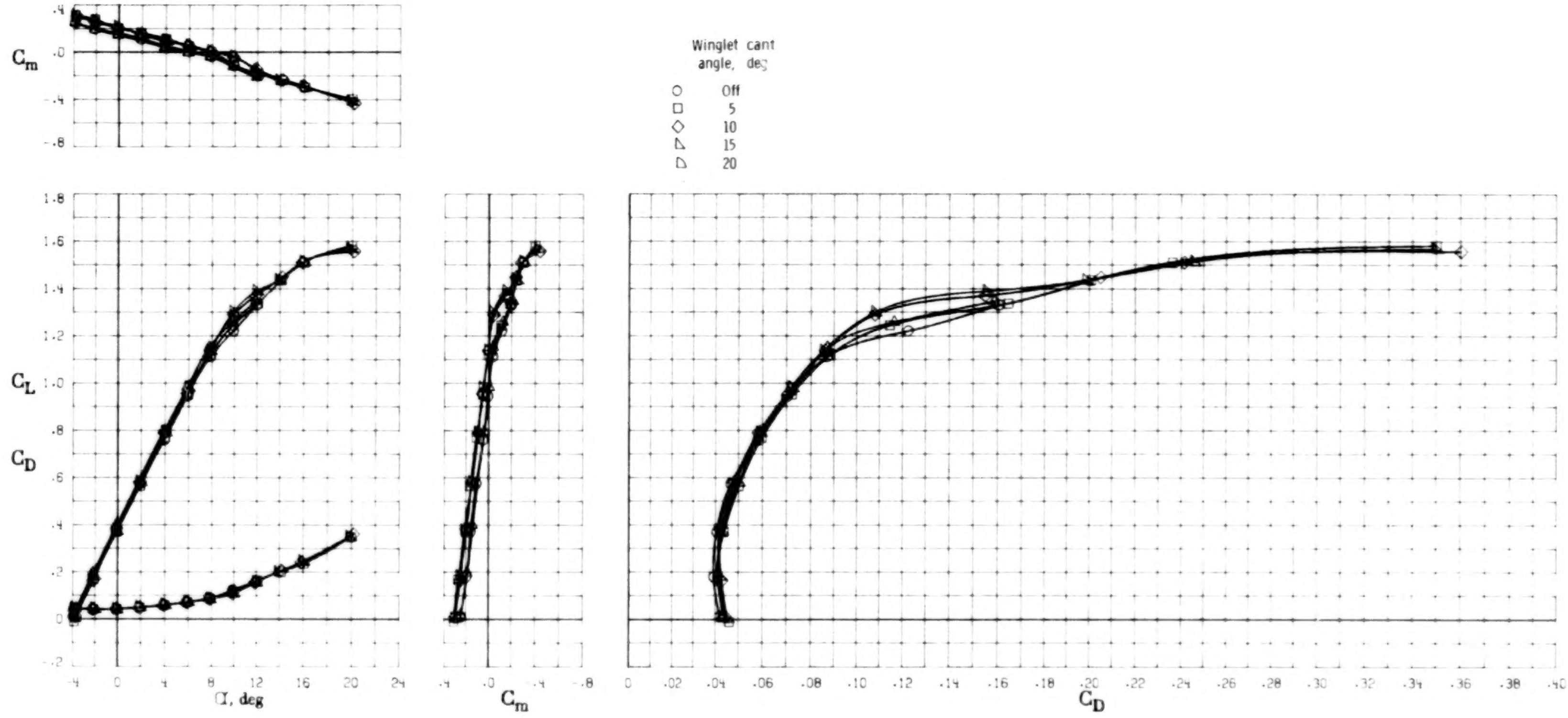

(a) Longitudinal characteristics.

Figure 46.- Effect of winglet cant angle for winglet skew angle of -5° at $R = 3.50 \times 10^{6}$.

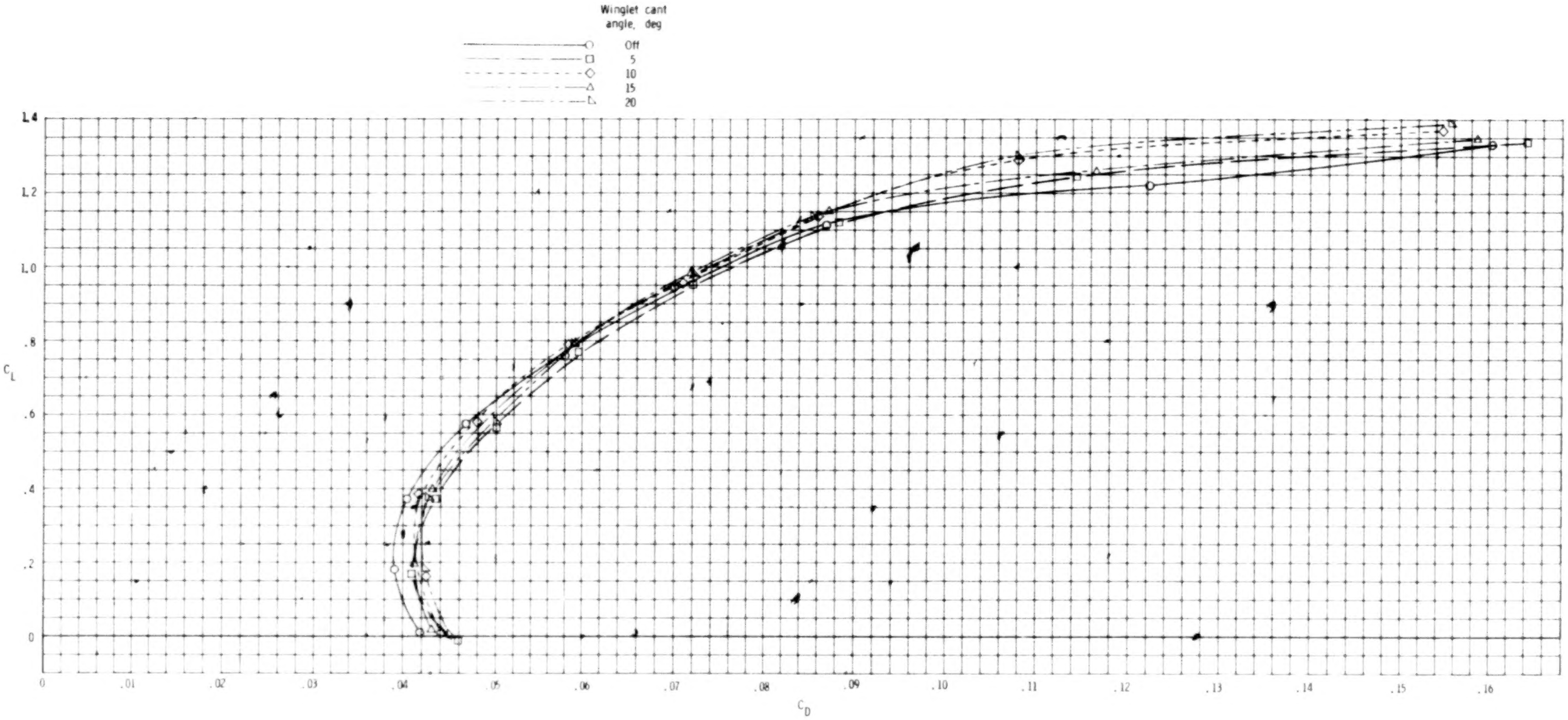

(b) Expanded lift-drag polars.

Figure 46.- Concluded.

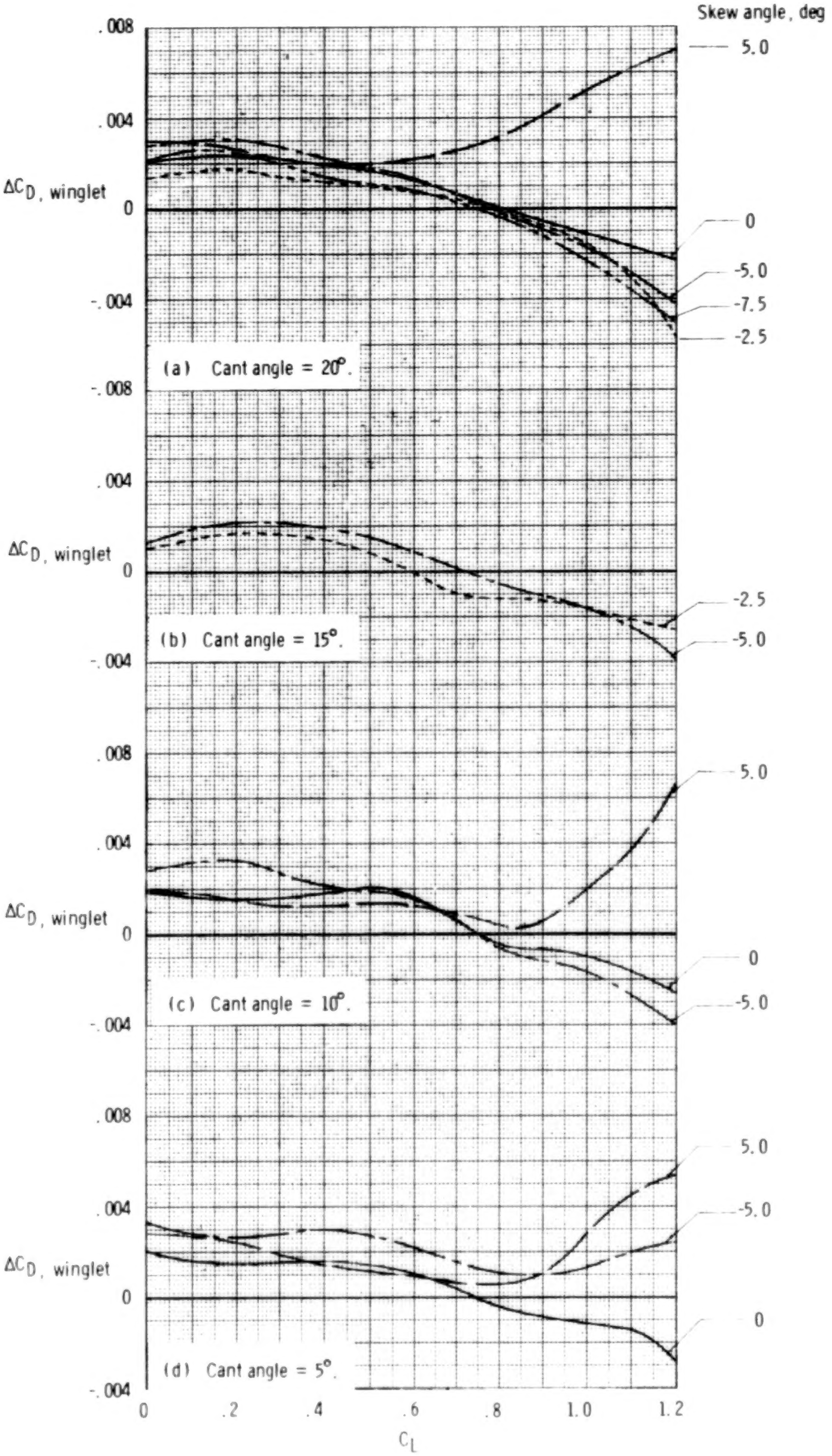

Figure 47.- Summary of effect of winglets at R = 3.50 × 10^6.

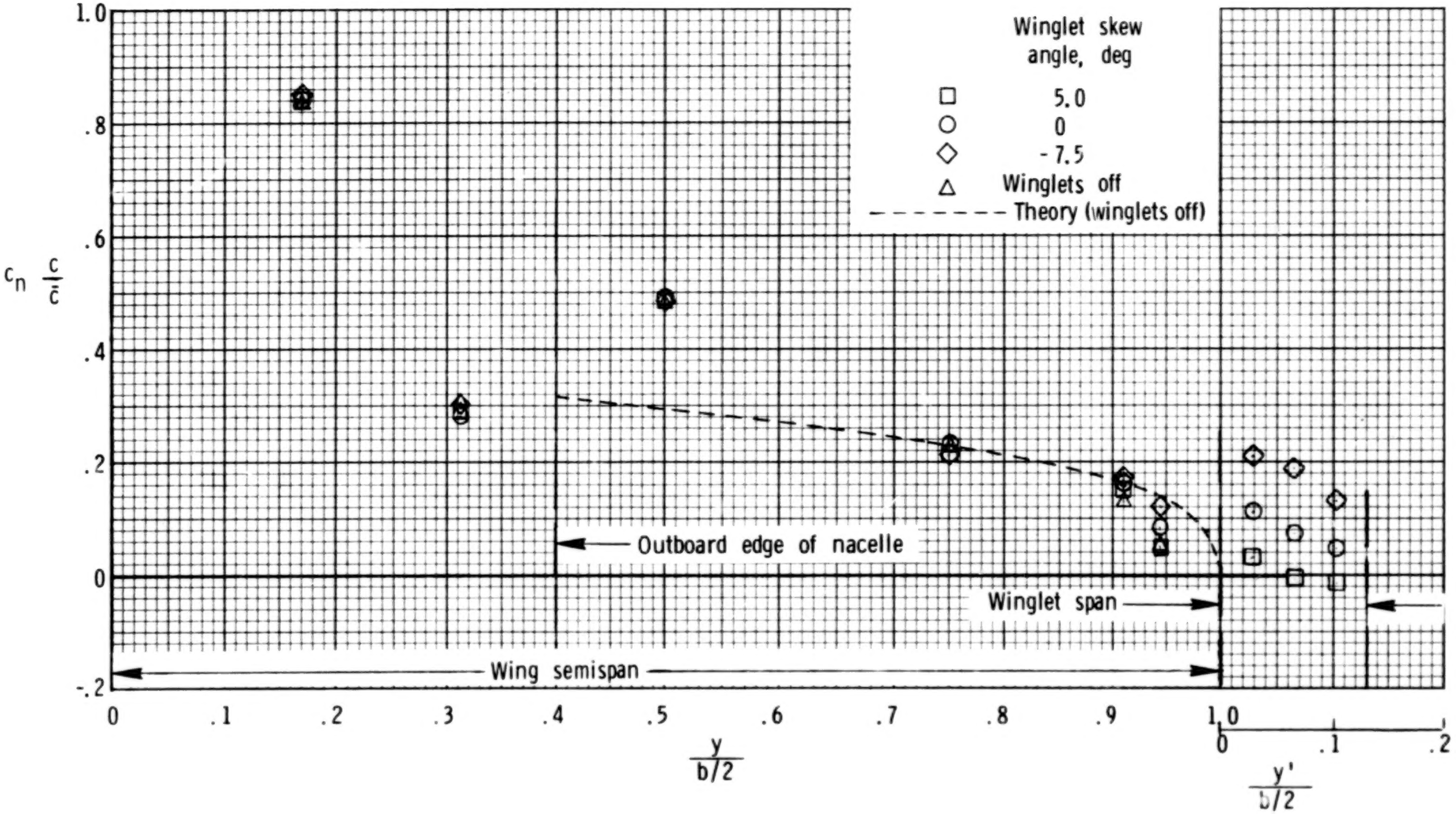

(a) Cruise condition; $\alpha = 0^{\circ}$; $C_L = 0.38$.

Figure 48.- Effect of winglet skew angle on span-load distribution. Winglet cant angle, 20°; $R = 3.50 \times 10^6$.

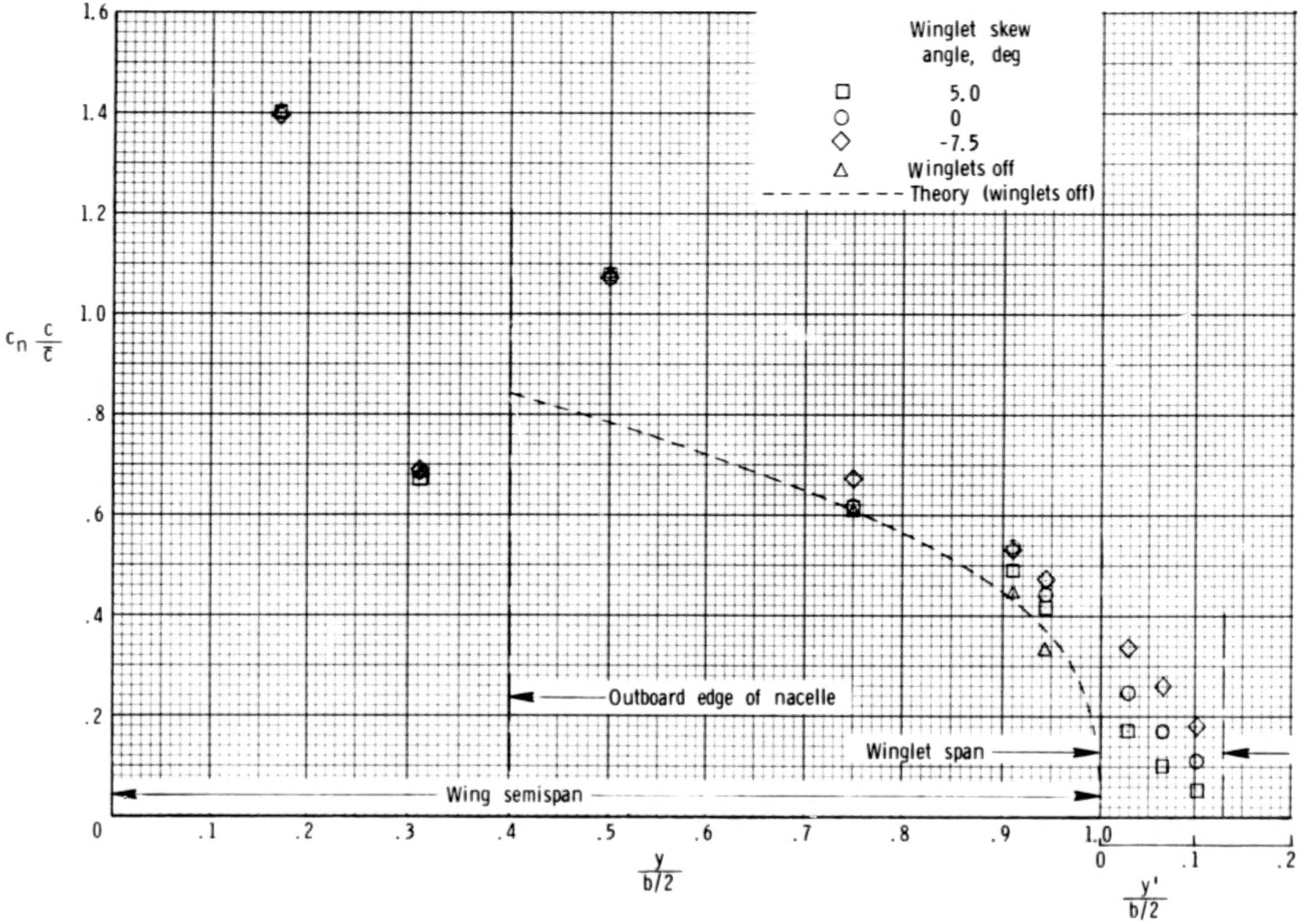

(b) Climb condition; $\alpha = 6.50^{\circ}$; $C_L = 1.00$.

Figure 48.- Concluded.

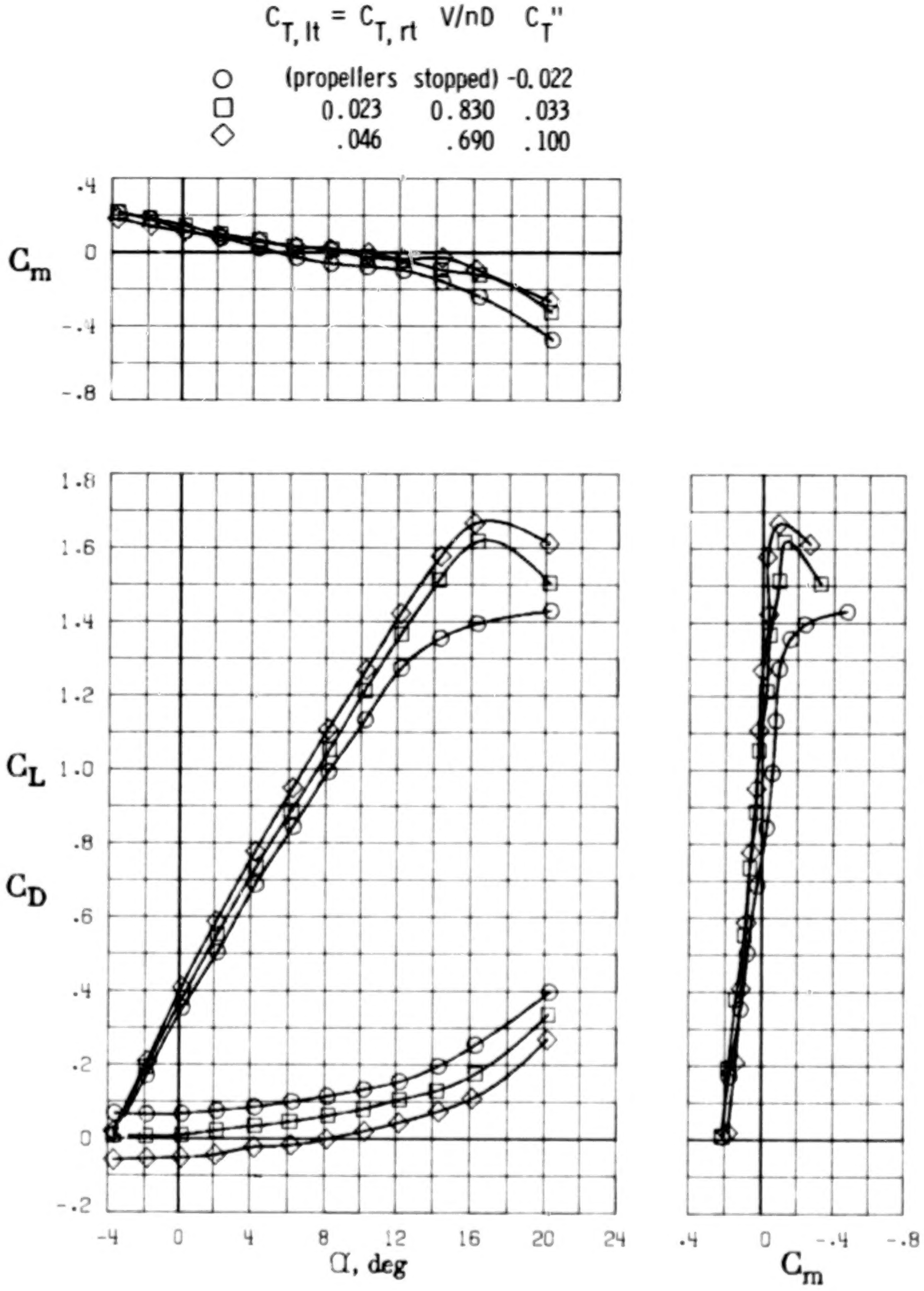

(a) $\delta_{stab} = 0^{\circ}$.

Figure 49.- Effect of power on longitudinal aerodynamic characteristics with $\delta_f = 0^{\circ}$. $R = 2.30 \times 10^6$.

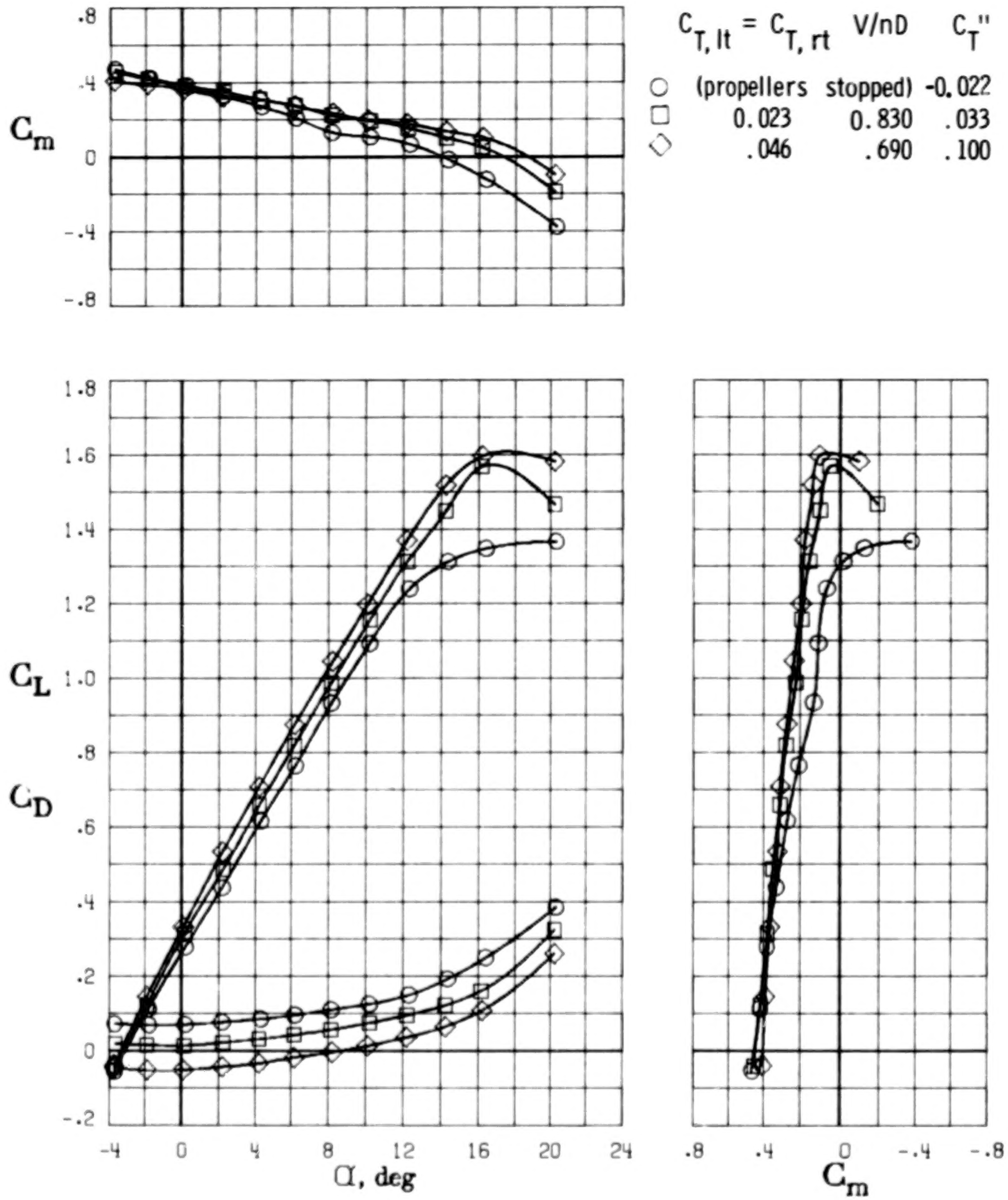

(b) $\delta_{stab} = -4^{\circ}$.

Figure 49.- Continued.

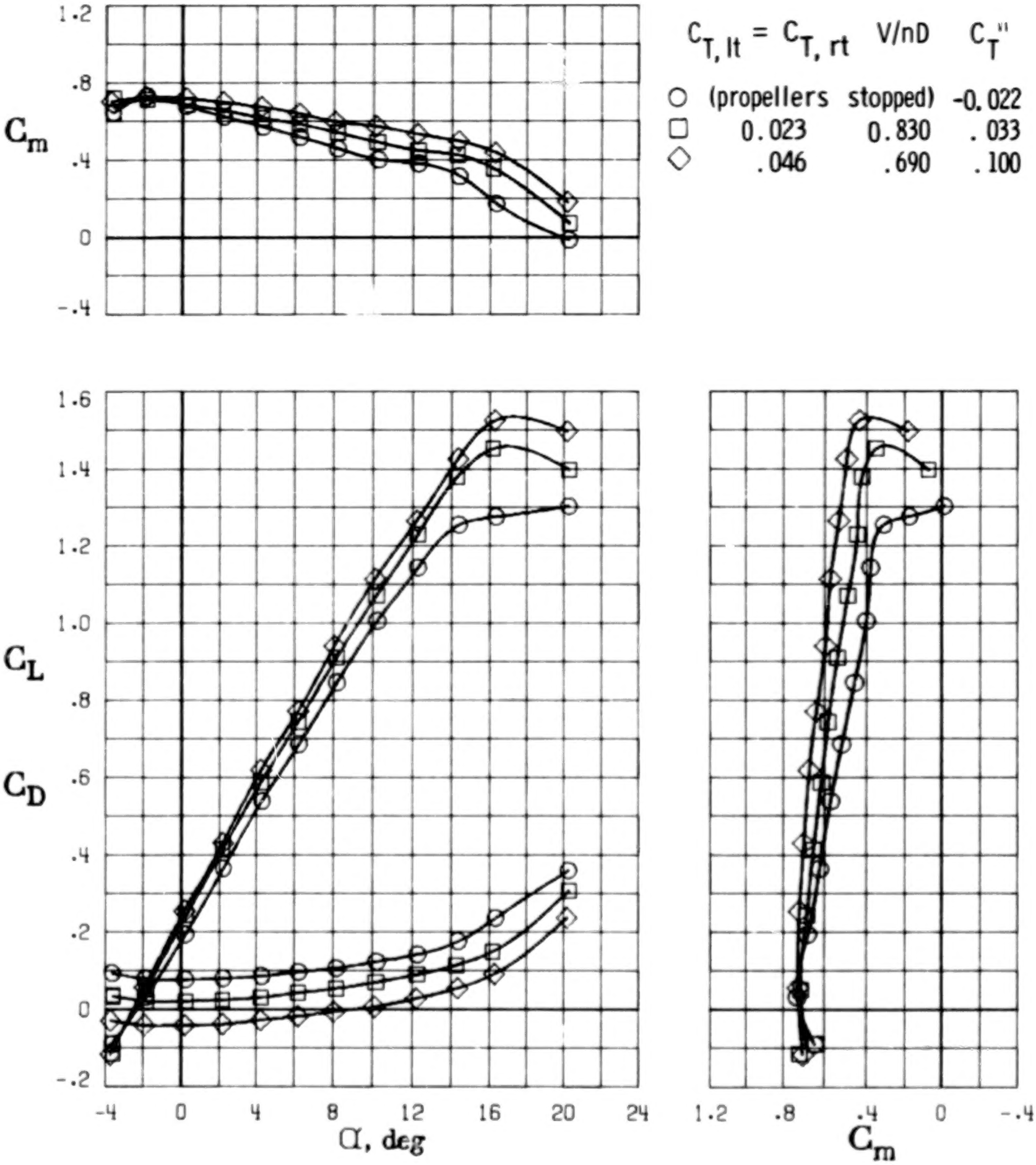

(c) $\delta_{stab} = -8^{\circ}$.

Figure 49.- Continued.

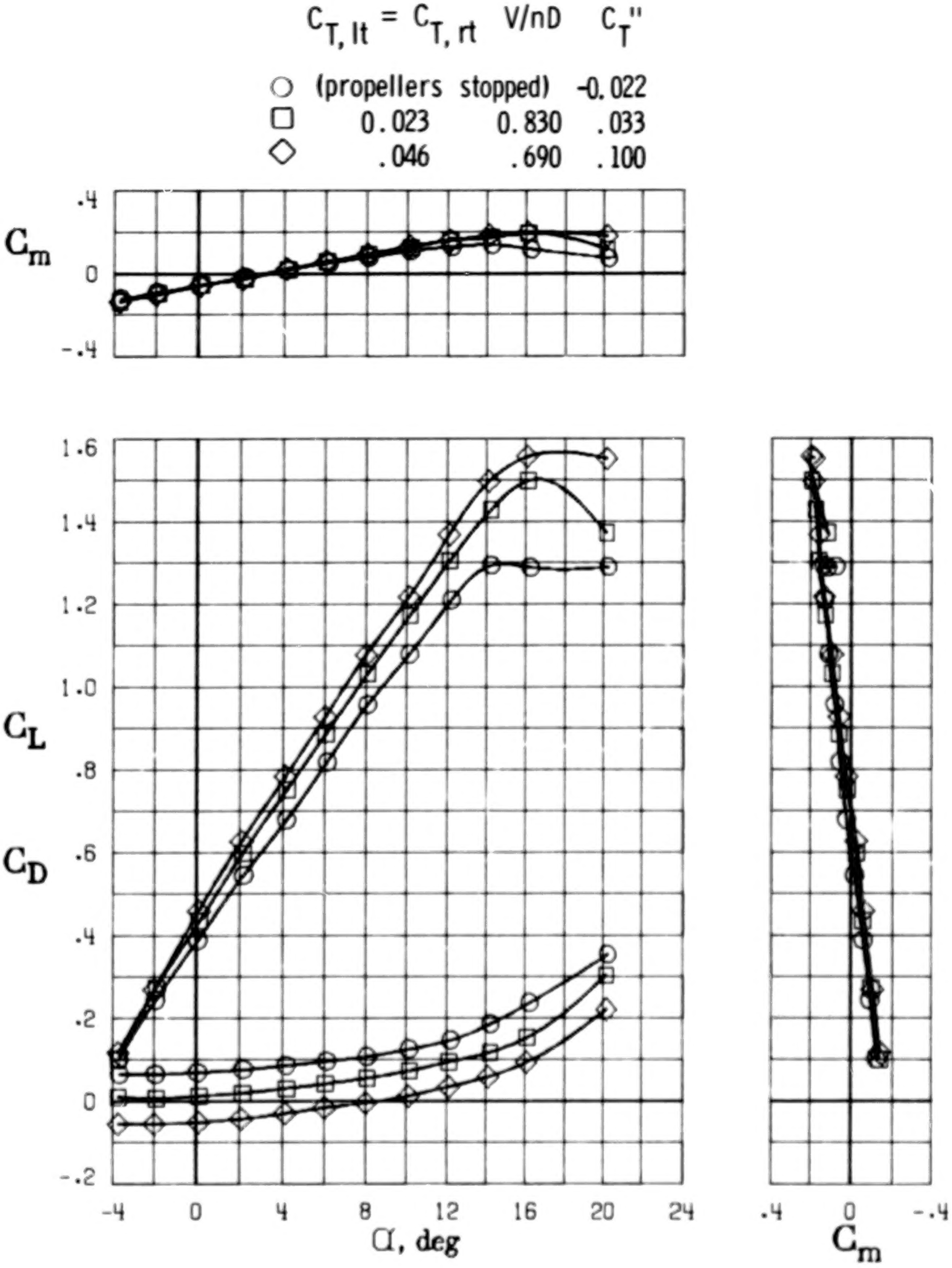

(d) Horizontal tail off.

Figure 49.- Concluded.

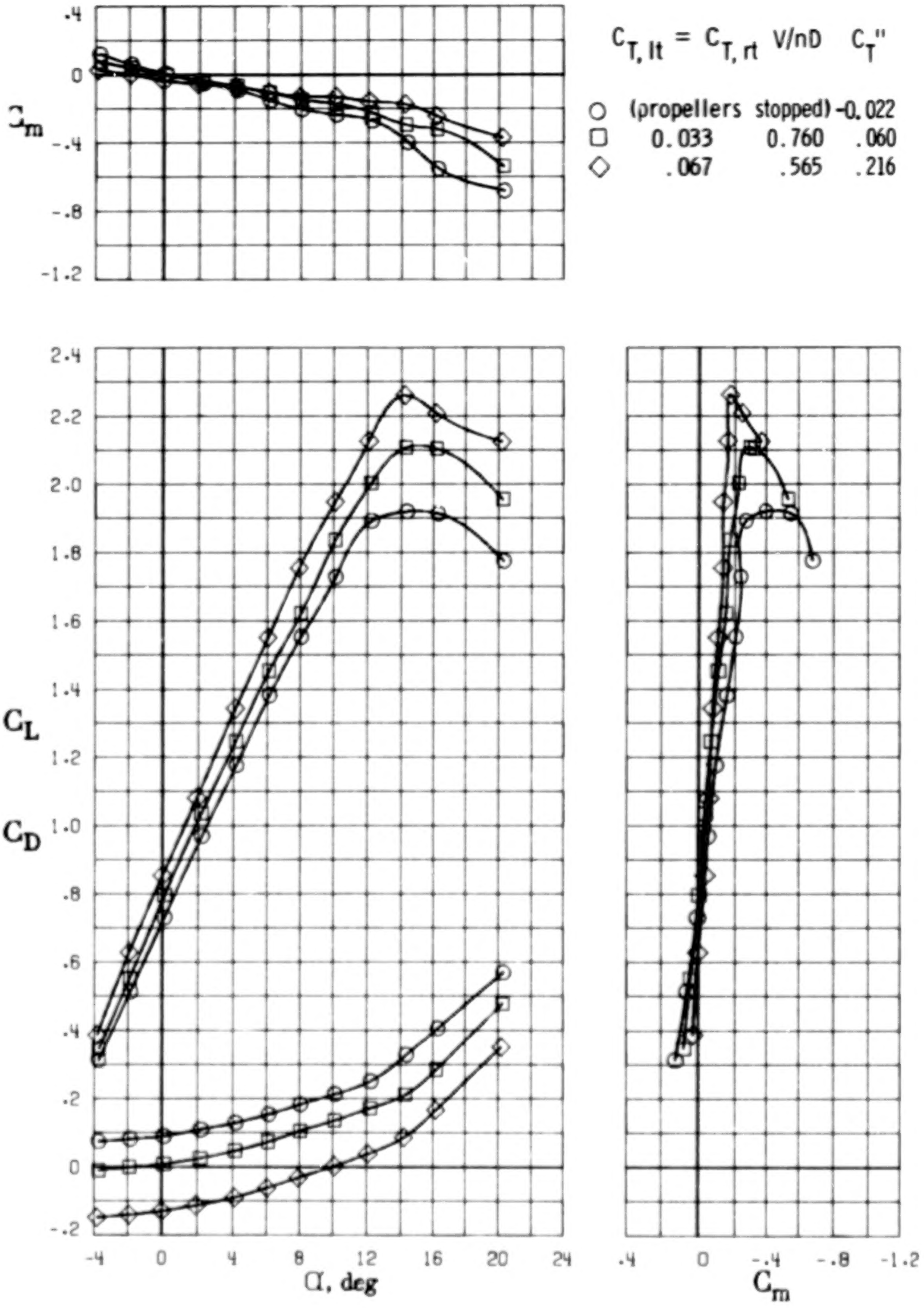

(a) $\delta_{stab} = 0^{\circ}$.

Figure 50.- Effect of power on longitudinal aerodynamic characteristics with $\delta_f = 10^{\circ}$. $R = 2.30 \times 10^6$.

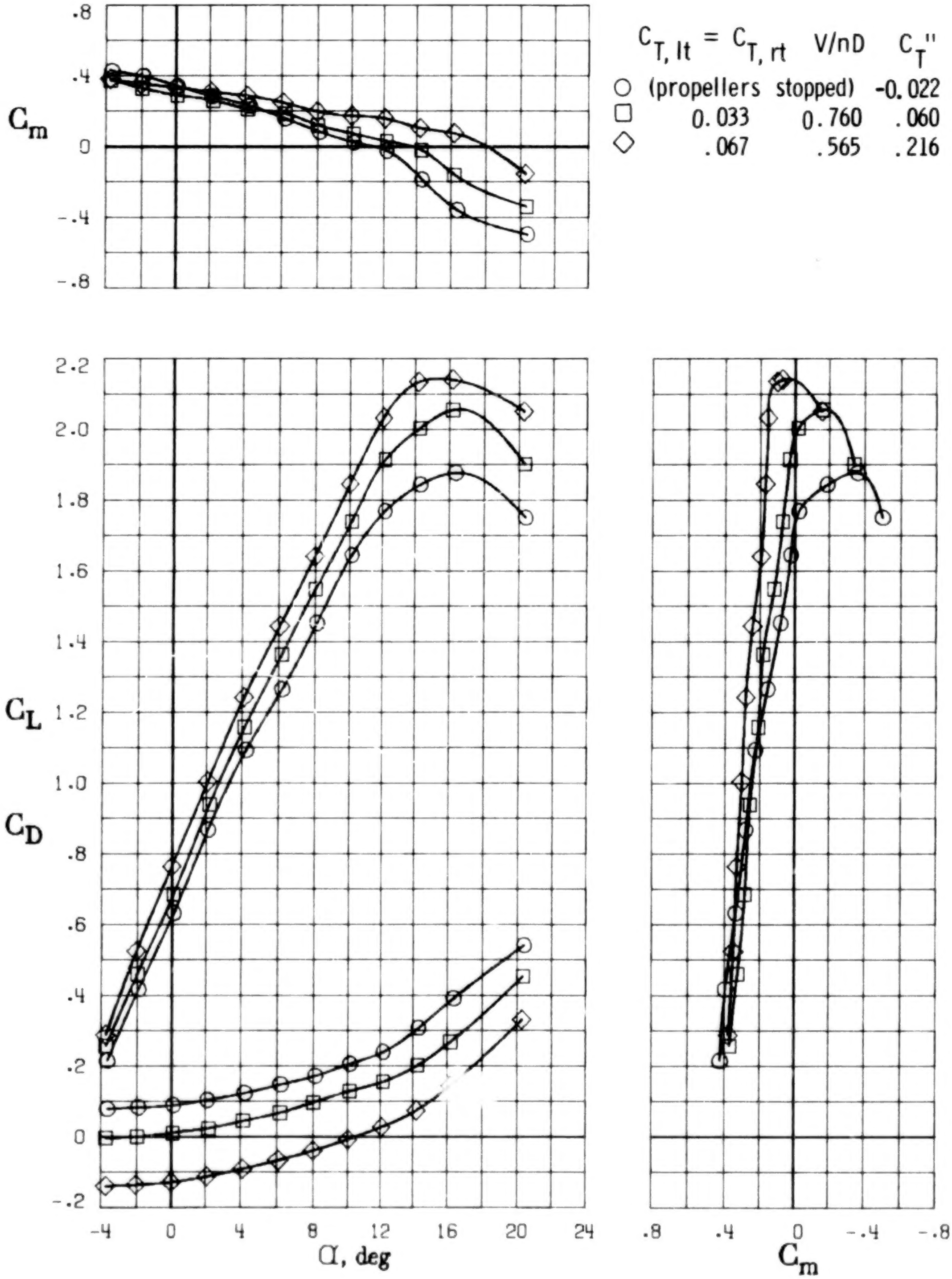

(b) $\delta_{stab} = -4^{\circ}$.

Figure 50.- Continued.

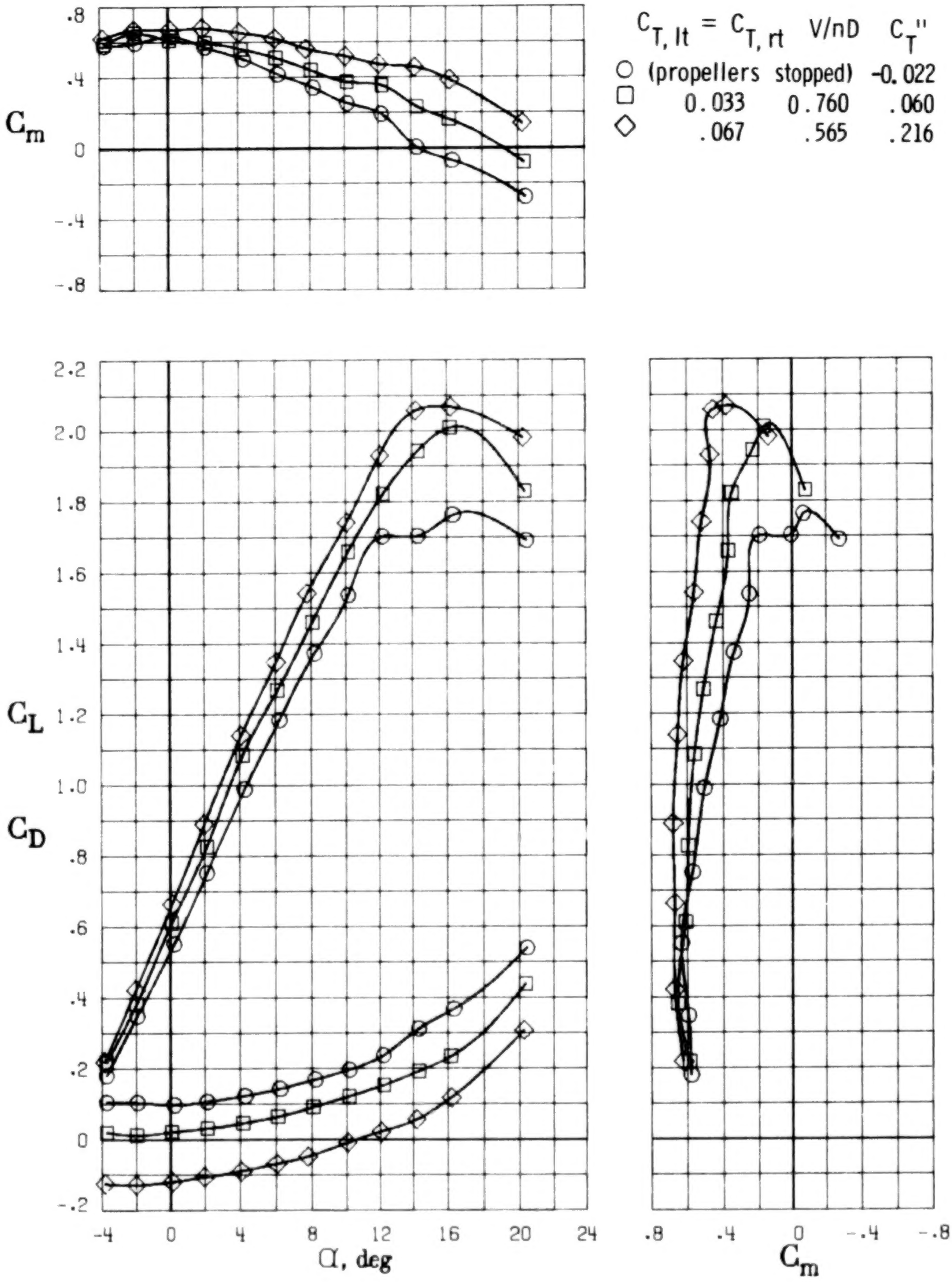

(c) $\delta_{stab} = -8^{\circ}$.

Figure 50.- Continued.

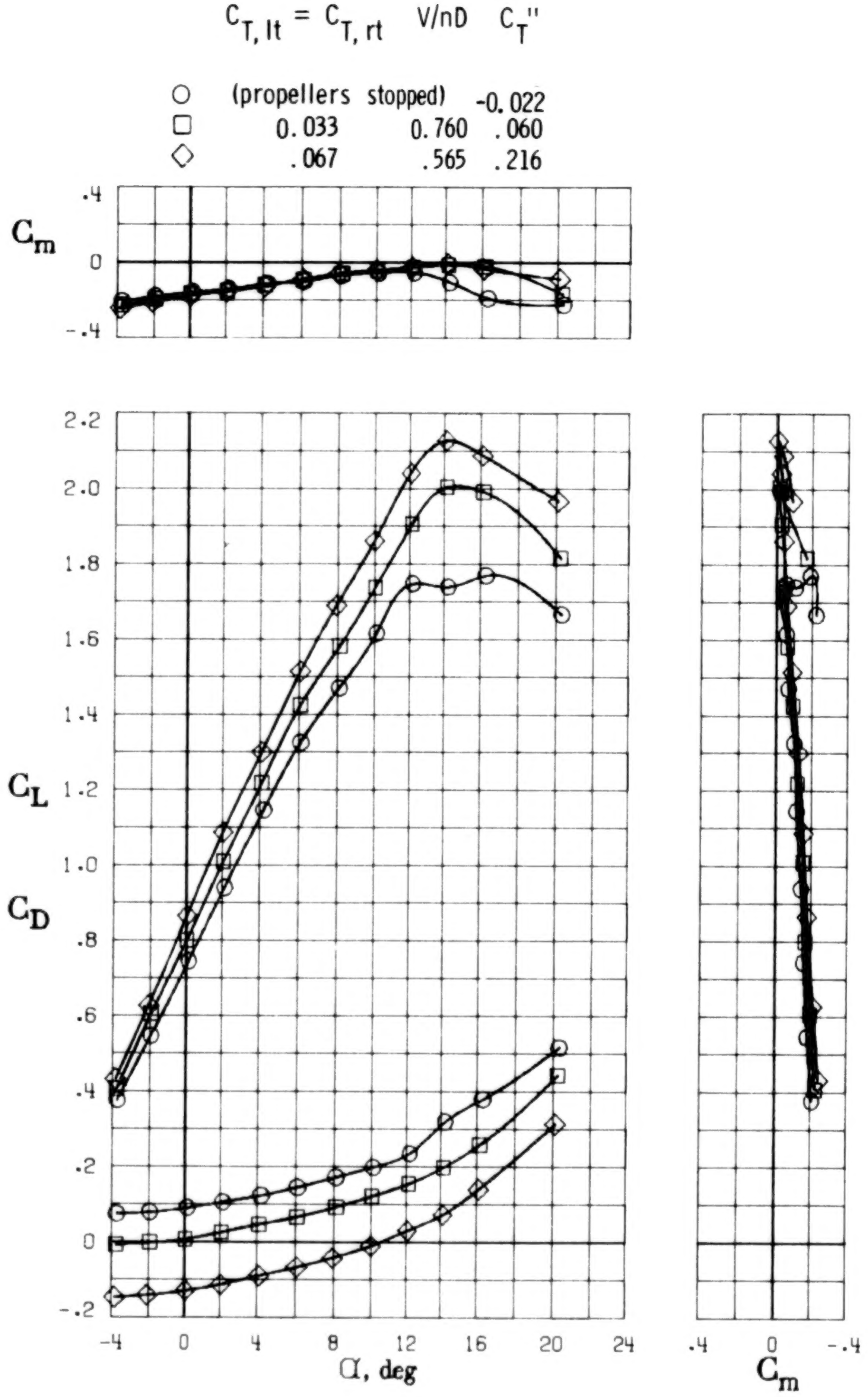

(d) Horizontal tail off.

Figure 50.- Concluded.

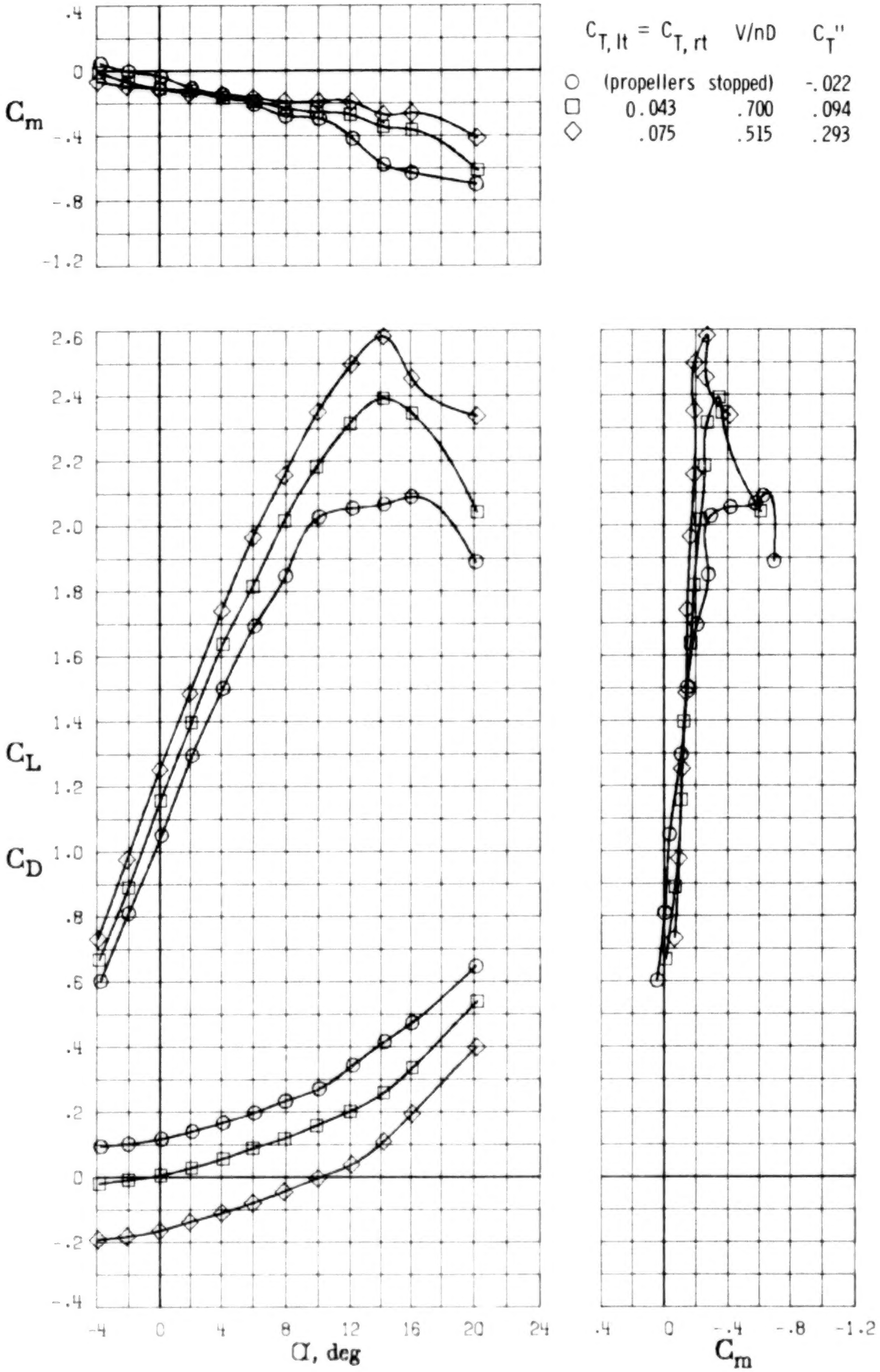

(a) $\delta_{stab} = 0^{\circ}$.

Figure 51.- Effect of power on longitudinal aerodynamic characteristics with $\delta_f = 20^{\circ}$. $R = 2.30 \times 10^6$.

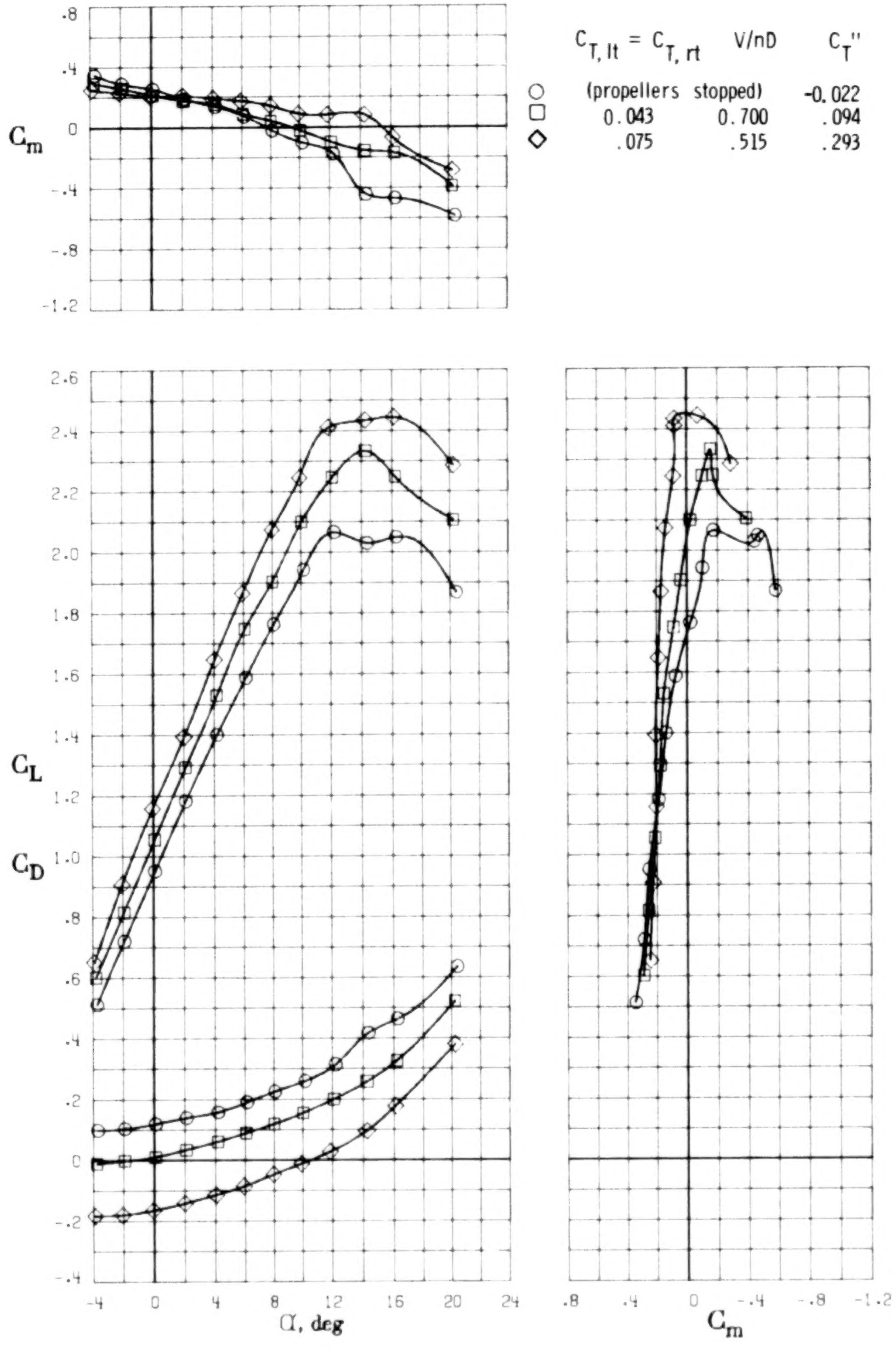

(b) $\delta_{stab} = -4^{\circ}$.

Figure 51.- Continued.

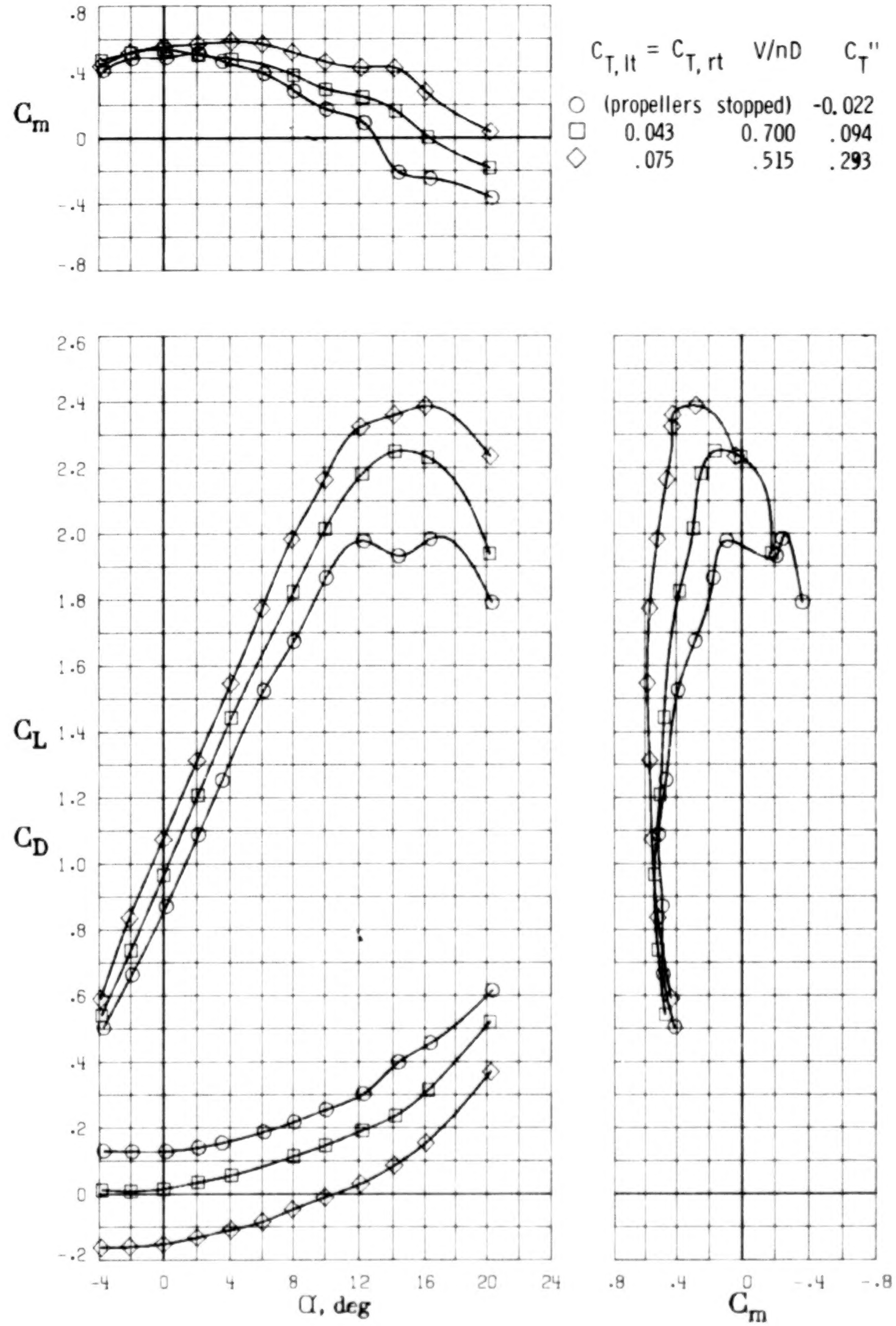

(c) $\delta_{stab} = -8^{\circ}$.

Figure 51.- Continued.

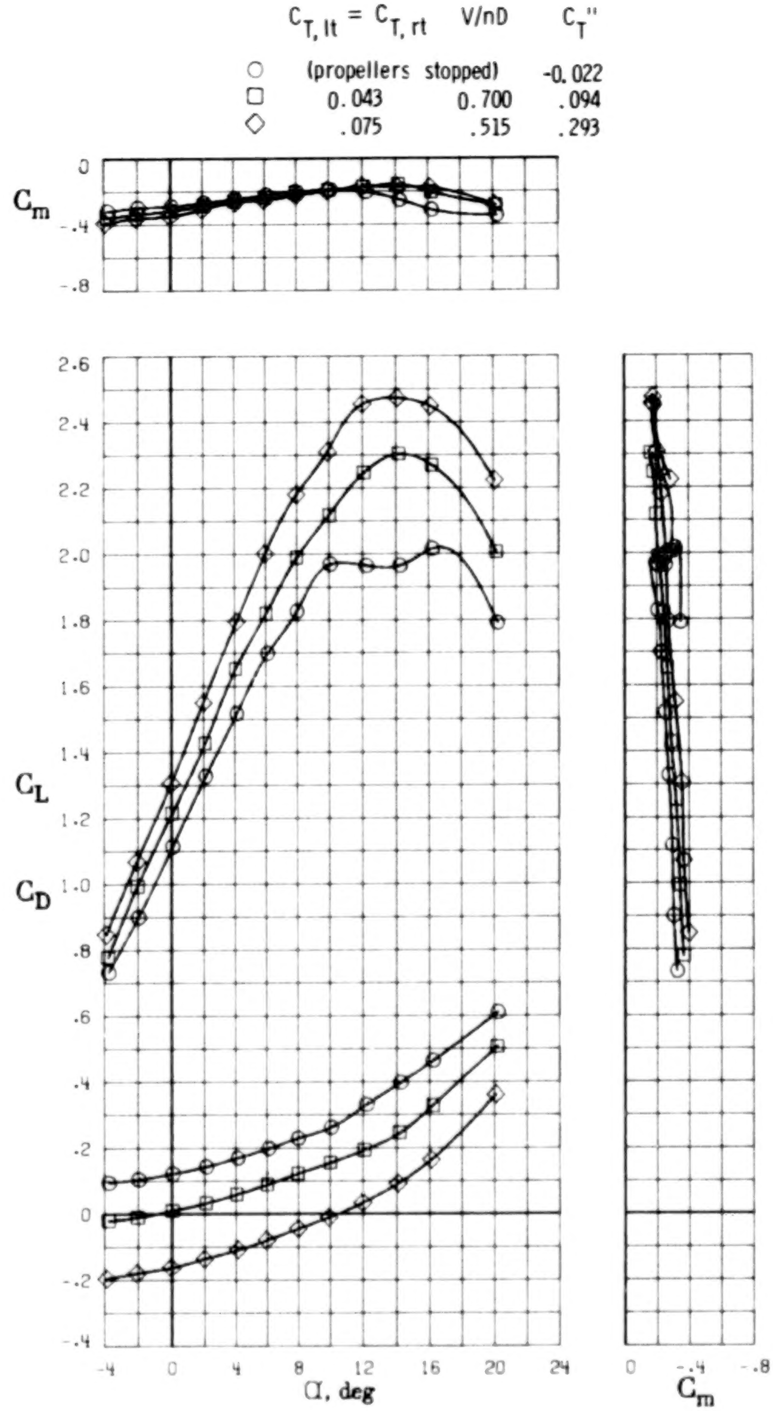

(d) Horizontal tail off.

Figure 51.- Concluded.

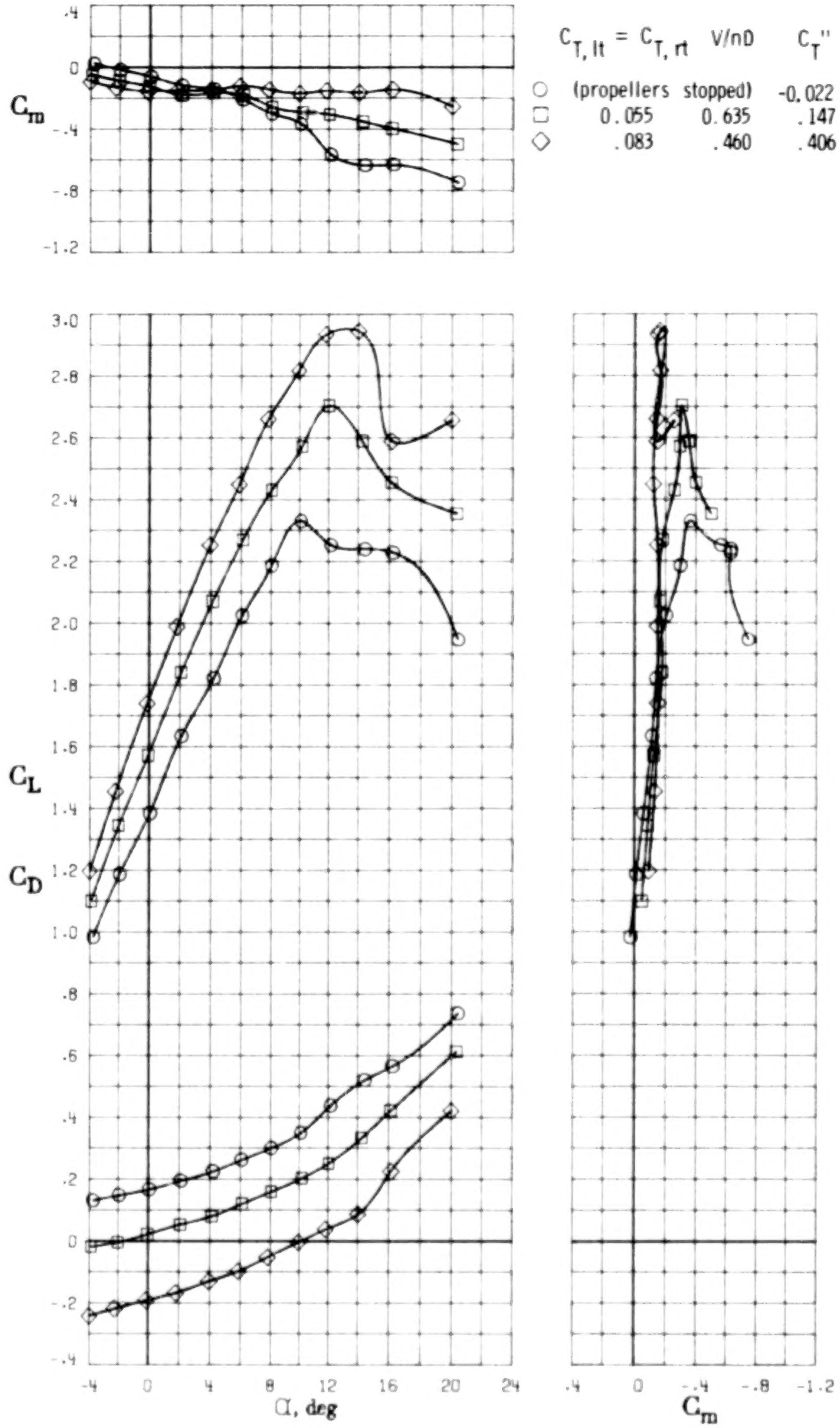

(a) $\delta_{stab} = 0^{\circ}$.

Figure 52.- Effect of power on longitudinal aerodynamic characteristics with $\delta_f = 30^{\circ}$. $R = 2.30 \times 10^6$.

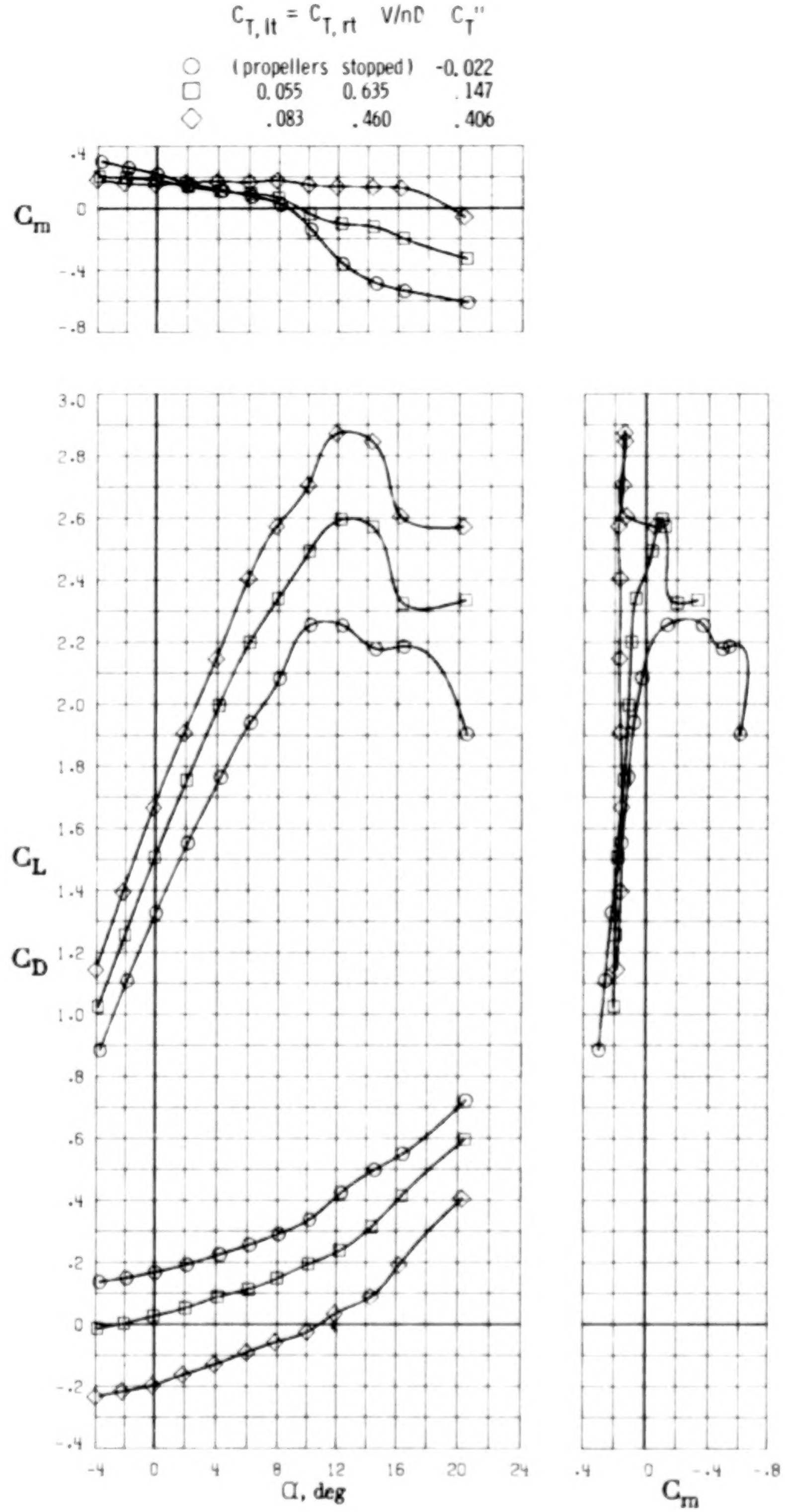

(b) $\delta_{stab} = -4^{\circ}$.

Figure 52.- Continued.

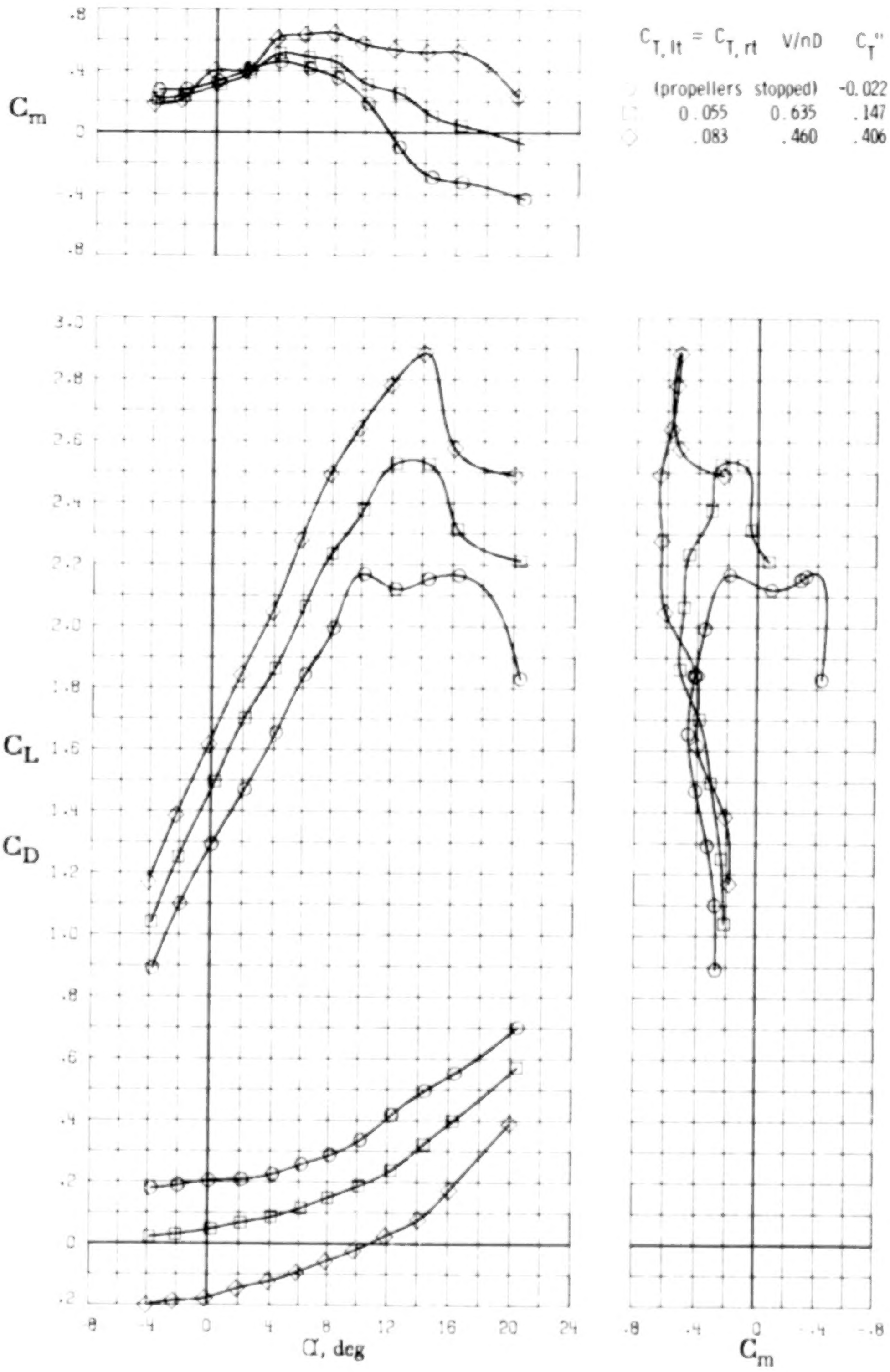

(c) $\delta_{stab} = -8^{\circ}$.

Figure 52.- Continued.

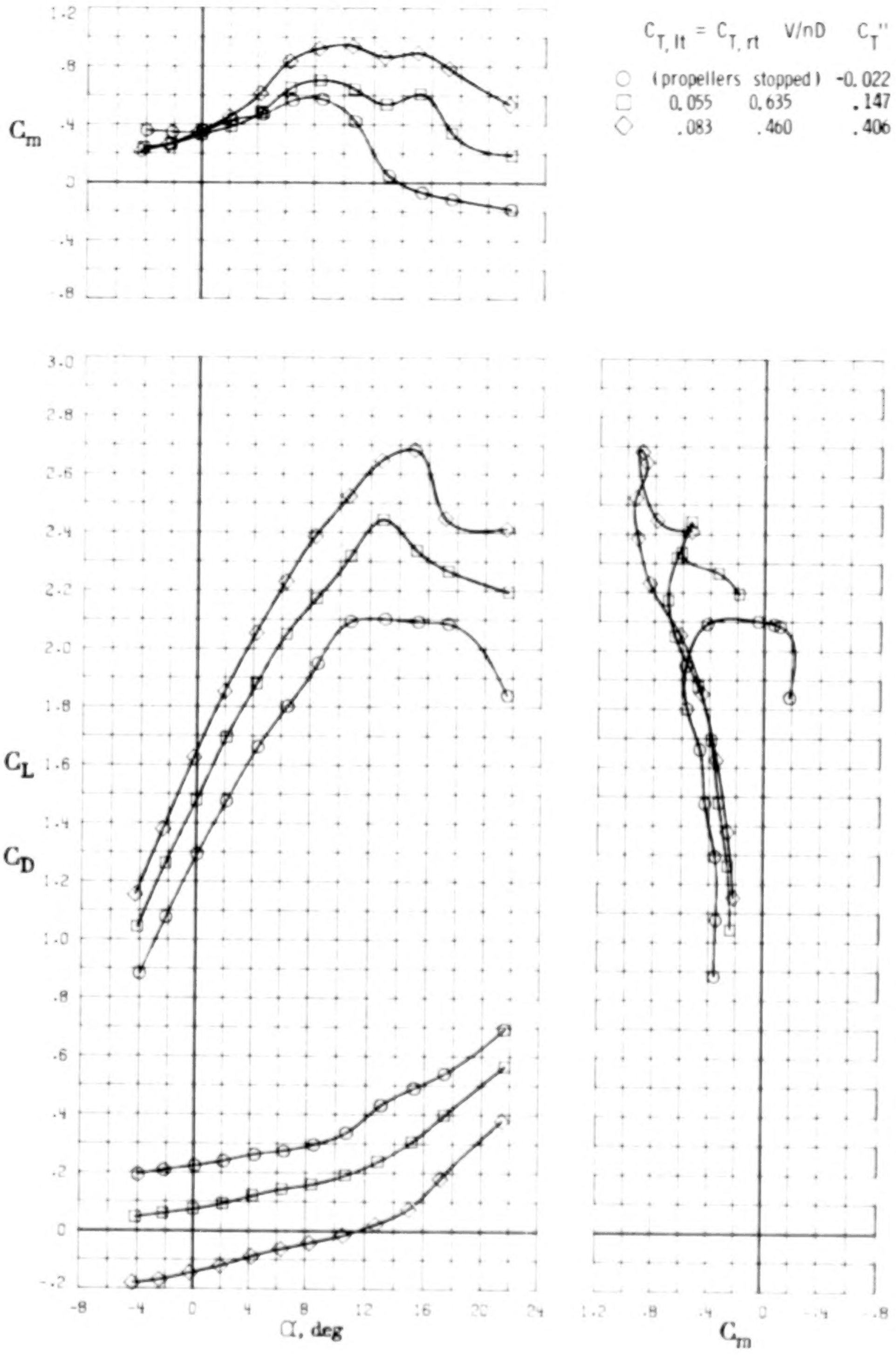

(d) $\delta_{stab} = -12^{\circ}$.

Figure 52.- Continued.

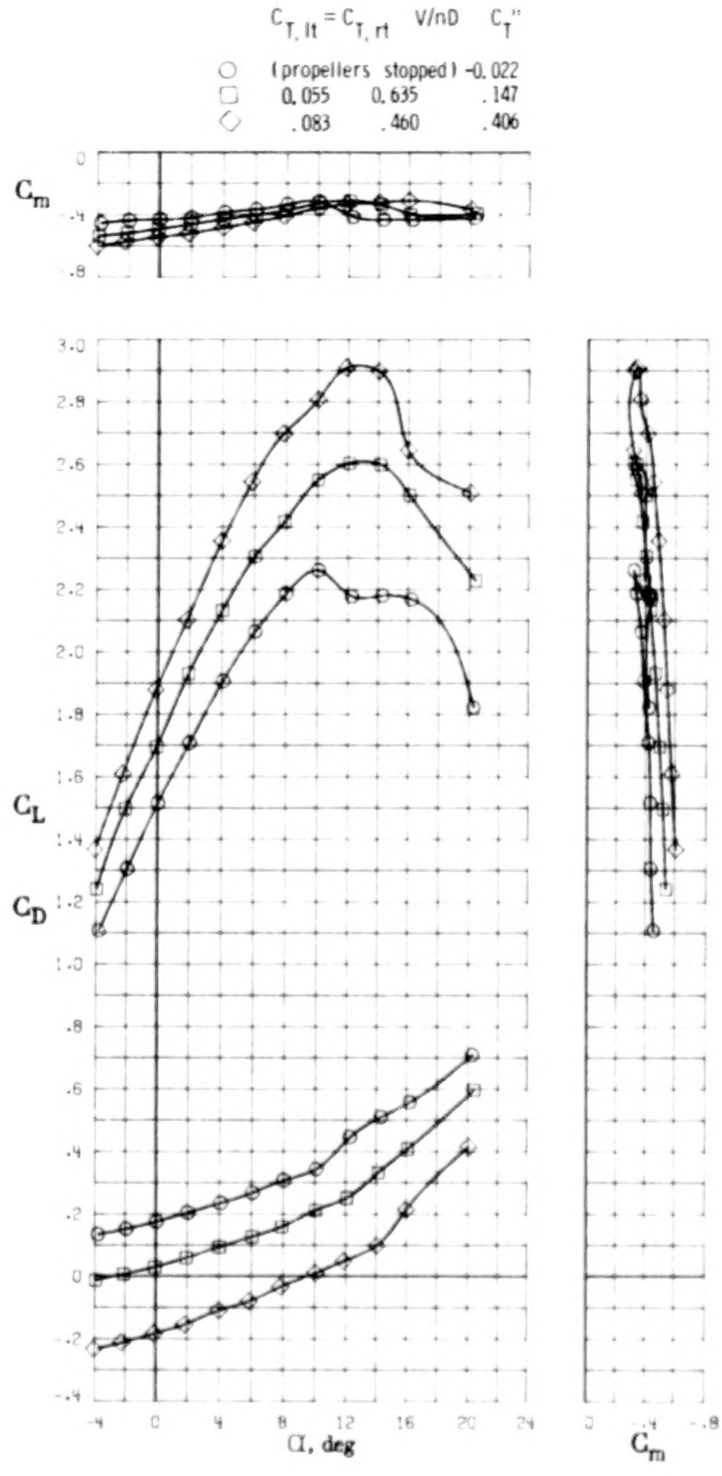

(e) Horizontal tail off.

Figure 52.- Concluded.

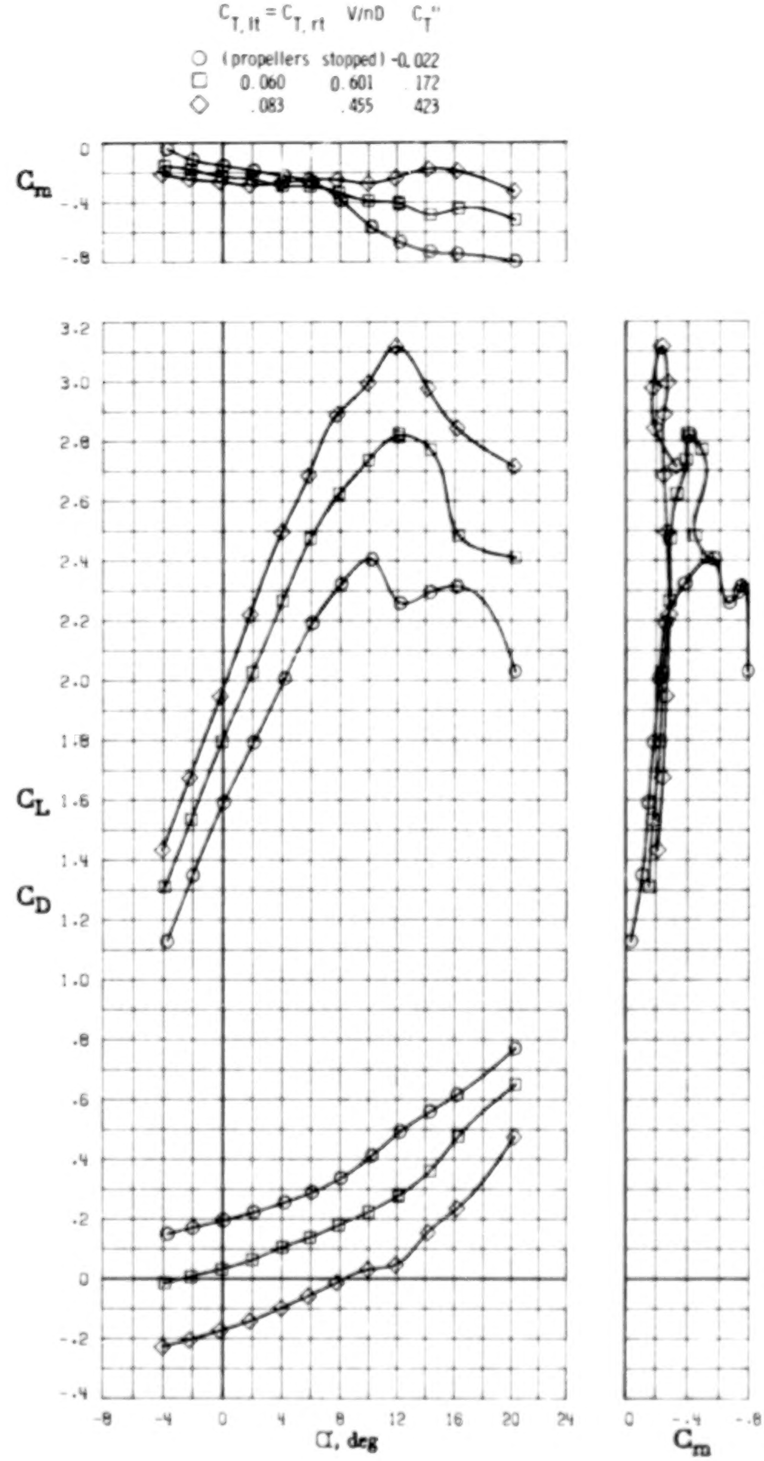

(a) $\delta_{stab} = 0^\circ$; aft center of gravity $(0.25\bar{c})$.

Figure 53.- Effect of power on longitudinal aerodynamic characteristics with $\delta_f = 37^\circ$. $R = 2.30 \times 10^6$.

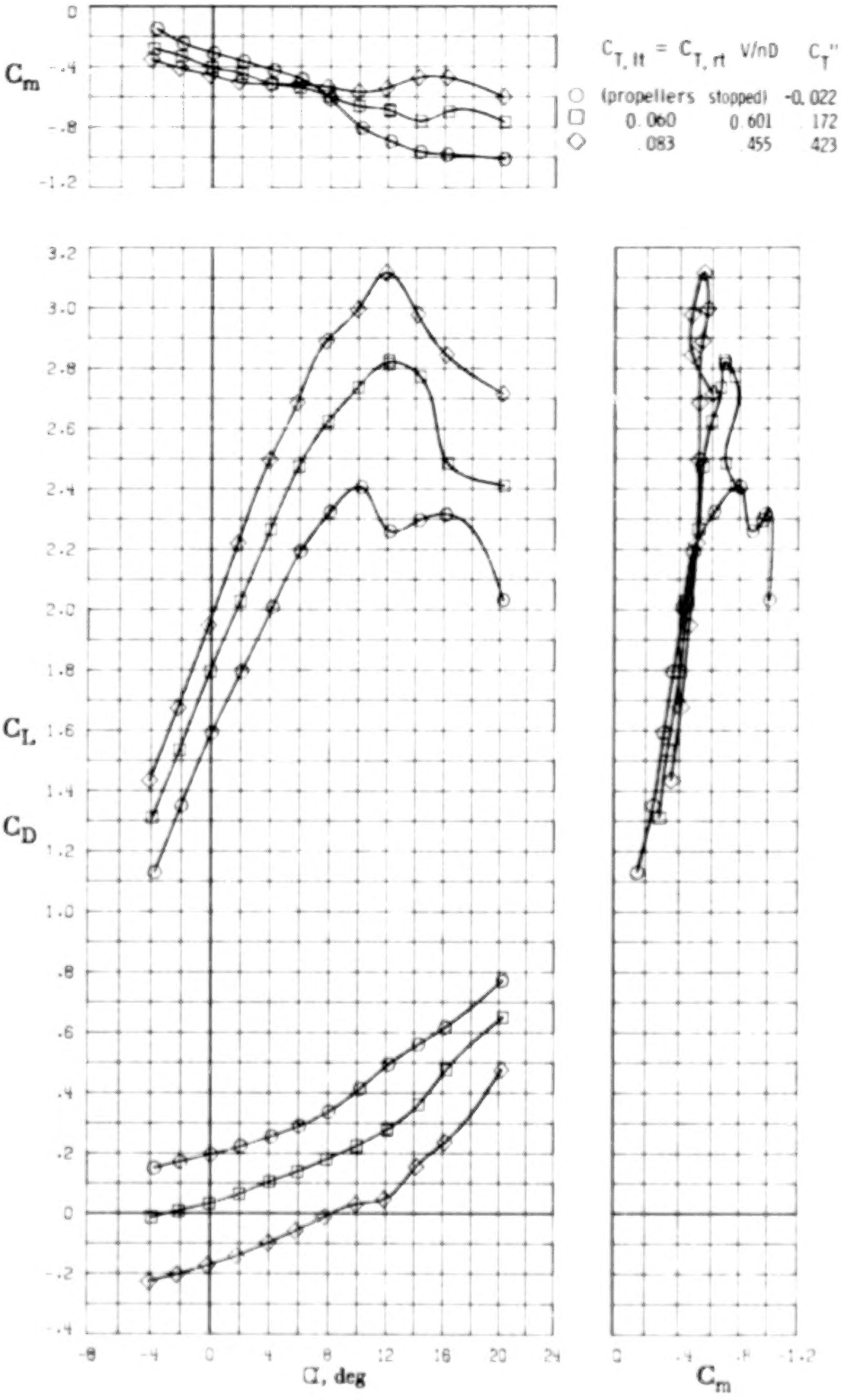

(b) $\delta_{stab} = 0^\circ$; forward center of gravity $(0.15\bar{c})$.

Figure 53.- Continued.

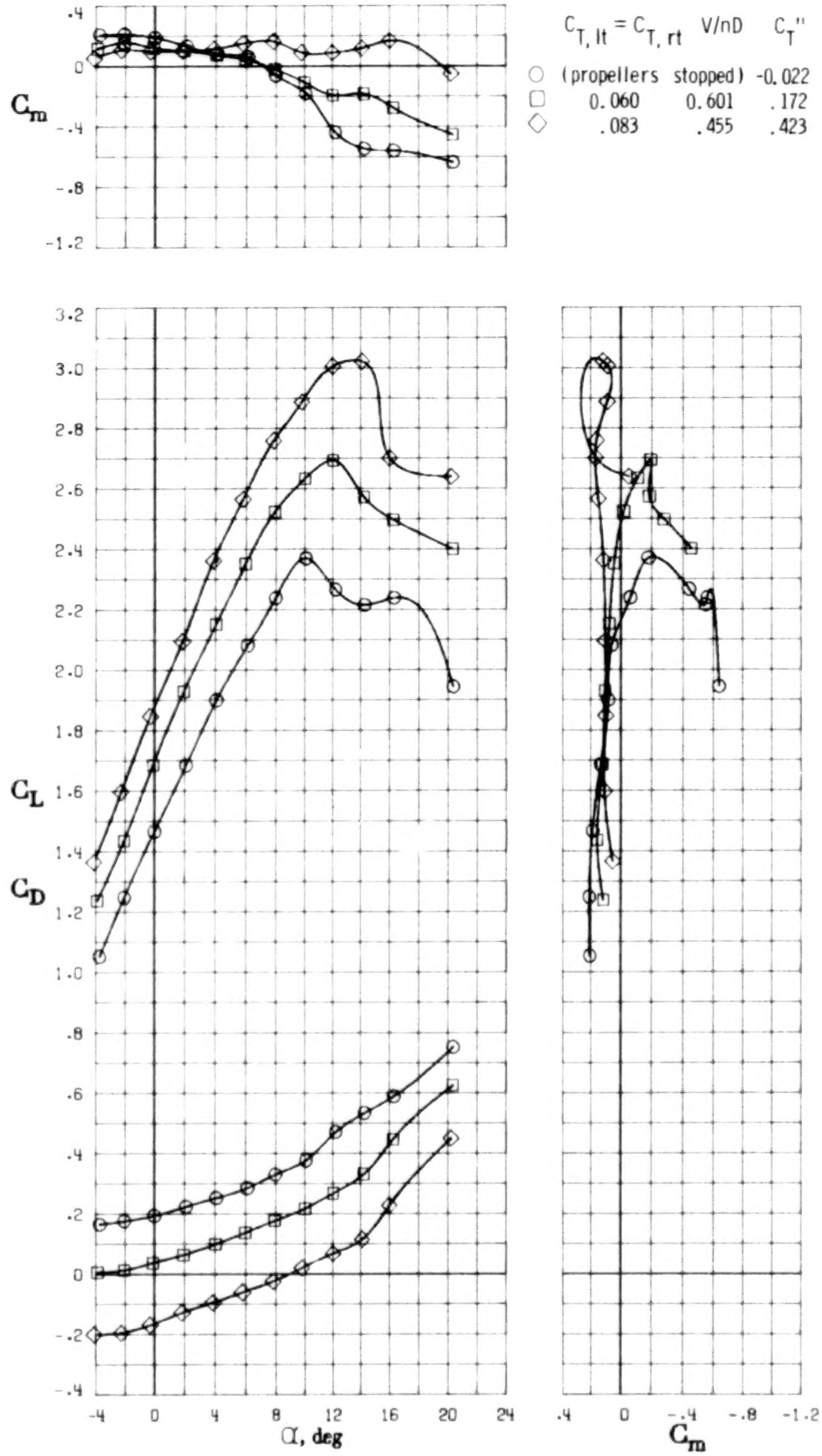

(c) $\delta_{stab} = -4^\circ$; aft center of gravity $(0.25\bar{c})$.

Figure 53.- Continued.

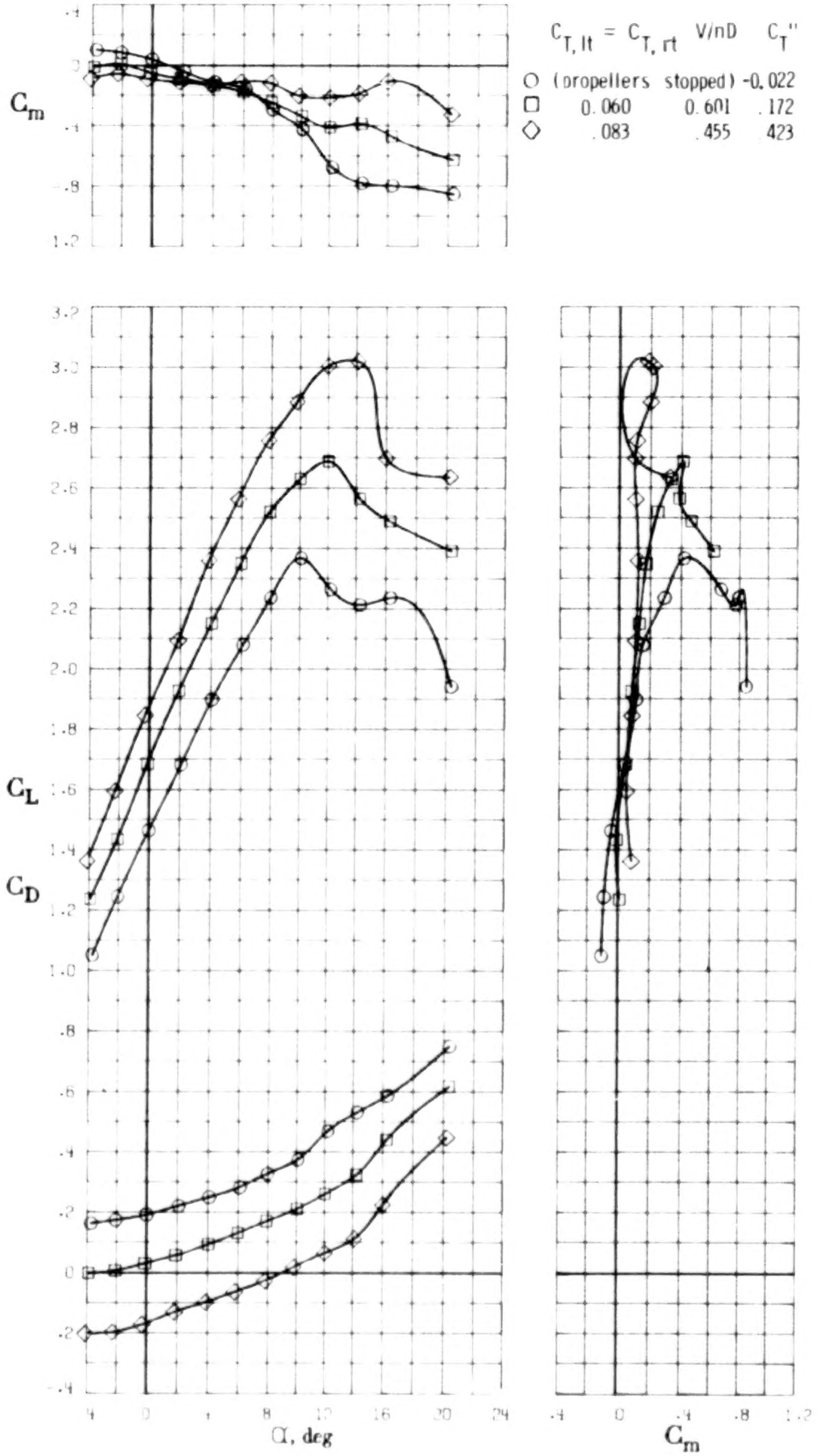

(d) $\delta_{stab} = -4^{\circ}$; forward center of gravity $(0.15\bar{c})$.

Figure 53.- Continued.

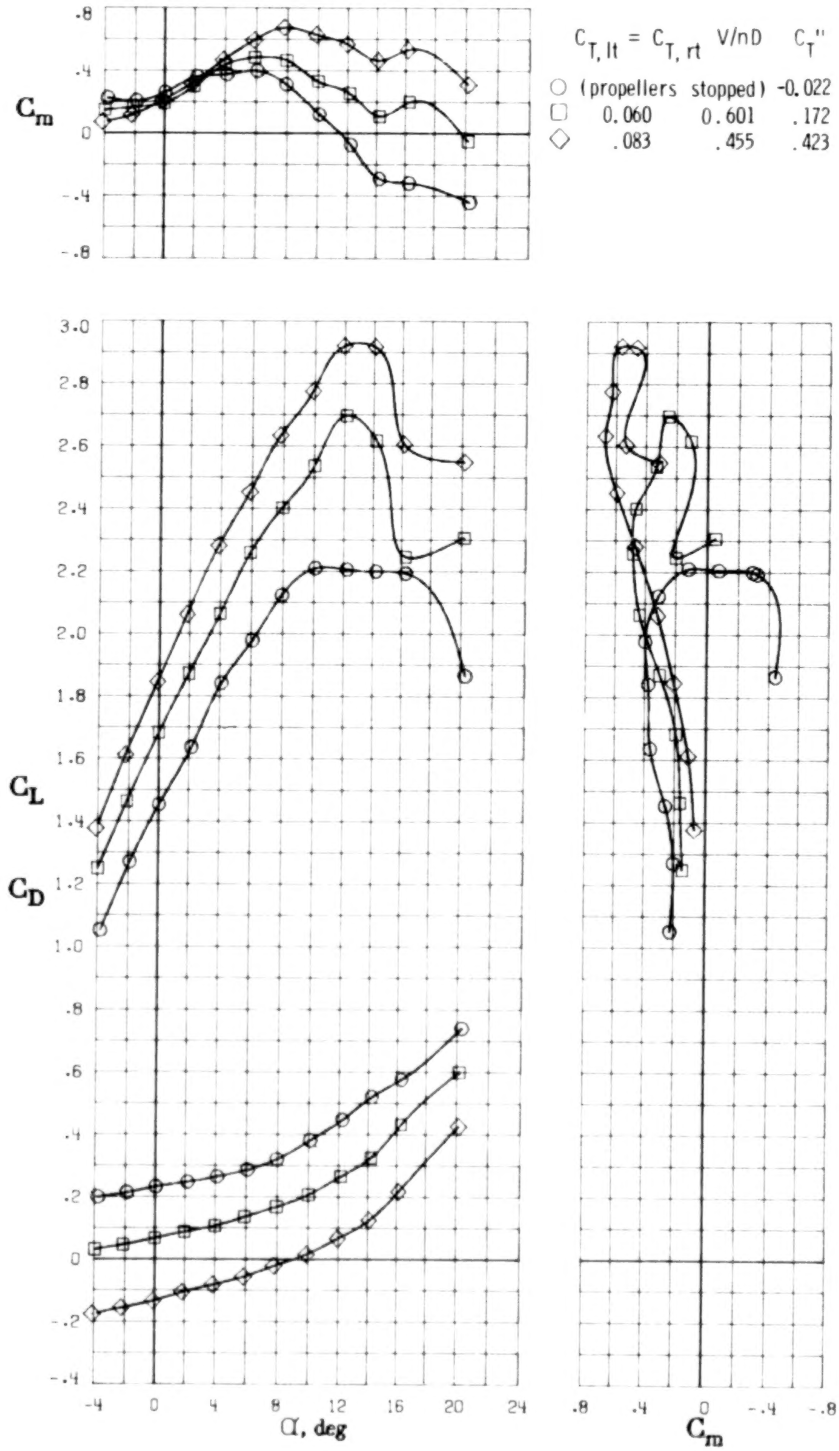

(e) $\delta_{stab} = -8^{\circ}$; aft center of gravity ($0.25\bar{c}$).

Figure 53.- Continued.

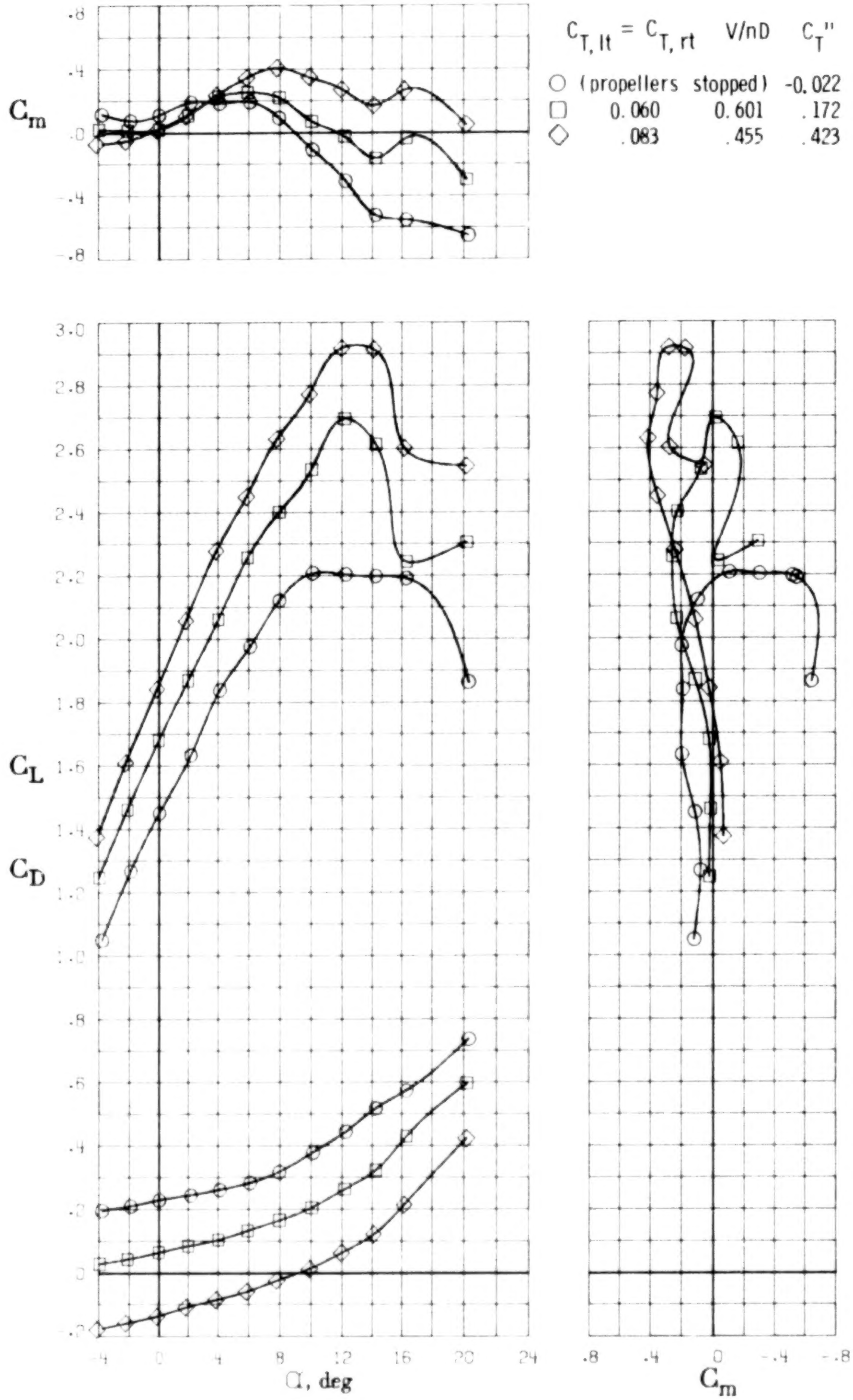

(f) $\delta_{stab} = -8^{\circ}$; forward center of gravity ($0.15\bar{c}$).

Figure 53.- Continued.

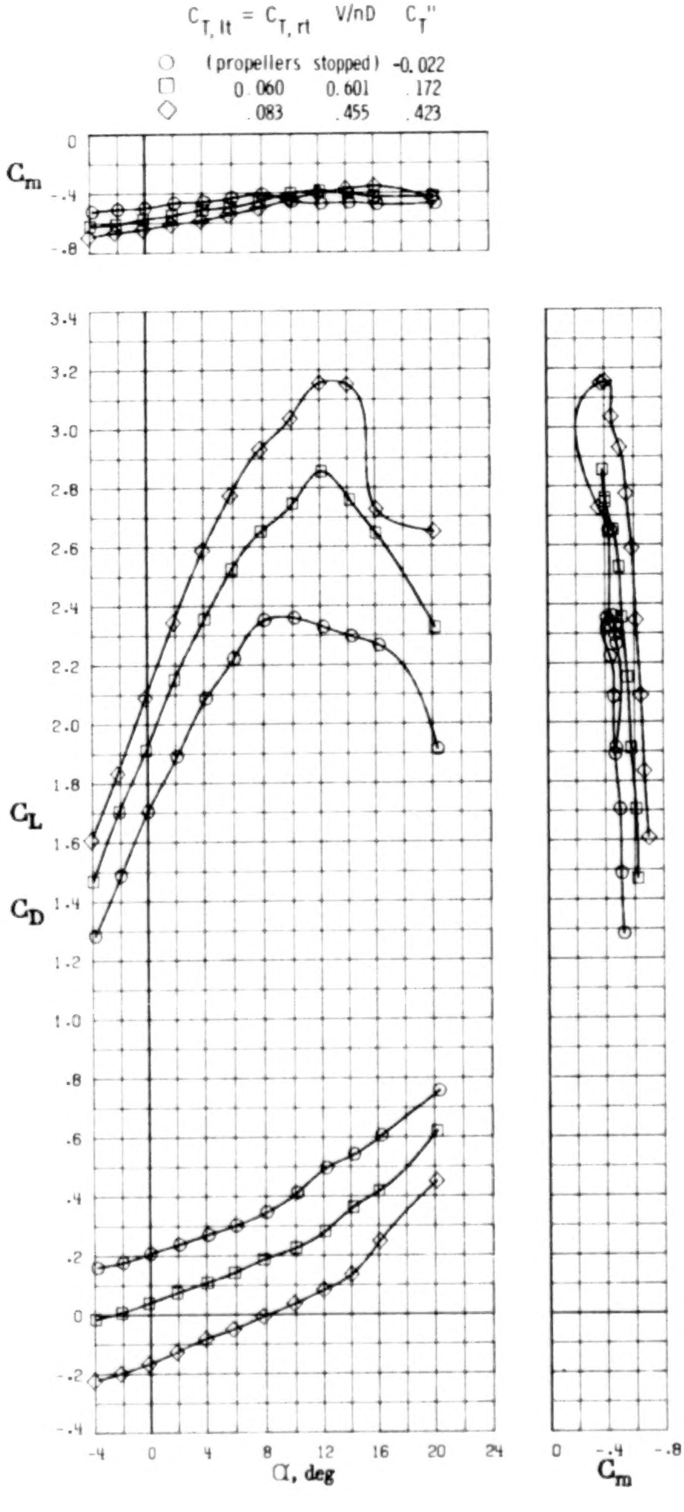

(g) Horizontal tail off; aft center of gravity ($0.25\bar{c}$).

Figure 53.- Continued.

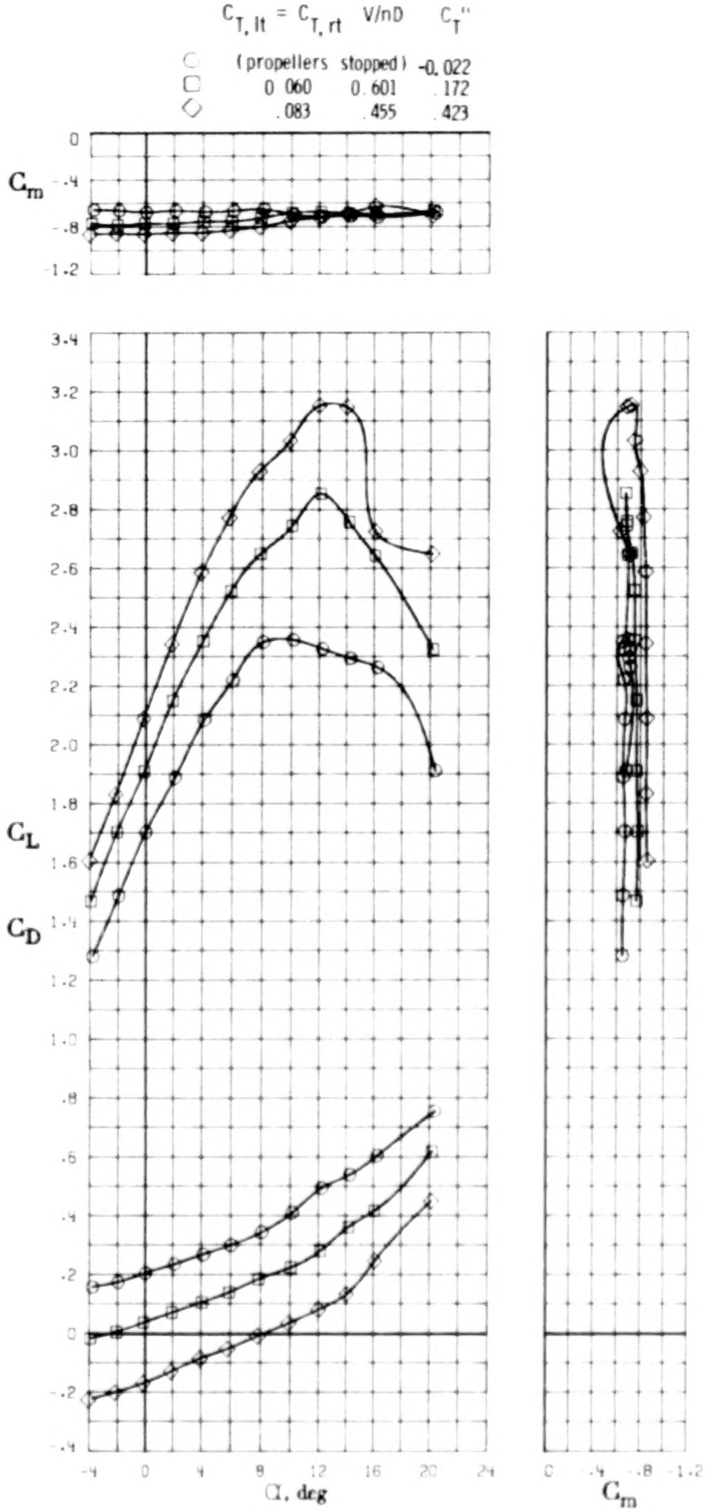

(h) Horizontal tail off; forward center of gravity ($0.15\bar{c}$).

Figure 53.- Concluded.

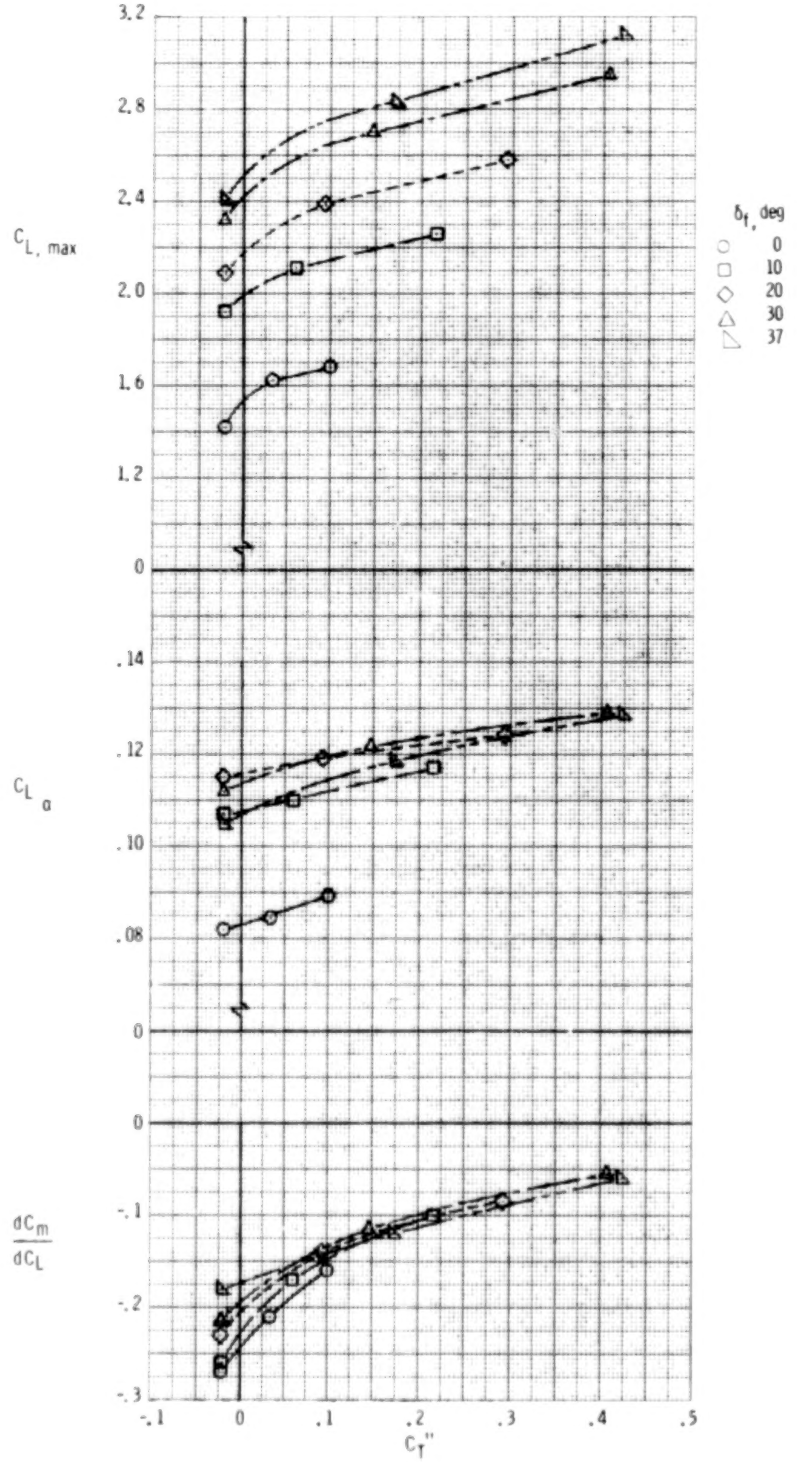

(a) $\delta_{stab} = 0^{\circ}$; c.g. at $0.25\bar{c}$.

Figure 54.- Summary of effects of power and flap deflection on $C_{L,max}$, C_{L_α}, and dC_m/dC_L.

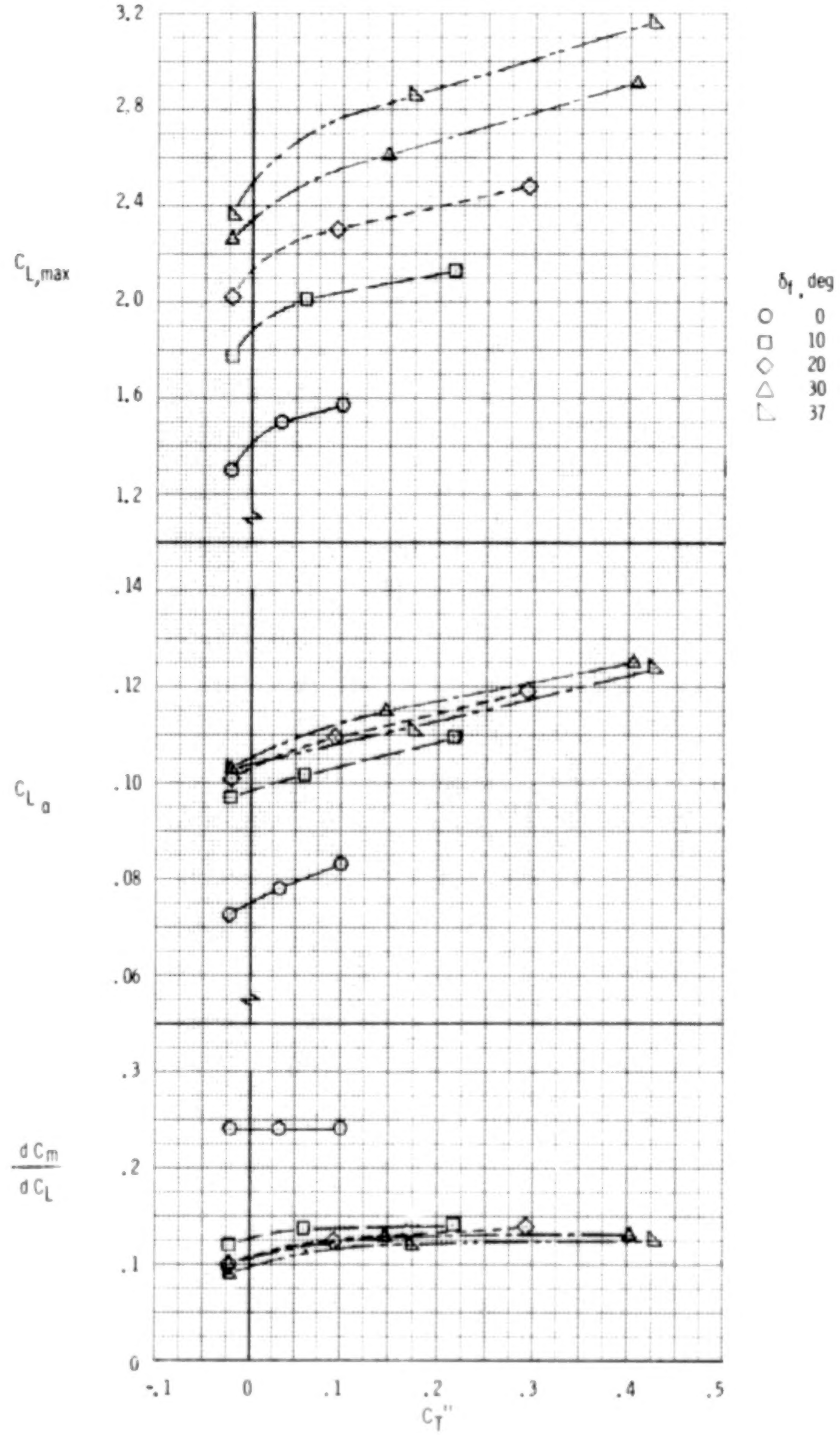

(b) Horizontal tail off; c.g. at 0.25$\bar{c}$.

Figure 54.- Concluded.

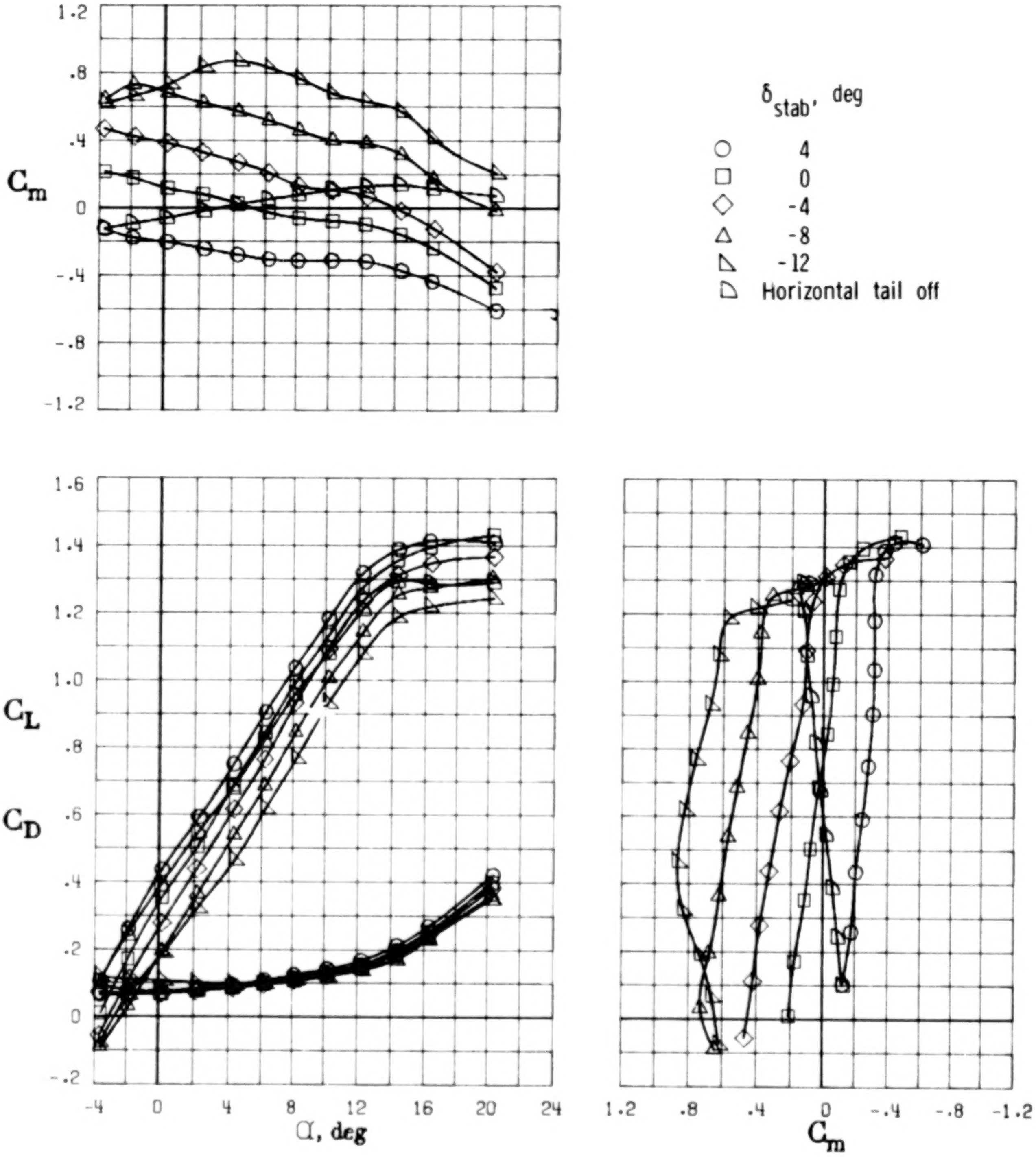

(a) $C_T'' = -0.022$ (propellers stopped).

Figure 55.- Effect of stabilator deflection on longitudinal aerodynamics with $\delta_f = 0^\circ$. $R = 2.30 \times 10^6$.

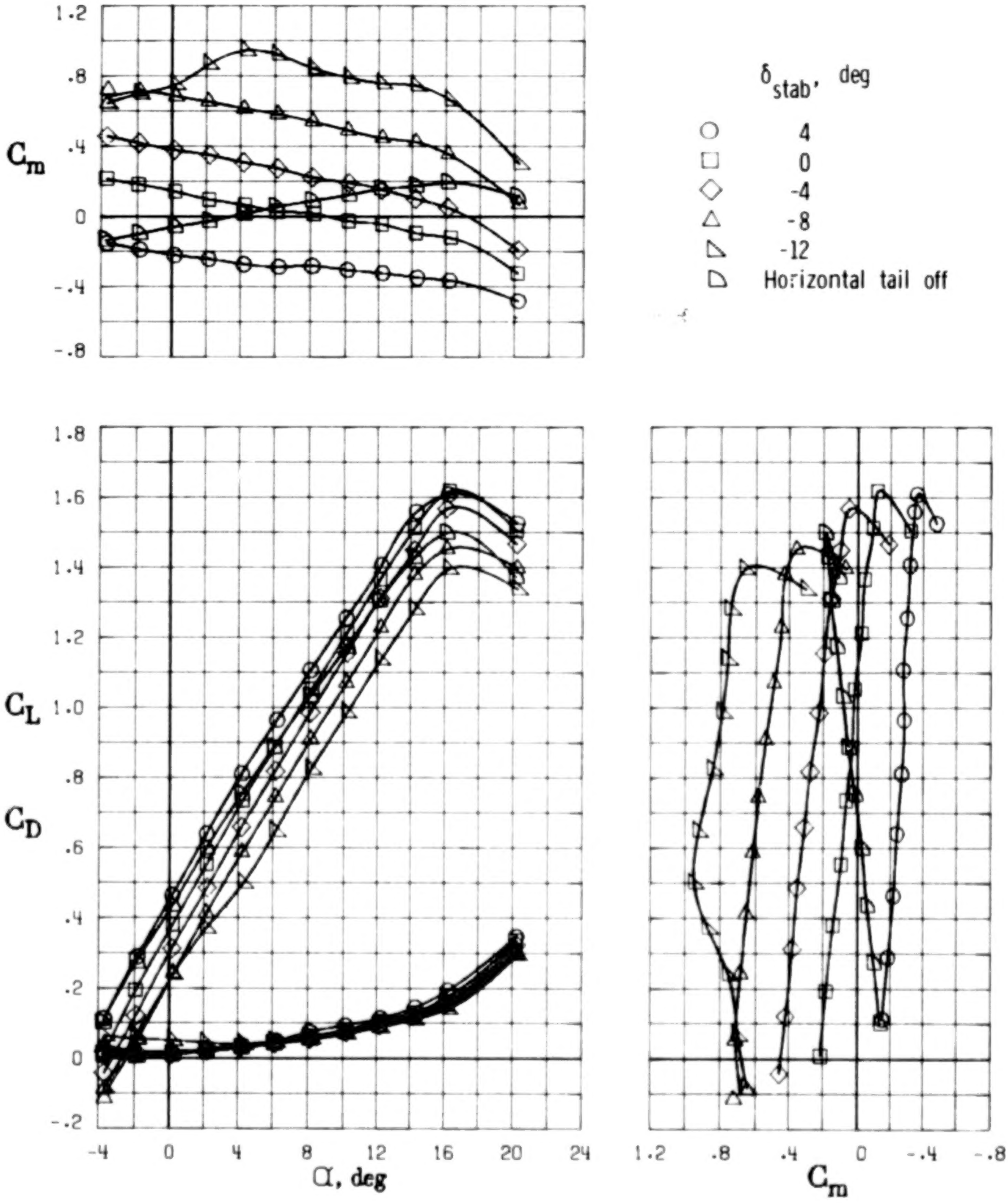

(b) $C_T'' = 0.033$; $C_{T,lt} = C_{T,rt} = 0.023$; V/nD = 0.830.

Figure 55.- Continued.

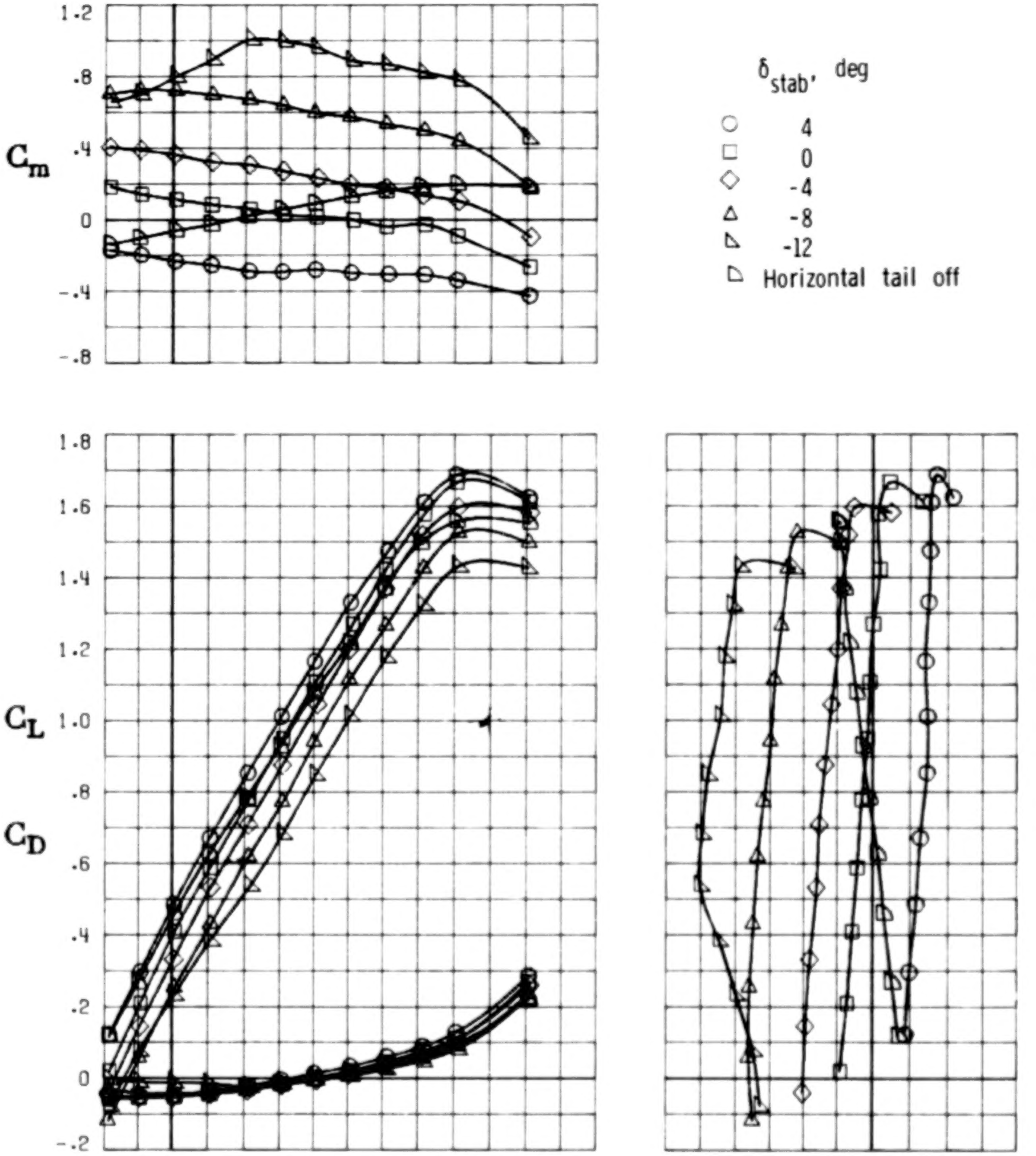

(c) $C_T'' = 0.100$; $C_{T,lt} = C_{T,rt} = 0.046$; $V/nD = 0.690$.

Figure 55.- Concluded.

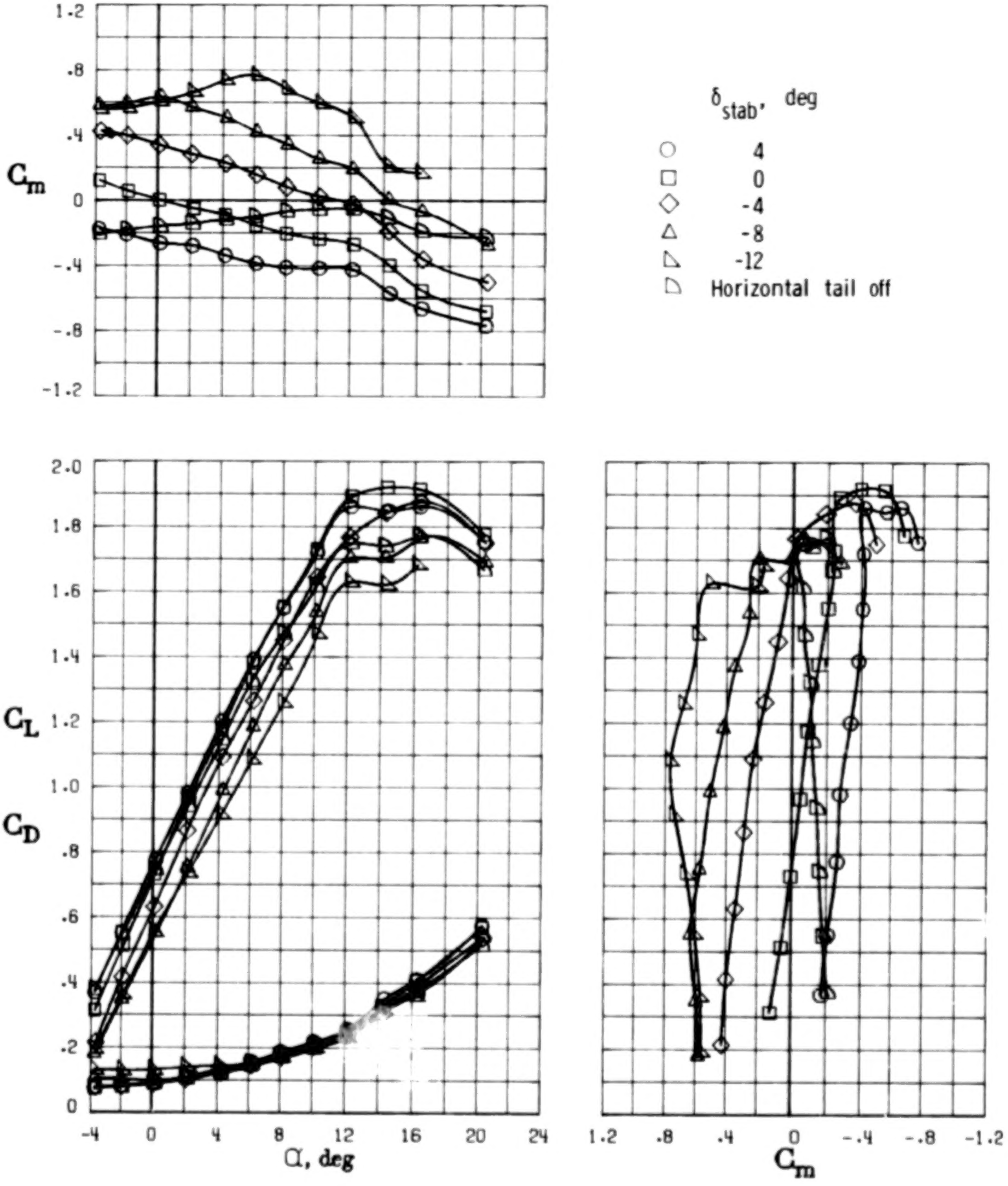

(a) $C_T'' = -0.022$ (propellers stopped).

Figure 56.- Effect of stabilator deflection on longitudinal aerodynamics with $\delta_f = 10^\circ$. $R = 2.30 \times 10^6$.

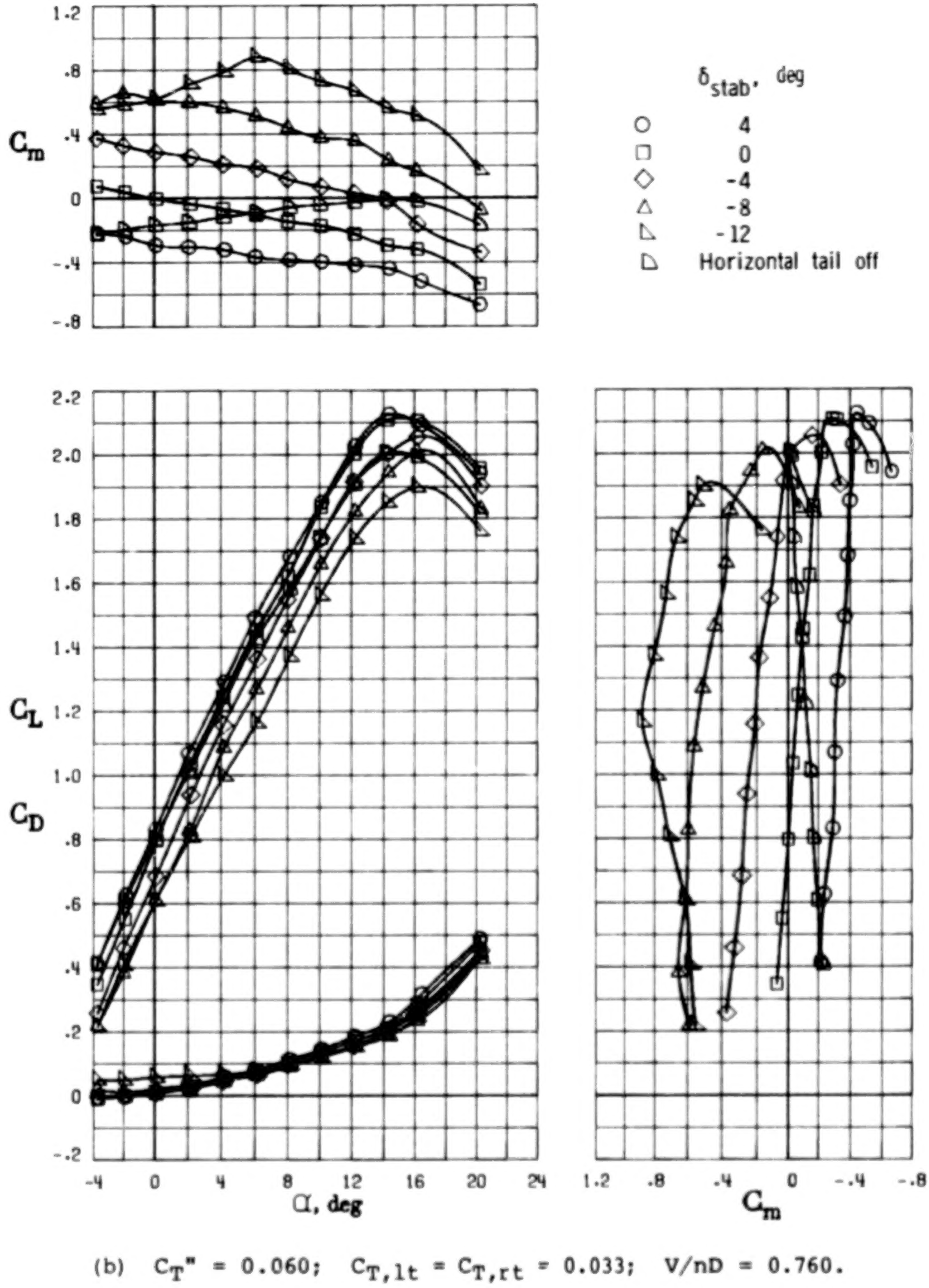

(b) $C_T'' = 0.060$; $C_{T,lt} = C_{T,rt} = 0.033$; V/nD = 0.760.

Figure 56.- Continued.

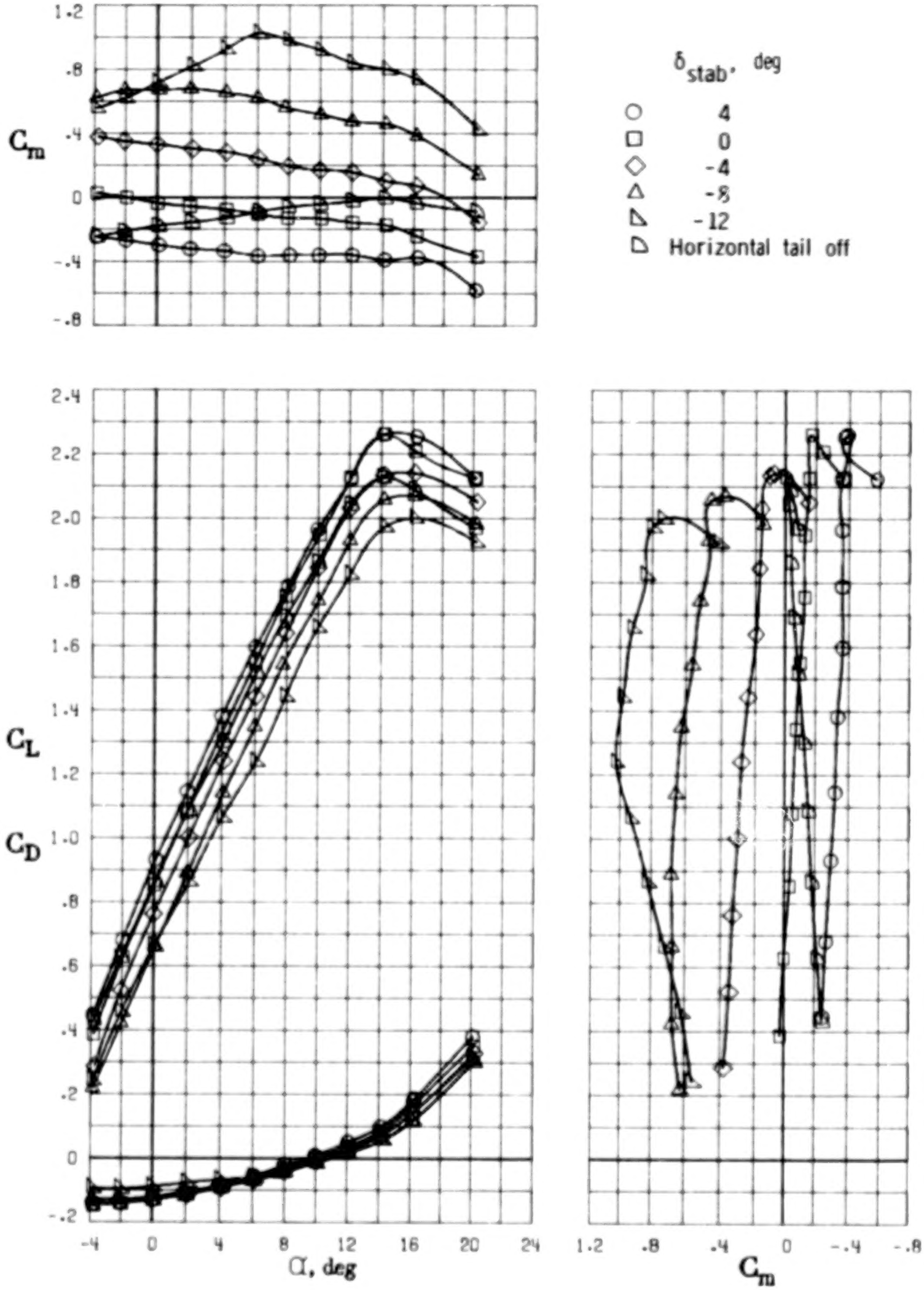

(c) $C_T'' = 0.216$; $C_{T,lt} = C_{T,rt} = 0.067$; $V/nD = 0.565$.

Figure 56.- Concluded.

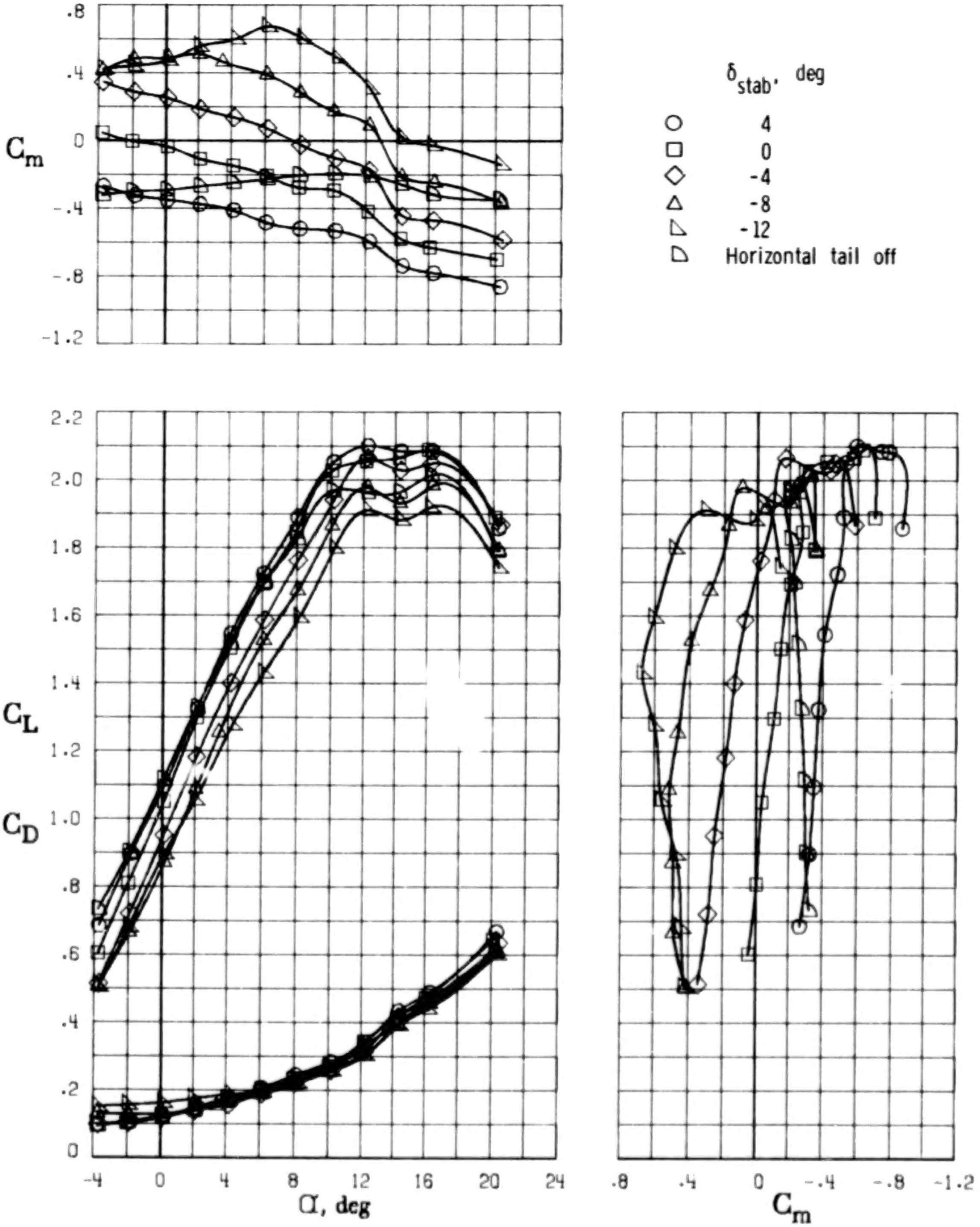

(a) $C_T" = -0.022$ (propellers stopped).

Figure 57.- Effect of stabilator deflection on longitudinal aerodynamics with $\delta_f = 20^\circ$. $R = 2.30 \times 10^6$.

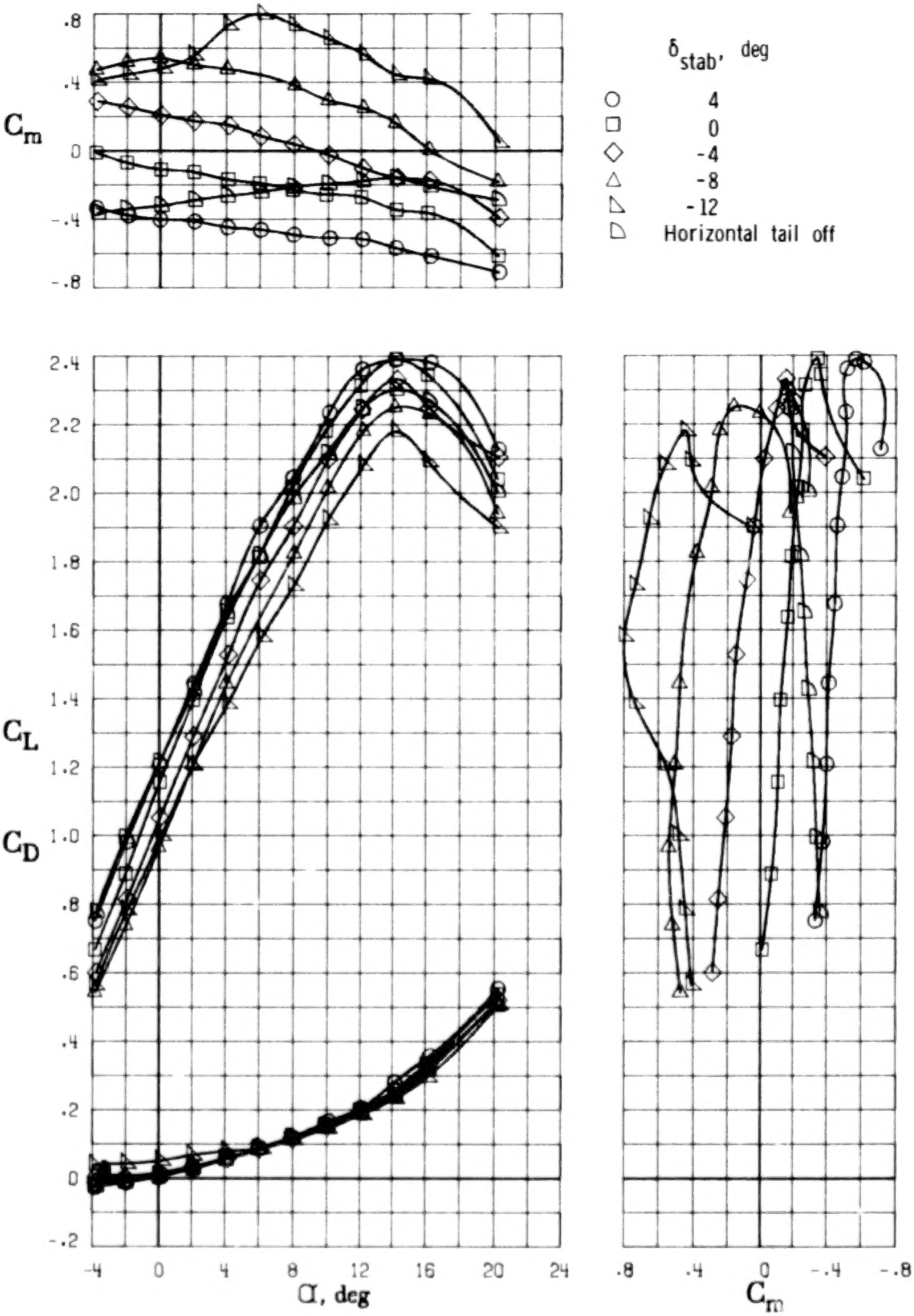

(b) $C_T'' = 0.094$; $C_{T,lt} = C_{T,rt} = 0.043$; $V/nD = 0.700$.

Figure 57.- Continued.

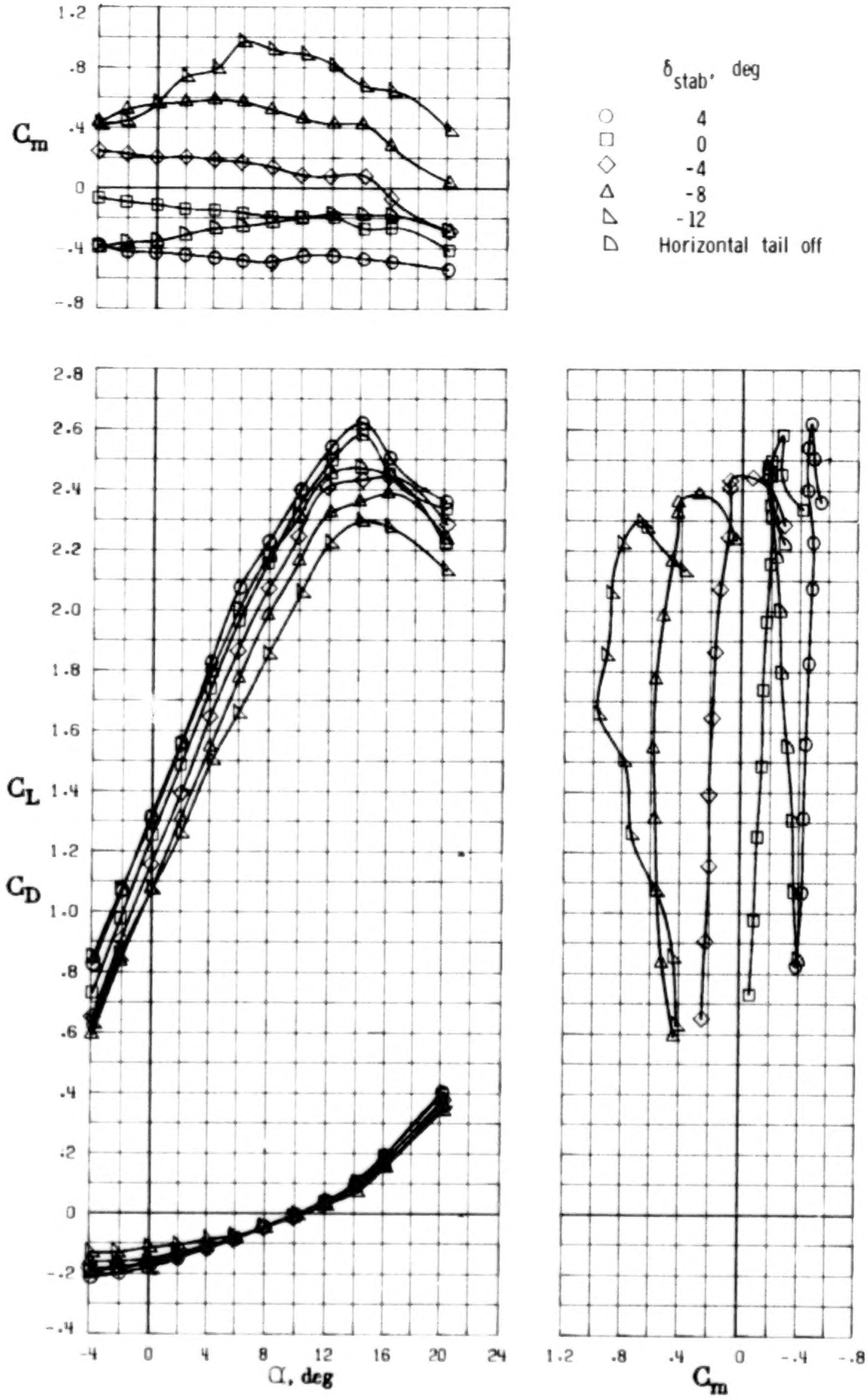

(c) $C_T'' = 0.293$; $C_{T,lt} = C_{T,rt} = 0.075$; $V/nD = 0.515$.

Figure 57.- Concluded.

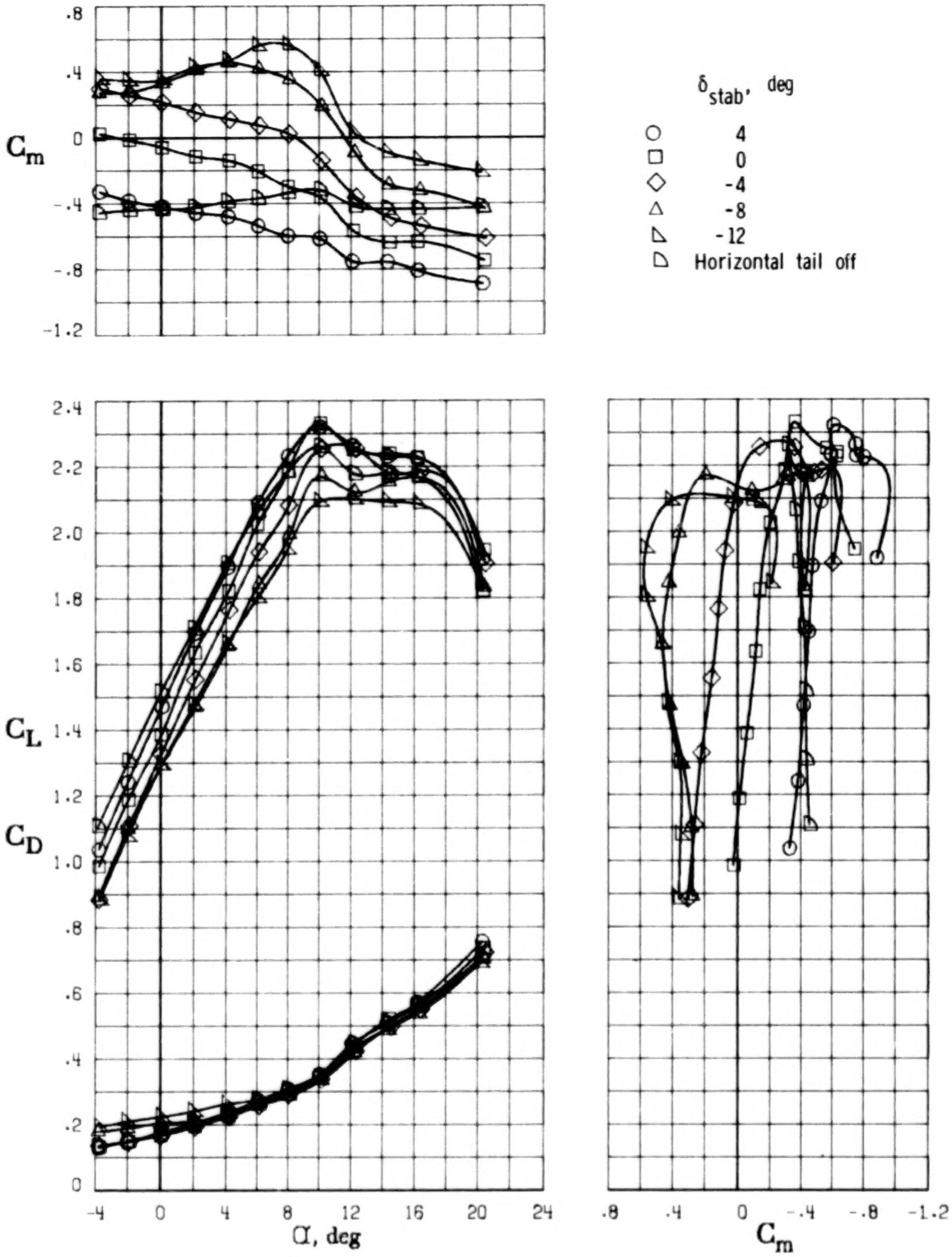

(a) $C_T'' = -0.022$ (propellers stopped).

Figure 58.- Effect of stabilator deflection on longitudinal aerodynamics with $\delta_f = 30^\circ$. $R = 2.30 \times 10^6$.

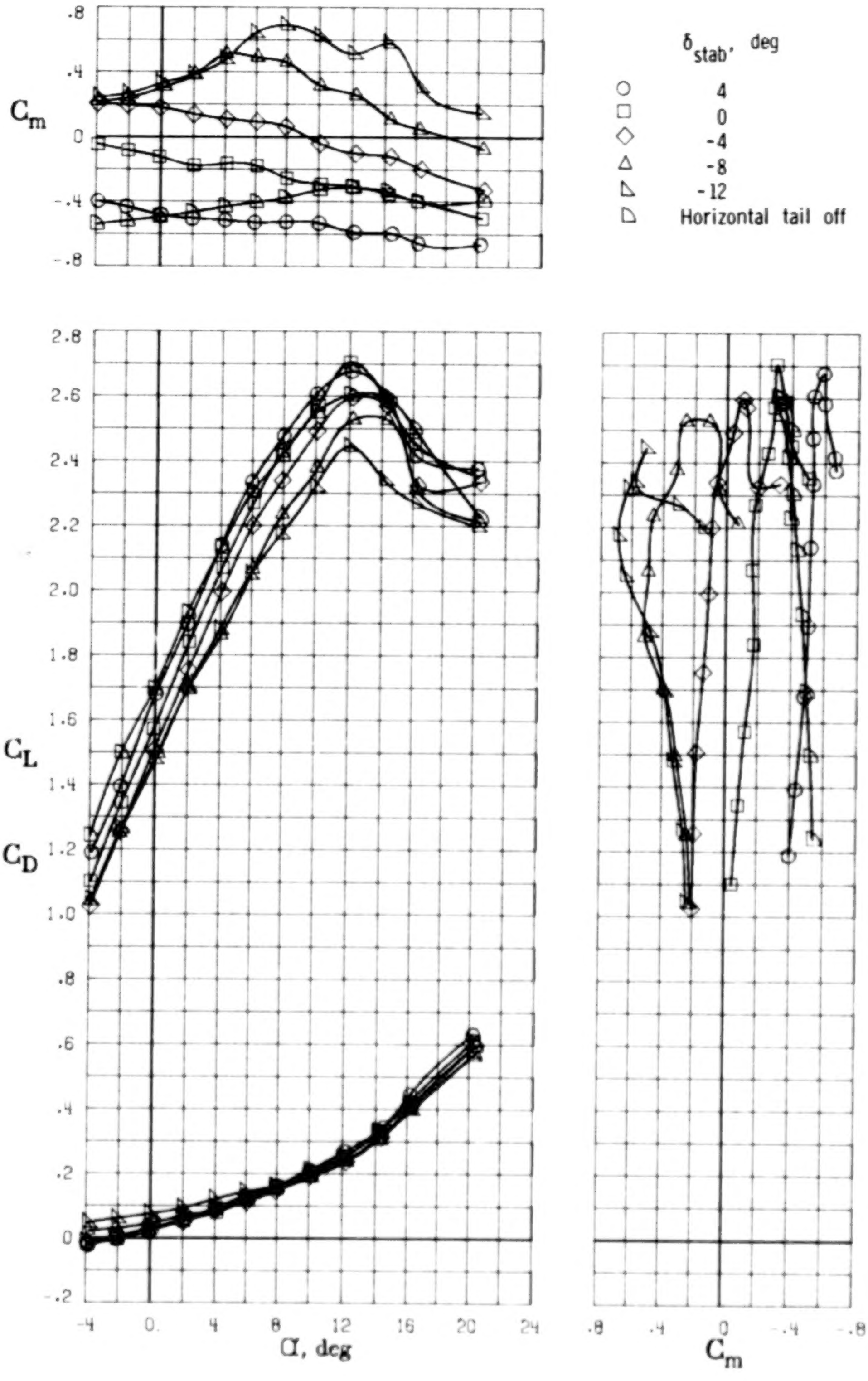

(b) $C_T'' = 0.147$; $C_{T,lt} = C_{T,rt} = 0.055$; $V/nD = 0.635$.

Figure 58.- Continued.

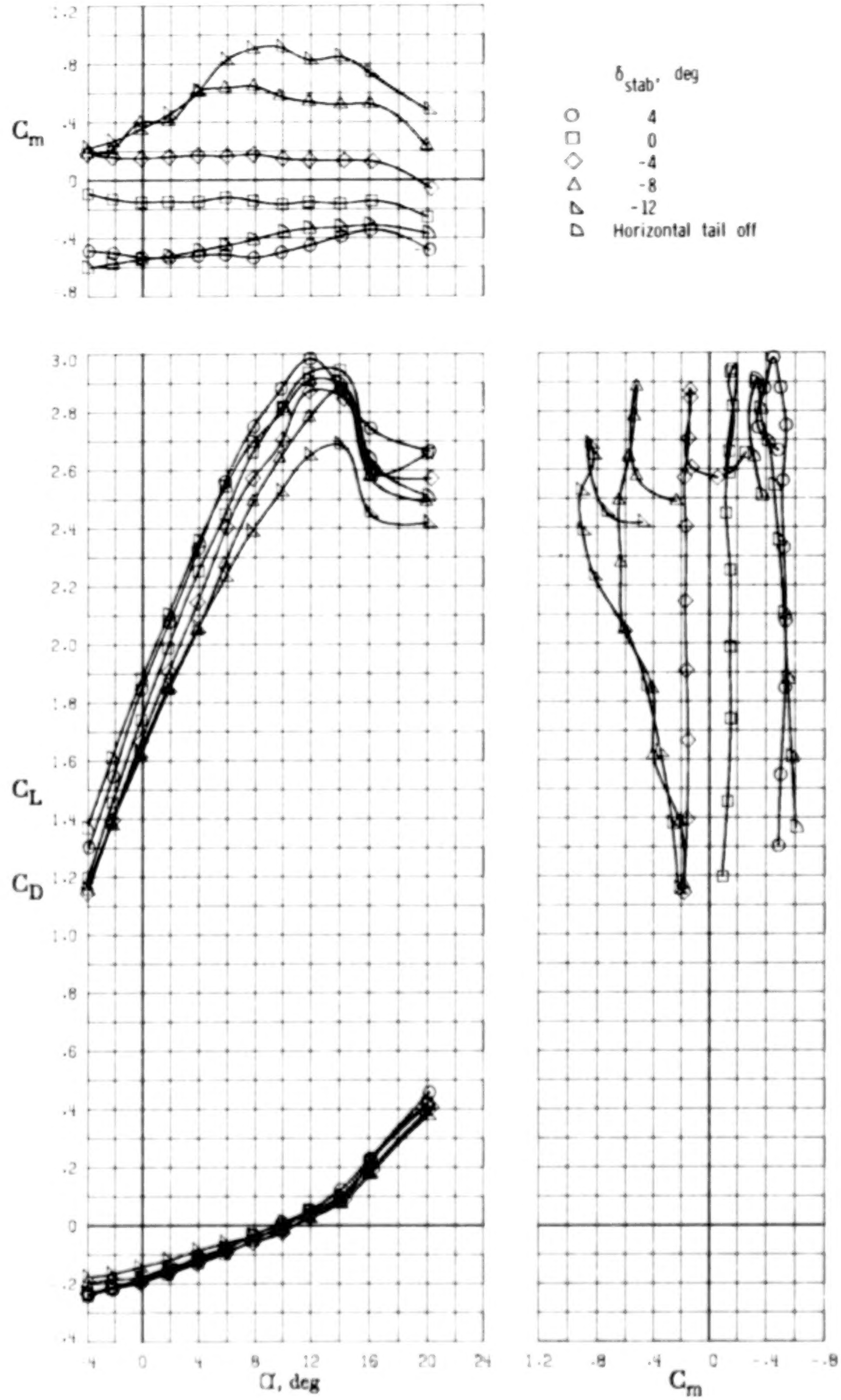

(c) $C_T'' = 0.406$; $C_{T,lt} = C_{T,rt} = 0.083$; $V/nD = 0.460$.

Figure 58.- Concluded.

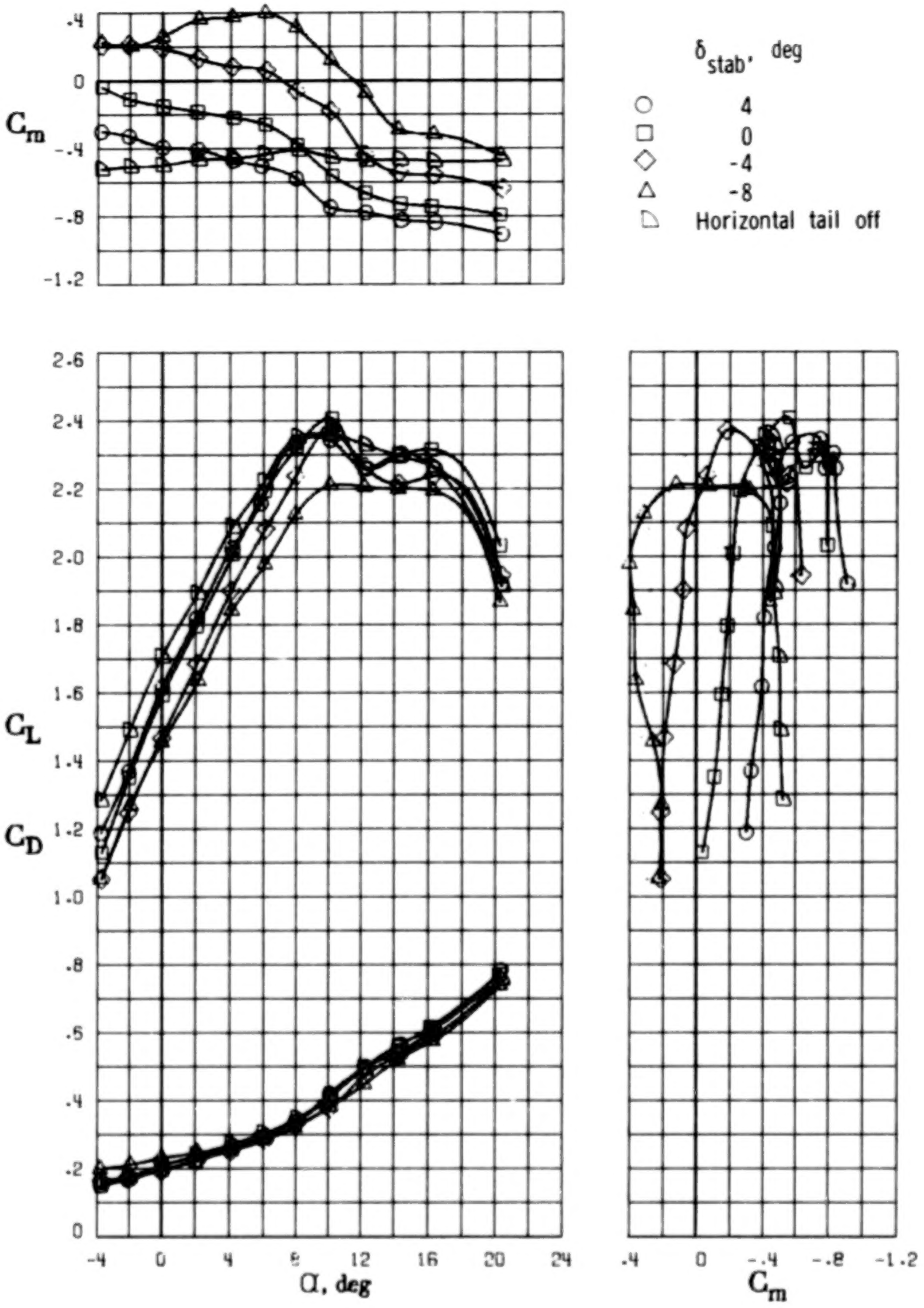

(a) $C_T'' = -0.022$ (propellers stopped); c.g. at $0.25\bar{c}$.

Figure 59.- Effect of stabilator deflection on longitudinal aerodynamics with $\delta_f = 37^\circ$. $R = 2.30 \times 10^6$.

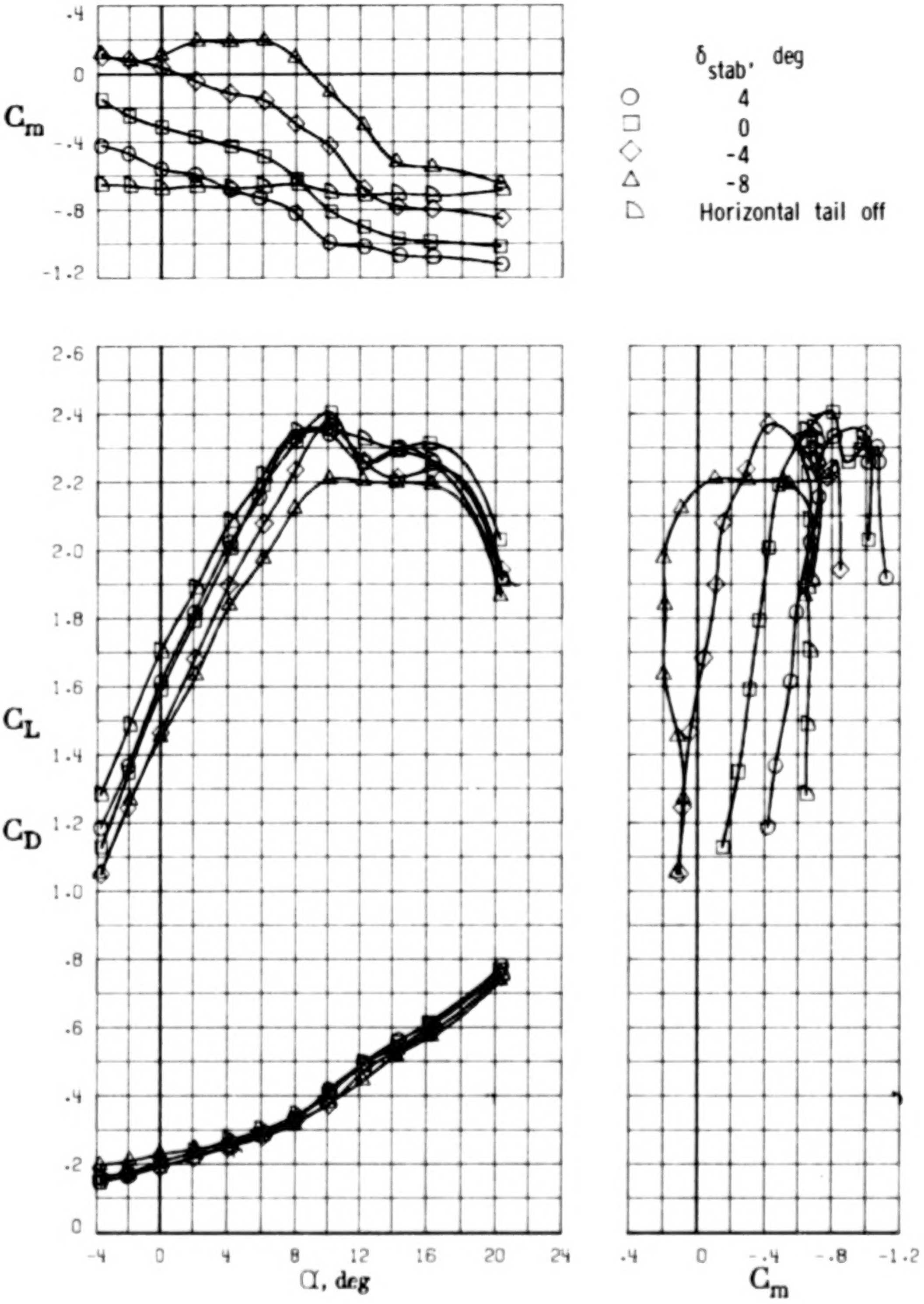

(b) $C_T'' = -0.022$ (propellers stopped); c.g. at $0.15\bar{c}$.

Figure 59.- Continued.

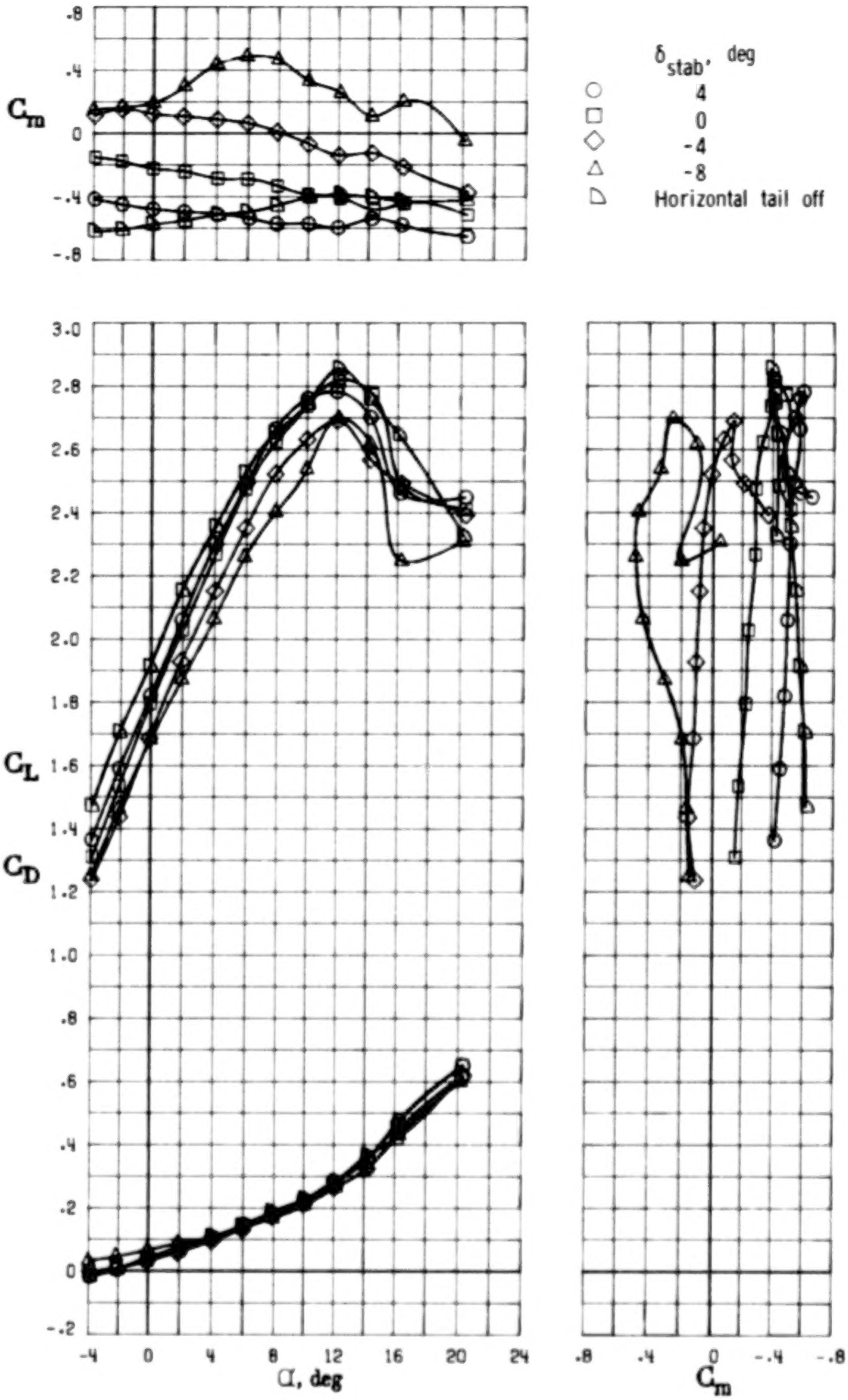

(c) $C_T'' = 0.172$; $C_{T,lt} = C_{T,rt} = 0.060$; $V/nD = 0.601$; c.g. at $0.25\bar{c}$.

Figure 59.- Continued.

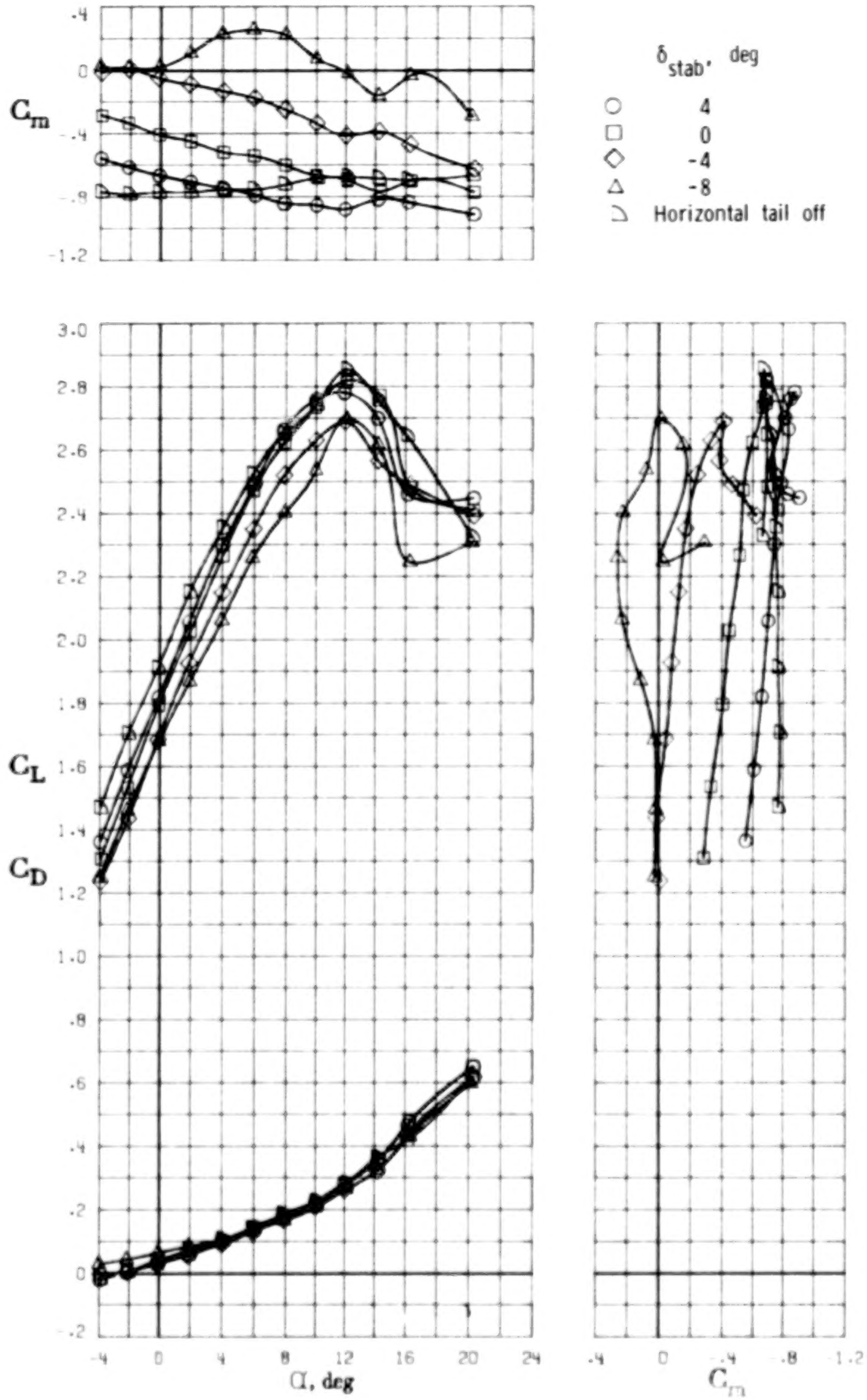

(d) $C_T'' = 0.172$; $C_{T,lt} = C_{T,rt} = 0.060$; V/nD = 0.601; c.g. at $0.15\bar{c}$.

Figure 59.- Continued.

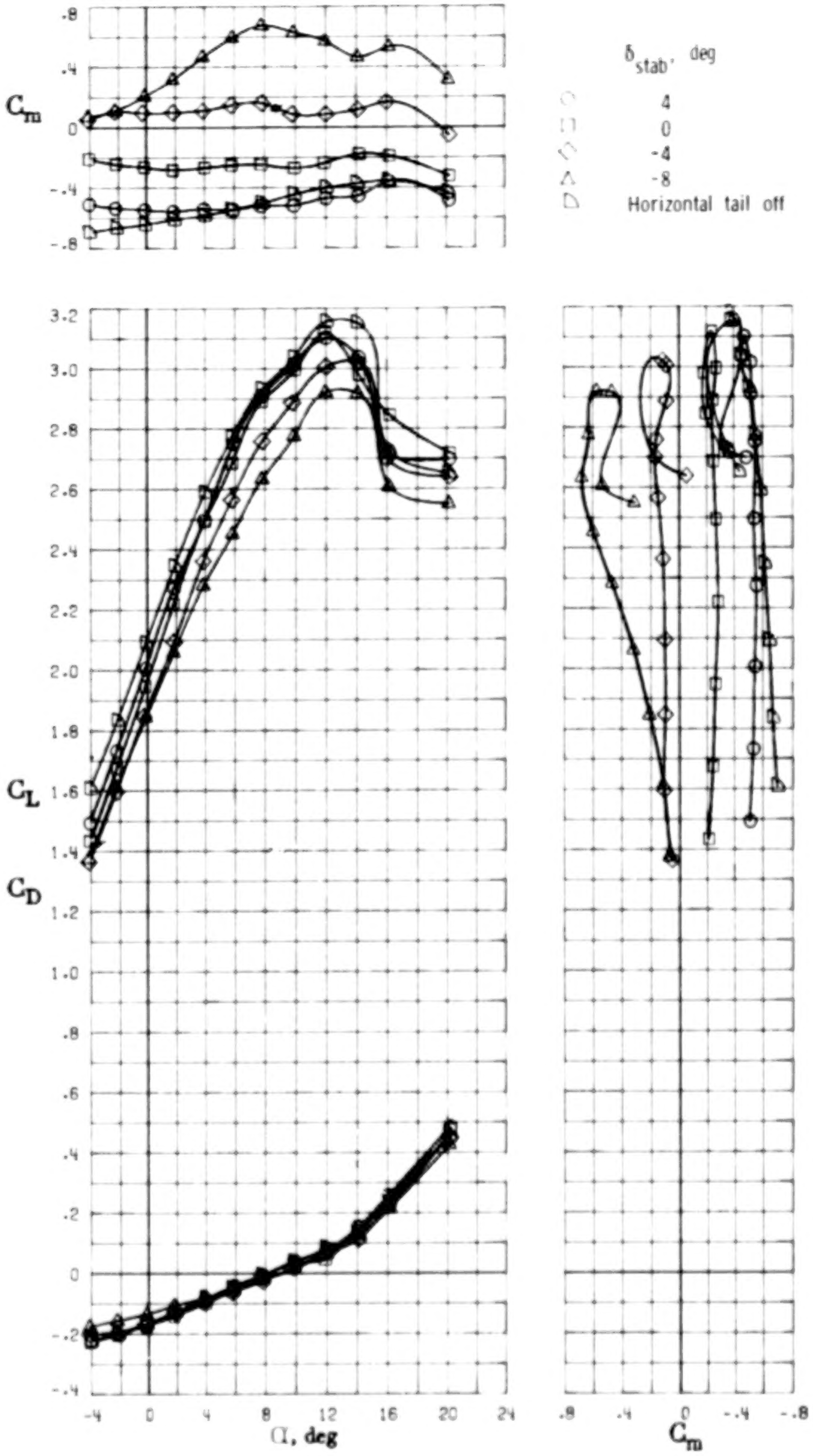

(e) $C_T'' = 0.423$; $C_{T,lt} = C_{T,rt} = 0.083$; $V/nD = 0.455$; c.g. at $0.25\bar{c}$.

Figure 59.- Continued.

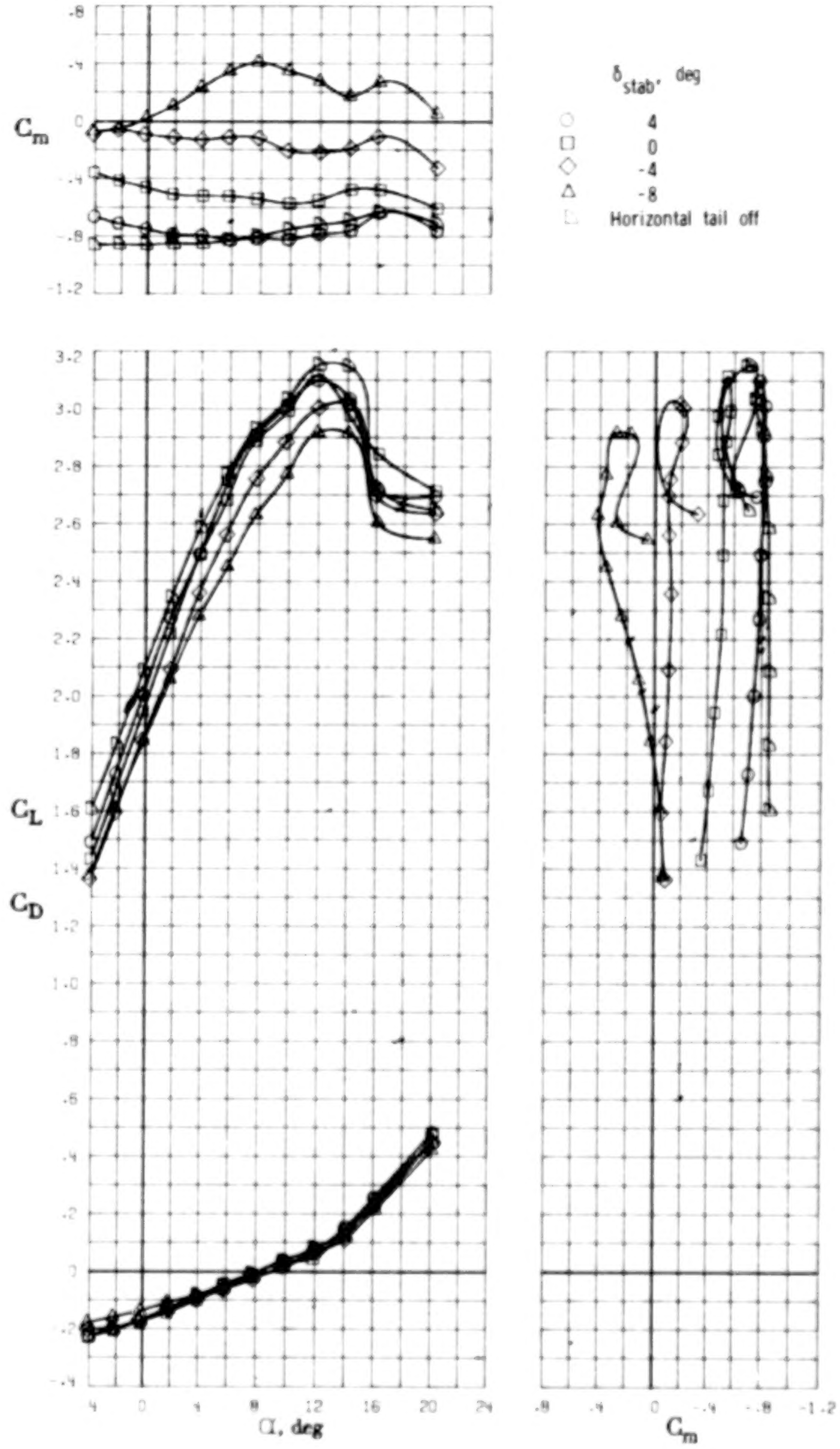

(f) $C_T'' = 0.423$; $C_{T,lt} = C_{T,rt} = 0.083$; $V/nD = 0.455$; c.g. at $0.15\bar{c}$.

Figure 59.- Concluded.

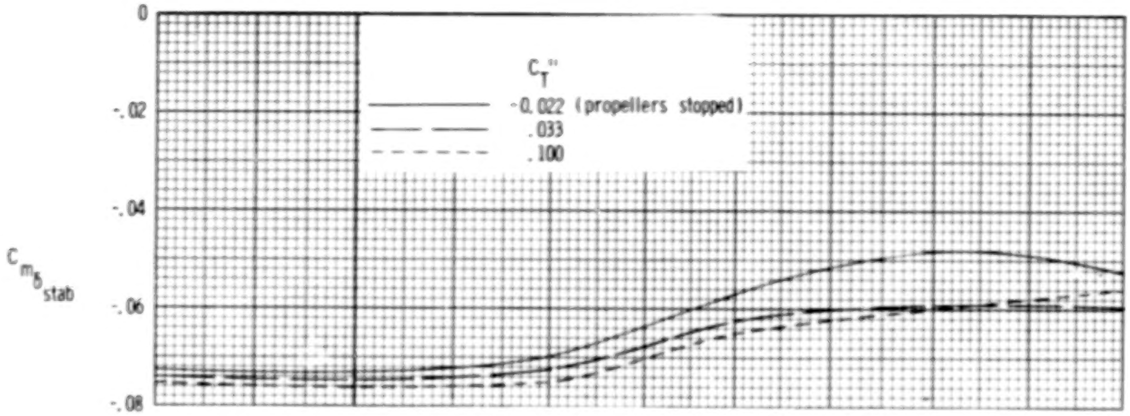

(a) $\delta_f = 0^{\circ}$.

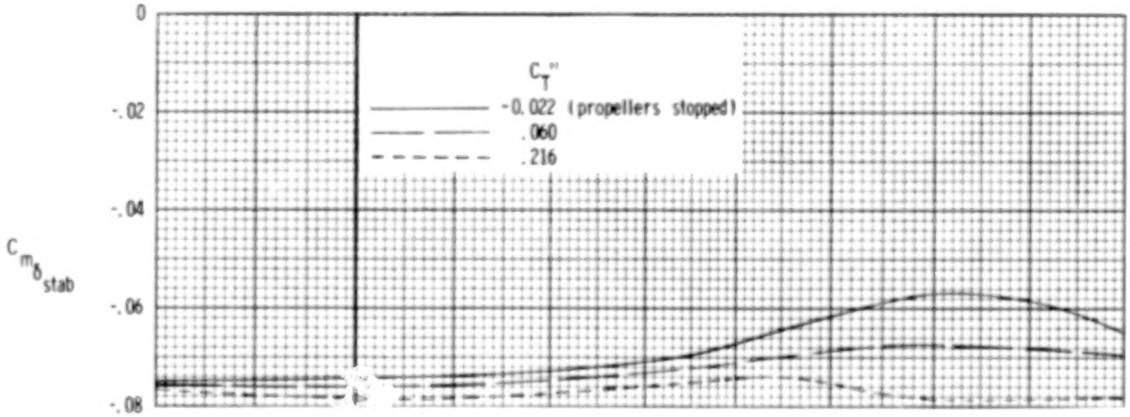

(b) $\delta_f = 10^{\circ}$.

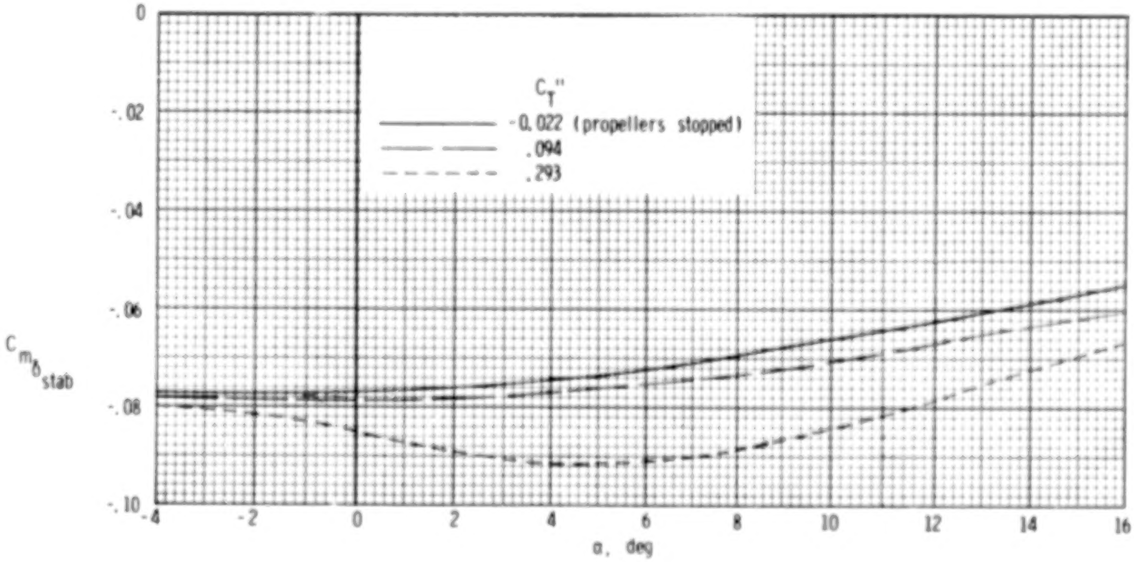

(c) $\delta_f = 20^{\circ}$.

Figure 60.- Effect of power on stabilator effectiveness for various flap deflection angles. c.g. at $0.25\bar{c}$.

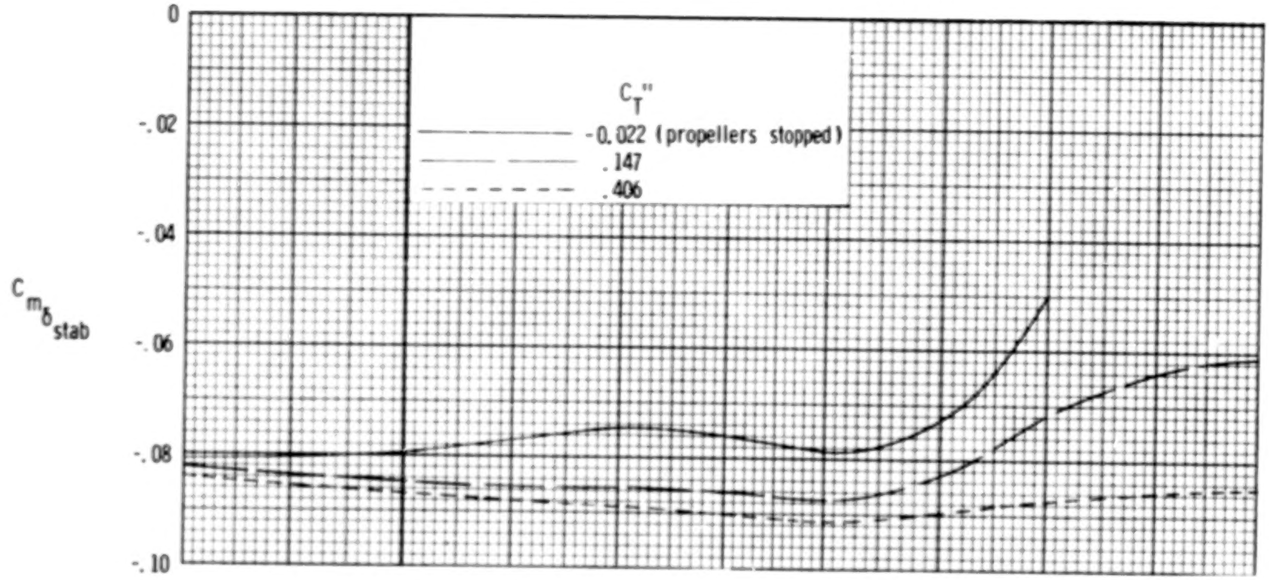

(d) δ_f = 30°.

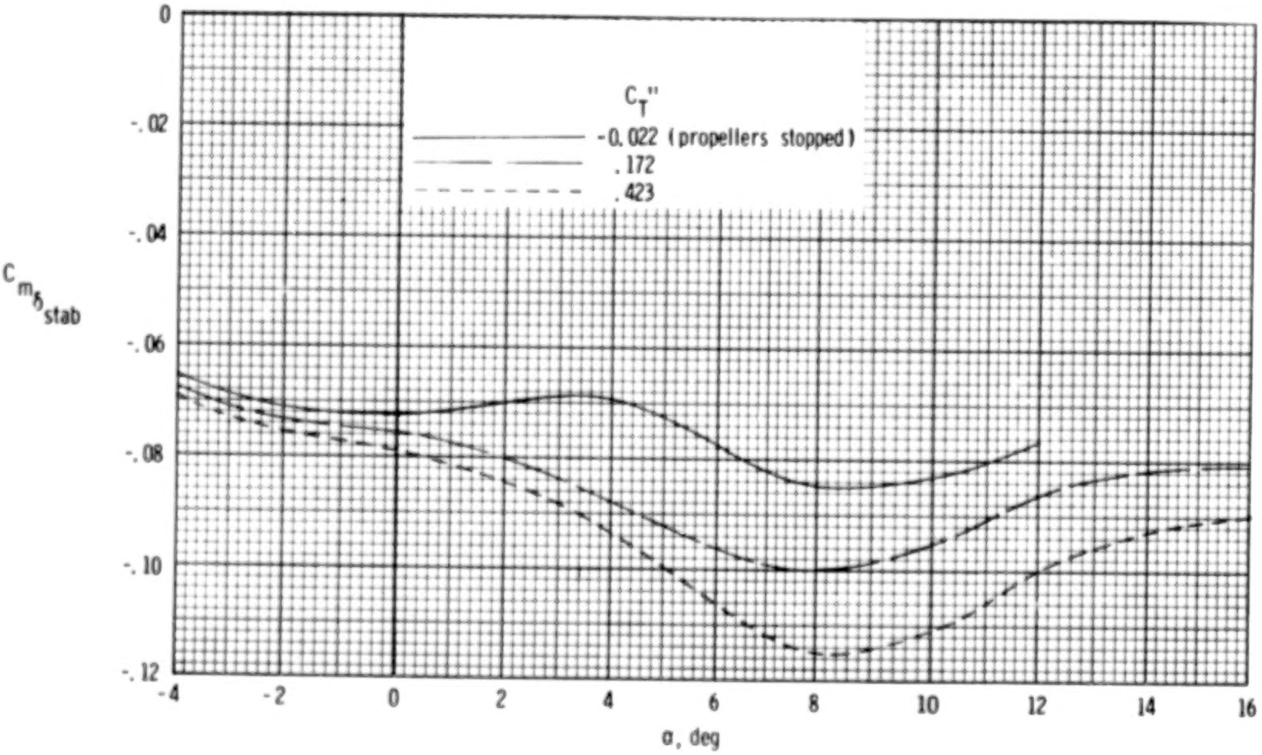

(e) δ_f = 37°.

Figure 60.- Concluded.

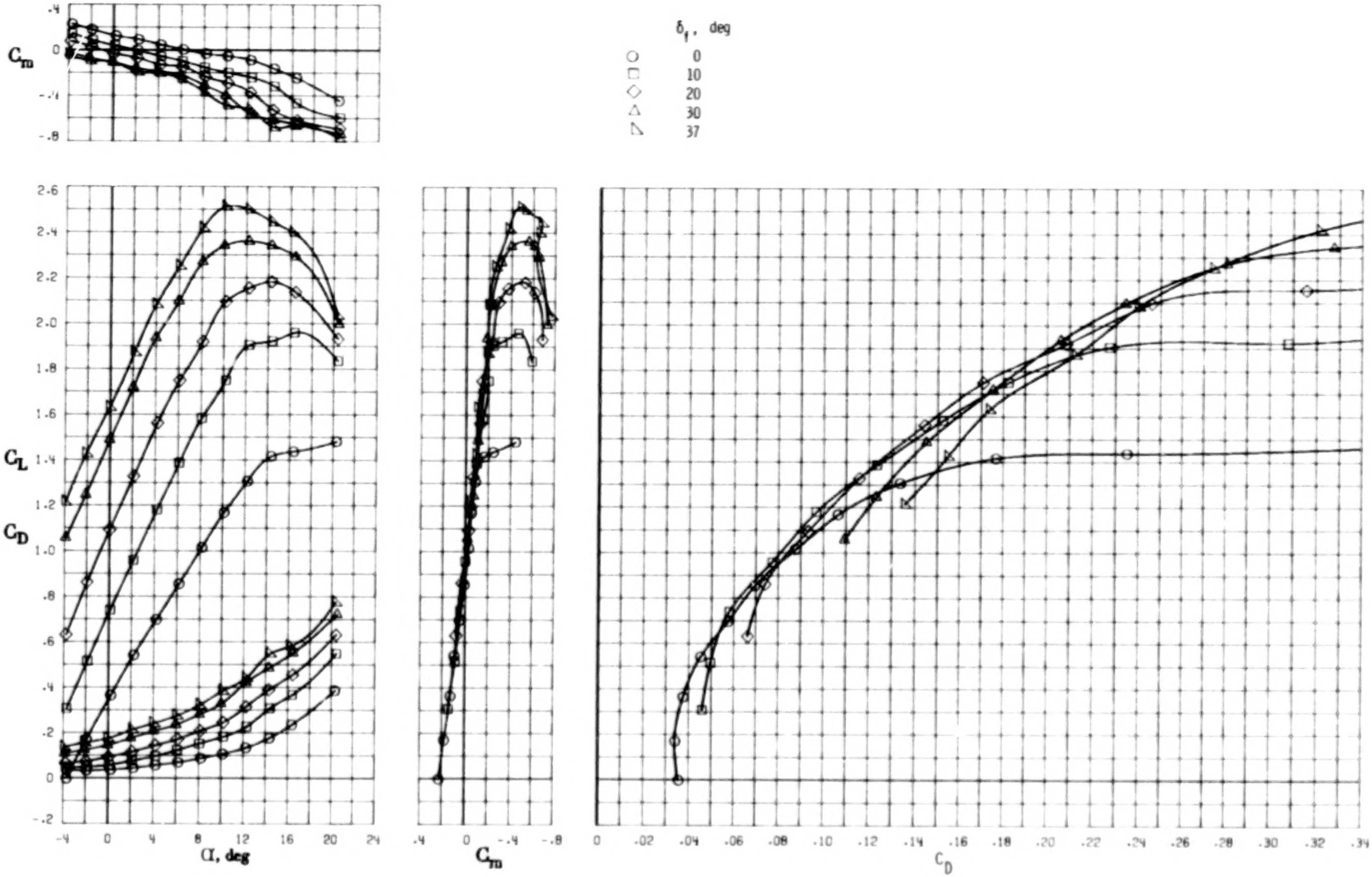

(a) Propellers off; engine inlets sealed; cowl flaps closed; $\delta_{stab} = 0^{\circ}$.

Figure 61.- Effect of Fowler flap deflection on longitudinal aerodynamics of airplane. $R = 2.30 \times 10^6$.

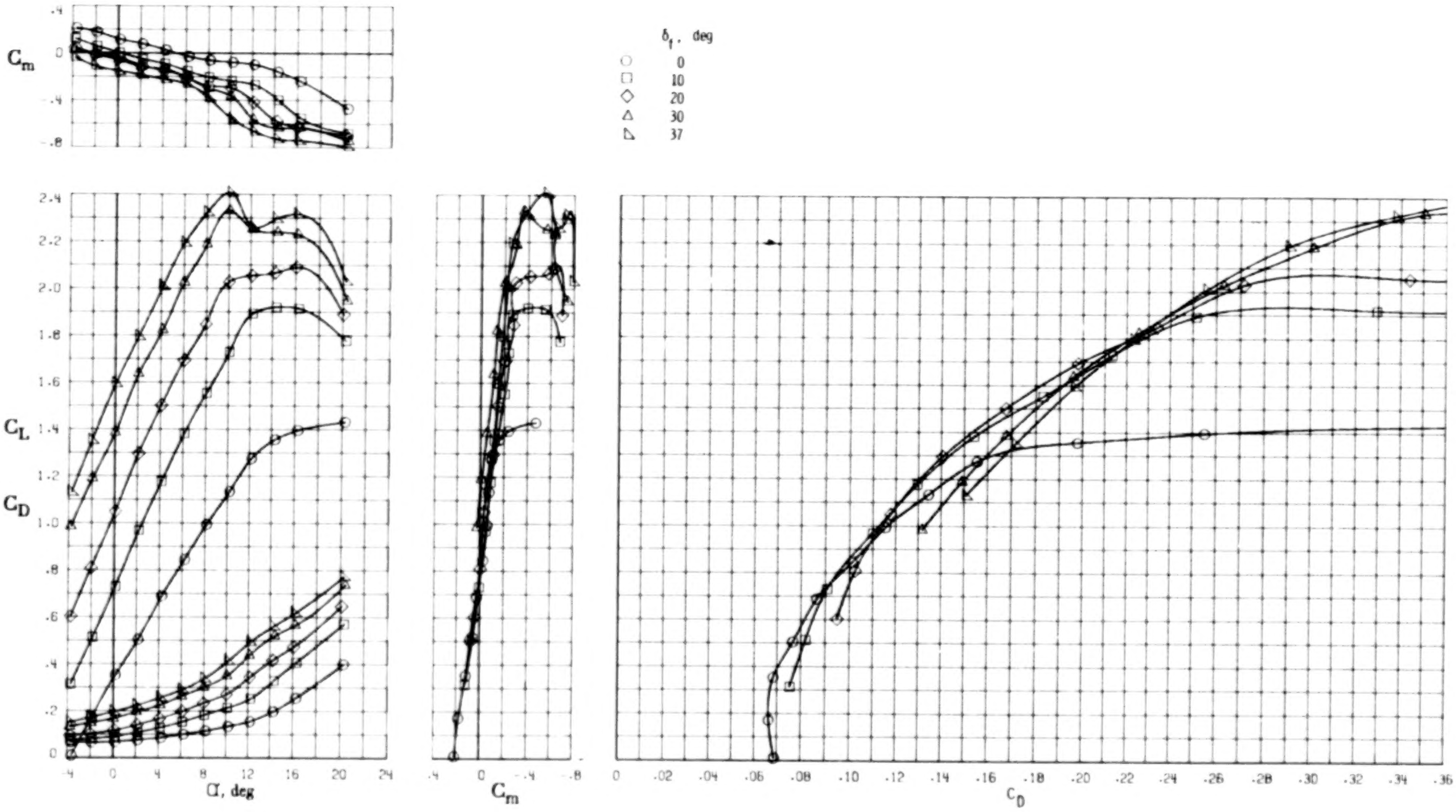

(b) Propellers on (propellers stopped); engine inlets unsealed; cowl flaps open; $\delta_{stab} = 0^{\circ}$.

Figure 61.- Continued.

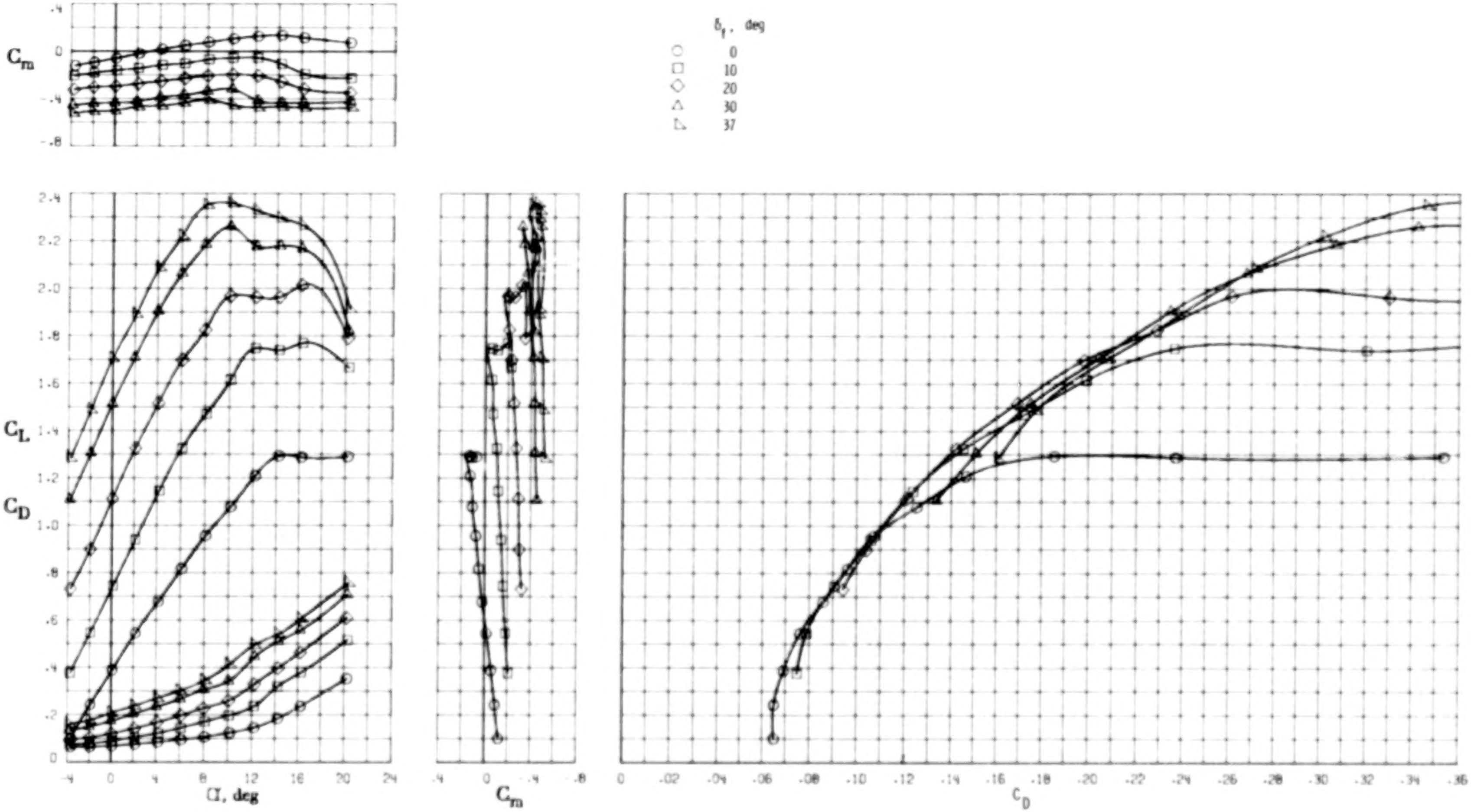

(c) Horizontal tail off; propellers on (propellers stopped); engine inlets unsealed; cowl flaps open.

Figure 61.- Concluded.

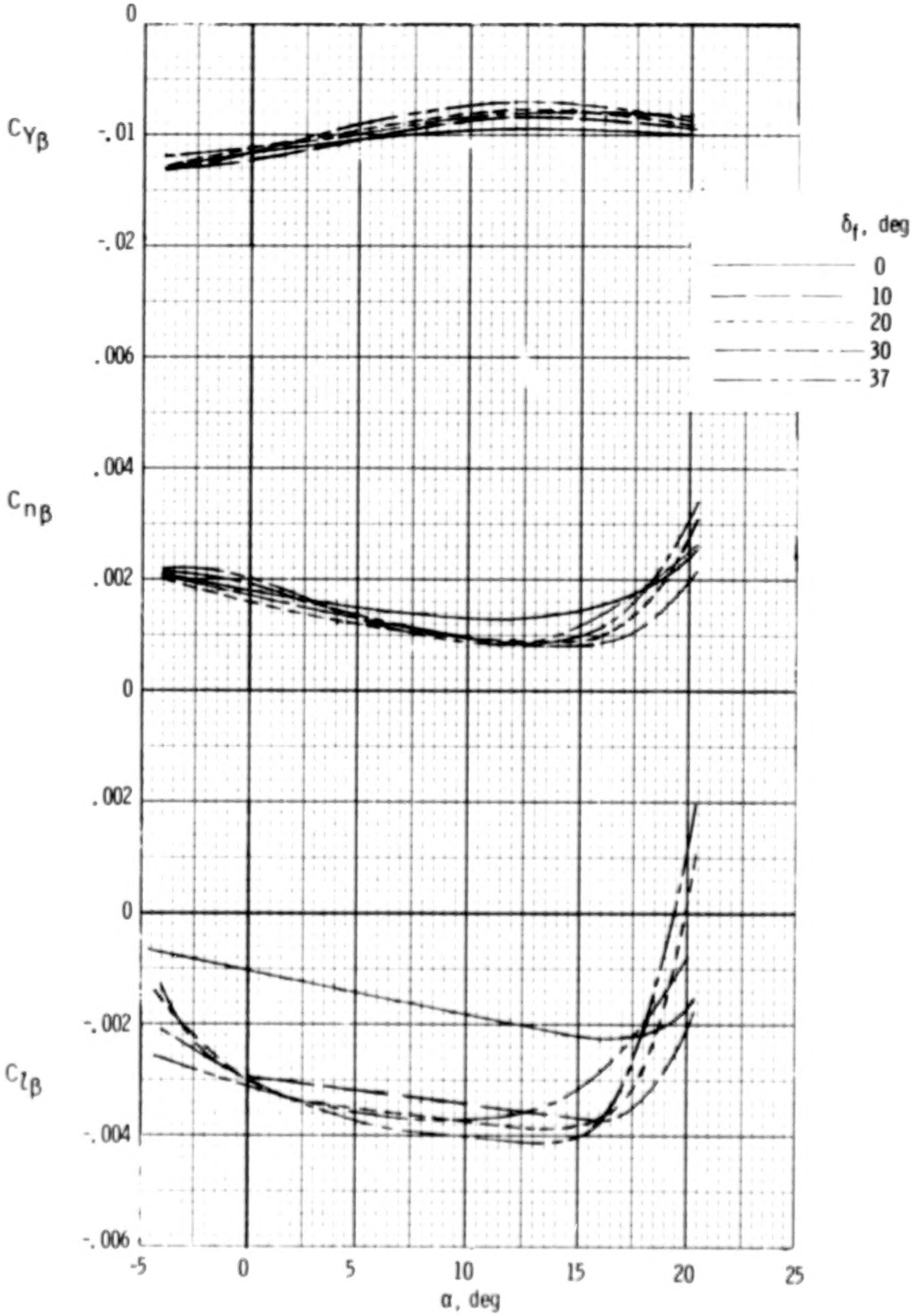

Figure 62.- Effect of flap deflection on static lateral-directional stability derivatives. $C_T = 0$ (stopped propellers).

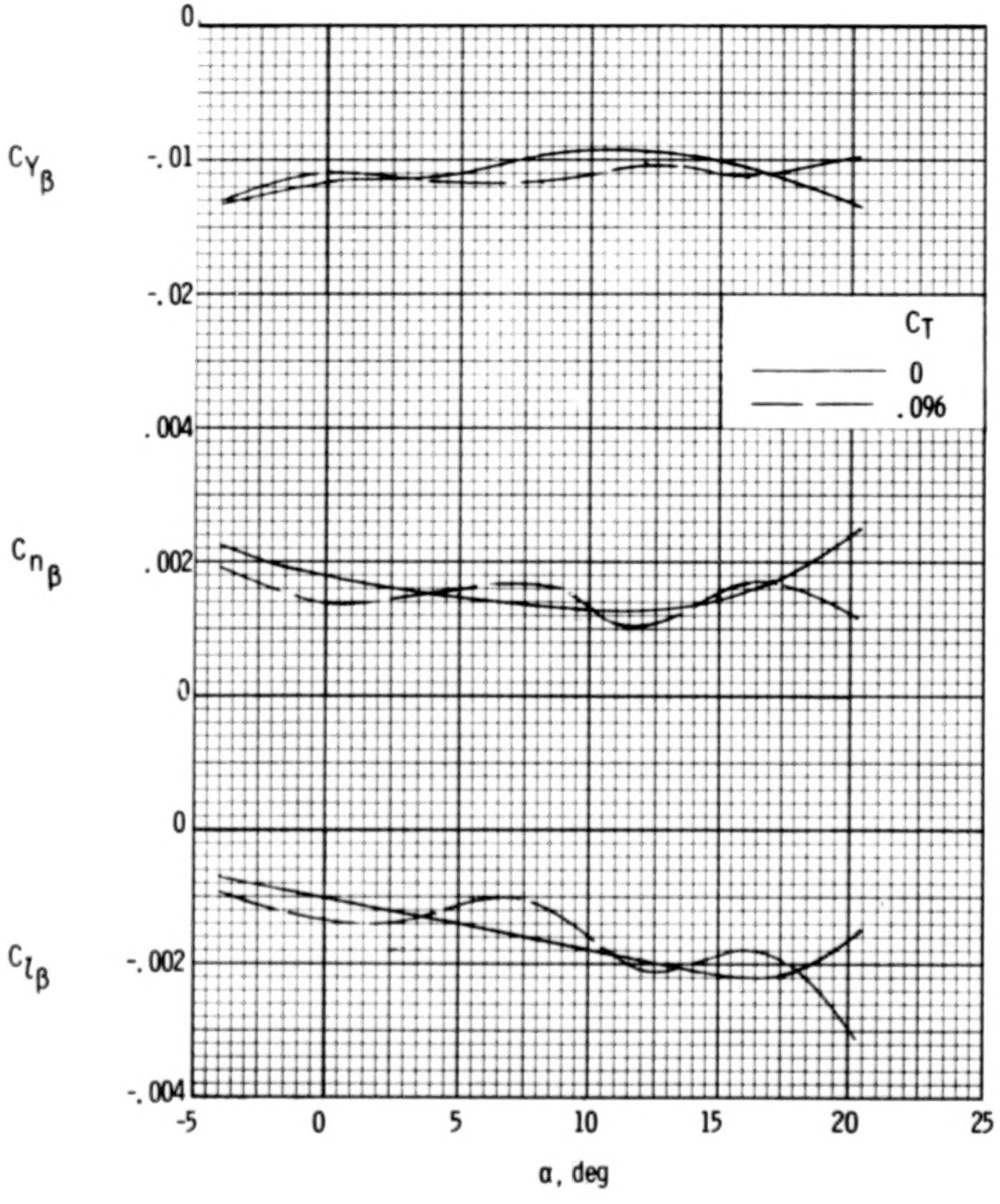

(a) $\delta_f = 0^\circ$.

Figure 63.- Effect of power on static lateral-directional stability derivatives.

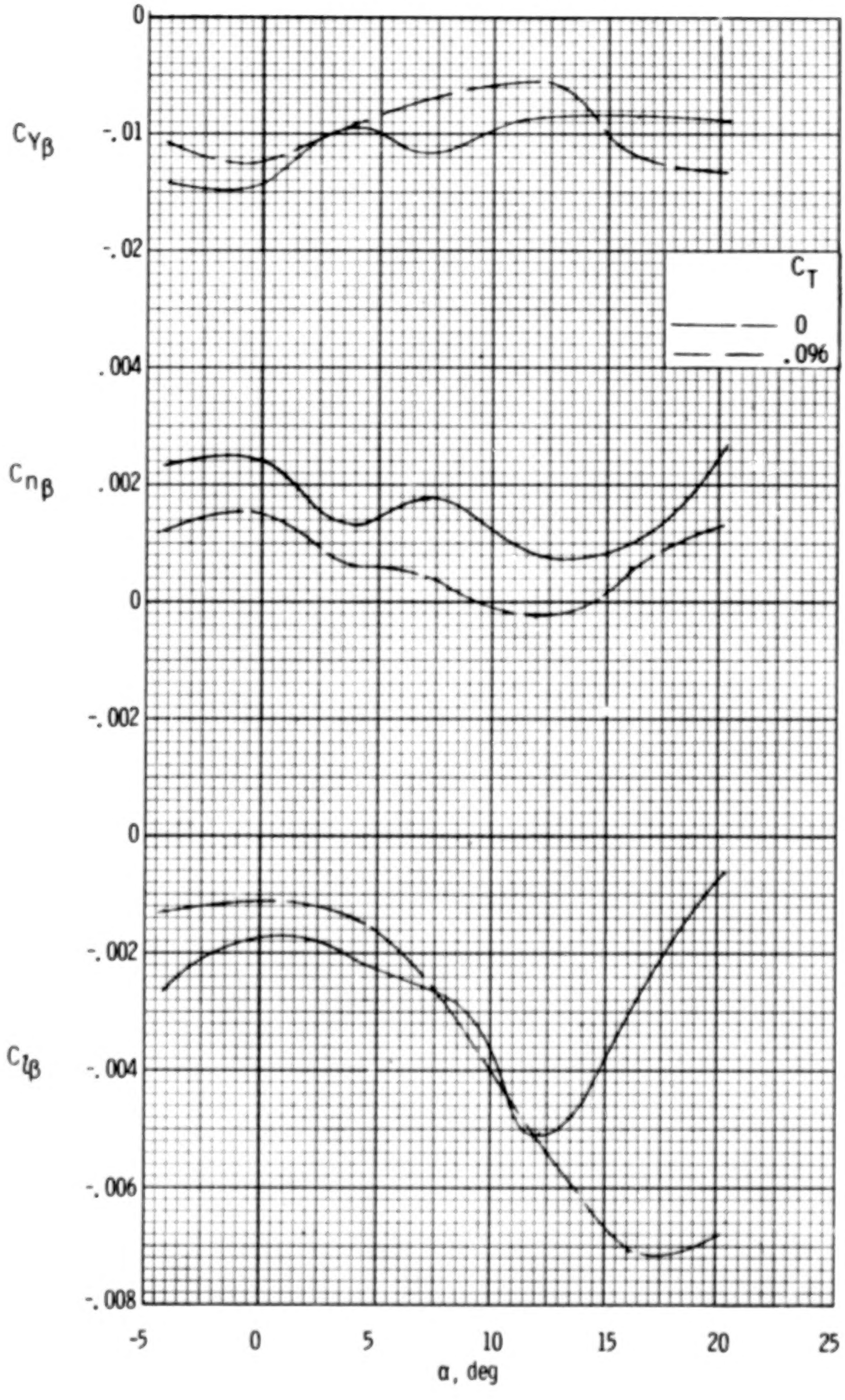

(b) $\delta_f = 37^\circ$.

Figure 63.- Concluded.

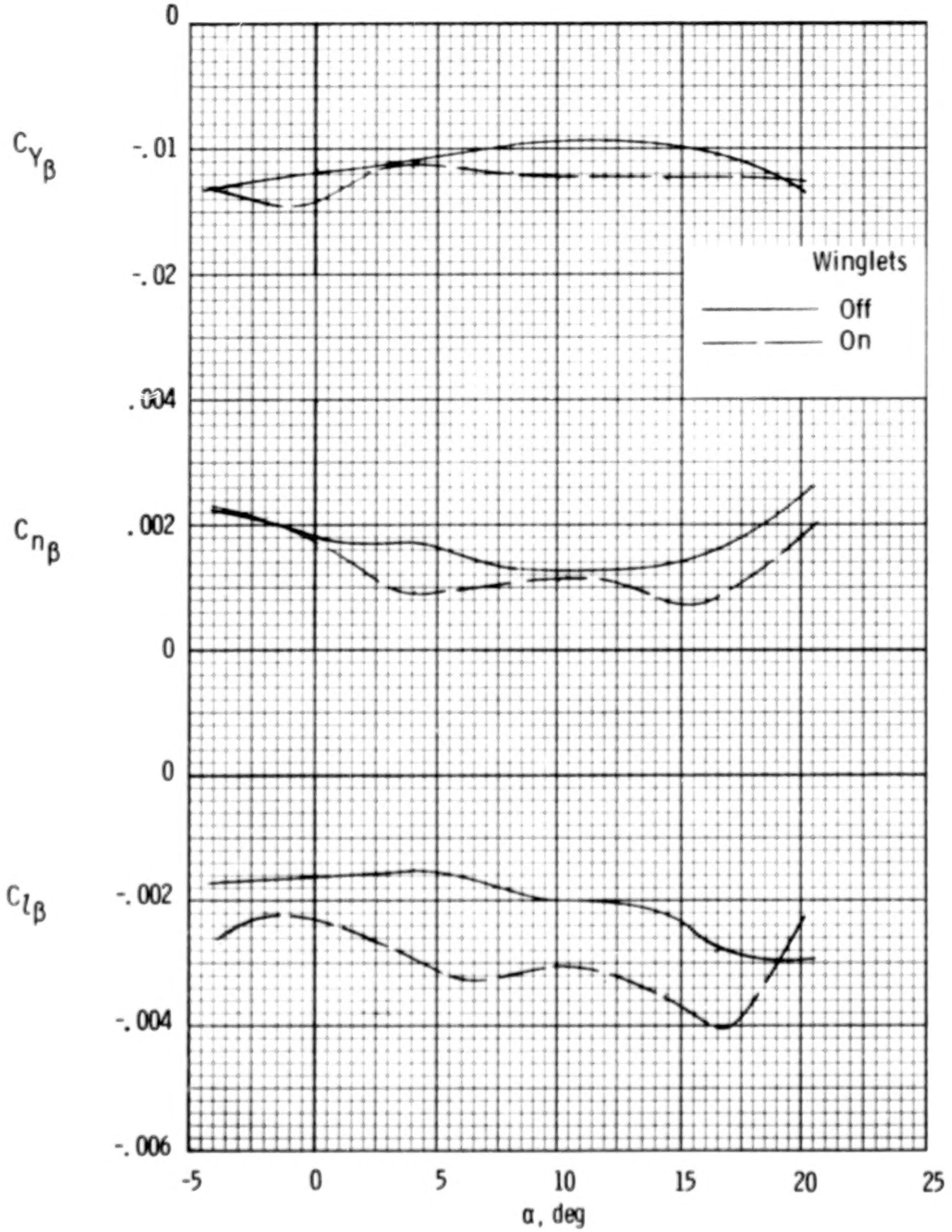

Figure 64.- Effect of winglets on static lateral-directional stability derivatives. $\delta_f = 0^\circ$; power off; propellers off; $R = 2.30 \times 10^6$.

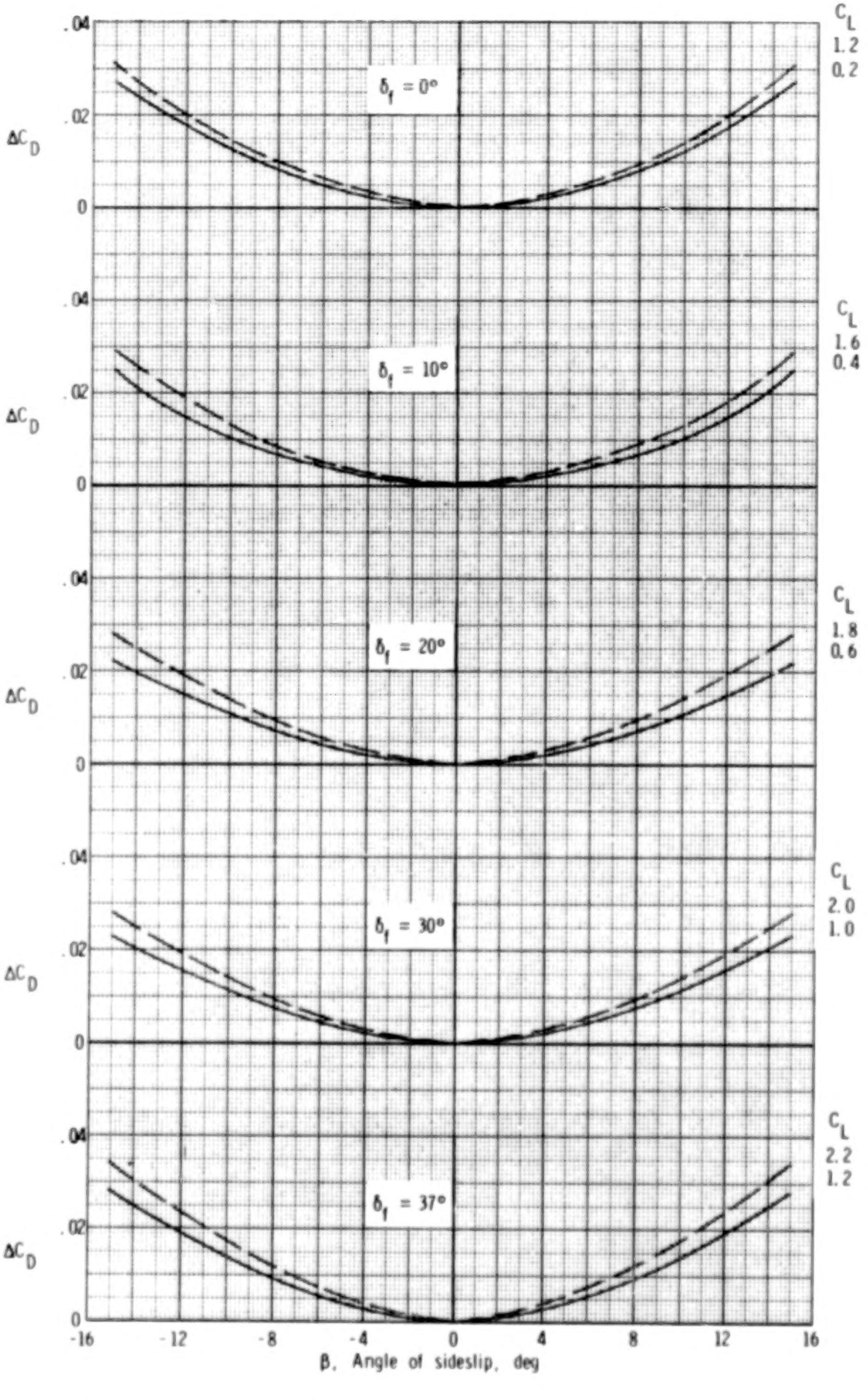

Figure 65.- Effect of sideslip on incremental wind axes drag coefficient for various flap deflections.

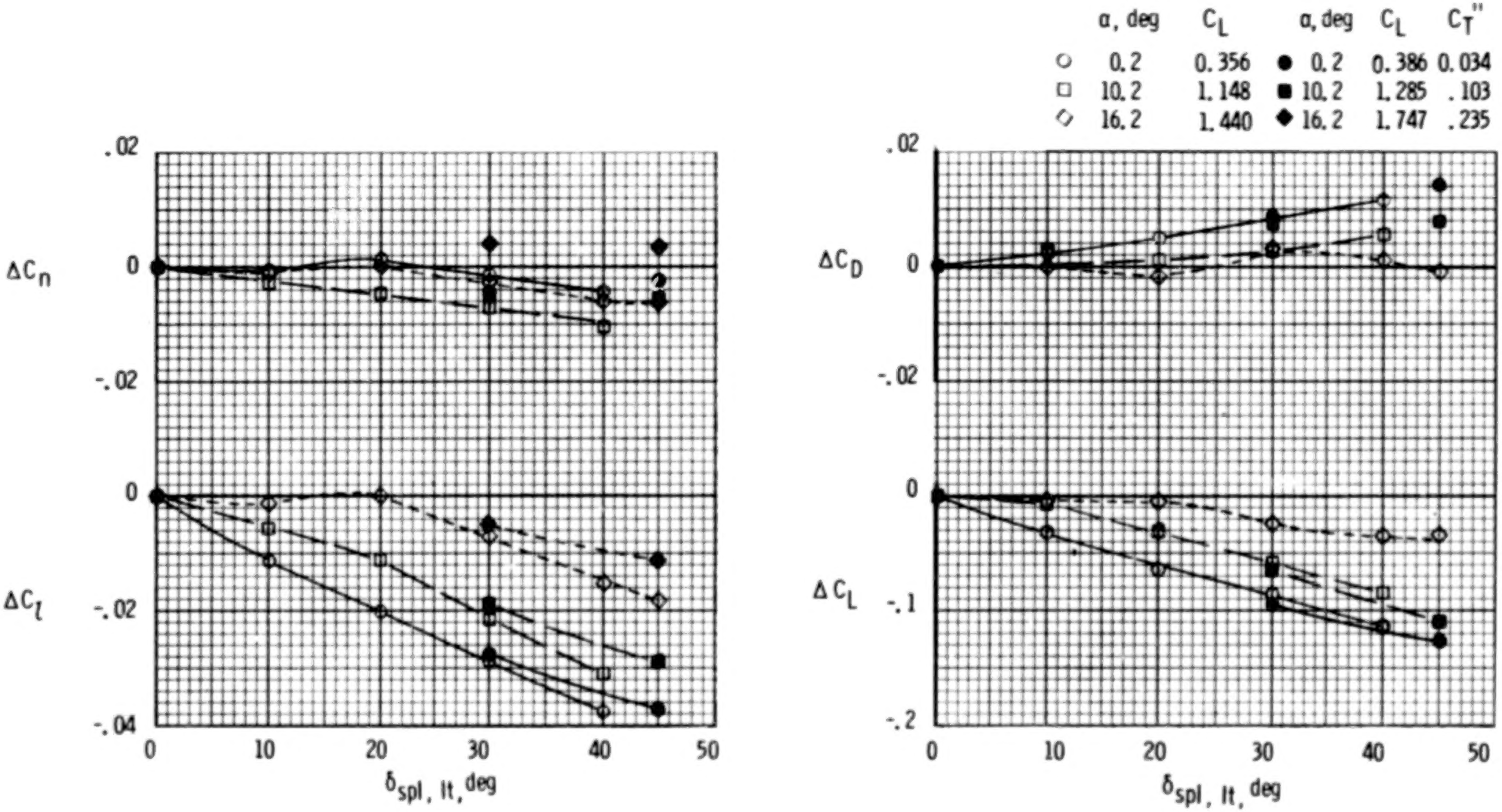

(a) $\delta_f = 0^\circ$.

Figure 66.- Effect of angle of attack, flaps, and power on spoiler effectiveness. (Solid symbols denote power for level flight at corresponding values of α.)

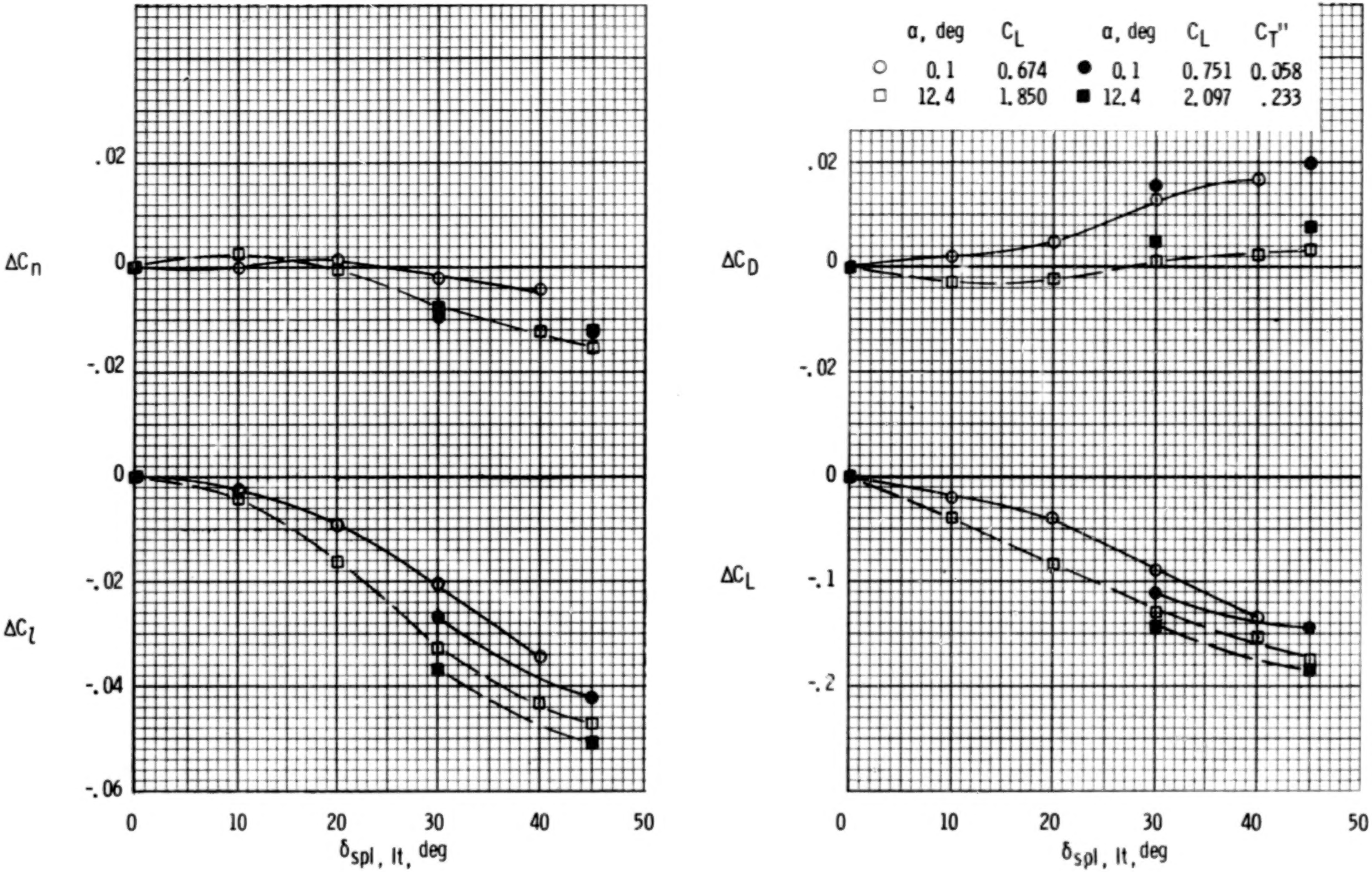

(b) $\delta_f = 10^\circ$.

Figure 66.- Continued.

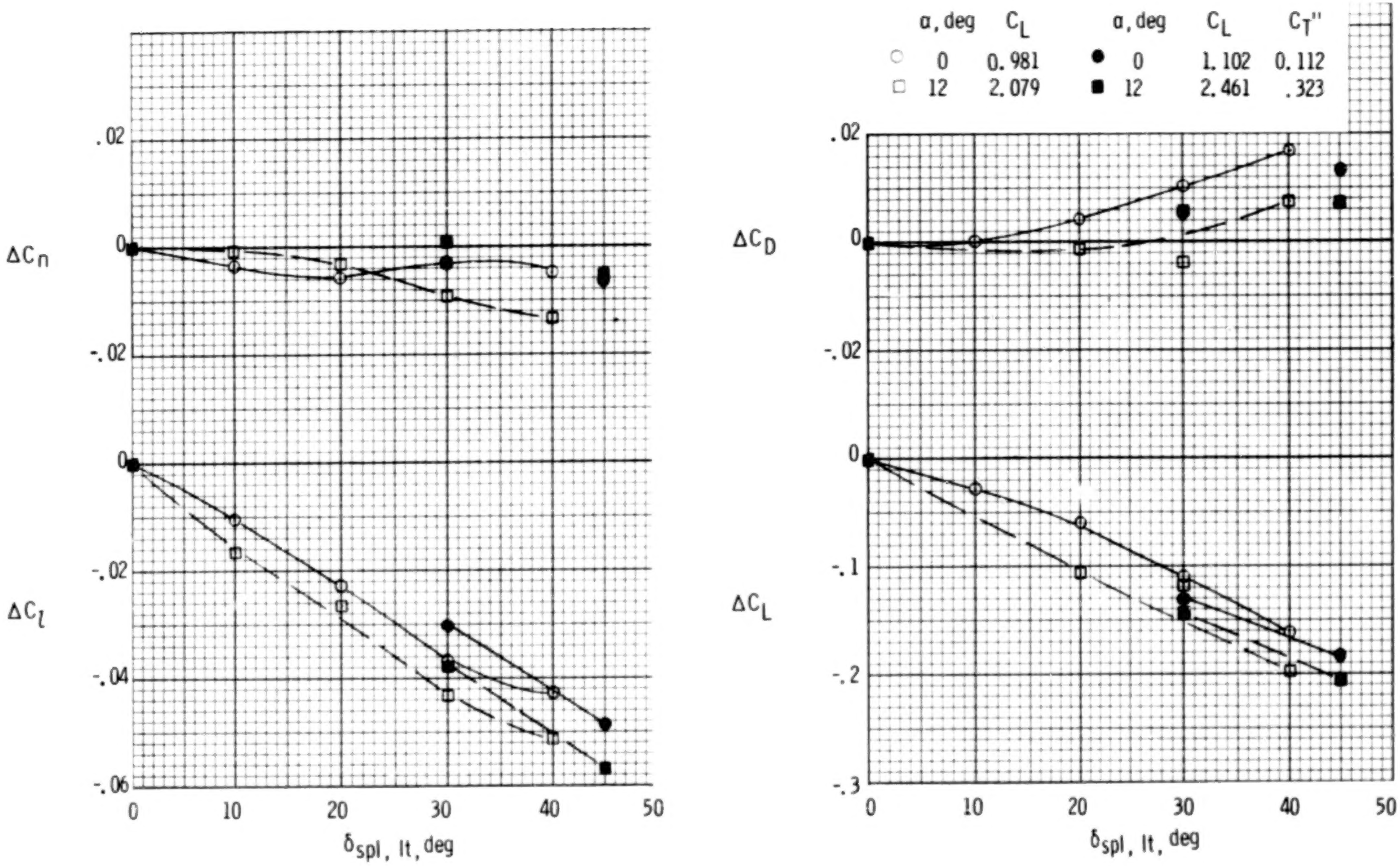

(c) $\delta_f = 20^\circ$.

Figure 66.- Continued.

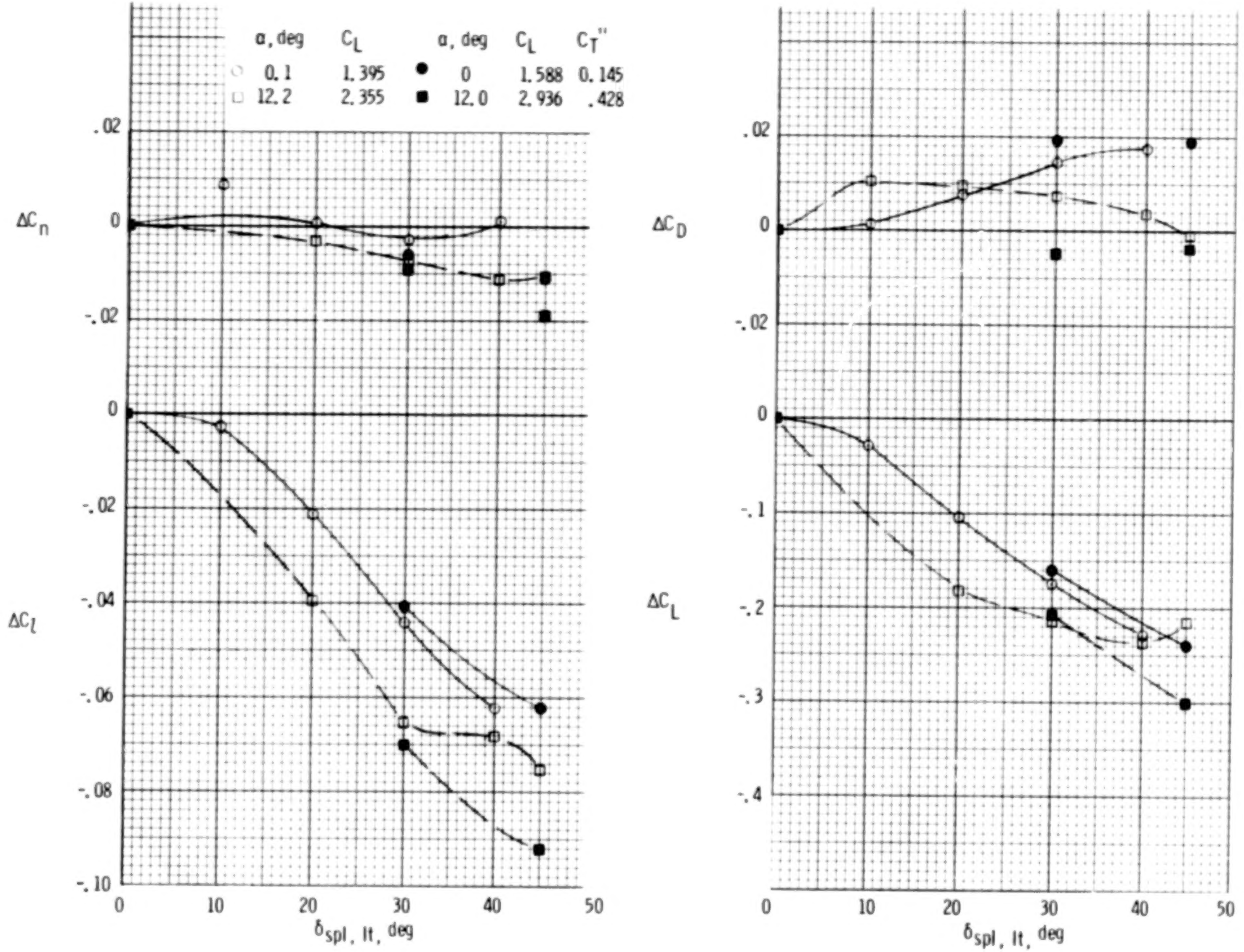

(d) $\delta_f = 30^{\circ}$.

Figure 66.- Continued.

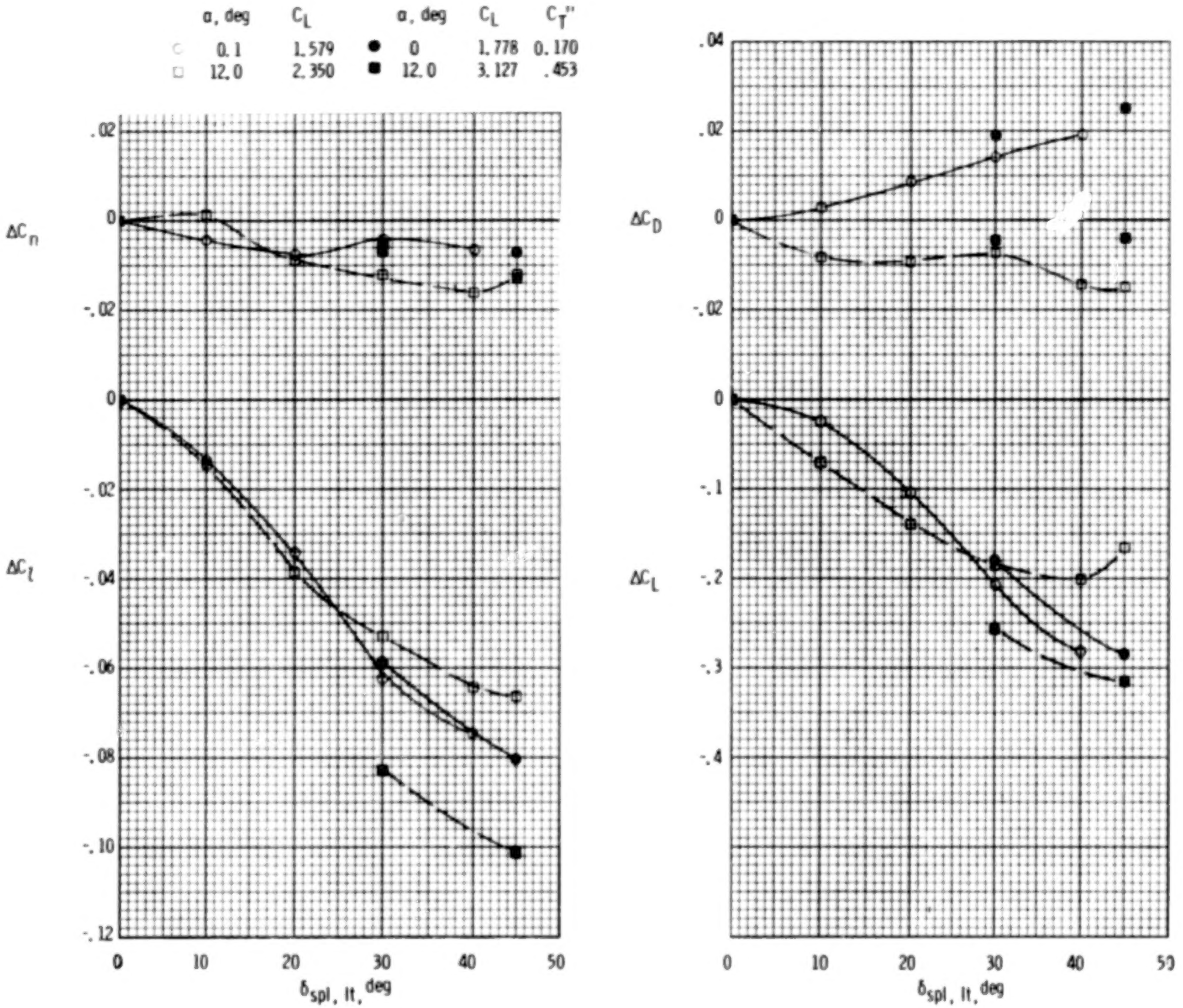

(e) $\delta_f = 37^{\circ}$.

Figure 66.- Concluded.

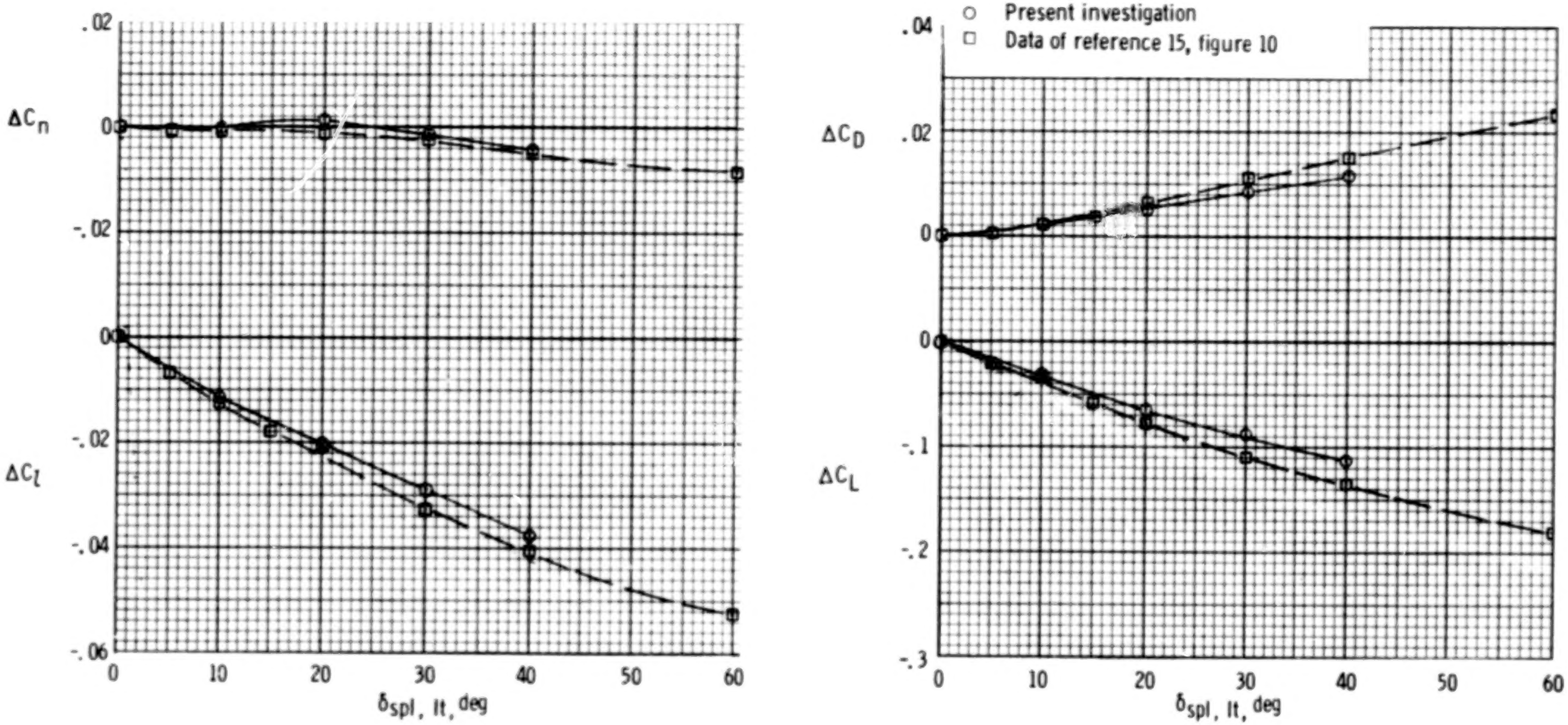

(a) $\delta_f = 0^\circ$.

Figure 67.- Comparison of spoiler effectiveness with results from tests of 1/4-scale semispan model (ref. 15). Power off; $\alpha = 0^\circ$.

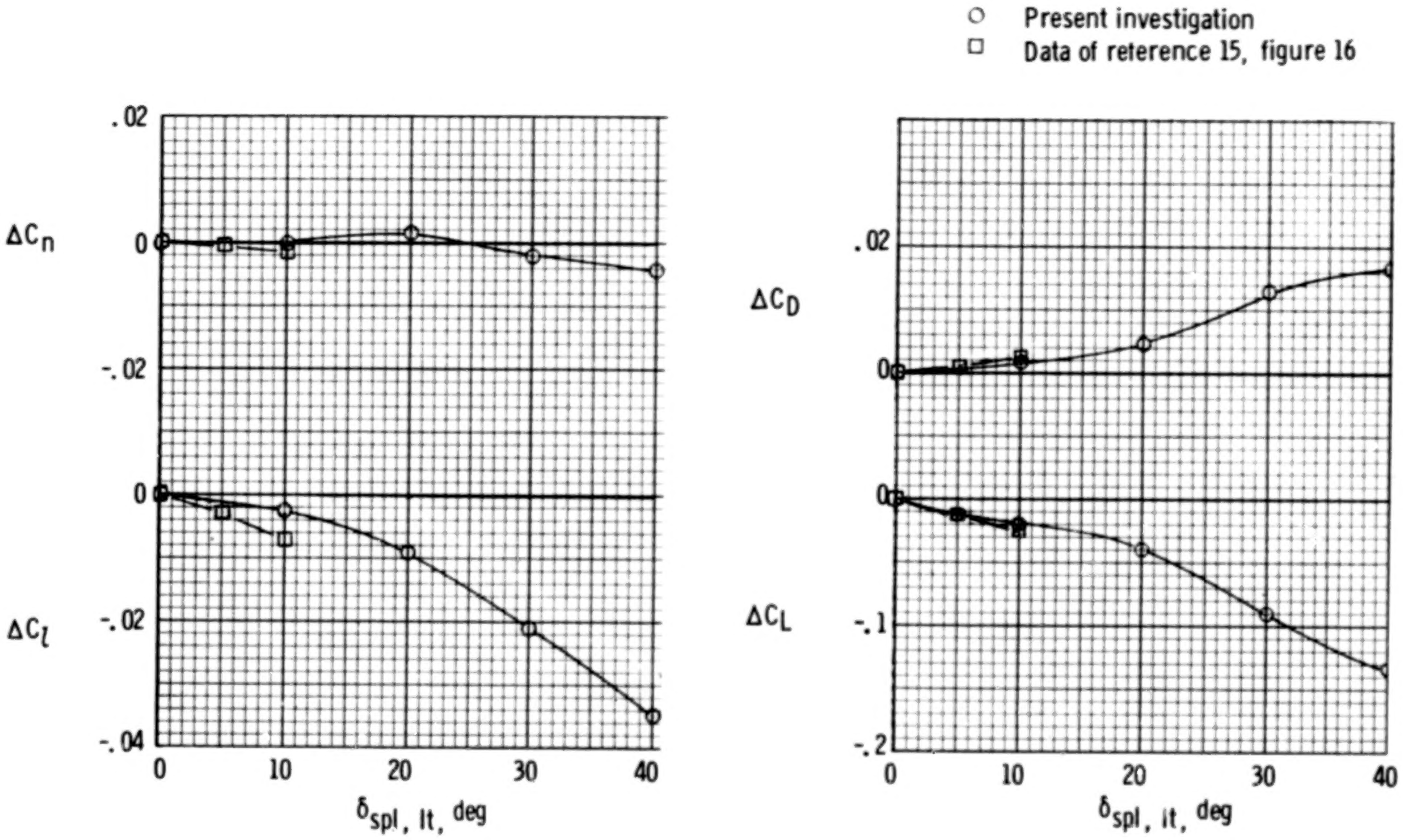

(b) $\delta_f = 10^\circ$.

Figure 67.- Continued.

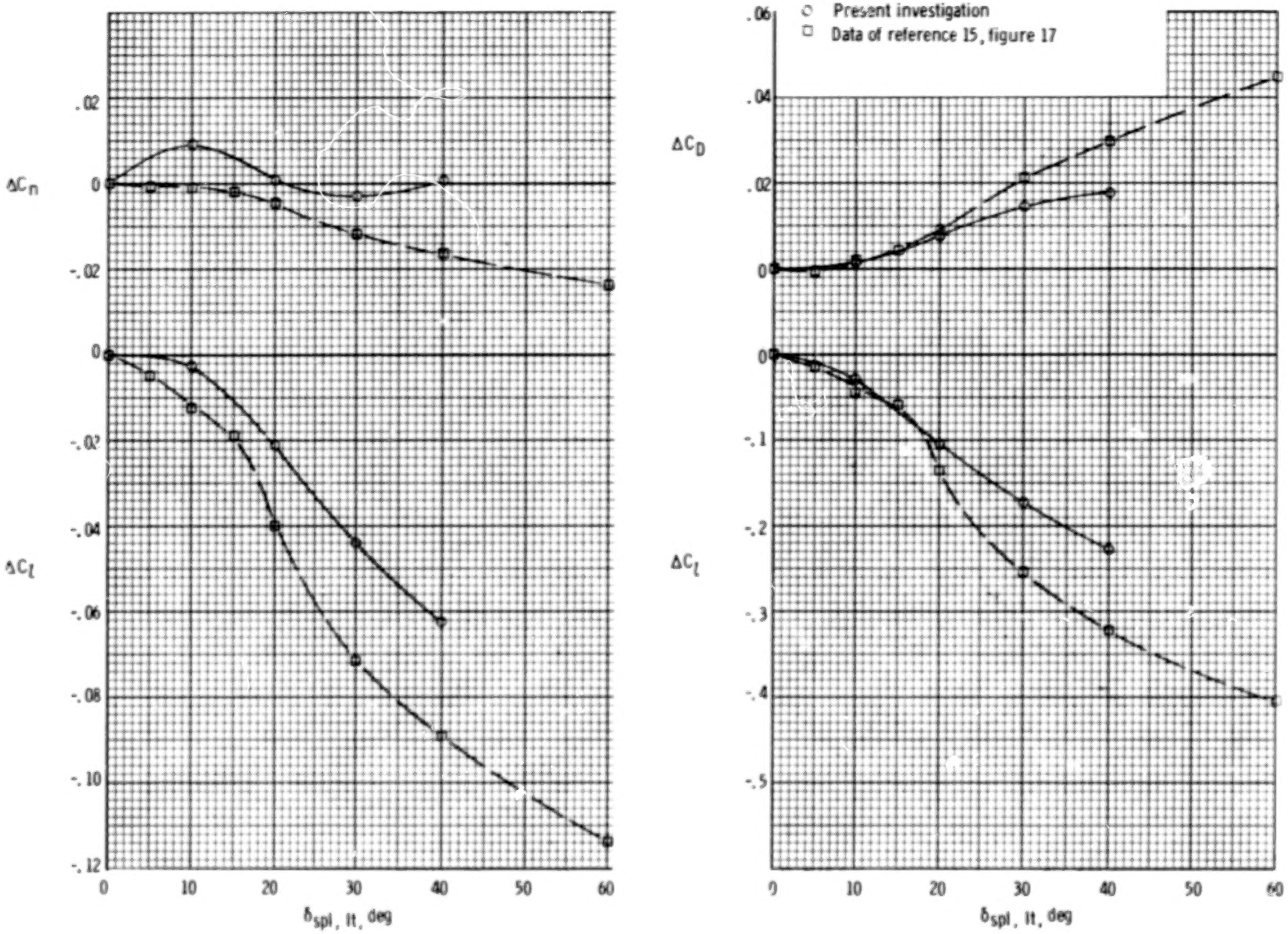

(c) $\delta_f = 30^\circ$.

Figure 67.- Continued.

NAS 1.60:1591

FULL-SCALE WIND-TUNNEL INVESTIGATION OF THE ADVANCED
TECHNOLOGY LIGHT TWIN-ENGINE AIRPLANE (ATLIT) ...
NASA TECHNICAL PAPER 1591... NATIONAL AERONAUTICS
AND SPACE ADMINISTRATION... MAY 1980

4 OF 4
24X
SUPTDOCS
GPO

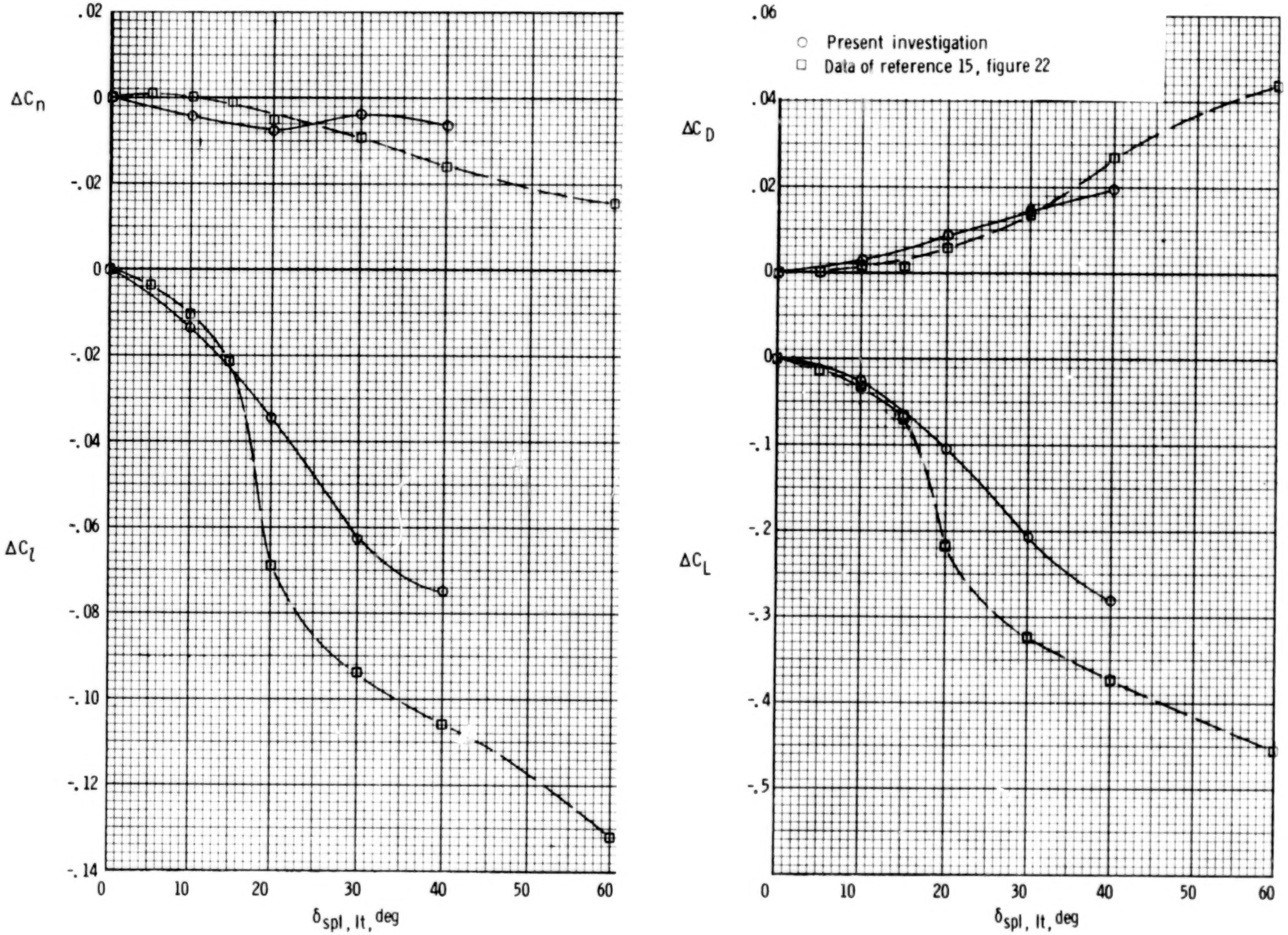

(d) $\delta_f = 37^\circ$.

Figure 67.- Concluded.

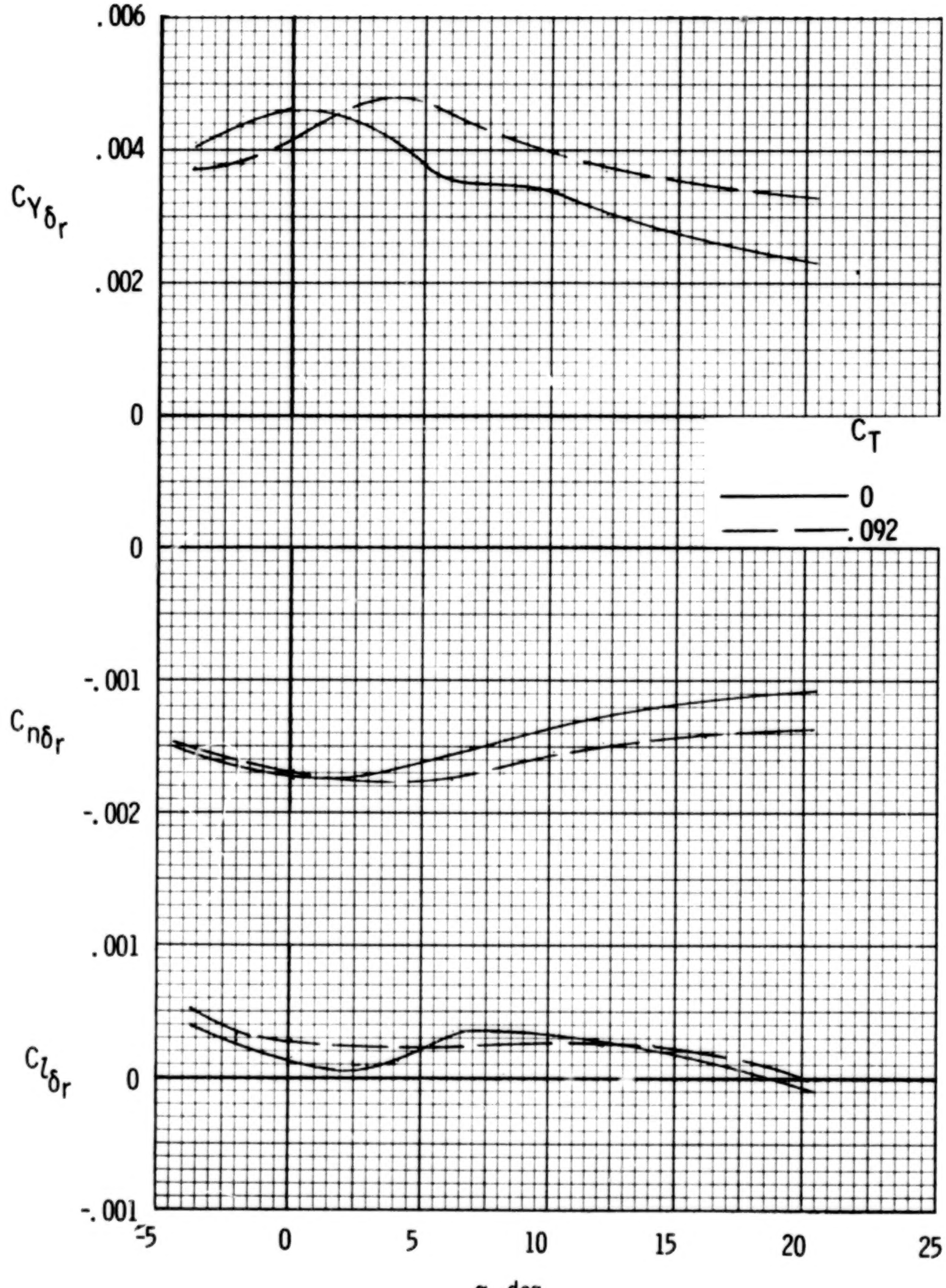

Figure 68.- Effect of power on rudder effectiveness with $\delta_f = 0^\circ$ (based on data for $\delta_r = \pm 10^\circ$ at $\beta = 0^\circ$).

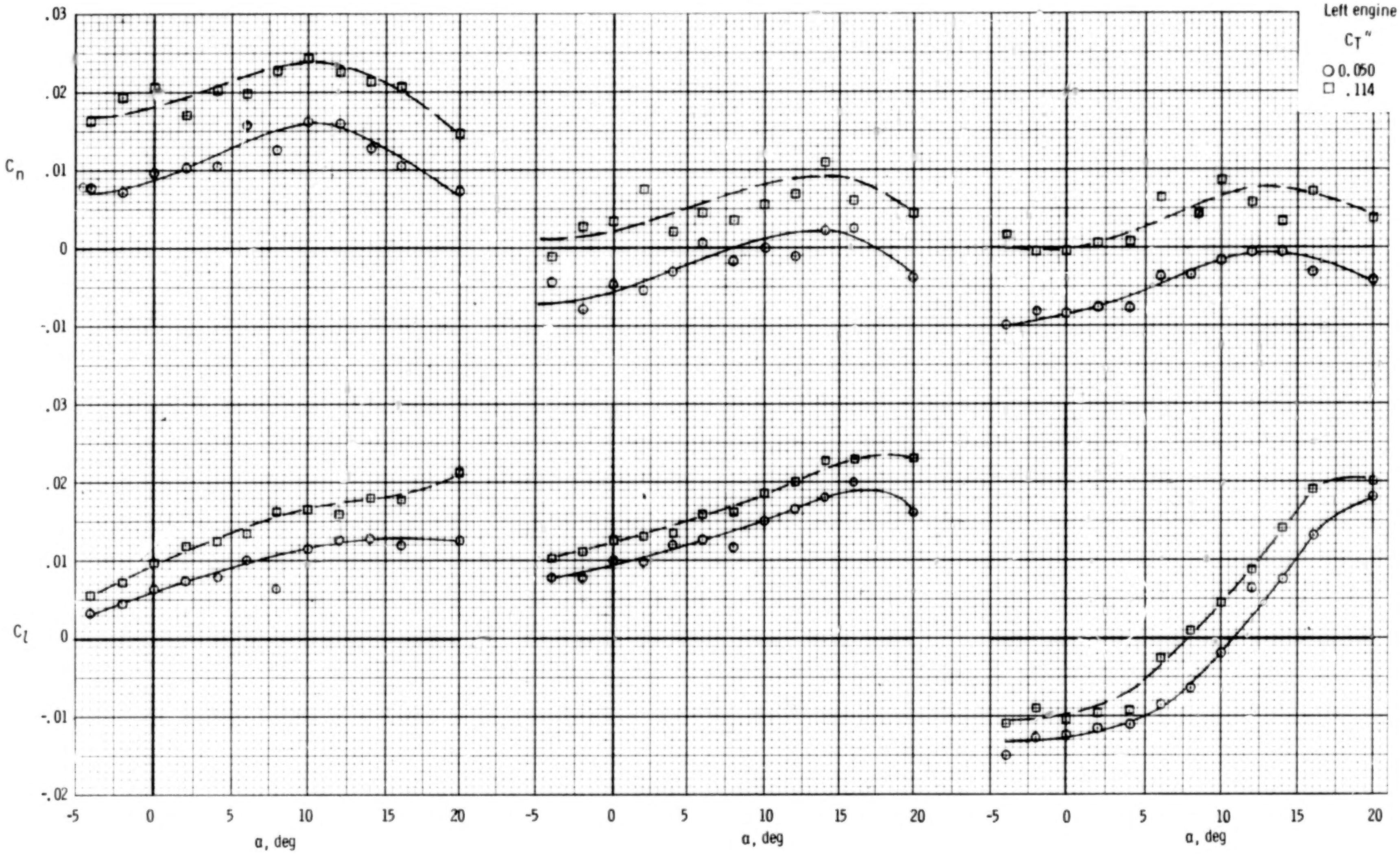

(a) Right engine out; controls neutral.

(b) Right engine out; $\delta_r = 10^\circ$; $\delta_{spl} = 0^\circ$.

(c) Right engine out; $\delta_r = 10^\circ$; $\delta_{spl} = 20^\circ$.

Figure 69.- Lateral-directional characteristics with right engine inoperative and with $\delta_f = 0^\circ$. $\beta = 0^\circ$.

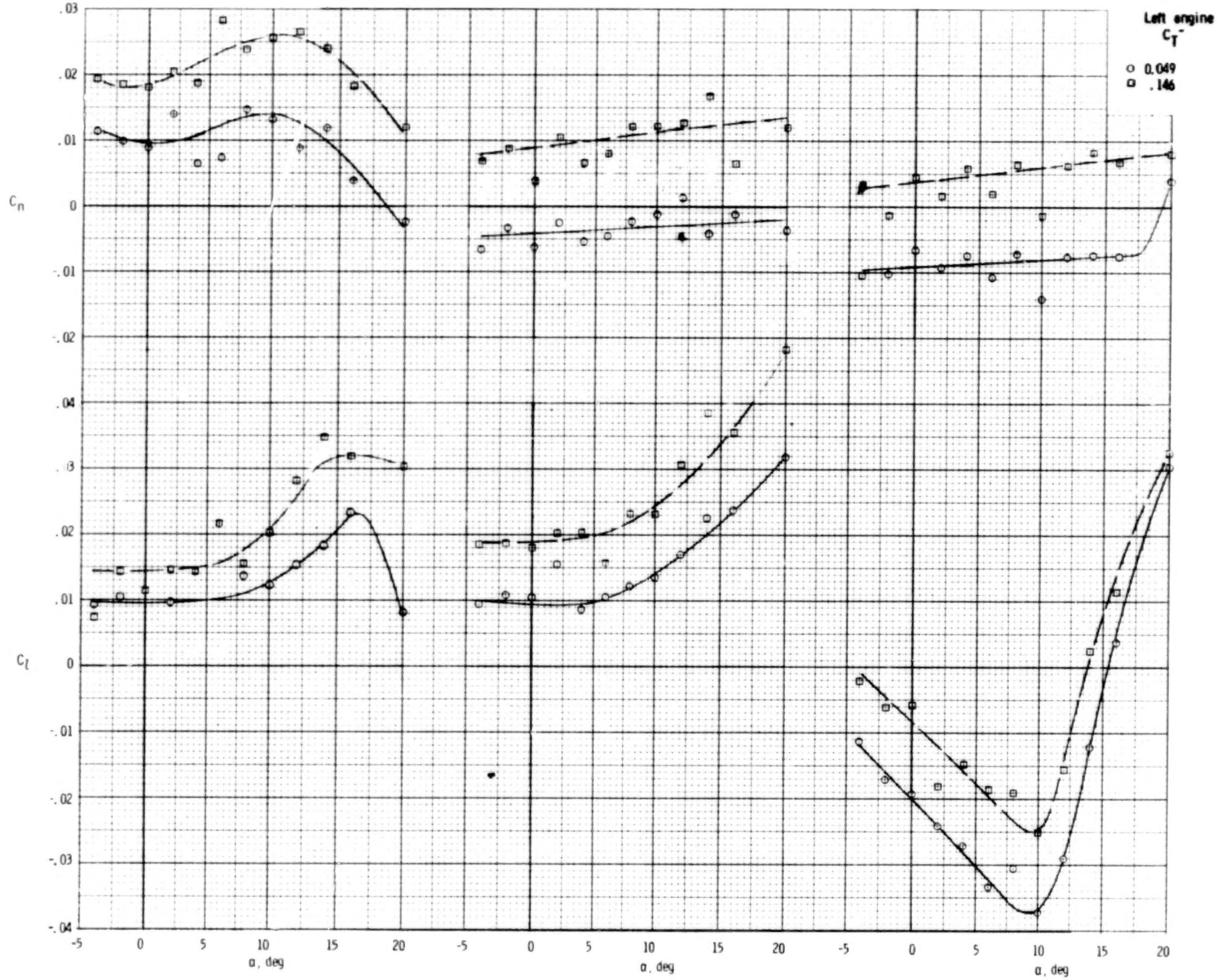

(a) Right engine out;
controls neutral.

(b) Right engine out;
$\delta_r = 10^\circ$; $\delta_{spl} = 0^\circ$.

(c) Right engine out;
$\delta_r = 10^\circ$; $\delta_{spl} = 30^\circ$.

Figure 70.- Lateral-directional characteristics with right engine inoperative and with $\delta_f = 20^\circ$. $\beta = 0^\circ$.

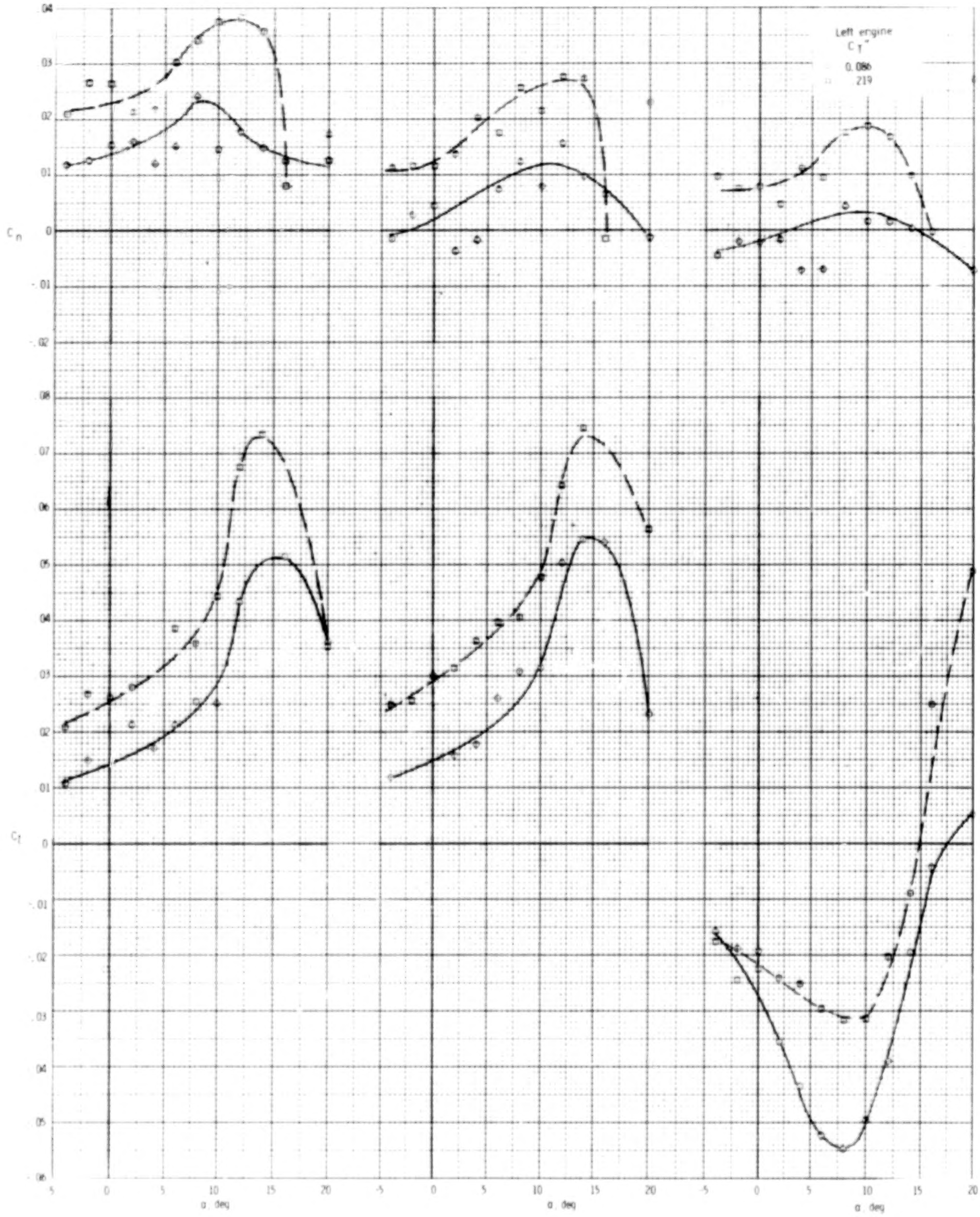

(a) Right engine out; controls neutral.

(b) Right engine out; $\delta_r = 10^\circ$; $\delta_{spl} = 0^\circ$.

(c) Right engine out; $\delta_r = 10^\circ$; $\delta_{spl} = 30^\circ$.

Figure 71.- Lateral-directional characteristics with right engine inoperative and with $\delta_f = 37^\circ$. $\beta = 0^\circ$

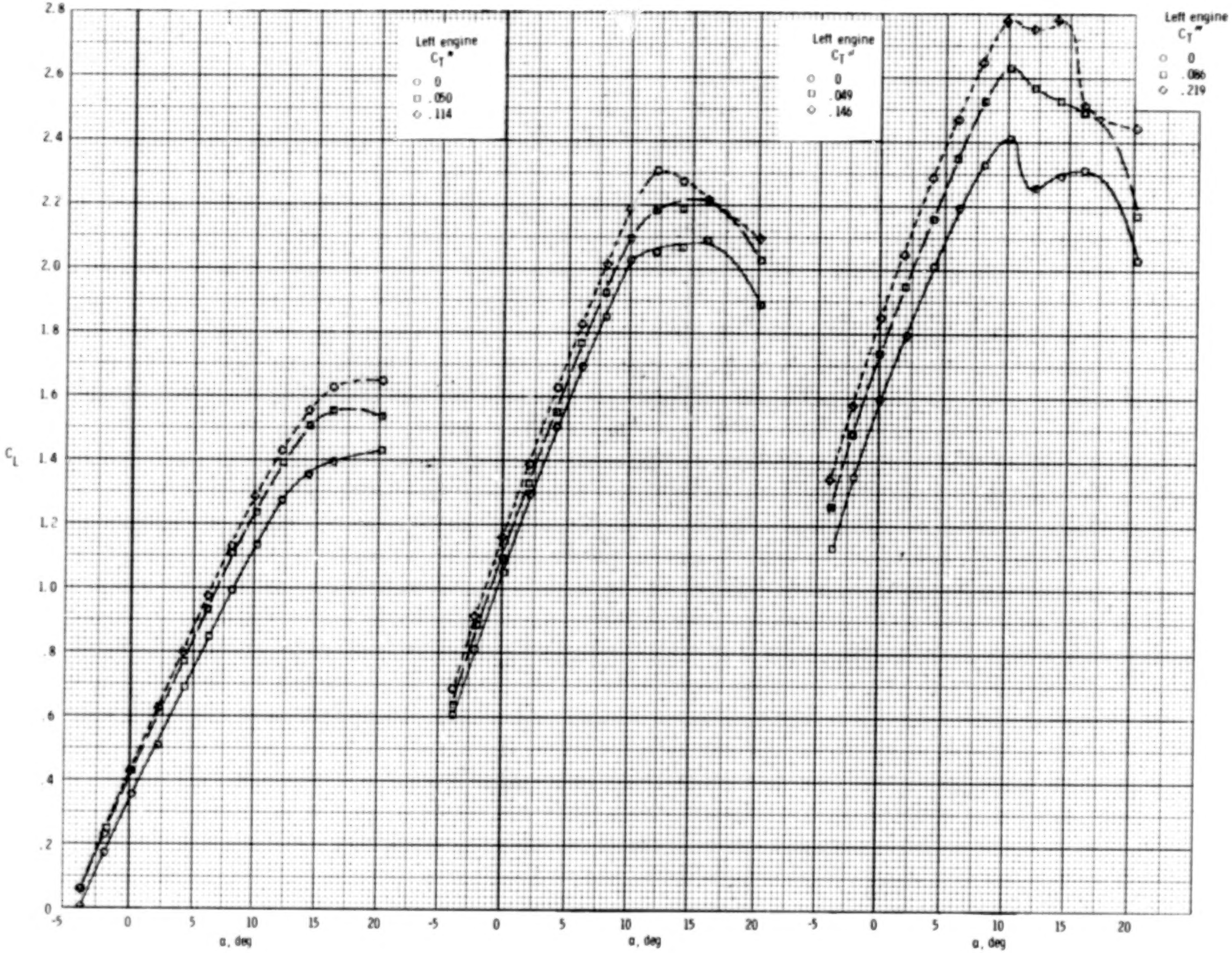

(a) $\delta_f = 0^\circ$.

(b) $\delta_f = 20^\circ$.

(c) $\delta_f = 37^\circ$.

Figure 72.- Effect of asymmetric power on lift characteristics. Right engine stopped with left engine at indicated shaft thrust coefficient; $\beta = 0^\circ$.

1. Report No. NASA TP-1591	2. Government Accession No.	3. Recipient's Catalog No.

4. Title and Subtitle FULL-SCALE WIND-TUNNEL INVESTIGATION OF THE ADVANCED TECHNOLOGY LIGHT TWIN-ENGINE AIRPLANE (ATLIT)	5. Report Date May 1980
	6. Performing Organization Code
7. Author(s) James L. Hassell, Jr., William A. Newsom, Jr., and Long P. Yip	8. Performing Organization Report No. L-13135
	10. Work Unit No. 505-10-13-02
9. Performing Organization Name and Address NASA Langley Research Center Hampton, VA 23665	11. Contract or Grant No.
	13. Type of Report and Period Covered Technical Paper
12. Sponsoring Agency Name and Address National Aeronautics and Space Administration Washington, DC 20546	14. Sponsoring Agency Code

15. Supplementary Notes

16. Abstract

An investigation has been conducted in the Langley Full-Scale Tunnel to evaluate the aerodynamic performance, stability, and control characteristics of the Advanced Technology Light Twin-Engine airplane (ATLIT). Data were measured over an angle-of-attack range from -4° to 20° for various angles of sideslip between -5° and 15° at Reynolds numbers of 2.30×10^6 and 3.50×10^6 for various settings of power and flap deflection. Measurements were also made by means of special thrust-torque balances to determine the installed propeller characteristics. Part of the investigation was devoted to drag cleanup of the basic airplane and to the evaluation of the effect of winglets on drag and stability.

17. Key Words (Suggested by Author(s)) Performance Stability Control General aviation Drag reduction Winglets	18. Distribution Statement Unclassified - Unlimited Subject Category 02

19. Security Classif. (of this report) Unclassified	20. Security Classif. (of this page) Unclassified	21. No. of Pages 209	22. Price* $6.00

*For sale by the National Technical Information Service, Springfield, Virginia 22161

NASA-Langley, 1980

90 %